The University of Sheffield
Department of Mechanical Engineering

Shaken Baby Syndrome:- Simulation via Computational and Physical Modelling

---

PhD Thesis

By J. Cheng

Supervised by Professor I. C. Howard, Dr. A. Yoxall

May 2008

The University of Sheffield
Department of Mechanical Engineering

Shaken Baby Syndrome:- Simulation via Computational and Physical Modelling

---

PhD Thesis

By Jingjing Cheng

Supervised by Professor Ian C. Howard, Dr. Alaster Yoxall

May 2008

TO ZHIFANG CHENG AND XIAOZHANG ZHEN

ACKNOWLEDGMENT

I would like to thank Professor Ian C. Howard and Dr. Alaster Yoxall, for providing the necessary support and supervision for completing this work. I would also like to thank Dr. Serge Cirovic for being so inspirational and helpful during many discussions. Special appreciation goes to Mr. Mike Rennison for providing numerous technical support and suggestions during the construction of experimental apparatus. I wish to thank Dr. P.V. Lawford and Dr. M.A. Parsons for contributing to this work with helpful medical knowledge and support. I wish to thank the Universities UK, University of Sheffield, for providing a PhD studentship for the author, and Arup UK for software and technical support. Finally, I would like to thank Zhifang Cheng and Xiaozhang Zhen, for providing the necessary atmosphere of understanding and support during the untold amount of hours required by this project.

ABSTRACT

The terms "abusive head injury" and "shaken baby syndrome" refer to a unique pattern of non-accidental traumatic injury occurring in children that many clinicians and researchers have good reason to believe is caused by violent shaking. Typical injuries include subdural haemorrhage, retinal haemorrhage as well as tears to cortical bridging veins. A major paradox is that the injuries induced by a shaking event are much more severe than those caused by even violent single impact head trauma, despite the relatively low accelerations in shaking. Infants younger than 6 months are significantly more vulnerable to the shaken baby syndrome than older infants and children, and one possible explanation is given that the softness of the infant brain and compliant skull structure allows violent motions to be set up (Cheng et al. 2005). These new mechanisms, could have an important role in explaining the basic mechanics of shaken baby syndrome.

Several models of infant head have been created with the optimized anatomical detail and accurate constitutive material properties from literature. The driving input to these models is derived from data generated in our research programme at the Transport Research Laboratory (TRL) (Brudenell 2000) with the theory of kinematics rigid body reconstruction. Numerical simulations are applied by using the finite element system LS-DYNA, and the consequences have been correlated with clinically observed damage in infant victims, and the brain skull boundary condition is investigated via the fluid structure interaction (FSI) method.

A shaking testing apparatus has been custom designed with computer aided design methodology (CAD), and is manufactured and assembled in the workshop. The driving of the rig is able to apply stable, repetitive linear motion within the range of accuracy and magnitude of human shaking. An experimental model has been constructed and mounted on the rig with important structures consisting of brain, cerebrospinal fluid (CSF), skull and infantile membrane.

The system validates the computational modelling by demonstrating the relative motion of the continuum system within the transparent skull replica. The research, as a first exploration in this area, contributes to the study of the infant abusive head injury, and is able to draw the data together in a discussion of the implications for the mechanics of the shaken baby syndrome.

CONTENTS

NOMENCLATURE

$a_{C\xi}$, $a_{A\mu}$, $a_{A\varsigma}$, $a_{B\mu}$, $a_{B\varsigma}$	acceleration tensor in local head frame	ms^{-2}
$a_{T\xi}$, $a_{T\mu}$, $a_{T\varsigma}$	acceleration tensor in local torso frame	ms^{-2}
β	decay factor	s^{-1}
δ	phase angle	rad
$\varepsilon_{C\xi}$, $\varepsilon_{C\mu}$, $\varepsilon_{C\varsigma}$	angular acceleration tensor in local head frame	$rads^{-2}$
ε	strain	
$\dot{\varepsilon}$	strain rate	s^{-1}
θ	rotation angle	rad
μ	viscosity	Pas
v	velocity of pneumatic cylinder rod	rad
v_{fr}	flow rate in the cylinder	rad
ξ_T, μ_T, ς_T	local torso cartesian coordinates	m
ξ_C, μ_C, ς_C	local head cartesian coordinates	m
ρ	mass density	kgm^{-3}
ρ_e	density of eulerian element	
ρ_l	density of lagranian element	
ρ_l^j	density of adjacent lagranian element j	
σ	stress	Pa
υ	Poisson's ratio	
$\dot{\varphi}_1$, $\dot{\varphi}_2$, $\dot{\varphi}_3$	three successive angle rates	rad s^{-1}
φ_1, φ_2, φ_3	three successive rotational angle	rad
ω_1, ω_2, ω_3	angular velocity tensor in local head frame	$rads^{-1}$
a_{real}	the acceleration from pneumatic ram	ms^{-2}
c	speed of sound	ms^{-1}
d	diameter	mm
dx, dy	gelatine horizontal and vertical displacement	mm
f	frequency	Hz
g	gravity acceleration	mms^{-2}
k	scale factor	
k', k''	dynamic stiffness	Nm^{-1}
m_{ram}	the mass on the platform	

m	mass	kg
o	local frame origin	
q_p	pure quaternion	
s, q_0	scalar component in quaternion	
$tg(\delta)$	loss factor	
t	time	s
u, u_x, u_y, u_z	unit magnitude vector of rotation axis	
$\vec{v}$, q_1, q_2, q_3	vector component in quaternion	
x_{gel}, y_{gel}	gelatine horizontal and vertical position	mm
x_{al}, y_{al}	reference horizontal and vertical position	mm
x, y, z	local cartesian coordinates	m
E	Young's modulus	Pa
E'	shortage modulus	Pa
E''	loss modulus	Pa
$Flux_j$	volume flux through adjacent element j	
F_{ram}	the load that the pneumatic ram can provide	Pa
G_0	short term shear modulus	Pa
G_∞	long term shear modulus	Pa
L_R	loading on right bearings	N
L_F	loading on left bearings	N
L_{life}	life time of linear guidance system	N
L, l	length	m
L_G	global translation vector	m
O	global frame origin	
P_G	global position vector	m
P_L	local position vector	m
P_{ram}	the pressure from the air compressor	
Q	quaternion	
R_1, R_2, R_3	three successive rotation matrix	
R	rotation matrix	kg m^{-4} s^{-1}
S_{ram}	the cross area of pneumatic cylinder (ram)	
T	transformation matrix	
T	depth	m
V	volume	m^3

V_e	volume of eulerian element	
V_l	volume of lagranian element	
W	width	m
X, Y, Z	global cartesian coordinates	m
$Xy'x'', Zx'z''$	the axis rotation sequence in euler convention	
$Xy'z'', Yx'z''$	the axis rotation sequence in cardan convention	

GLOSSARY

GENERAL TERMS

ALE	Arbitrary Lagrangian Eulerian
CAD	Computational Aided Design
COG	Centre of Gravity
Coronal Plane	Any vertical plane that divides the body into ventral and dorsal (front and back) sections.
Euler Angle	The three successive angles of rotation developed by Leonhard Euler to describe the orientation of a rigid body in 3-dimensional Euclidean space.
FE	Finite Element
FLR	Filter Lubricator Regulator
FSI	Fluid Structure Interaction
HIC	Head Injury Criteria
LVDT	Linear Variable Differential Transducer
MADYMO	Mathematical Dynamic Models
Quaternion	A non-commutative extension of complex numbers in mathematics that applied to mechanics in three-dimensional spaces.
Rotation Matrix	A 3×3 matrix that represents the orientation of the local frame with respect to global axes
Sagittal Plane	An imaginary plane that travels from the top to the bottom of the body, dividing it into left and right portions.
Transverse Plane	Any imaginary slice made that cuts the body into top and bottom sections.
TRL	Transportation Research Laboratory (UK)

MEDICAL TERMS (Stedman's 2006)

ABI	Acquired Brain Injury, the brain injury that is not inherited
Acute	Severe and sharp, high intensity
ADH	Acute Dura Haemorrhage, severe bleeding between the arachnoid mater and pia mater
Anterior	Denoting the front surface of the body in human anatomy

Arachnoid Mater	A delicate fibrous membrane forming the middle of the three covering of the central nervous system
Axon	The single process of a nerve cell that under normal conditions conducts nervous impulses away from the cell body and its remaining processes
ASDH	Acuate Subdural Haemorrhage, severe bleeding between the dural and arachnoidal membranes
Bilateral	Relating to, or having, two sides
Contra-coup injury	One which occurs at the opposite side of the brain to the site of impact
Contusion	A bruising of the brain, usually of the surface without rupture of the pia-arachnoid
CSF	Cerebral Spinal Fluid
CT	Computated Tomography
DAI	Diffused Axonal Injury, the spread axonal injury
Diaphragma Sellae	A fold of dura mater
Dura, Dura Mater	A tough, fibrous membrane forming the outer covering of the central nervous system
EDH	Extradural Haemorrhage, bleeding between the skull and the dura mater
Falx, Falx Cerebri	The scythe-shaped fold of dura mater in the longitudinal fissure between the two cerebral hemispheres
Fontanelle	One of several membranous intervals between the angles and margins of the cranial bones in the infant
Foramen Magnum	The large opening in the base part of the skull through which the spinal cord becomes continuous with the brain
Fossae	A depression usually more or less longitudinal in shape below the level of the surface of a part
Haemorrhage	Bleeding, an escape of blood from the intravascular space
Hypoxia	Decrease below normal levels of oxygen in tissue

ICP	Intro-cranial Pressure
Inferior	Situated below or directed downward
In vitro	Describing biological phenomena that are made to occur outside the human body
In vivo	Describing biological phenomena that are observed to be occurring within the human body
Medical Luer	A standardized system of small-scale plumbing fittings used for making leak-proof connections between a male-taper fitting and its mating female part on medical and laboratory instruments.
Meninges	The membranous coverings of the brain and spinal cord, e.g. arachnoid mater, dura mater, and pia mater
MRI	Magnetic Resonance Imaging
Myelination	The formation of a myelin sheath (a complex protein) around a nerve fiber (the axon)
Oedema, edema	An accumulation of an excessive amount of watery fluid in cells or intercellular tissues
Para	Beside or close to
Parasagittal	Close to the Sagittal plane
Pia, Pia Mater	A delicate vasculated fibrous membrane firmly adherent to the surface of the brain and spinal cord
Posterior	Denoting the back surface of the body
RH	Retinal Haematoma (Haemorrhage), Bleeding of the retina, the inner coating of the back of the eye
SAH	Subarachnoid Haematoma (Haemorrhage), bleeding into the subarachnoid space between the arachnoid and pia
SBS	Shaken Baby Syndrome
SDH	Subdural Haematoma (Haemorrhage), bleeding into the subdural space between the dura and arachnoid
Superior	Situated uppermost in the body in relation to another structure or surface.

Suture, Cranial Suture	A form of fibrous joint between the two bones of the skull
TBI	Traumatic Brain Injury
Tentorium Cerebri	A strong fold of dura mater which runs between the two hemispheres of the cerebellum

FIGURE LIST

TABLE LIST

CHAPTER 1: *INTRODUCTION*

1.1. THE RESEARCH BACKGROUND

The paediatric population is the most vulnerable group to be subject to intentional injury (homicide) (Ommaya, Goldsmith et al. 2002), 50% to 80% of which is trauma induced by the injury to the head. Shaken Baby Syndrome (SBS) is one of the major causes of fatality and morbidity for infants under one year. Estimates suggest that in each year, in the United States there are as many as 50,000 infants with more minor symptoms of SBS (Hoffman 2005), whilst in the United Kingdom approximately 200 infants are diagnosed with minor symptoms of SBS (Hose, Howard et al. 2003).

To summarise, clinically, there are three common signs that are considered to be an indicator of SBS: bleeding within the skull and up to the brain surface associated with brain swelling, bleeding on the back of the eye, and bruising to the shoulder or neck with the further possibility of rib fracture.

The victims could also be seen to suffer from short term effects such as vomiting, lethargy, seizures, breathing problems, or loss of consciousness, to the long term effects such as blindness, deafness, paralysis or mental impairment (Stein et al., 2005).

SBS is caused mostly by exhausted parents or babysitters who have lost patience during nursing and hence shake the baby violently for punishment or to stop the infant crying. Compared with dropping a child, which is widely considered to be harmful, shaking an infant moderately or casually, appears to be practised to some degree by many caregivers. They may not be aware that the misbehaviour of shaking is dangerous and a form of physical abuse, though the person who is accused of shaking the baby causing injury or death will be actually judged to have committed manslaughter or murder. One such example is the Paul Owens case in 1999, when a doctor received a female infant with no heartbeat in hospital, who later was declared dead. The autopsy showed extensive bleeding on the eyes and fracture of the ribs which made the doctor believe the infant was a victim of SBS. The 29-year-old father Paul Owens was charged with murdering and "causing her cruelty", although he has consistently denied the charges (BBC, 1997-2005).

The mechanism of SBS was accepted to be the rupture of the brain vessel inducing bleeding, until engineering testing (Duhaime et al. 1987) made a controversial declaration that shaking alone could not damage the brain because the loading during

shaking was too low to rupture the cerebral vessel unless impact was associated with the shaking.

Although cases which only involved shaking and which were reviewed by the neuropathologists do exist and became the protocol of the judgement, some other neuropathologists also called for caution in the diagnosis, as the sign of injury could be incorrectly attributed to other causes (Morad, Avni et al. 2004). An example of this is Rioch Edwards Brown's case in 2003 (BBC 1997-2005), where she was accused of shaking her baby son of six months and was later cleared as the trauma was produced during birth.

As a result, the court conviction of SBS, which could be made by the testimony of the expert witness, despite lack of other evidence previously, became less embraced by the many researchers in this field and indeed the legal system (Harding et al. 2004). Although there are other hypotheses to explain the mechanism, neither pathologists nor engineers have come to a consensus despite a series of clinical examinations and reconstructive tests.

It seems that in the absence of injury, the diagnosis criteria must be revised, if an accurate diagnosis is to be made. Biomechanical studies may give a valuable contribution, because the head injury criteria, which is scaled from the short pulse impact test with either adult cadaver or mammal, is criticized as inappropriate for long duration and repetitive shaking. In addition, a biomechanical study of head injury in recent years with numerical methods has demonstrated the different response of the brain between the skull with adult and paediatric structure (Cheng, Cirovic et al. 2005), the latter is compliant and not fully closed, which results in significant deformation to the brain tissue. Therefore at least one conclusion was reached within the biomechanical community: that further biomechanical investigation of SBS will not provide more evidence unless the infant head with delicate paediatric properties is considered.

1.2. The Objectives And Strategy

This PhD research intends to provide an understanding of the relationship between the specific paediatric head structure-anterior fontanelle and the intracranial injury mechanism of the infant head during violent shaking.

This aim was fulfilled by a three-year research programme divided into the following tasks:

1. Understand the trajectory and kinematic motion of the infant head.
2. Design an experimental rig with a simplified infant head model.
3. Understand physical tests using the test rig designed.
4. Record and analyse the results.
5. Reconstruct FE (Finite Element) model and analyse the result.
6. Study the skull brain boundary condition using FSI (Fluid Structure Interaction) methods.

1.3. The Organization Of The Thesis

The thesis is structured as follows: Chapter 2 gives the review of the research background. Chapter 3 discusses the head motion reconstruction. Chapters 4, 5 and 6 describe the process of the design, production, and analysis of the physical shaking phenomenon. Chapter 7 and 8 include the numerical simulation of the experimental tests and SBS. The final two chapters 9 and 10 summarize the overall study and provide the recommendations for future work.

CHAPTER 2: *LITERATURE REVIEW*

2.1. INTRODUCTION

Shaken Baby Syndrome (SBS) is diagnosed as an abusive infantile head injury whereby the victim normally suffers severe central nervous system damage whilst having rare external signs of injury.

It was firstly reported by Guthkelch (1971) and Caffey (1972) to identify typical injuries to infants from violent shaking after the authors had reviewed several cases of young infants suffering from intracranial bleeding without external trauma and whose parents or assailant had admitted to shaking the infant "in an insane rage" (Caffey 1972).

The neuropathological diagnosis of the SBS was widely interpreted as the triad criteria (Shannon and Becker 2001): the subdural haemorrhage (Figure 2.11), the retinal haemorrhage (Figure 2.13), and the skeletal injury such as neck and rib fracture (Figure 2.1). Some other less frequent injuries are also reported such as the cerebral edema, subarachnoid and epidural haemorrhage, or parenchymal contusion. The initial clinical inspection may also include vomiting, respiratory distress, or concussion (a common symptom shares by other paediatric illnesses). It is age dependent and most of the victims are younger than 6 months. Approximately one third of SBS victims die, whilst two thirds survive with either seriously permanent brain damage, or minimal long term brain effects, including neuromotor, visual, or hearing impairments ranging from minor to complete loss of function (Wolfson et al. 2005; Hoffman 2005). SBS once defined, is always considered to be violent and intentional, implying that it is caused by impatient parents losing their temper. The involved parents could be judged in the court for murder or manslaughter. If the infant is not killed, it will be invariably taken away from them. Each year in the United States, as many as 50,000 infants are reported with minor symptoms of SBS, while in the United Kingdom, as many as 200 infants each are diagnosed as the victims of the abusive shaking (Hose et al. 2003; Hoffman 2005).

The injury mechanism for SBS was defined and postulated from the early research of Guthkelch (1971) and Caffey (1972) to be the result of shaking an infant with a relatively large head supported by relatively weak neck (Figure 2.1). The resulting rotational acceleration-deceleration of the head causes the relative rotational motion of the brain inside the skull cavity due to the inertia effects. The bridging veins connected to the cortical surface and the dural venous sinuses are stretched and hence fail, leading

to neurological damage (Figure 2.1). There may also be fracture at the cervical junction. At the time the hypothesis was being raised, no biomechanical experiment could be used directly to testify the theory, except Ommaya (1968)'s whiplash test, where he set up an experiment using an anaesthetised rhesus monkey mounted on a piston-driven rig. The repetitive motion of the piston drove the head that whiplashed around the mounted neck. The resultant anatomical examination firstly exposed the ruptured vein and diffused axonal injury under the rotational acceleration, even though the magnitude of the load is much higher than human shaking and as strong as the car crash, and experimentally it proves the shearing injury mechanism.

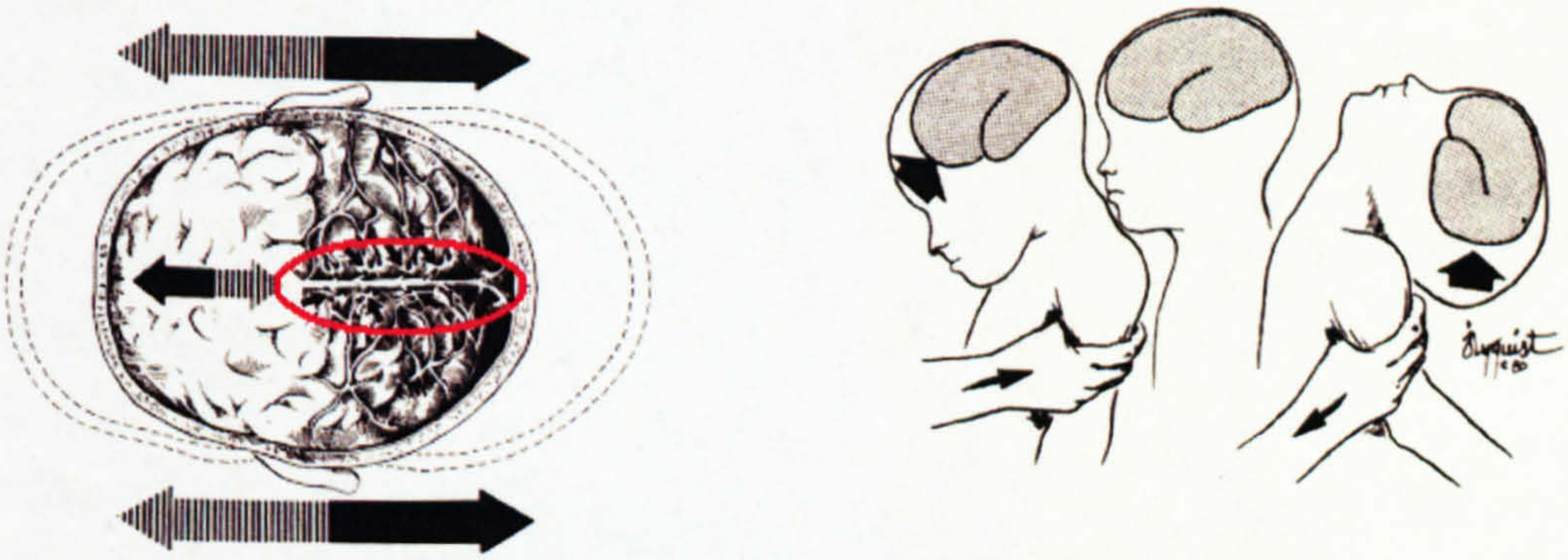

Figure 2.1. *Anterioposterio motion of shaken baby syndrome in which the red circle highlights the position where the bridging vein ruptured (Owen 2002).*

Combining with the clinical-pathological evidence afterwards, SBS became a broadly defined concept with which the pathologist can separate the non-traumatic infant head injury from other accidental head trauma, moreover shaking an infant is undoubtedly dangerous and abusive.

It was not until 1987 that Duhaime et al. (1987) and later her colleagues Prange et al. (2003) produced the infant surrogate dummy to reconstruct the shaking, falling and impact situation to investigate the dynamic mechanism of head injury. By measuring the rotational acceleration with the loading interval, the shaking was found to produce the least rotational response equal to that of a minor fall and hence far lower load than that experienced during impact from a fall. The result was scaled into a tolerance scale curve, which was firstly summarized by Thibault and Gennarelli (1982), and later by Duhaime et al. (1987) to give the relationship between injury threshold and the angular loading from the previous test on primates and adult corpus, the shaking response is found out

to be well below the injury range. The fact that such biomechanical models did not comply but conflict with the popular pathological deduction, concludes that head injury does not occur by shaking unless impact occurs. This discrepancy produced a major contradiction between the biomechanician and the paediatrician. The possible doubt on Duhaime model's reliability inspired Cory et al. (2003) and Wolfson et al. (2005) to physically and numerically reproduce the model as well as the test. The slight variation of the outcome could not deny the argument anyway.

This contradiction leads to the appearance of the new suspicion within the pathologist community that a misunderstood interpretation may have existed in reviewing suspected shaken baby cases from the very beginning. Donohoe (2003)'s argument "the evidence for shaken baby syndrome appears analogous to an inverted pyramid" reflected one of the major arguments that the evidence of impact has company with the large percent of the report shaken baby cases. The evidence of shaking only induced injury becomes ambiguous (Shanoon and Becker 2001; Donohoe 2003; Geddes and Plunkett 2004; Uscinski 2006).

Meanwhile, some neuropathologists started looking for an alternative explanation, that if shaking alone does not give enough force to rupture the tissue, there may be some indirect procedure that damages the tissue spontaneously and gradually. Geddes gives out a profound hypothesis after reviewing 50 cases of infantile diffused brain injury, that shaking produced cervical fracture leading to brain swelling, which is the major factor to generate the subdural and retinal haemorrhage (Geddes and Hackshaw 2001; Geddes and Vowles 2001; Geddes and Tasker 2003; Geddes and Whitwell 2004). This hypothesis, known as the "Geddes Hypothesis" and embraced by a few, was used in the court proceedings as a reverse evidence for the suspects to appeal from the murder or manslaughter charge. Although this hypothesis was accepted by other neurological experts to some extent, its estimation that the minor force might have caused serious injury gains inevitable suspicion, that if it is true, such injury would be found out in normal life but actually it is extremely rare. Therefore Geddes claims that such a concept was meant to stimulate debate rather than to be taken as fact.

Until the present there was no better explanation to reduce the gap between the paediatrician and biomechanician of their divergent opinions. The only agreement reached so far is that none of the methods carried out, including the clinical injury comparison, animal studies, biomechanical reconstruction, mathematical modelling, or

the tolerance scale of the head injury criteria, has ever fully explained, and hence been comparable to, the human infantile head injury.

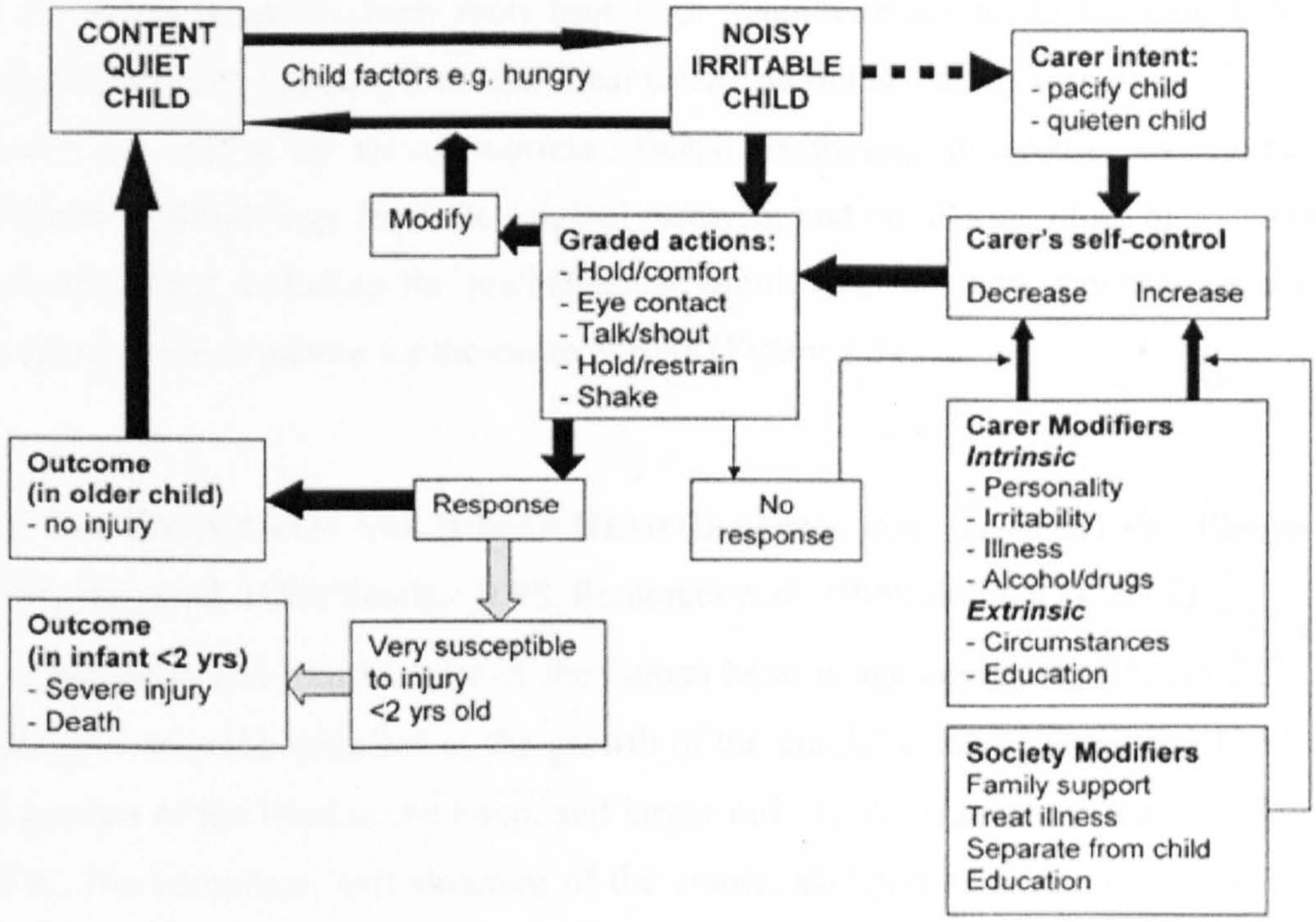

Figure 2.2. *The various scenarios, responses and relationships that might govern how appropriate and inappropriate actions on children and infants could arise (Cheng et al. 2005).*

The reasons for this lack of comparability maybe explained for the following reasons. Non-intrusive methods to the clinical inspection on the neurological injuries such as ruptured bridging veins, breaking neck etc., should be improved to avoid the second damage during the post-mortem autopsy (Stein et al. 2005). The other alternative but credible cause of the triad of injuries is waiting to be found out by further careful investigation of cases (Richards et al. 2006). The compliant infant skull model with appropriate paediatric properties is required to be applied during the physical multi-body dynamic simulation (Cory and Jones 2003). The material characteristics of the biological tissue not only in vitro but also in vivo, associated with the age dependent properties need to be tested and summarized by some proper constitutive equations. For power assistant analysis, numerical modelling such as the finite element method, the accuracy of the geometrical modelling, the material constitutive equation, and the skull-brain boundary condition are required with more accurate description (Margulies and

Thibault 2000; Ommaya et al. 2002). The scaling factors also need to be carefully considered such as: from the animal to the human head injury tolerance, from the adult to the infant response, from short time high magnitude impact to the long time low magnitude cyclic impulse, from the linear to the rotational loading forces.

Hence by setting up an appropriate clinical examining procedure, evaluating the scientific methodology from the original research, and combining other biomechanical reconstructions including the mathematical simulation, one will probably be able to produce a clearer picture for the cause of SBS (Figure 2.2).

2.2. The Growth Of The Human Head (Buchenco and Hansman 1966; Illingworth 1987; Hall et al. 1995; Sinclair 1998; Remontet et al. 1999; Boito et al. 2002)

The geometry and the structure of the human head is age dependent (Figure 2.3). The head growth is the indicator of the growth of the cranial content. The infant has larger proportion of the head to the torso, and larger ratio of the cranium to the face than the adult. The compliant, soft structure of the cranial skeleton helps the labour procedure and the rapid development of the brain. Understanding the head development helps to investigate and predict the mechanical response of the tissue under loading and to analyse the relative motion due to certain initial conditions. All of these will be discussed separately in the following sections.

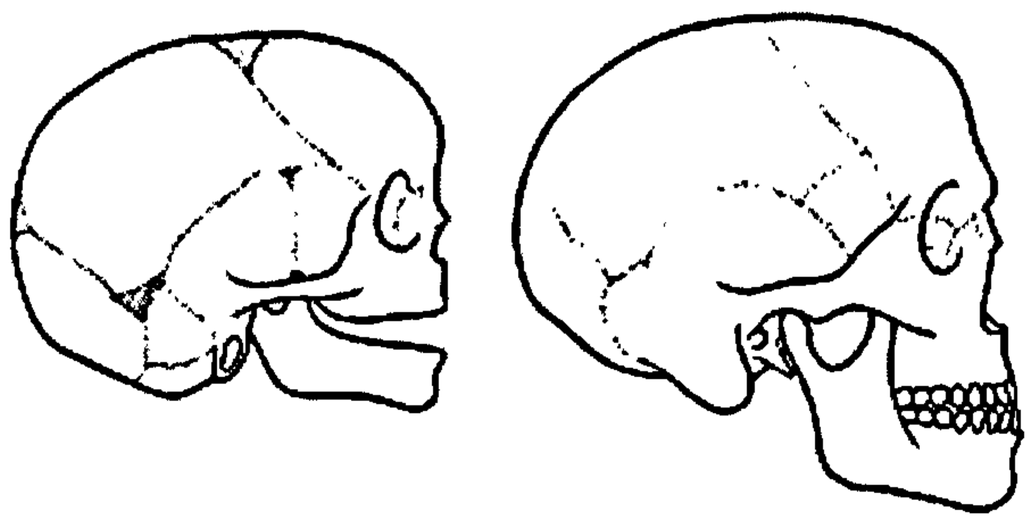

Figure 2.3. *The infant and adult skull as well as the different proportion of facial and calvaria skeleton.*

Most importantly, the head circumference is the essential pointer to the neurology growth and related to the infancy intelligence, in which a smaller or larger abnormality will refer to the mental subnormality or hydrocephalus. The head circumference increases rapidly during the first year of life, normally 10cm, and 2.5cm for the second

year. After 2 years it is about 75% of the adult size. After that it grows 2-3 cm for the next 10 years (Cote et al. 2001).

	Males (Total approximately 360)				Females (Total approximately 310)			
	Head circumference		Weight		Head circumference		Weight	
	(in)	(cm)	(lb oz)	(g)	(in)	(cm)	(lb oz)	(g)
Birth	13.7	34.8	7.5	3180	13.8	35.0	7.5	3180
6 weeks	15.3	38.9	10.13	4860	14.9	37.8	10.0	4500
6 months	17.5	44.4	18.12	8520	17.0	43.2	17.7	7840
10 months	18.4	46.7	22.2	10,460	17.9	45.5	20.1	9380

Table 2.1. The average head circumferences of new born infant by Illingworth in 1987.

The head circumference has to be discussed in relation to the size of the body. Illingworth (1987) gives the head circumference against the weight in 670 babies in Sheffield, England, across the ages from full term to the adulthood, divided into male and female groups. Lubhenoco and Hansman (1966) published the head measurement from gestational ages of 26 weeks to the full term 42 weeks, with more than 7827 samples from various ethic backgrounds in Colorado, USA from 1948 to 1961. In this curve there is no sex separation. Remontet et al. (1999) plotted the growth charts with weight, height, and cranial circumference according to sex, by choosing 7000 children from 0 to 6 years old in Rhone-Alpes region of France. All the measurements for the healthy group do not reveal much discrepancy with the different sample group or time. The head circumference was found to be approximately 35(34 for female) cm from birth to 56 (55 for female) cm at 18.

2.2.1. The Growth Of The Human Skull

The skull is the skeleton of the human head. It can be divided into facial skeleton (viscerocranium), which constructs the face, and the calvaria (neurocranium), which contains the brain. Comparing between the newborn infant and adult, the infant calvaria is disproportionately larger than the facial skeleton with the ratio of 8:1, but for an adult it is only 3:1 (Figure 2.4). The large size of the calvaria allows the growth of the brain precociously for the first year after born, and the facial structure starts to expand later. The infant skull skeleton has also much larger proportion against the body skeleton than

an adult. Therefore the neck with weaker muscle in the infantile age is less controllable with such a relatively bigger and heavier head.

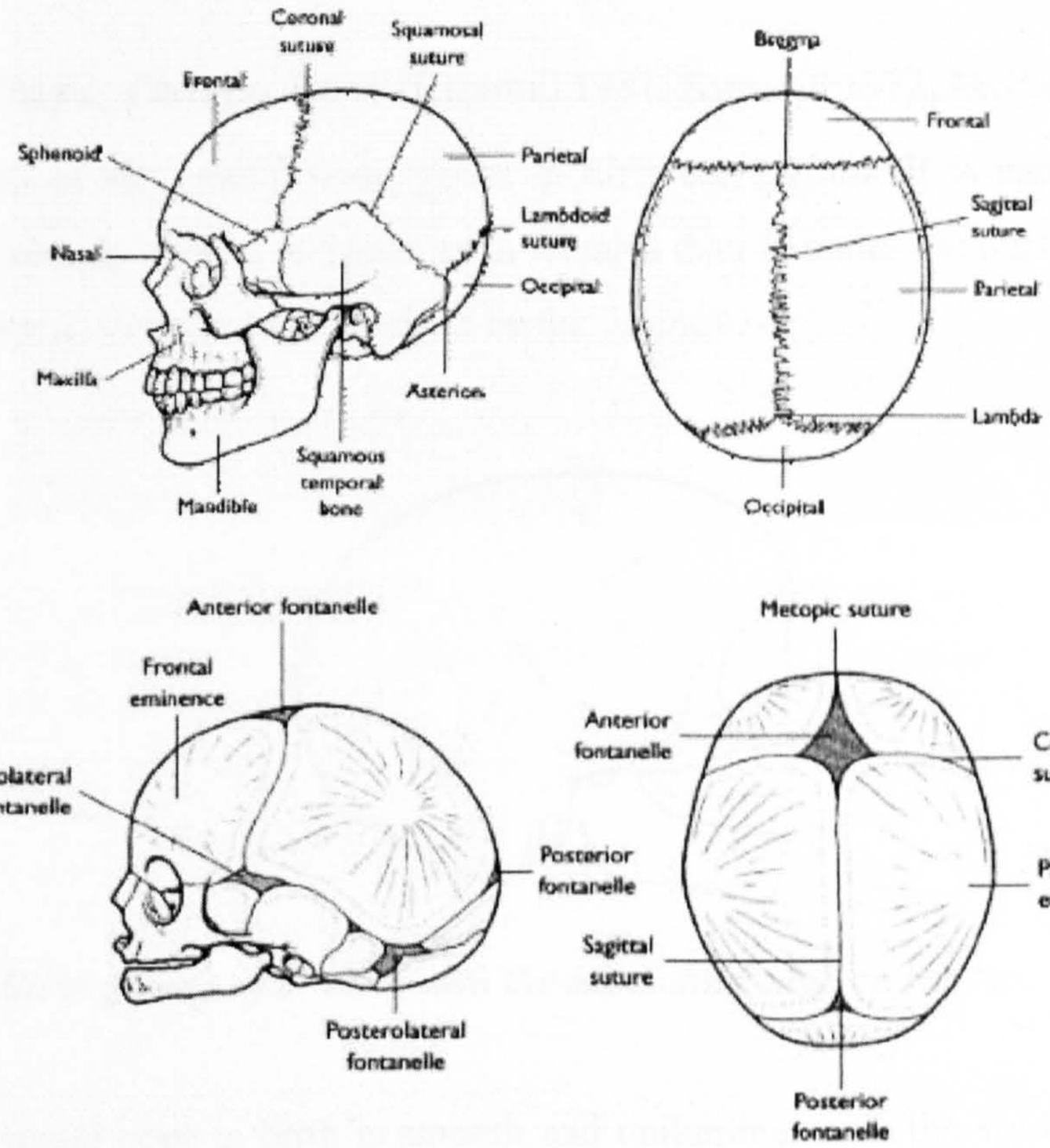

Figure 2.4. *The adult and infant skull with the major bones, fontanelles and sutures.*

The development of the human skull can be regarded as the development of the bone thickness, bone stiffness, intracranial cavity, the paediatric feature such as the fontanelle and the suture, which will be discussed separately.

The skull of a full-term fetus contains the same individual bones as the adult skull. The most individual bones of the fetal skull are obviously smaller than their adult counterparts. Many have slightly different shapes because of the different proportions of their constituent parts.

The skull growth mainly consists of three parts: sutural growth, cartilaginous growth and bone remodelling (Figure 2.4). The growth force of the skull is generated by the expansion of an adjacent organ. The cranial vault grows primarily by suture growth by the expansion of the brain. The base of the cranium grows by cartilaginous and suture. At about the age of 10 years, the cranium reaches almost adult size. Once sutural growth has diminished, the skull remodelling becomes the predominant growth method, which

involves both bone deposition and resorption. By the remodelling procedure, the bone increases not only the size but also changes its shape and position.

2.2.2. THE FOETAL CRANIAL BONE (Kirewall 1981, Kirewall 1982, McPherson 1980)

The thickness of the cranial bone varies in different regions. It is usually thinner in children and elderly people, and thinner in females than in males. At the area that is well covered with muscles, the bone tends to be the thinnest.

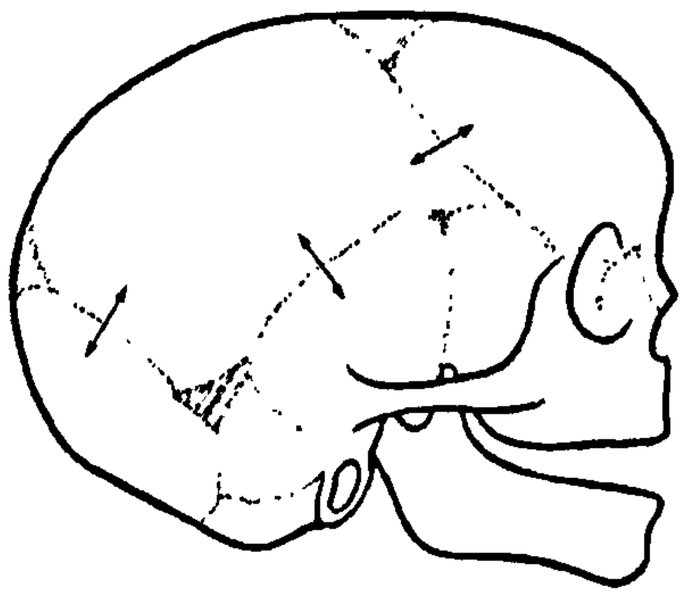

Figure 2.5. *Bone growth after birth with the expanding edge on sutures.*

The foetal cranial bone at birth is smooth and unilaminar with the voids on and inside through which blood vessels pass. During its development, the fetal cranial bone changes not only in thickness but also undergoes structural differentiation (Figure 2.5). The internal and external tables of the compact bone are separated by an intermediate layer of spongy bone known as the diplöe. The diplöe is cancellous bone containing red bone marrow, which the diplöic veins run through. Such structural differentiation is known as "sandwich structure" in aerospace industry for its high stiffness to weight ratio (merit index), so that the stiffness of the cranial bone increase dramatically from infant to adulthood without increasing the bone ash content.

2.2.3. THE FONTANELLE (Menke et al. 1982; Brandt et al. 1986; Adeyemo and Omotade 1999)

The full-term foetus contains the same individual bones as the adult skull, but with different proportions size and the shape. The skull does not fused and the bones articulate each other by fontanelle and suture (Figure 2.6). The fontanelle is the

prominent feature that consists of the fibrous membranes that fill in deficiencies between the bones of the vault of the skull. The function of the fontanelle during the birth is mainly to permit some sliding of the cranial bones during passage through the canal. The distortion usually disappears within a week. There are six fontanelles altogether (Figure 2.6).

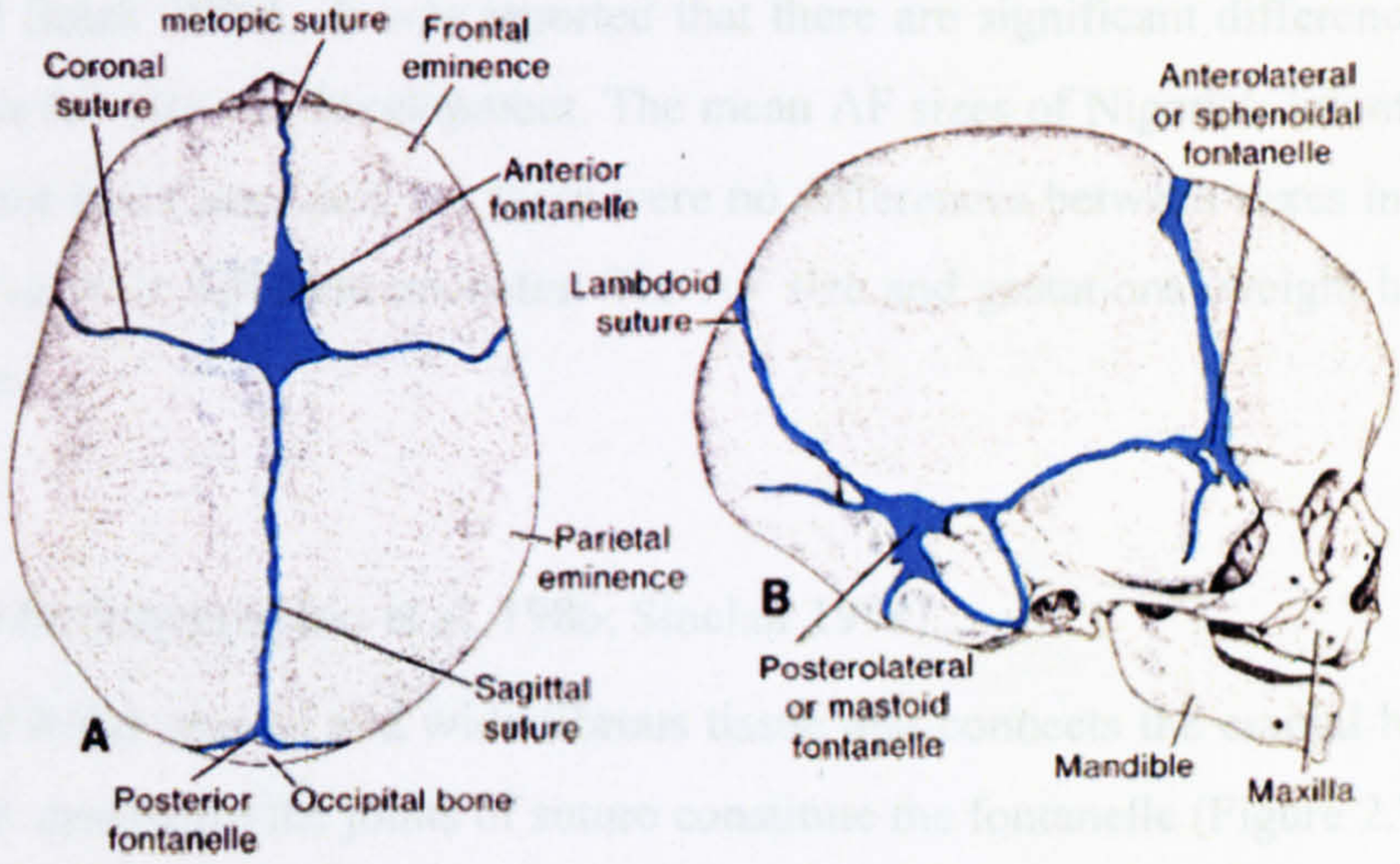

Figure 2.6. *Fontanelle and suture on newborn infant skull.*

The anterior and the posterior fontanelles are on the top of the skull vault. The anterior fontanelle is the largest of all the fontanelles and is diamond-shaped. It lies between the frontal bone and the parietal bones. The posterior fontanelle is small and triangular. It corresponds with the lambda, being situated between the occipital bone and the parietal bones. Sphenoidal (antero-lateral) fontanelle and a mastoid (postero-lateral) fontanelle are lying on each side of the skull. Both are small and irregular in shape.

The posterial and sphenoidal fontanelles close within three months of birth. The mastoid fontanelle closes at 12 months. The anterior fontanelle is the last to close; it is reduced to fingertip size by the first half of the second year, and closed gradually later.

The anterior fontanelle is also known as the baby's “soft spot”, and it's the most prominent as the indicator of the healthy condition of the newborn infant. The neonate's anterior fontanelle is folded at the birth because of the overlapping of the cranial bones moulding during the labour. And after birth the anterior fontanelle turns flat. A bulging fontanelle may indicate increased intracranial pressure but it normally bulges during crying. The pulsations of the fontanelle reflect the pulse. A depressed fontanelle may be

observed when the baby is dehydrated. An unusually small AF related to age may be secondary to brain growth retardation craniosynostosis or hyperthyroidism (Malas and Sulak 2000). Measuring the intra-cranial pressure of the neonate via anterior fontanelle is the premier non-intrusive method above all the ICP measurement.

The anterior fontanelle (AF) size was measured and the curve of the longitudinal and transverse diameters along the sagittal and coronal sutures against age (Illingworth 1987; Malas and Sulak 2000). It was reported that there are significant differences between races in the AF size and development. The mean AF sizes of Nigeria's infants are wider than Chinese and Caucasian, but there were no differences between sexes in both black and white races in full-term neonates. The AF size and gestational weight has negative correlation.

2.2.4. THE SUTURES (Bylski et al. 1986; Sinclair 1998)

The suture is the smooth and wide fibrous tissue that connects the cranial bones of the foetal skull, and hence the joints of suture constitute the fontanelle (Figure 2.7).

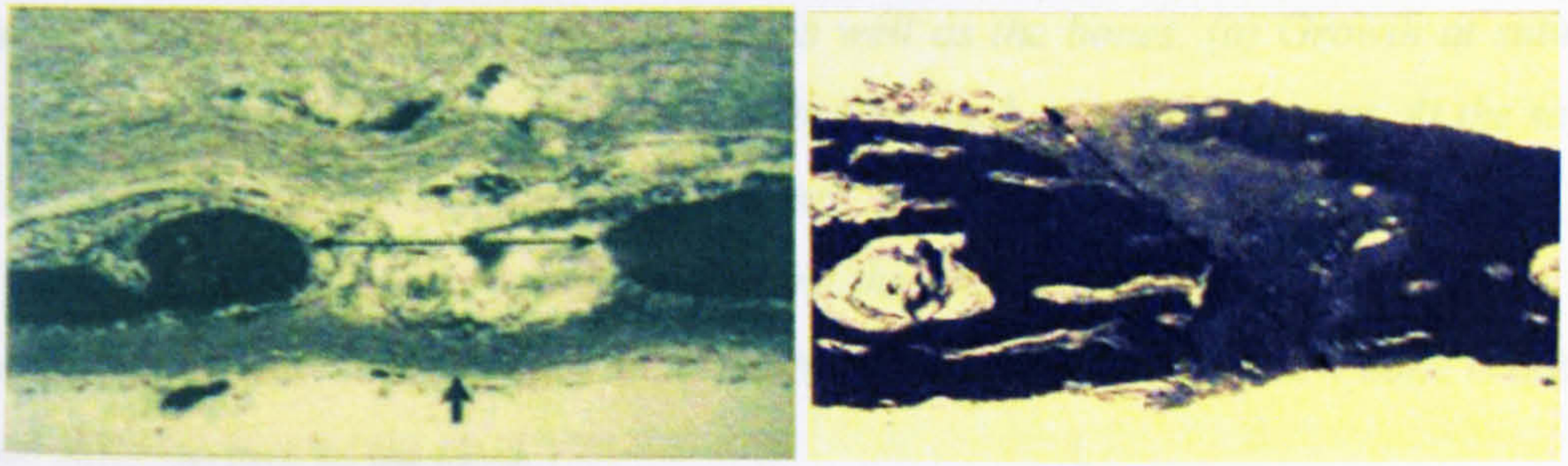

Figure 2.7. *The suture's cross-section through sonography. (a) Gives end-to-end appearance, (b) gives bevelled appearance.*

The frontal (metop) suture divides the frontal bone down the middle of the forehead. Its presence is responsible for the large size and diamond shape of the anterior fontanelle. The frontal suture gradually disappears usually by the age of seven.

Suture growth indicates the development of the skull, and it is one of the three main methods for skull expansion (Figure 2.8). This development of the suture occurs passively by a growth force from such as the expanding brain and eyes. During the growth, the fibrous tissue of the suture increases in amount and pushes the bones further

apart, with the ossification at the margin of the bone. Sutural growth is important in the first few years after birth. Some sutures eventually become obliterated with age.

Soboleski et al. (1997) measured the normal major cranial sutures in neonates and infants by the sonography method, in which the width and thickness of the suture showed no correlation with age due to their sample groups.

Margulies and Thilbault (2000) measured the elastic modulus of 2-3 day old porcine sutures by engineering a 3 point bending method and hence obtained the elastic modulus for porcine sutures of 171.5MPa (Figure 2.25). The comparable properties between human infant cranial bone and the porcine skull gives the possible correlation between the human suture and porcine. Therefore for their finite element model (Figure 2.26) the elastic modulus of human infant suture is given 200MPa and the one for adult is 10000MPa.

Figure 2.8. *Two ways of growth in suture as well as the bones. (a) Growth at suture. The fibrous tissue separating the bones and pushes the bones further apart. At the same time it is invaded by ossification spreading from the margins of the bones. (b) Appositional growth. Suture growth maintains the thickness of the vault relative to the total size of the skull and allowing the brain to expand, during which new bone is added to the outer surface of the skull.*

2.3. TRAUMATIC INJURY AND NON-TRAUMATIC HEAD INJURY (Ommaya et al. 2002, Stein et al. 2005, Kleiven and Holst 2002, Margulies and Thibault 2000)

Traumatic brain injury (TBI, or "intracranial injury", "head injury") refers to a brain damage caused by external circumstances. Often associated with a non-traumatic brain injury for example after a stroke, menigitis, or anoxia, they are two subsets of acquired brain injury (ABI).

The major cause of TBI in people under age 75 is transportation accidents including automobiles, motorcycles, bicycles, and pedestrians, and for the over 75 group is found to be accidental falling. The head injury in younger infants can result in higher rate of morbidity and mortality than in older children.

TBI can be either closed head injury or penetrating head injury, which depends if the object that violently hits the skull pierces into it or not.

2.3.1. HEAD INJURY BY IMPACT AND FALLING

The mechanical causation of TBI can be either accidental injury, by impact or whiplash during vehicle collision, short or high distance falling, or non-accidental injury, such as child abuse. The higher rate of TBI suffered in infant group younger than six month old is believed to be non-accidental injury (Prange et al. 2003; Chadwick et al. 1991; Williams 1991; Lehman and Schonfeld 1993).

In the United States, about 2 million TBI cases were reported in 1990 of most of which are due to vehicle crashes, and 51600 resulted in fatal outcomes. The TBI in children is the most common cause of death (Prange et al. 2003), in the United States for instance, about 150,000 children are hospitalised or die each year. In Sweden, 40% of TBIs are related to vehicle occupants, and in United Kingdom, over two million head injury cases are recorded each year (Johnson and Young 2005), of which 1/5 are severe enough to require hospitalisation. The 60% of all TBIs are motor accident injuries.

For the paediatric population, accidental falls are also a common cause of TBI (Prange et al. 2003). The TBI caused by falls normally accounts for 25% to 34% of hospital paediatric trauma, and 6% of fatalities. Although accidental falls are often (obviously) considered as an unintentional (accidental) injury, the fatality by a suspected short distance falls is sometimes considered as an abuse. Although the force produced in a short distance fall is lower than that in impact such as a vehicle accident, there is still a disagreement of whether such fall can cause death or not between different biomechanical and pathological studies.

The earlier studies like Lehman and Schonfeld (1993) disclaimed that falls from short distances are unlikely to produce serious injury. If a child was reported with a short distance fall and shows significant injury, more attention should be paid to the possible abuse involved. Plunkett (2001) investigated 18 fall-related head injury fatalities during January 1st 1998 and 30th June 1999 in United States between the ages of 12 months and 13 years. His conclusion confirmed that a fall of less than 3 meters (10 feet) may produce fatal head trauma. However, a firm conclusion has not been reached, because Bertocci et al. (2003) who used test dummy experiments to investigate fall injury

concluded that a side-lying posture presented low risk of contact-type head injury and leg injury on all tested impact surfaces.

2.3.2. HEAD INJURY BY SHAKING

SBS is defined as a lethal brain whiplash injury produced by rapid shaking of an infant back and forth. The weak braced infant neck is not able to hold the relatively large head so that the rotational acceleration tears the bridging vessels along the sagittal plane of the brain to produce the intracranial haemorrhage. There is no external injury on the victim's head nor does any contact happen on the head.

Hoffman (2005) reported in the United States each year, that 600-1400 SBS victims are sent into the emergency departments with 50,000 infants present with more minor symptoms of SBS. Of all the SBS victims, about 1/3 died, 1/3 suffer permanent brain injuries and 1/3 survive with minimal long-term effects. The morbidity during the permanent brain injury includes mental impairment, subtle learning deficits, cognitive processing problems, neuromotor impairment (paralysis seizures, cerebral palsy), visual impairments ranging from mild deficits to cortical blindness, hearing impairments ranging from minor losses to complete deafness. It was estimated that the direct costs of child maltreatment including judicial, law enforcement, and health system responses to the maltreatment, are estimated at $24 billion each year while indirect costs including long-term economic consequences of child maltreatment exceed an estimated $69 billion annually in the USA (2001).

This classic concept was discussed for decades since 1970s by Guthkelch (1971) and Caffey (1971, 1972). However, the injury theory does not meet with universal acceptance (Shannon and Becker 2001) due to the inconsistency between the biomechanical modelling study (Duhaime et al. 1987; Prange et al. 2003; Wolfson et al. 2005) and the head injury criteria (Duhaime el al. 1987, Ommaya et al. 2002). The shaking force was thought to be insufficient to rupture the weakest bridging veins unless associated with impact. The following case review by the clinical experts gave various evidences that supports either of the views that shaking alone may or may not be the original incidence but did not reach any conclusion (Alexander et al. 1990; Gilliland and Folberg 1996). Geddes and her colleagues gave out the "Geddes hypothesis" after post-mortem neuropathological studies on 50 infants aged 9 months or less that the subdural haematoma (SDH) and retinal haemorrhage (RH) may come from the spinal-

cord or low brainstem injury that lead to apnoea and subsequent hypoxic-ischaemic to account for the SDH and RH (Geddes and Plunkett 2004) (Figure 2.9(a)-(b)). However, the "Geddes hypothesis" does not remove the shadow from the confusion over the explanation for SBS even though it was embraced by some experts and gave some influence by the legal system. It was argued by others that the "Geddes hypothesis" points to the fact that such injury could come from a minor force such as rough handling by the infant, which is extremely rare in reality (Richards et al. 2006). Therefore the controversial evidence given by the clinical and biomechanical experts asks for the pending of the completion of the theory, nor was any scientific testimony in the court could ascertain the baby who suffered the SBS is due to the abuse.

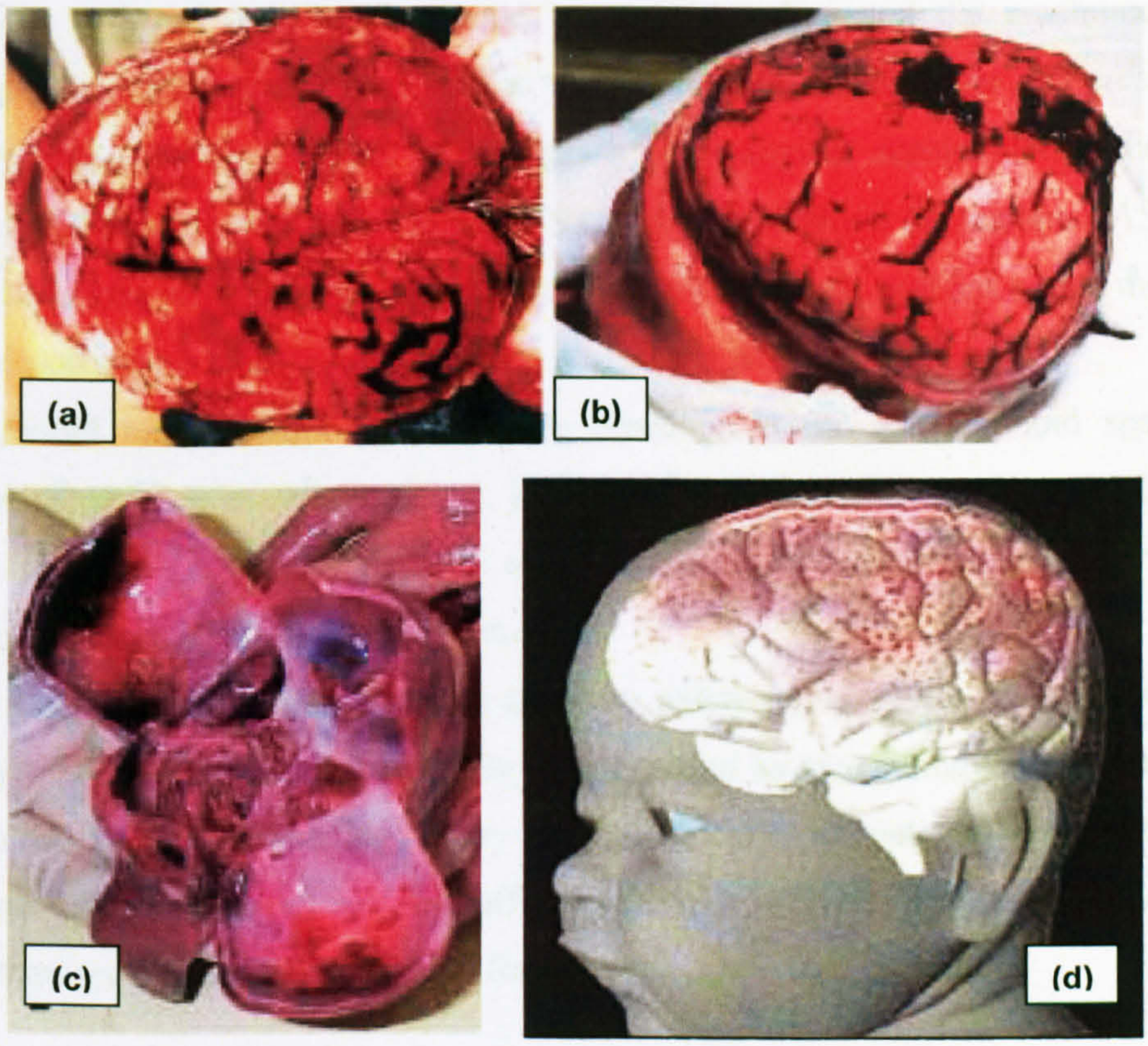

Figure 2.9. *The rupture of the bridging veins and subdural haemorrhage. (a)-(c) The pathological anatomy of the victims (Reproduced from Geddes et al. 2003); (d) diagram of the injury (BBC 1998).*

2.3.3. THE INTRACRANIAL HAEMORRHAGE IN HEAD INJURY (Figure 2.9-2.12, Table 2.2)

The intracranial haemorrhage can be divided into extra-axial haemorrhage and intra-axial haemorrhage. The intral-axial haemorrhage is the bleeding within the brain, and

the extra-axial haemorrhage is the intracranial bleeding that is found outside the brain surface. It can be divided as epidural (extradural) haematoma, subdural haematoma, and subarachnoid haemorrhage.

Epidural haematoma is the bleeding build up between the skull and the dura (Figure 2.10). It is caused by impact when the fractured skull pierces into the arterial channel inside the bone (Shepard 2004). Epidural haematoma can raise intracranial pressure that causes the brain to loose blood supply or crash against the skull. About 15% to 20% of patients with epidural haematomas die of the injury (Sanders and McKenna 2001).

Subdural haematoma (SDH) is the bleeding between the dura and the arachnoid membrane (Figure 2.11). It usually results from tearing veins in the subdural space, which can only be seen by the blood between the dura and the arachnoid layer. Subdural haemorrhages can also lead to the increase of the ICP that compresses and hence damages the brain tissue. The whiplash onset angular acceleration is the major cause of SDH (Gennarelli and Thibault 1982). Acute subdural haematoma (ASDH) is due to the severe whiplash that happened during vehicle crash, and has a high mortality. Abusive shaking an infant cannot produce ASDH but SDH.

Subarachnoid haemorrhage (SAH) is the bleeding in the subarachnoid space that between the arachnoid and pia mater, just above the brain surface (Figure 2.12). The rupture of the blood vessels (cerebral aneurysm, cerebral arteriovenous malformation) on the brain surface is usually the cause.

Diffuse axonal injury (DAI) refers to a tearing axons injury of the brain white matter (myelination). It is typical diffuse brain injury caused by severe angular acceleration to the brain. It is a devastating injury that over 90% of patients never regaining consciousness (Wasserman 2007). Traffic accidents as well as the sports and sadly, for child abuse are all common causation for DAI.

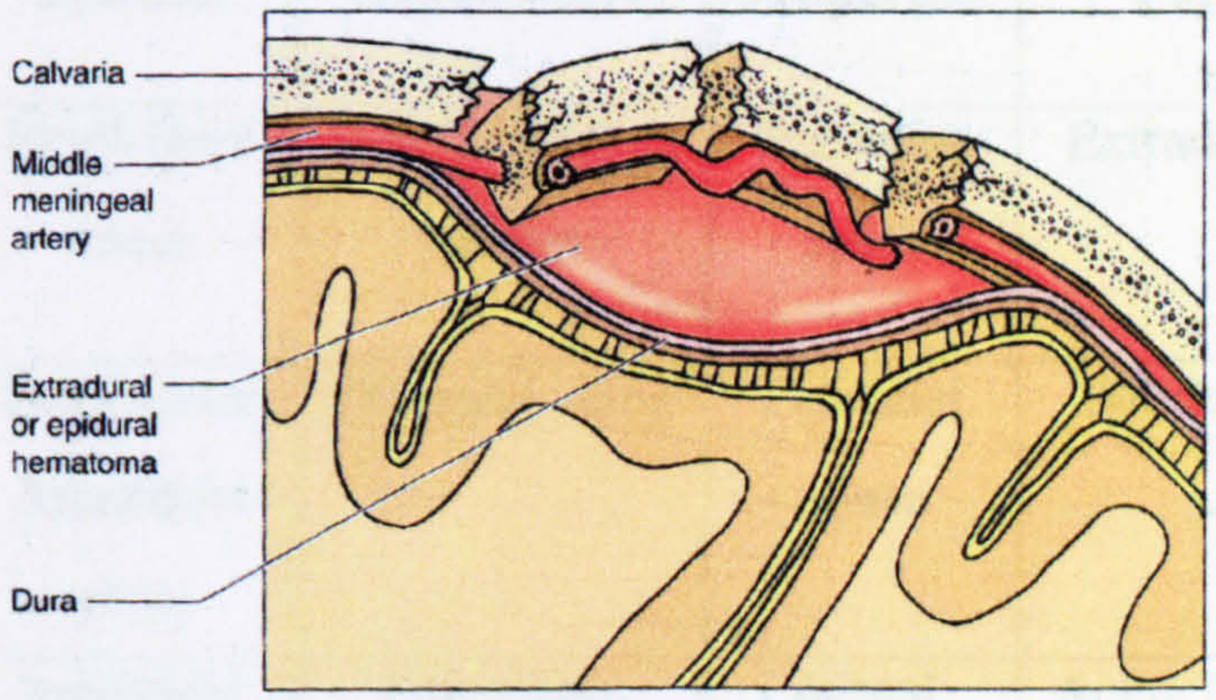

Figure 2.10. *Extradural Haemorrhage caused by rupture the arteries in the epidural space by bone fracture.*

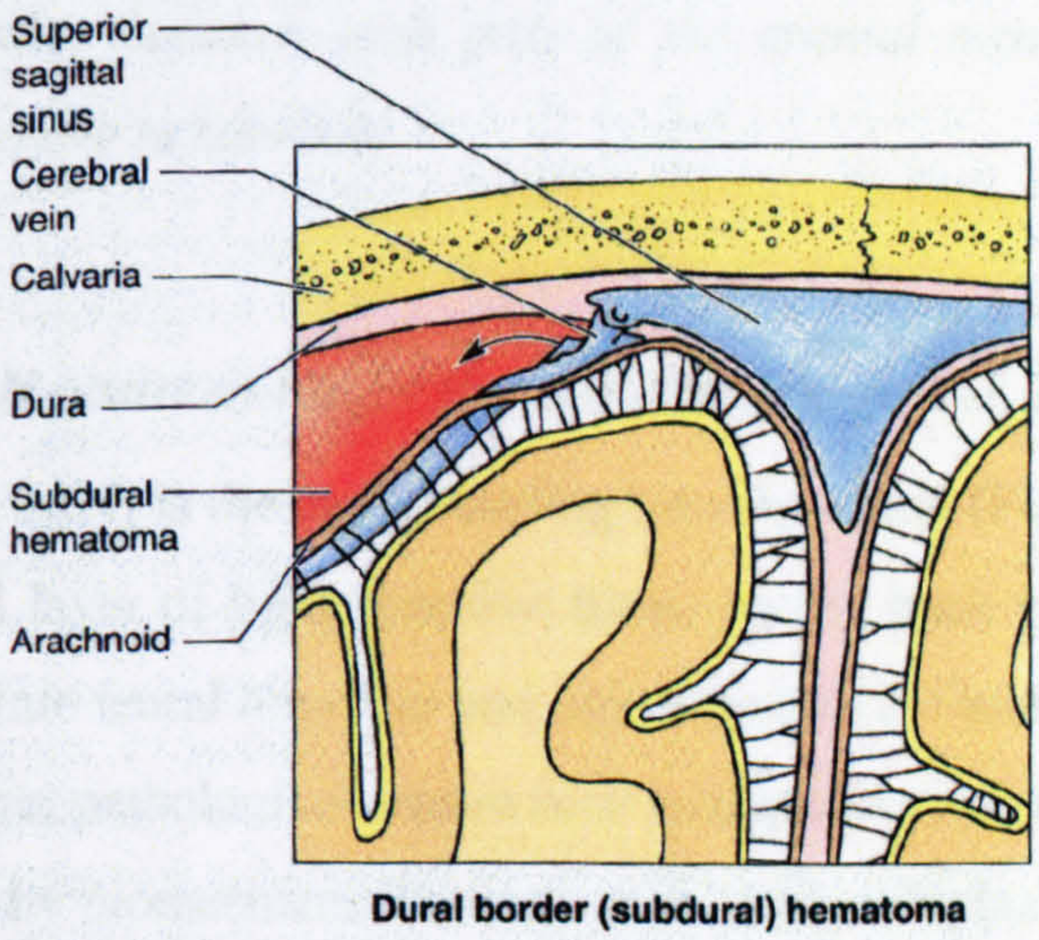

Figure 2.11. *Subdural Haemorrhage caused by rupture the vein in the subdural space.*

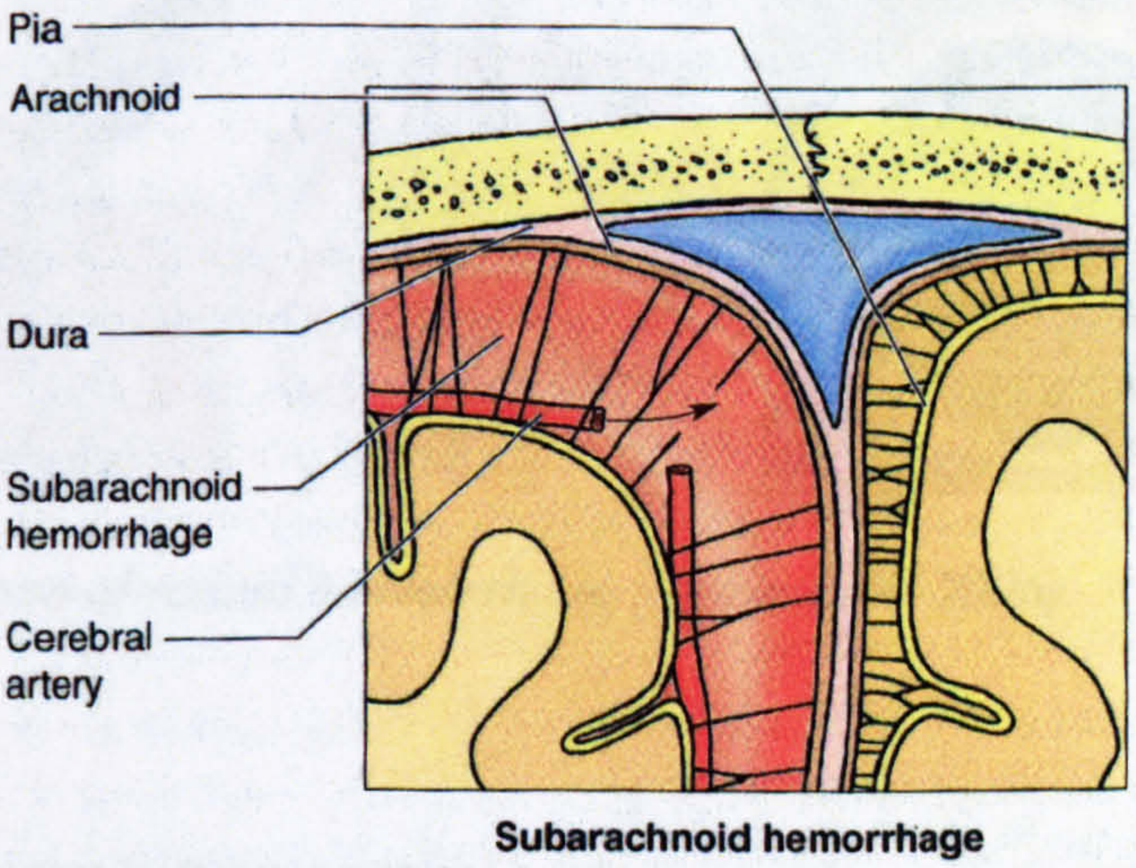

Figure 2.12. *Subarachnoid Haemorrhage caused by rupture the vessels on the surface of the pia mater.*

Space	Position	Vasculature	Properties	Potential Injuries
Extradural Space	Skull-Dura mater	Sphernoid wing arteries	Potential space	Extradural Haemorrhage (EDH)
Subdural Space	Dura mater Arachnoid mater	Bridging veins	Potential space	Subdural Haemorrhage (SDH)
Subarachnoid Space	Arachnoid mater-Pia mater	Fine blood vessels network	Actual space	Acute Dura Haemorrhage (ADH)

Table 2.2. *The relation between each part of the cranial meninges, as well as its vasculature and the space in between.*

2.3.4. THE RETINAL HAEMORRHAGE IN HEAD INJURY (Hose et al. 2003)

Retinal haemorrhage (RH) is the eye's bleeding into the retina (Figure 2.13). The retina is a thin disc-shaped layer of light-sensitive tissue on the back wall of the eye, and it translates the image into ieural impulses and sends them to the brain via optic nerve. RH can be caused by either pathological reason such as hypertension, retinal vein occlusion, diabetes mellitus, or by biomechanical reason such as the whiplash or impact. RH is an important indicator that a baby suffers SBS when combined with the SDH.

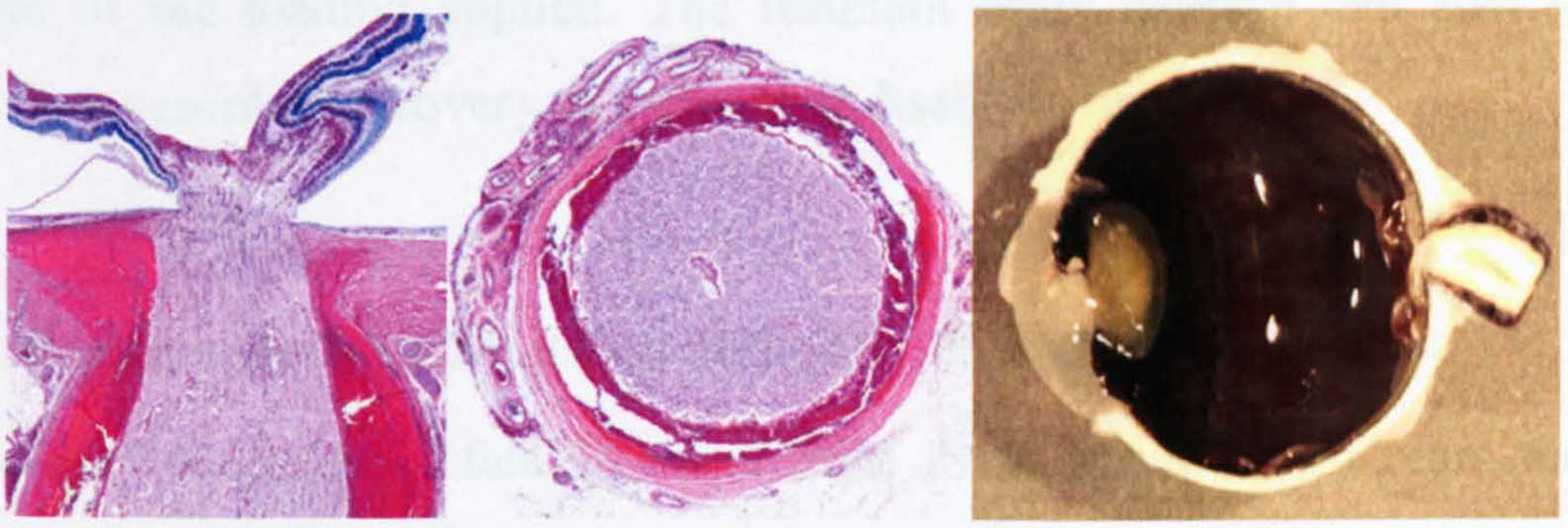

Figure 2.13. *Diagram of retinal haemorrhage (Agamanolis 2006).*

2.3.5. NON-TRAUMATIC INJURY-ANOXIA

Besides traumatic injury induced SDH, a non-traumatic injury anoxia is an alternative reason to produce paediatric SDH that mimics the traumatic SDH (Geddes 2001, 2002).

Anoxia means the absence oxygen to an organ's tissues. The brain swells when suffering anoxia, and then the raised ICP lead to SDH and RH. This type of injury is often seen in drowning, shock or other reason that caused apnoea (Brousseau et al. 2005).

2.3.6. THE DIAGNOSIS OF THE HEAD INJURY IN IMPACT, FALLING AND SBS (Aoki and Masuzawa 1984; Medele et al. 1998; Harding et al. 2004; LeFanu and Edwards-Brown 2004; Minns and Busuttil 2004; Morad et al. 2004)

The TBI can be focal, confined to one area, or diffuse, involving more than one area, or both. Impact and fall onto a solid surface normally produce focal injury to the brain while whiplash has diffuse brain damage, from either traffic collision or shaking.

The outcome of the focal brain injury can be manifested as; coup and contra-coup contusion (bruising of brain tissue), intracranial haemorrhage and epidural haemorrhage in the skull. Diffused trauma to the brain is frequently associated with concussion that is the shaking of the brain relative to the head motion; diffuse axonal injury (DAI), and the coma.

Specifically, the SBS is always diagnosed with the triad called: Subdural haemorrhage (SDH), retinal haemorrhage (RH), and neck or rib fracture with skin bruise on the torso. There is no external trauma on the scalp. Neither DAI nor ASDH can be found without skull fracture.

All the TBI discussed can of course be mild, moderate, or severe depending on the magnitude of the loading applied. The resultant brain damage can also vary in its severity from complete recovery to permanent disability or death.

2.4. THE FAMOUS COURT CASES FOR SBS (BBC 1997-2005)

SBS, as one of the potential fatal forms of child abuse, has in recent years become both a social and scientific topic. The review of the court convictions of shaken baby cases, mostly in the UK and a few between the UK and the US from BBC reports since early 1990s, demonstrates the importance of expert witness as a powerful evidence and how scientific research could lead to the true or false allegation by the juridical justification.

2.4.1. THE CASES WITH THE "TRIAD" EVIDENCE

The triad of the SBS, consisting of brain haemorrhage, retina haemorrhage, and the shoulder or torso bruising (with possibly rib fracture), is considered by many experts as the indicator that the victim was physically abused by shaking.

In April 1998, Australia nanny Louise Sullivan was accused of murdering a six month old Caroline Jongen by shaking him to death, with the pathological evidence in the post mortem revealing severe retina bleeding in the baby's eyes and brain damage. Sullivan, who denied the charge of murder initially, admitted to unintentionally killing and pleaded guilty to gross negligence in January 1999. The prosecution was told that on the morning of the incidence "she shook Caroline with severe force for a period which is difficult to quantify precisely but which must were in order of five to ten seconds" while the defendant thought the baby was having a convulsion. Sullivan was sentenced 15 months in jail, suspended for two years for manslaughter. Afterwards she was allowed to return to Australia for psychiatric and psychological treatment due to her poor mental health identified by psychologists during the investigation, after which it was recommended that she should not be allowed to become a childminder.

In February 2004, 27-year-old Joseph Wainwright from Salisbury was convicted for shaking his four-month-old son Joshua to death in September 2002, he was sentenced to jail for three and a half years, being found guilty of manslaughter. At the time of the incident, Joshua was sent to an emergency department and was described as "Choking on his own vomit and stopped breathing" by Wainwright, later a massive head trauma was discovered and Joshua died two days later. A jury unanimously told the media that Joseph shook his son and caused the fatal injuries on head and chest by losing his temper. There was no report of whether the perpetrator admitted to the crime.

In December 2001, 29-year-old Mark Stephenson from Cricklade was found guilty of shaking his three-month-old daughter Sacha to death in January 2001. The baby suffered massive brain and eye bleeding which made her blind and deaf and she died shortly after. Although the perpetrator described that he had shaken her only in an effort to revive her after dropping her, the jury were convinced he had caused her death by deliberately shaking her with considerable force for being "stressed out" and losing his temper.

In March 2001, 27-years-old Owain Huw Owen from North Wales was jailed for three years for violently shaking his girlfriend's daughter, seven-month-old Shauna and left

her blind, with brain damage and a broken arm. Shauna requires 24 hours nursing and constantly remains on life support. Owen pleaded guilty for inflicting grievous bodily harm by unintentionally losing control.

In March 2003, 32-year-old Quentin Starling from Redford, Nottingham has convicted for shaking his six-week-old daughter in 2001, causing her bleeding in the brain and a fractured spine. Although he denied causing her grievous bodily harm and announced that the forceps during delivery may have produced the injury, the jury sentenced him to jail for two years.

In January 1994, a judge held the case against council-registered childminder Christine Walton, who allegedly severely shook Thomas Harrison in 1989 when he was six months old and left him with brain damage and a permanent mental impairment. Mrs Walton denied the accusation and there was no criminal charge against her. By 2001, 12-year-old Thomas has received nearly £3m in compensation.

In June 2005, 46-year-old father Christopher Pink from Newton was convicted of manslaughter of his five-month-old son Bobby by deliberately shaking or throwing him to the cushion, and hence theoretically causing brain damage, heart murmur and death. He denied the charges but eventually was convicted and jailed for four years.

In December 2001, 20-year-old father Peter Mocha from Camelon had shaken his four-week-old son to permanent brain damage and left him permanently blind. He pleaded guilty to "shaking him about three times" before realising the severity. He was jailed for four and half year of assault.

In October 1999, 23-year-old Joseph Dunlop shook the 7-week-old baby to death due to uncontrollable impatience. Dunlop stated he shook the baby gently after the baby appeared to stop breathing. However the internal bleeding due to the post mortem demonstrated the classic signs of SBS and Dunlop was sentenced to two years in jail.

In February 2003, 40-years-old childminder Tina McLeod was accused of murdering one-year-old Alexander Graham at her home while she was looking after him on 26 July 2001. The injury, sustained two sides bleeding inside the victim's brain, was considered as typical evidence of SBS told by the expert witness Professor Jeanne Bell, who also denied the perpetrator's claims that the child fell off the sofa. Instead, Professor Bell said only severe flexion or extension or twisting could have produced the injury pattern but not falling. Mrs McLeod was acquitted of the accusation in 2003.

In 1998, childminder Helen Stacey was charged of murdering a five-month-old baby Joseph Mackin in May 1997 who then died of a serious brain injury as a classic victim

of SBS. Her charge by 2001 was reduced from murdering to manslaughter and obtained 8 years sentencing instead of previous life sentencing.

British childminder Manjit Basuta, 44 in 1999 was found guilty of shaking 13-month-old US citizen, Oliver Smith to death who was in her care. The autopsy showed the victim suffered bleeding and swelling brain in the skull, which is attributed to SBS by experts. Although her lawyers insisted that the death referred to a head injury some months prior to the incident and a bumping but not shaking, a witness testified Basuta's shaking behaviour as "very badly". Mrs Basuta pleaded guilty and was sentenced to eight years in jail. She was reported due to be released in 2003 after four years service in prison in the US.

2.4.2. THE CASES WITH THE CONTROVERSIAL MEDICAL EVIDENCE

Although the triad of injuries described above helps to identify the shaken baby victim, the theory, as agreed by most experts, has been based on observations and never been proven. One or more symptoms could also appear on a baby that dies of minor falls, birth trauma or genetic defect, therefore the expert allegation that convinced the shaking abuse by simply any of the symptoms without critically reviewing the medical literature or other indicators could be misleading.

British youngster Louise Woodward from Eton, Cheshire, 19 in 1997, worked as childminder for a Boston family caring their two children. On 4 February 1997, one of the children, 8-month-old Matthew Eappen was taken to a hospital emergency ward suffering with severe brain haemorrhage and breathing difficulties, he died six days later. Woodward was arrested on 5 February and was accused of first-degree murder.

Two medical opinions were heard from the experts in both for the prosecution and the defence. The prosecution told the jury of the evidence that the infant had "a two and a half inch fracture to the skull, a massively swollen brain, and bloody retinal haemorrhage" that the baby "had been violently slammed against a hard surface and severely shaken back and forth". On the other hand, the defence medical group testified that Matthew Eappen had died of a blood clot inside his brain that reached the crisis on the day he was alone with Louise, a so-called "chronic subdural haematoma".

On 30 October 1997 Woodward was found guilty of second-degree murder and sentenced to life in prison. Six days later on 4 November, the case was dramatically

overturned by the jury into involuntary manslaughter. She was sentenced to 279 days which she had already taken during the trial in prison. Woodward was set free immediately and was allowed to return to Britain.

In 1999, Sally Clark from Wilmslow, Cheshire was convicted of the murder of her sons, eight-week-old Harry in 1996, and Christopher, aged 11 weeks in 1998. The evidence of shaking abuse given by the expert witness was later found to be flawed, and the bacterial infection was found in the children's brain. Clark was cleared and freed in 2003.

Angela Cannings was jailed for life in April 2002 for the murdering her children of seven-week-old Jason in 1991 and 18-week-old Matthew in 1999. The expert witness testified that the probability of two natural unexplained cot deaths in the family was 73 million to one, which led to the conclusion that her two children were died of shaking abuse. The evidence was later disputed by the Royal Statistical Society and other experts that suggested it is more likely to be 200 to one, once the genetic and environmental factors are considered. The disease history of cot baby death was found in the Cannings's family and she was eventually released after 18 months in jail.

Rioch Edwards-Brown who was wrongly accused of abusing her son and cleared by later evidence demonstrating that her son's injury was due to birth trauma, set up the group in order to talk for the parents and carer with similar experiences. They are calling for a new rules-Riordan's law to be set up which asks that all suspected cases would be examined by a specialist paediatrician within 24 hours and again within two weeks to prevent misdiagnosis.

The overturn of the Canning's case associated with the new research in recent years has demonstrated that some of the shaken baby triad could actually be the result of a lack of oxygen from a low trauma or no trauma causation, Lord Goldsmith had ordered a review of 297 cases of infant death convictions since 1994, 88 of which are SBS.

Research published in the past four years has suggested that some of these injuries, such as subdural haematoma, could instead be the result of a lack of oxygen resulting from a much less severe trauma, or possibly no trauma at all.

Attorney General Lord Goldsmith ordered a review of all infant death convictions since 1994 after the Appeal Court overturned the verdicts on Angela Cannings in 2003. It led to the review of all 297 cases, including 88 involving SBS. Although they said "only a very small number which actually give rise to concern", there were still two cases quashed and one was reduced due to the unsecured medical evidence.

2.4.3. THE CONCLUSION

Although the triad or other indicators of SBS were questioned in certain circumstances, it can never been denied or underestimated that the fact of shaking the infant is dangerous. The UK police service experts believe that the true number of the shaking abuse cases could be far higher than the estimated 200 every year in UK, with 50 infant homicides each year in the UK, among which many are the result of violent shaking (BBC 1997-2005). It is therefore crucial to set up a standard process to evaluate the SBS with more accuracy. The scientific research that involves other approaches such as biomechanics and engineering could be an important direction to help to prove the theory.

2.5. DYNAMIC LOADING AND HEAD INJURY

The mechanical characteristic of the biological tissue was determined by the force-deformation and failure behaviour, or stress-strain curve of the material.

The material properties can be described as elasticity, viscoelasticity and the plasticity. When a substance subjected to a loading, the elastic material immediately returns to the original shape along the same path as the loading curve, the deformation of the viscoelastic material to its original state and the unloading path is significantly below the loading curve due to internal energy dissipation (Fung 1993). The plastic material retains a permanent deformation. For the human tissue, only the adult bone, teeth and the nails have an elastic property, all other tissues behave viscoelasticly.

The head injury is caused when the tissue under the critical load that exceeds the ultimate stress corresponding to ultimate strain, and hence causes mechanical disruption such as skull fracture, or shear failure such as bridging veins tearing.

The failure stress of the skull has an increase of more than a factor of 10 from the human newborn to adult (Thibault and Margulies 1998, Goldsmith and Plunkett 2004). For the human cerebral blood vessels, the average ultimate stress and strain reported is 2.0MPa and 20% respectively (Monson and Goldsmith 2003).

The brain is a complex rheological substance permeated cerebro-spinal fluid (CSF). The damage of the brain tissue could be either focal, the coup, counter-coup contusion, or diffused. Diffused axonal injury (DAI) is the sever damage of the vascular on the surface of the brain. The focal and the diffused brain injury are caused by linear and

angular accelerations, and the injury tolerance can be measured by linear and rotational head injury criteria (HIC) (§2.5.4) separately (Figure 2.14).

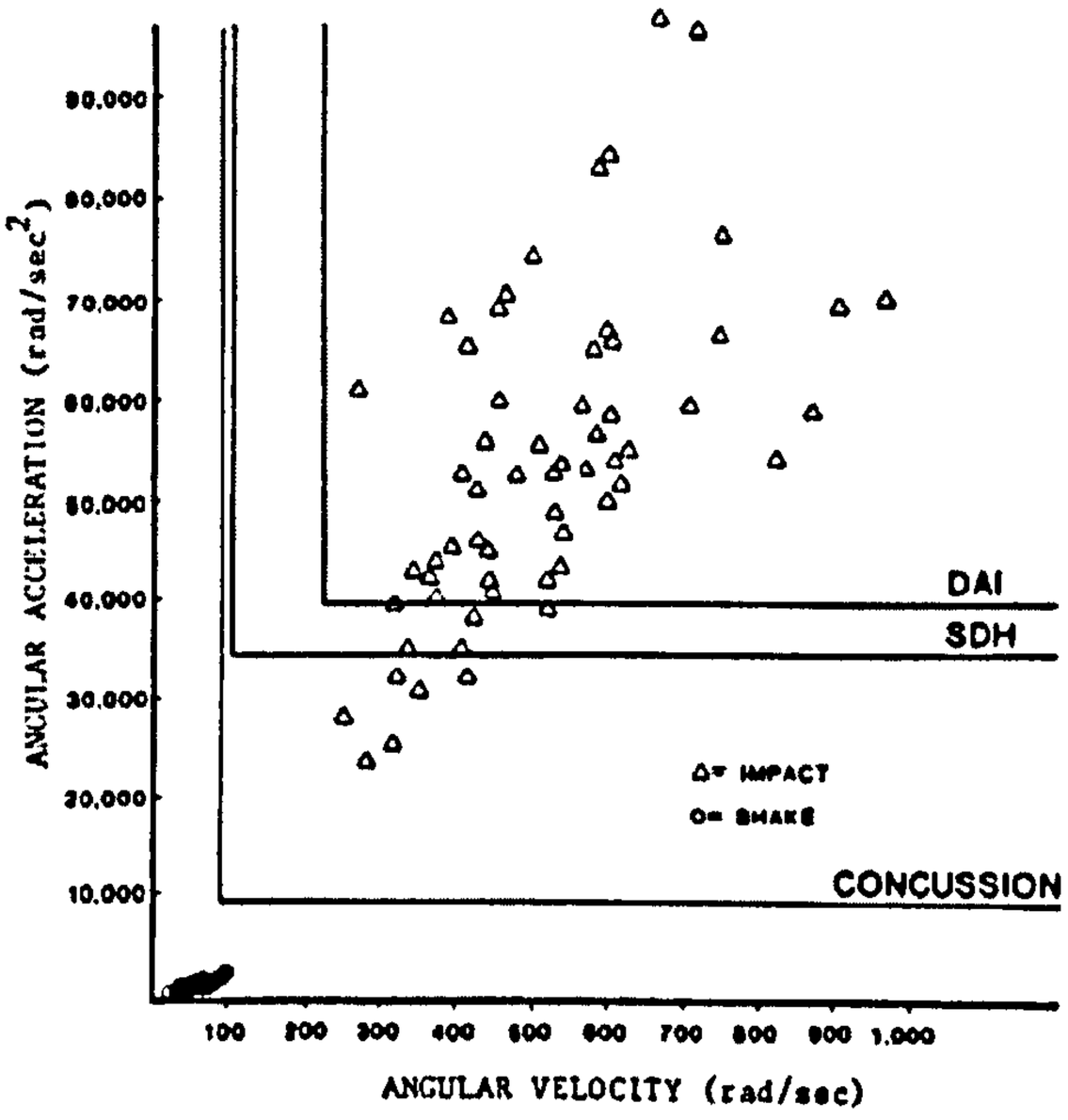

Figure 2.14. *Angular acceleration as a function of angular velocity scaled to a 500 g brain mass, showing thresholds of concussion, Subdural Haemorrhage (SDH) and Diffused Axonal Injury (DAI) for both shaking and impact(Duhaime et al. 1987).*

2.5.1. THE LINEAR AND ROTATIONAL LOADING

The loading on the head, no matter if it is from impact or whiplash, can be divided into a translation and a rotational pattern (Figure 2.15). The translational loading is produced by the total applied force that passes through the centre of gravity of the head. The rotational loading is produced by the moment of a force or a couple about that centre of gravity. By both loading patterns, various degrees of head injury can be simultaneously presented (Goldsmith and Plunkett 2004).

The translational loading can cause direct failure of the skull as well as the vasculature system. The linear loading without skull failure could generate a pressure gradient inside the skull through the liquid, in the direction of motion proportional to the acceleration and the cavitation appears on the contra side of the loading site, such phenomenon can produce brain contusion.

The rotational loading generates differential displacements on the adjacent spherical brain layers around the axis of rotation on the base of the neck. The stretch between different intracranial layers hence causes shearing injury of the brain.

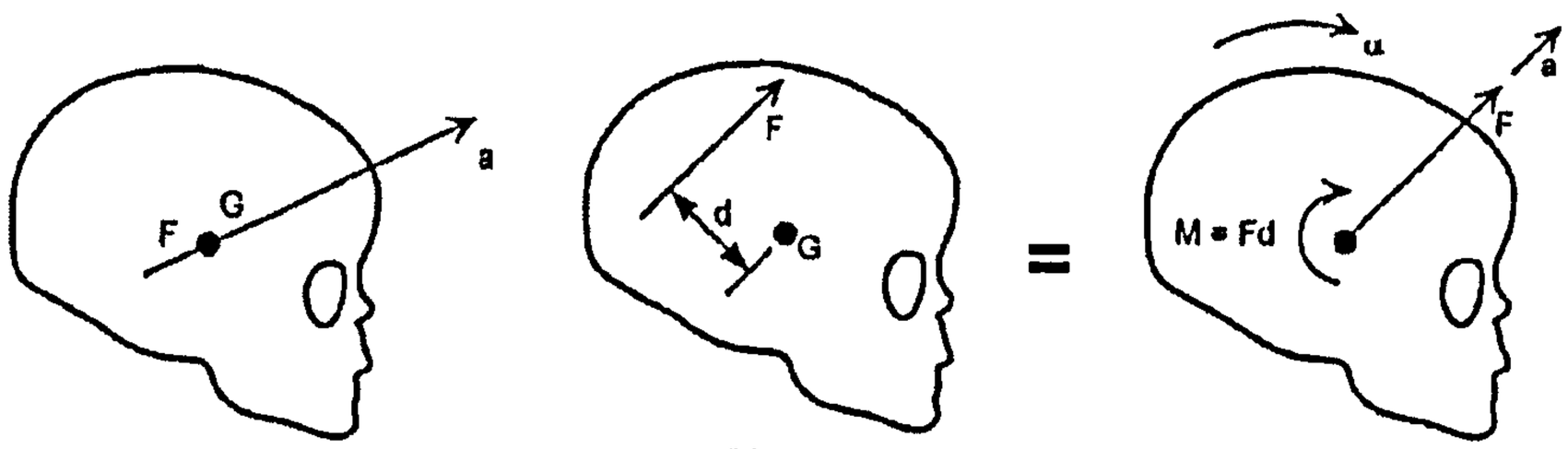

Figure 2.15. *Diagram of (a) Resulting force passes through mass centre G of head; (b) Resultant force passes at a distance d from mass centre G and equivalent force system (Ommaya and Goldsmith 2002).*

2.5.2. THE IMPACT LOADING (Ommaya and Goldsmith 2002, Goldsmith and Plunkett 2004)

Impact loading is as the head strikes an object at speed sufficient to cause observable effects. A head impact phenomenon is always combined with two typical patterns: firstly the collision effect such as a bruise of the scalp or the fracture of the skull, secondly, the transmission wave through the system with pressure gradient. The head contact with objects without any of the both phenomenon cannot be called impact, such as baby slamming into pillow, and the pillow absorbs most of the translational energy. Unless the force is transmitted directly through the centre gravity of the head, impact will always have both translational and rotational acceleration. Therefore the subsequent injury may be primarily focal, or primarily diffuse, or a combination of both. The head motion path before impact is irrelevant to the injury. The impact injury can be seen mostly from traffic accidents, falls, sports or intentional abuse.

2.5.3. THE IMPULSIVE LOADING (Ommaya and Goldsmith 2002, Goldsmith and Plunkett 2004)

Impulsive loading is as the head rotates around the axis on the base of the neck, the tangential acceleration on different layer of the calvarium produces shear and tears to the tissue due to the difference of radial distance from the rotation axis and the mass.

The impulsive injury is determined by angular acceleration tolerance. The impulsive loading can combine with linear and rotational acceleration but there is no impact occurs.

A traffic collision with the occupant secured by the safety belt, and the shaking baby are the two major causes of the impulsive injury. Most of the impulsive studies focus on high magnitude, single applied loads such as the sudden arrest of a torso bundled onto the seat during a car crash while the head is free to whiplash. The recent investigation of repetitive, low magnitude loading was developed and showed to some extent that increasing damage of the brain tissue is possible with successive load after significant periods of quiescence. This will contribute to the understanding of SBS.

The orientation of the impulse involves different injury patterns, for example, the sagittal plane impulsive loading usually causes a subdural haematoma (SDH), and while coronal plane impulse results in focal or diffused traumatic axonal injury (DAI).

2.5.4. HEAD INJURY CRITERIA (HIC)

The Head Injury Criteria (HIC) is one of the most wide used tolerance injury severity index from cadaver and animal studies (Versace 1971; O'Riordain et al. 2003). It was mandated federally by several private organizations such as the American National Standards Institute, based on the kinematic parameters like linear (translational) peak acceleration (G's) and the acceleration time history. It is defined as:

$$HIC = \max_{T_0 \le t_1 \le t_2 \le T_E} \left[\frac{1}{t_2 - t_1} \int_{t_1}^{t_2} R(t)dt \right]^{2.5} (t_2 - t_1) \qquad (2.1)$$

where t_1 and t_2 are the start and the end times of the interval when the acceleration reaches maximum value. A HIC value of more than 1000 is considered that the injury is irreversible. The linear acceleration head tolerance for 6 year old children was investigated by reconstructing pedestrian-automobile impacts. If the loading lasts more than 3 milliseconds, 83g is the limitation for the linear peak acceleration, and 70g (HIC=350) or less produces a completely reversible injury, 110g (HIC=600) gives 25% irreversible injury (Goldsmith and Plunkett 2004).

Gennarelli and Thibault (1982) investigate the fall injury tolerance by conducting experimental in monkeys and scaled into humans. They concluded that a fall with linear head acceleration of 200g and duration of 3.5ms would necessarily produce the tearing bridging vein for ASDH.

Gennarelli and Thibault (1982) also scaled the linear acceleration from the adult head into the infant head with a 500g brain mass. The mean peak tangential acceleration from whiplash shaking was found to be 9.3g while from impact is 428g. Also they established angular acceleration tolerance severity index by scaling the former animal and human cadaver's data into 500g brain mass head. Duhaime et al. (1987) and her colleague (Prange et al. 2003), associated other biomechanician demonstrated that both angular velocity and angular acceleration generated by shaking is well below and injury threshold. The scaling rule between different injury thresholds from mammal species to human follows the empirical equation, that the ratio of the accelerations is equal to the inverse of the brain mass ratio raise to the 1/3 power for linear acceleration and 2/3 power for angular acceleration (Figure 2.16).

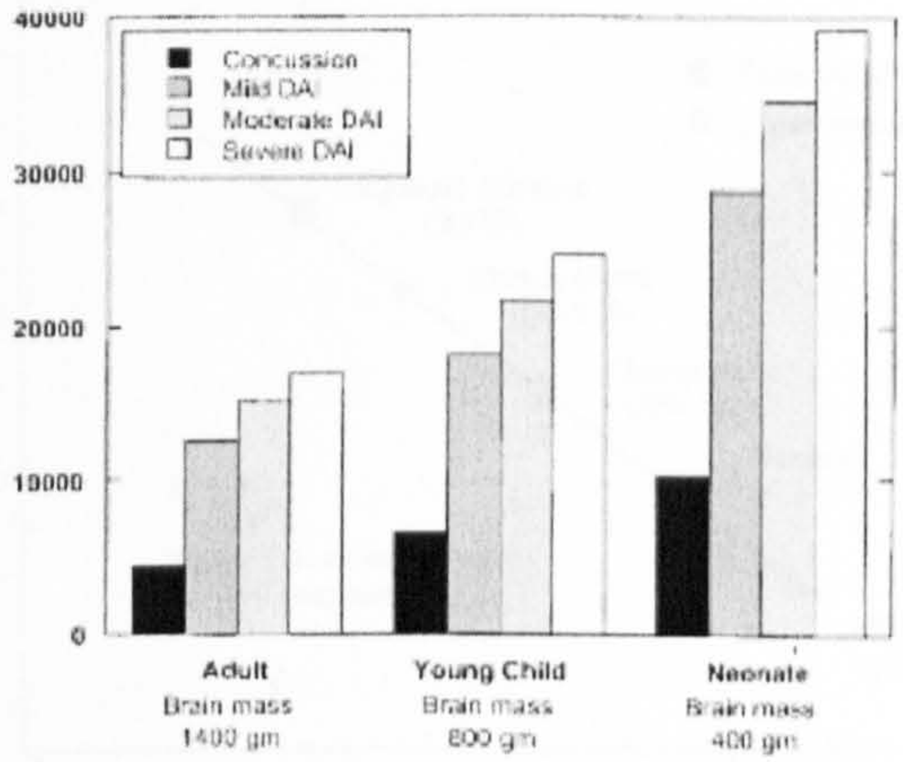

Figure 2.16. *Brain injury tolerance scaling in the adult, young child and neonate (Ommaya and Goldsmith 2004).*

The HIC is the most popular criteria that was adopted by industry for head injury, but it is also criticized widely by biomechanician and neurologists for the inconsistency of the clinical diagnosis and the engineering simulation.

2.6. Experimental Analysis Of Head Injury

Besides the clinical documentation analysis, the animal and human cadaver tests are the important engineering validation that evaluate the analytical model or the computational model of their accuracy and the ability to simulate and predict the head injury criteria. Ommaya (1968, 1971) conducted a series of tests on adult rhesus monkeys for whiplash injury investigation. His first tests exposed the rhesus monkeys into a whiplash head

acceleration associated with a terminal minor head impact under the car impact force. The acute subdural haematoma as well as the contusions over the brain surface and upper cervical cord was examined, with the angular velocity of 500 radians/s and accelerations of 10,000 radians/s^2 for 5.6 ms. The second test set up a comparison group that one was adopt translational force through the centre of gravity of the head and one was with both translational and angular force around the neck. None had impact contact during the test. The results correlated well with the shearing theory and shows the classical bilateral ASDH appeared in all-angular force subjects but not linear only subjects. Their species comparison test by Ommaya confirmed the Holbourn's hypothesis (Ommaya and Goldsmith 2002) that the increasing brain size increase the risk for brain damage, with three primate species of different brain size (Figure 2.17).

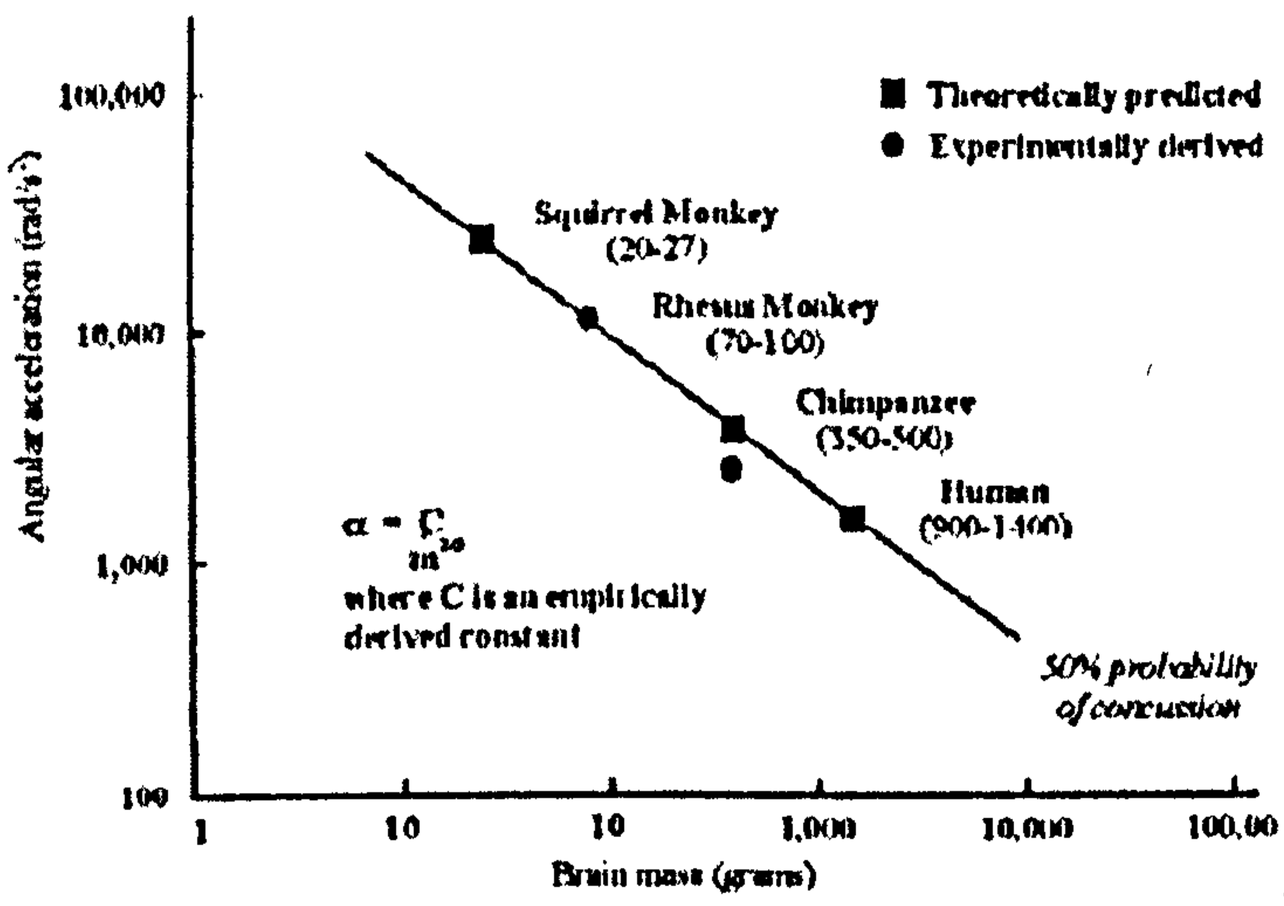

Figure 2.17. Concussion tolerance as a function of angular acceleration and brain mass (Ommaya and Goldsmith 2002).

Nahum (1977) and later Trosseille et al. (1992) used human adult cadavers to investigate intracranial pressure distribution under impact loading. Trosseille carried out 6 tests with 3 fresh and re-pressurised cadavers; the head was instrumented with several linear accelerometers and pressure transducers to obtain the acceleration and the pressure within the cranium during the impact. The results obtained have become the validation for the later several numerical simulation of human head impact injury by 3D finite element model (Turquier 1997).

Some other tests such as Van Lierde et al. (2005) focus on the tissue deformation. Van Lierde used 10 embalmed human cadavers to investigate the stretch ratio of the bridging veins by radioscopy. The data set is complement with Lõwehielm's (1974) result, and

obtained the angular rupture tolerance criteria of 4500 rad/s^2 for angular acceleration, 30 rad/s for the change of the angular velocity (Figure 2.18).

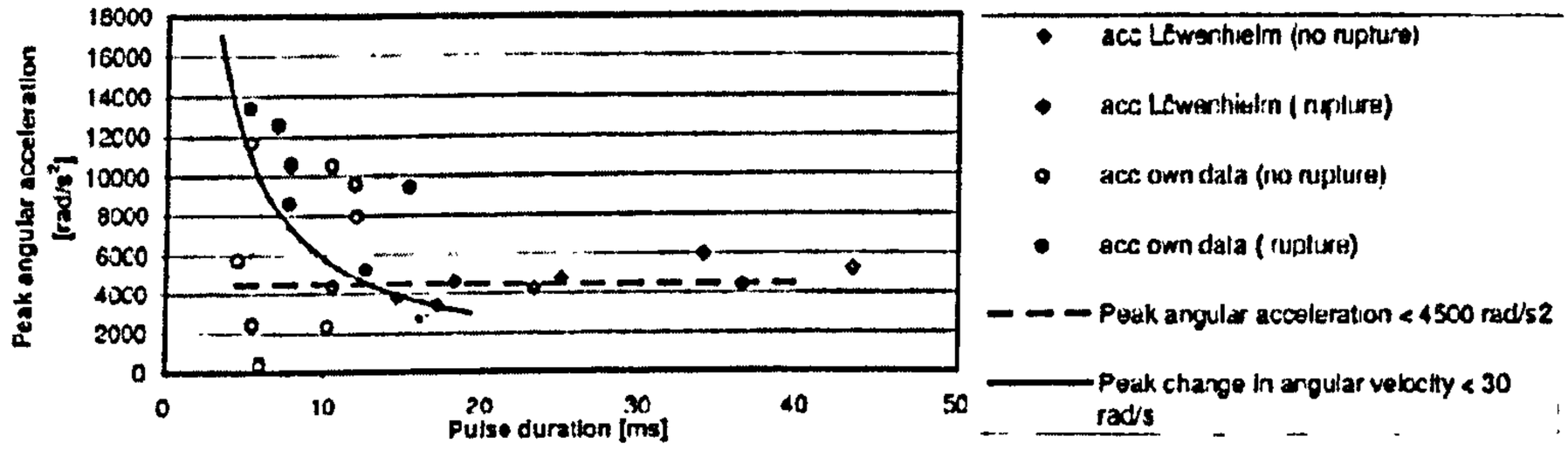

Figure 2.18. *Experimental data and tolerance curves for bridging vein rupture in humans (Van Lierde et al. 2005).*

2.6.1. THE MULTI-RIGID BODY MODELLING

The multi-rigid anthropomorphic dummy is a human shape surrogate used in dynamic motion reconstruction. It is constructed with multiple rigid components with specified shapes of human limbs, torso and head connected by linkages to simulate a biological joint. It is widely applied in the automobile industry to reconstruct a vehicle collision. It became an increasingly widely applied methodology to study the traumatic head injury caused by either a fall or from abusive shaking. During the motion reconstruction, the trajectory of the rigid body is traced using high-speed video cameras, and the impact force or acceleration is collected by transducers and accelerometers. There is no relative movement within any rigid component. The linkage of the joints in the dummy can be a simple hinge to rubber with a different friction factor. The result of the simulation gives either the dynamic validation for the kinematic analytical equation, or correlates with the clinical diagnosis to analyse the injury mechanism, moreover, the reconstruction of the kinematic motion as well as the outcome acceleration can be an important data input into further numerical modelling such as a finite element model.

A recent important test with a dummy understanding a short-distance fall was conducted by Bertocci et al. (2003). The repeatable fall tests were applied on a 3-year-old Hybrid II dummy from bed height (0.68m) onto various surfaces. The aim was to assess the relationship between the impact loading with different impact surfaces to establish the dynamic injury tolerance and hence understand the controversial opinion (in clinical pathological diagnosis), as to whether the short distance fall produces fatal head injury amongst the paediatric population. The surfaces chosen were; playground

foam, carpet, linoleum, and wood respectively. The results show that the wood surface can produce the highest impact with an acceleration 245g, and HIC 418, while the lowest is playground foam with the acceleration 114g, HIC 53. None of the impacts exceeded the minimum injury tolerance. The tests give the support to the opinion that a short-distance fall is not able to fatal damage the brain.

The most important study on SBS using engineering analysis methods comes from the anthropometrical dummy reconstruction. The earliest biomechanical study was undertaken by Duhaime et al. (1987), who produced a one-month-old anthropometrical dummy with three types of the neck from low to high friction and two types of head construction either with or without the skull. The dummy was set to free repetitive shaking and impact on two different surfaces separately. The mean peak tangential acceleration as well as the mean time interval data was collected and it was found that shaking (9.29g, 106.6ms) has much lower injury tolerance than impact (428.28g, 20.9ms). The model with or without skull produced the same magnitude of acceleration during both shaking and impact. The contact stiffness of the surface is proportional to the contact acceleration during the impact, in that the stiffest gives the highest force. Duhaime's result disagrees with the shaking induced shear injury embraced by most of the neuropathologist community and argues that head injury does not come with shaking alone but must therefore involve impact.

Cory et al (2003), believed the shaking alone injury does indeed exist and after reviewing many medical publications of the SBS, doubted the reliability of Duhaime's experiment. Therefore a reproduction experiment was designed and executed with an one-month-old anthropometrical dummy with stiff and soft rubber neck with large friction and a metal hinge neck with negligible friction. The result exceeded the angular acceleration of Duhaime's data by three important factors: the metal hinge-neck which maximises the whiplash phenomenon, high centre of gravity which allows chin-to-chest and occipital-to-back impact happened, and thirdly with a cotton wool chest and back material which was thought would improve the biofidelity of the surrogate. The angular acceleration and velocity reached the 50% possibility concussion of the injury tolerance criteria scaled by Ommaya in 1985 (Klinich 2002). Hence they called for the sufficient doubt in Duhaime's testimony that lack of biofiedelity may lead to wrongly interpreted medico-legal evidence (Figure 2.19).

In the same year Prange et al. (2003) also reproduced Duhaimes et al. (1987) experiments on shaking, short distance fall and inflicted impact (shaking followed

impact by the end). They designed a one-month-old infant with a non-friction hinged neck which was given repetitive shaking, then a short distance drop (0.3m, 0.9m, 1.5m) and shaking with inflicted impact on three surfaces. Again the angular acceleration and velocity were measured and compared. It was concluded that vigorous shakes gave responses similar to that resulting from minor falls, and the injury risk of inflicted impacts is significantly higher than even a 1.5-m fall onto concrete. As a result their consequences supported the Duhaime's conclusion that inflicted impacts against hard surfaces are more likely to be associated with inertial brain injuries than short distance fall or shaking.

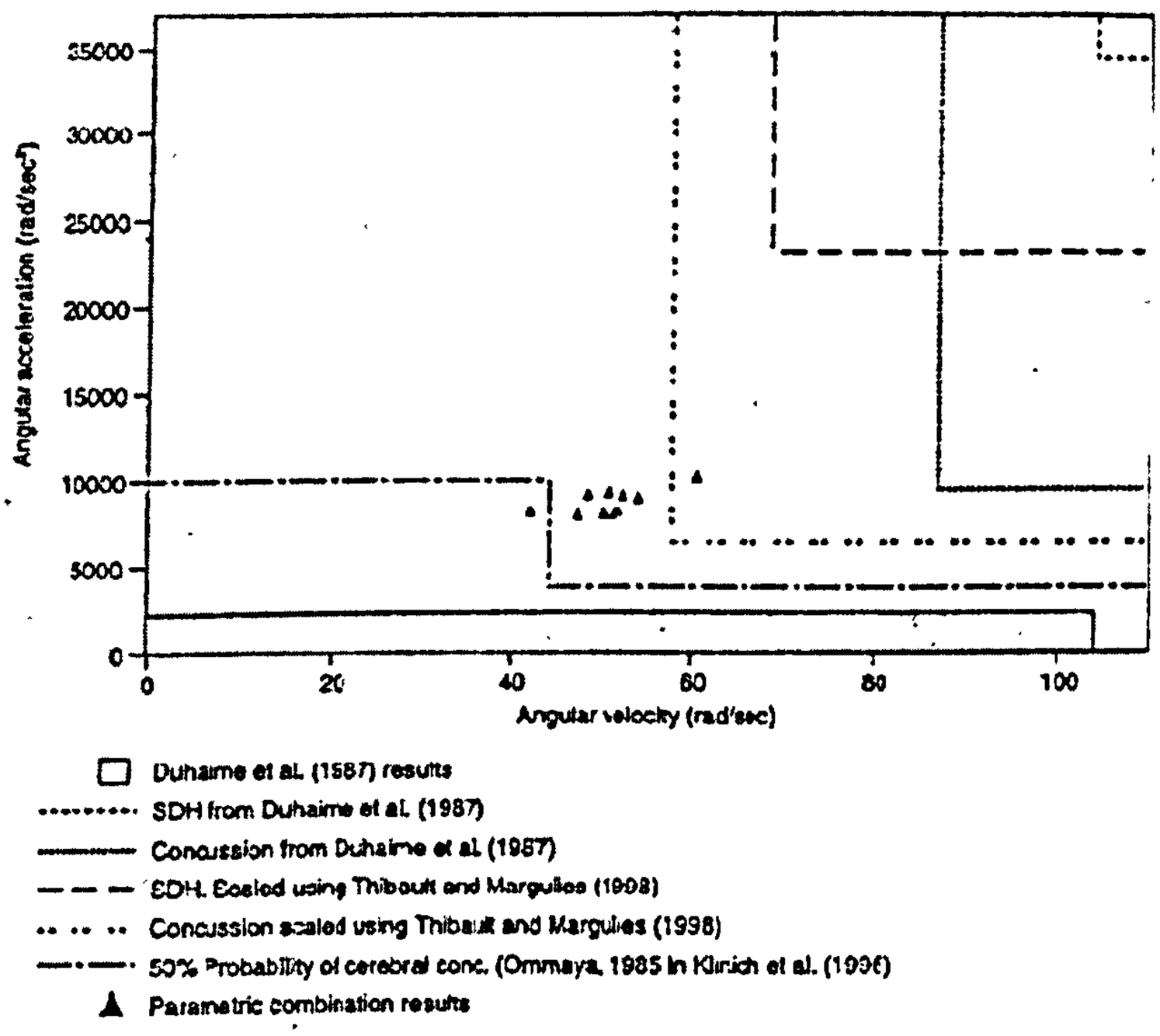

Figure 2.19. *The comparison between Cory et al. (2003)'s parameter combination model and the tolerance limits for concussion and Subdural Haematoma (SDH) scaled from Duhaime et al. (1987), Thibault and Margulies (1998) and Ommaya (1985).*

2.6.2. THE PHYSICAL SYSTEM MODELLING

The physical system modelling refers to a physical model of skull-brain structure, which is consisted with simple or sophisticated skull shell, filling with the intracranial tissue surrogate such as the brain or CSF. The accurate representation of the soft biological tissue provides the unique insight into the relationship between the head kinematic motion and mimics biological tissue deformation. The deformation pattern can then be

recorded, analysed, and compared to the pathological symptoms of traumatic head injury. It gives very profound demonstration and the evidence for the shearing induced injuries such as SDH and ASDH or the diffused brain surface injury such as DAI. The results can help the biomechanician to establish the principle of the specific injury associated with the specific kinematic motion.

Margulies et al. (1990, 1992) constructed adult baboon and human skull models with and without the falx in the midsagittal plane (Figure 2.20-2.21). The model was filled with silicone dielectric gel (Dow Corning Sylgard®. 527 A&B) (Dow Corning Corporation 2008) as a brain tissue and liquid paraffin as the CSF. The observation plane was a painted grid using ink. Only half of the model was produced and then sealed by a transparent cover to aid observation. The models were set up on the test rigid and excited by the non-contact rotation with the magnitude from a traffic collision whiplash for the DAI injury threshold. The displacement and strain of the grid was record using high-speed video and was analysed and normalized to specific brain mass. The shear strain and the pathology diffuse brain injury distributions mirror each other.

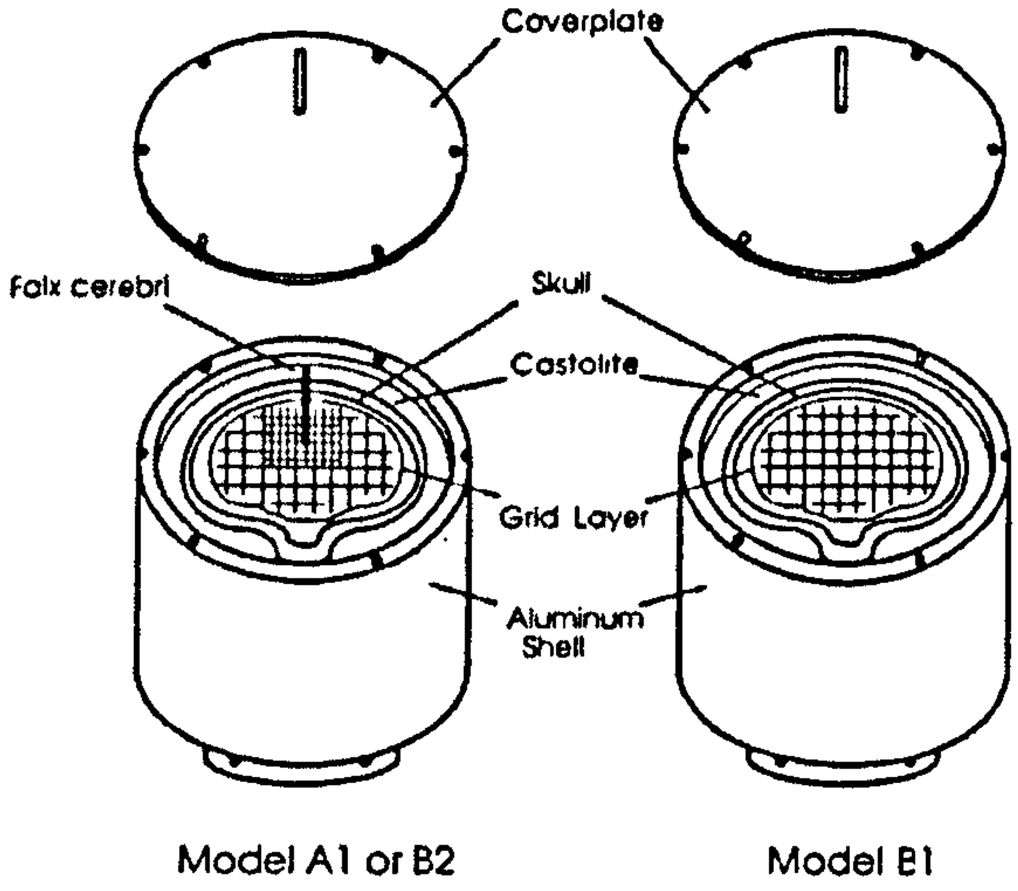

Figure 2.20. *Schematic of skull physical model with left: finer grid with falx cerebri; right: grid with no* falx cerebri (Margulies 1990).

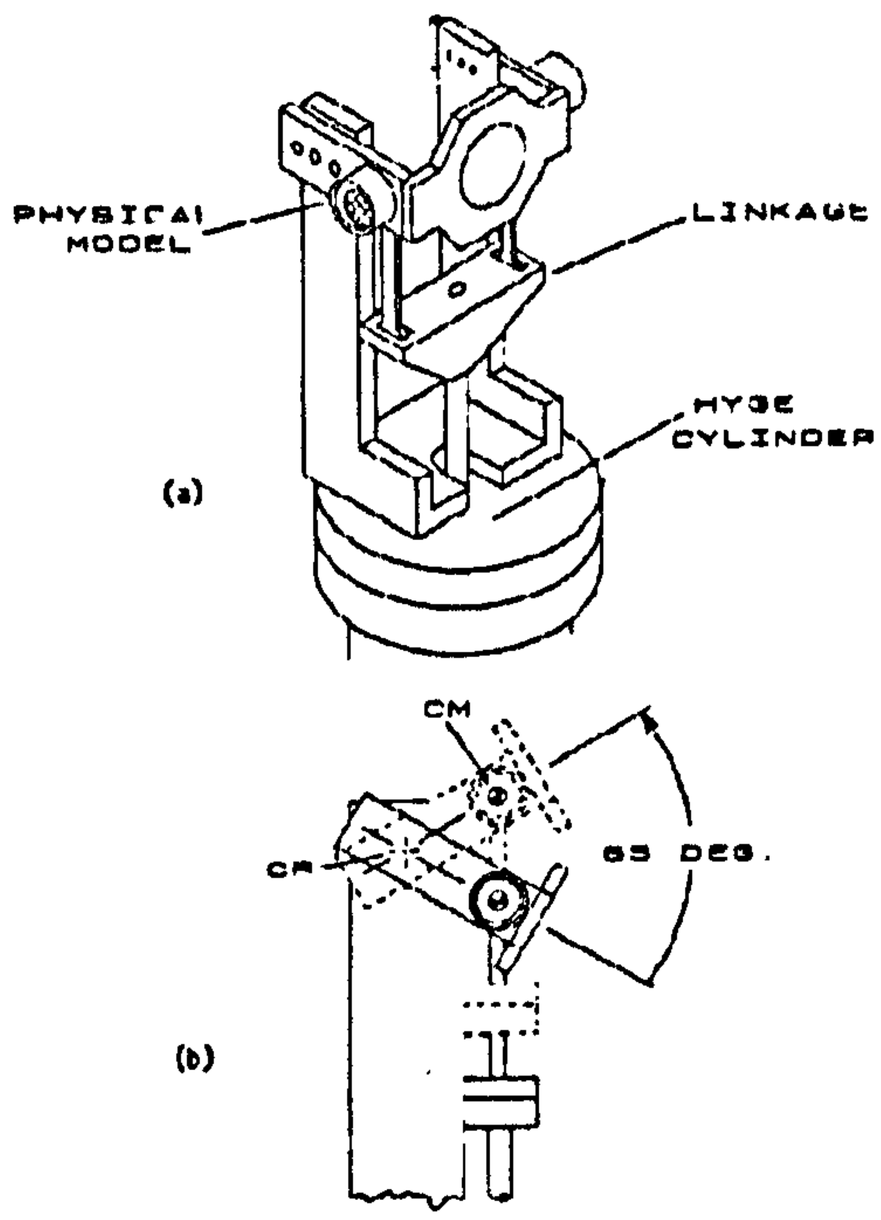

Figure 2.21. *Diagram of custom designed accelerating system: (a) mounting of the physical model; (b) linkage motion with 7.3cm between centre of model mass (CM) and centre of rotation (CR) (Margulies 1990).*

Ivarsson et al. (2000) built up the physical model of the parasagittal human skull-brain to test the biomechanical function of the cerebral ventricles to establish whether it could relieve the shearing deformation to protect the brain tissue from the rotational injury (Figure 2.22). The model was filled with the same substitute as with the previous Margulies et al. (1990) model for brain tissue (silicone dielectric gel Dow Corning Sylgard® 527 A&B) and CSF (liquid paraffin) and was exposed to 7600rad/s^2 rotational pendulum impact. The motion of the paper mark on the parasagittal plane was traced and analysed by Green-Lagrangian strain method and shows that the lateral ventricles relives the strain protect the brain tissue from traumatic brain injury.

Following this result, Bradshaw et al. (2001) used a similar model but with coronal head plane with or without sulci to investigate the head injury due to coronal impacts (Figure 2.23). The anthropometrical geometry of the model comes from 10 adult male MRI scans. The substitute material adopted was the same as with all previous models with an elastic membrane chosen for the sulci. The results demonstrated that the position of contra-coup side obtains the worst-case bridging vein strain which can be approximately doubled by adding sulci. The results also demonstrated that the peak angular velocity, as compared to one of the injury tolerance indicators, is more suitable for DAI but not ASDH.

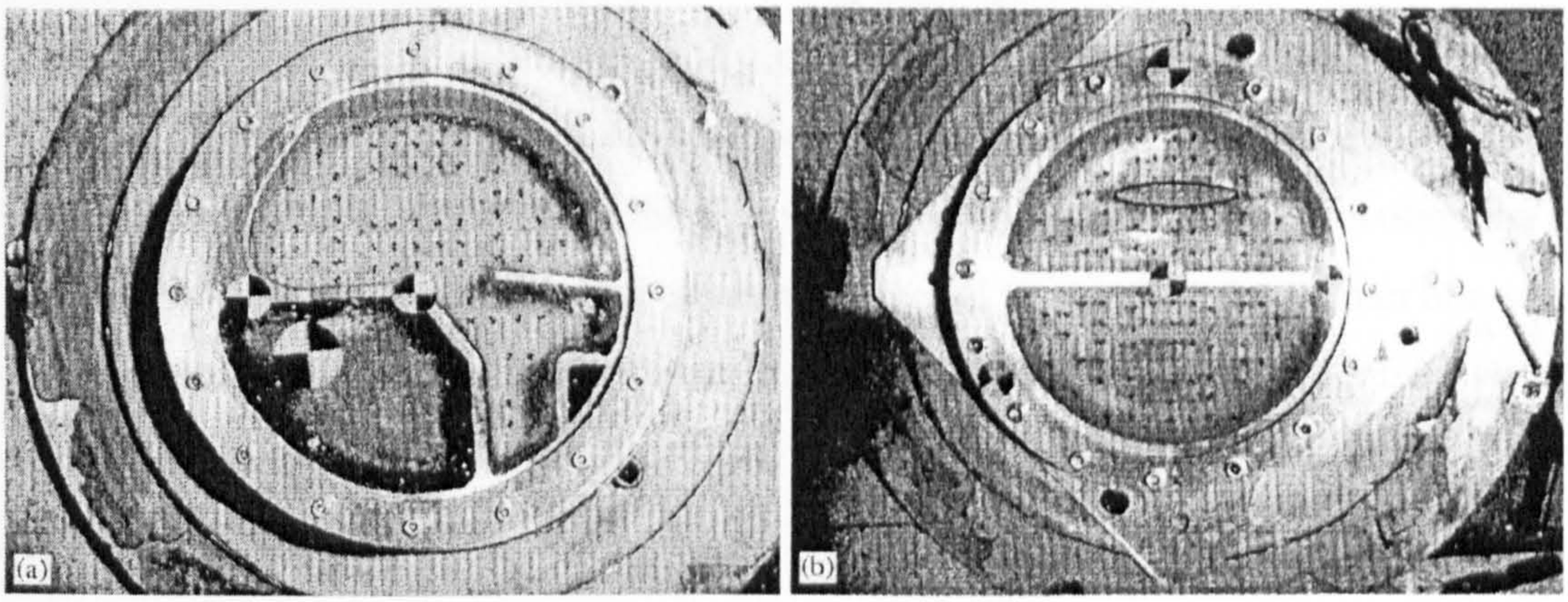

Figure 2.22. *Physical model of the human head sagittal plane: (a) The sophisticated model mounted on the rotation table. The acceleration direction is clockwise simulating a forehead impact; (b) The physical model with two semicircles contains an elliptical fluid-filled inclusion simulating a lateral ventricle (shown by the drawn ellipse). (Kelvin 2000)*

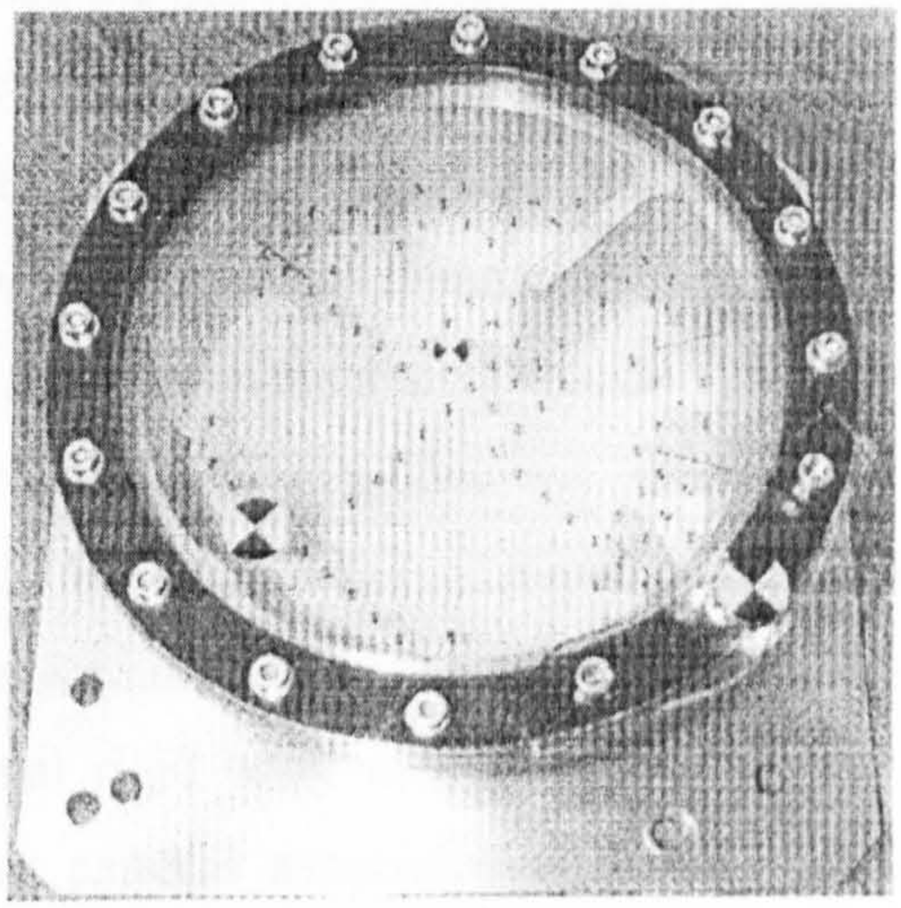

Figure 2.23. *Physical model of the human head sagittal plane with brain, falx, sulci and CSF modelled (Bradshaw 2001).*

2.6.3. THE MULTI-BODY DYNAMIC SIMULATION

The multi-body dynamic simulation is a mathematical simulation to define and analyse the dynamic multi-body system. The dynamic multi-body system is a collection of rigid and flexible bodies joined together by kinematic joints (e.g., revolute or translational joints) and force elements (e.g. springs and dampers) (Goldsmith and Monson 2005). By applying the inertial conditions and the inertial properties, the whole system is able to predict the three dimensional movement in global and local coordinate references by numerical algorithms. To modify the discrete joints and bodies with particular size and shape, it is possible to construct a human body model to simulate the human movement in various circumstances. The resulting contact and acceleration data, combined with the medical evidence helps to assert the type injury and hence establish the injury criteria.

2.6.3.1. IMPACT AND FALL INJURY

Traffic accidental head injury always combines the injuries from both impact and severe whiplash. To fully investigate the variation of head injury pattern, physical collision tests are usually conducted with an anthropometric dummy. Moreover, the computational multi-body system can be also adapted to either assist the test or specifically illustrated the head motion during the collision.

Canaple et al. (2003) used the multibody model of a Hybird III dummy to reconstruct a car accident. The input motion came from a physical collision reconstruction from the initial un-deformed state to the final deformed state of a vehicle during accident. The reconstructed head movement helps to identify the linear and angular accelerations of the victim's head. The study provided the 3D motion for further investigation of head injury using a nonlinear finite element model.

Falling, as another main causation of focal head injury, is difficult to investigate in vitro, due to the measurement difficulty of inertial motion and contact material properties. Computational rigid body modelling provides an alternative approach to understanding the injury patterns associated with the parameters of contact surface, height and age.

Gilchrist and Riordain (Gilchrist 2003; Horgan and Gilchrist 2003; O'Riordain 2003) adopted the computational software MADYMO (TNO Automotive) to construct the multi-body system on a fall head injury. MADYMO (Mathematical Dynamic Models) is a multi-body dynamic simulation software that was developed to design and optimise automotive occupant safety systems and accident reconstruction.

The particular strength of MADYMO is its database with the family of multibody pedestrian models, the joint stiffnesses and the contact characteristics, and is therefore able to simulate a wide range of impact situations. O'Riordain reconstructed 4 different injuries collected from hospital with the record of the initial condition and the contact surface. The acceleration and velocity obtained from the results helps to testify the intracranial injury according to the clinical diagnosis and helps the biomechanicians to understand the relationship between the different parameters. The motion information is also referred to the further simulation by finite element modelling.

2.6.3.2. SHAKEN BABY SYNDROME

The Physical anthropometric dummy is an important approach for parametric study of SBS. Duhaime et al. (1987) who identified the SBS by using a biomechanical dummy and her colleague Prange et al. (2003), and later Cory et al. (2003) respectively produced the surrogates and configured it by an empirical estimation for the neck system to produce various accelerations.

Later the computational approach was also introduced with Wolfson et al. (2005) adopting MADYMO to study SBS. The input motion was collected from the volunteer's

shaking of a surrogate with the full range of accelerations being measured (Figure 2.24). The result demonstrated that the maximum acceleration does not exceed the injury threshold which is consistent with the conclusion from physical experiments.

In brief, the kinematic rigid modelling of the SBS will not be able to interpret the mechanism of the injury, either the physical/numerical model involves the continuum system of biological components in the future, or the head injury criteria has to be investigated under the loading from single short pulse into the long cyclic pattern.

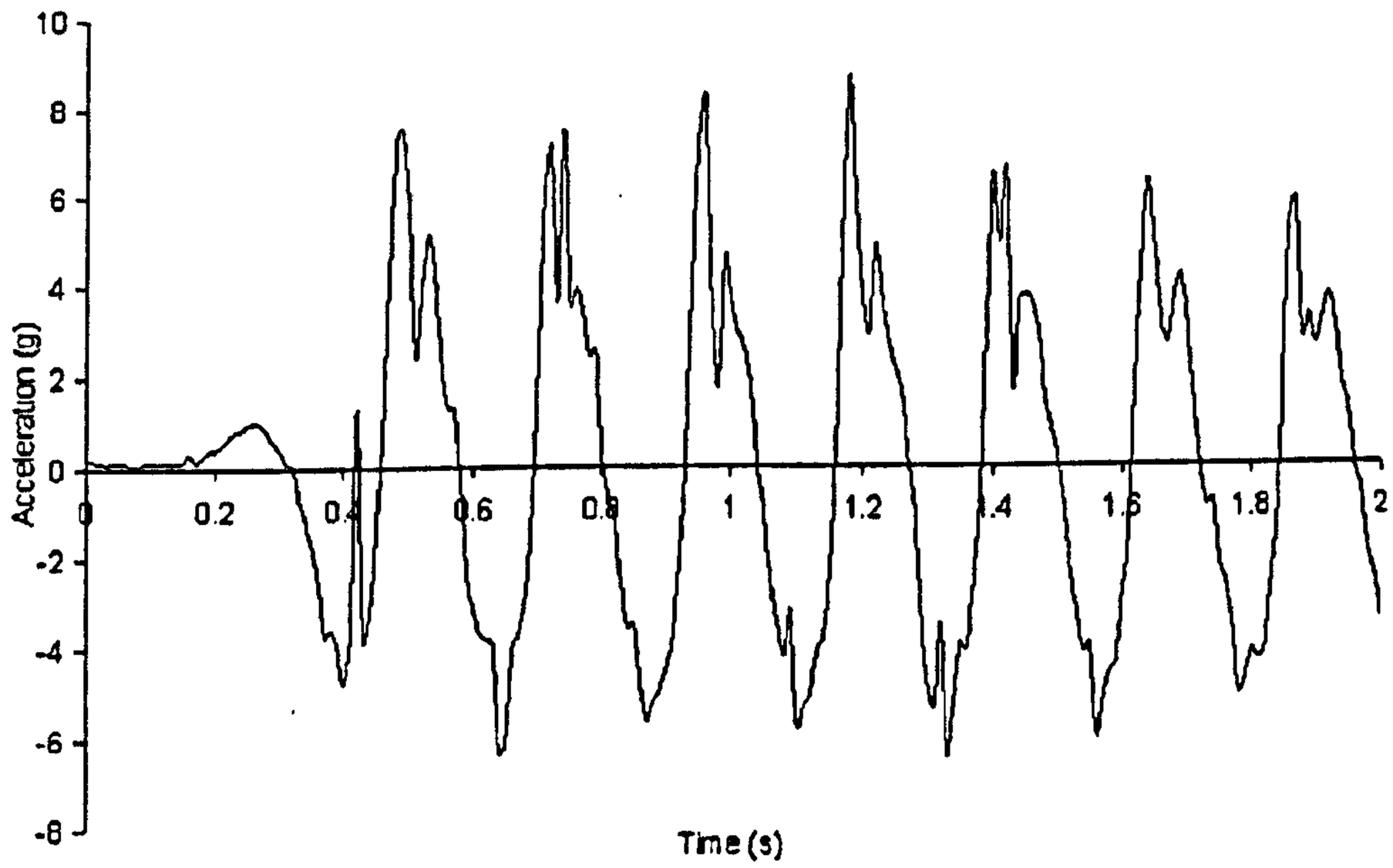

Figure 2.24. Sample torso acceleration trace cited from Wolfson et al. (2005).

2.7. The Finite Element Modelling Of The Human Head

The multi-body dynamic modelling, although very efficient at predicting and reconstructing the head motion, is not able to demonstrate the relative motion of the biological tissue interior the skull as a continuum system. Other more complex mathematical methods are considered including analytical and numerical models.

Analytical models formulate a set of explicit mathematical governing equations, based on the principles of mechanics, and give closed-form solutions in terms of mathematical functions. This approach is limited to problems with relatively regular geometry, simple boundary conditions and homogeneous material properties, owing to mathematical difficulties in formulation and solution (Goldsmith 2001), while numerical methods approximate the analytical solution with a numerical procedure.

The finite element (FE) model is superior to other numerical methods, as it solves problems by setting up a geometrically complex material domain with a collection of simple subdomains called finite elements, and then derives linear combination of algebraic polynomials as a continuous function. The parameters in these functions represent the values of each node on the boundary and in the interior of each element (Goldsmith 2001).

The finite element method includes three steps, pre-processing including geometry modelling and material representation, secondly a solution those that specifying boundary and loading conditions, executing the computation sequence and extracting numerical results, and finally post-processing with the presentation and interpretation of the computed results.

2.7.1. THE DEVELOPMENT OF THE FE MODEL

When the geometry detail of the biological organ is irrelevant to the mechanical response, the 2D or 3D model with spherical spheroid or ellipsoidal shape was adopted for the purpose of reducing the computational time.

The complicated 3D model with geometry accuracy is also very important when the anatomy structure details cannot be ignored and influence the consequence of the mechanical consequences. The details can be obtained from shape data of segmented images from magnetic resonance imaging (MRI) scans or computed tomography (CT) of the specific organs. This kind of model may better interpret the stress/strain distribution of the intracranium tissues as a continuum system.

Ruan et al. (1991) 's 3D FE adult head model, consisted of a layered shell cranial bone, a thin fluid layer CSF and invisicid brain continuum, was given frontal and occipital impact. The pressure-time history is quite consistent with previously published cadaver tests. According to the clinical diagnosis, the impact produced a linear acceleration leading to a wave propagation through the centre of gravity of the mass result in the brain tissue has the other side cavitation (negative pressure) due to the CSF suspension, to suffer so called contra-coup injury. Ruan's model predicted the contra-coup injury is more likely to result from occipital impact than from frontal impact, because of the higher contra-coup pressure in the frontal lobe. This result matches the clinical diagnosis that the frontal lobe injury was more often detected. Chu et al. (1994) used a 2D plane strain FE model to simulate a parasagittal section of the human head under

frontal and occipital impacts. The shear strain distribution compares very well with the clinical cerebral contusion.

Keliven and Holst (2002) studied the relationship between the human head size and the intracranial response under impact loading using a 3D FE model. During the frontal impacts, various head size and element mesh densities were applied, the result shows the intracranial stresses associated with injury is dependent with the head size, which cannot be predicted with the current HIC standard.

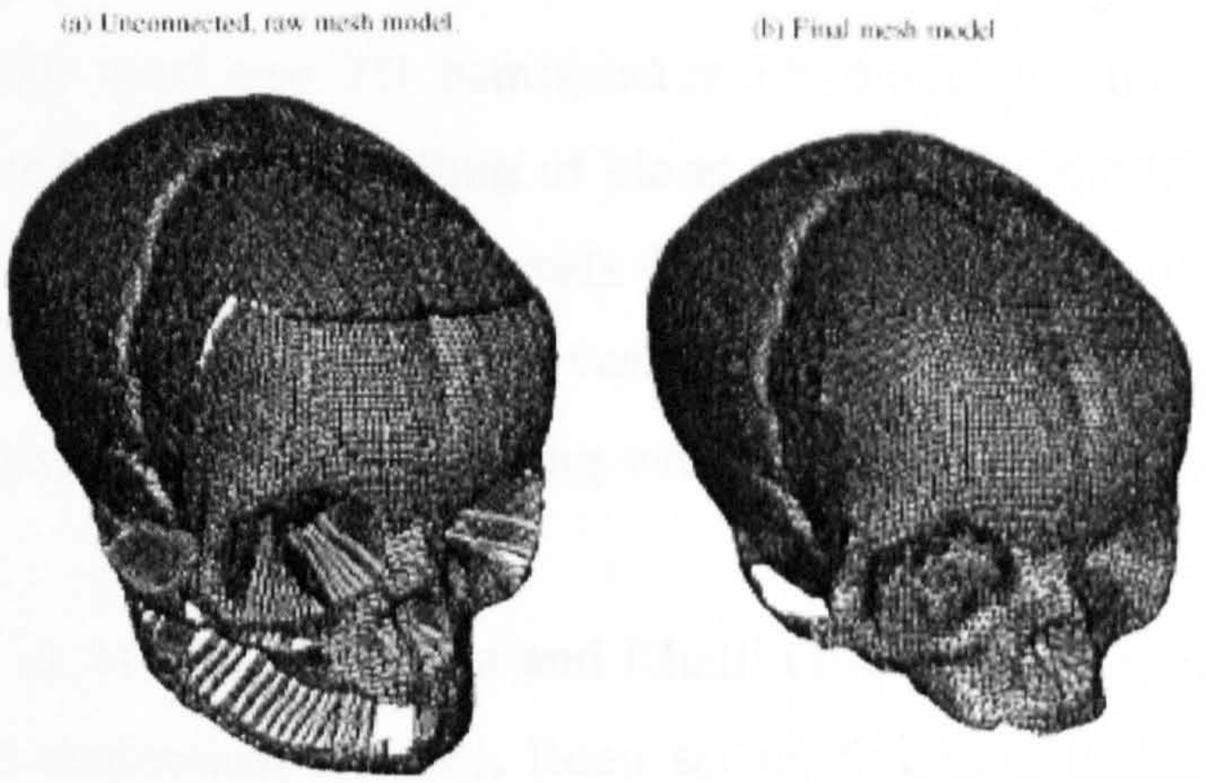

Figure 2.25. *The finite element fetal head model for labour simulation with (a) raw mesh; (b) fine mesh (Lapeer and Prager 2001).*

Besides the adult human head, the paediatric geometry as well as the details of the FE model becomes an important method to investigate the infant head injury. The earlier test by McPherson (1980) with 63 thin shell elements fetal FE model demonstrated the head mouldings shape change during the labour, it was found out that the preterm exhibits deformations 2-4 times greater than the term bone model.

Lapeer *and Prager* (2001), produced a non-linear model, and subjected the model with the pressures exerted by the cervix, during the first stage of labour. The analysis shows good agreement with the clinical deformation and gives the quantitative assessment of fetal head moulding (Figure 2.25).

2.7.2. THE MODELLING REPRESENTATION OF THE HUMAN HEAD

Sometimes the FE model can be optimised with the reduction of some anatomic structures, while it can be delicately constructed with more of the fine components of the human head represented. More biofidelity means the more complicated the mechanism involved during the dynamic loading, the boundary condition and the

constitutive relation of each structure requires accurate representation which can in many cases be extremely difficult to include in the model.

Horgan and Gilchrist (2003) used the finite element model to study the human head impact injury of simple pedestrian accidents. Their FE modelling was focusing on a series of parametric study of the CSF and skull modelling with different mesh densities and element formulations. Their model concluded that the correct prediction of intracranial pressure distribution depends on the accuracy and careful modelling of CSF and skull thickness.

Omori et al. (2000) used two 2D hemispheres FE model to study the shear strain distribution with and without modelling of blood vessels. The model was subjected to an angular acceleration and the result reveals the larger shear strain of brain tissue close to the blood vessel than the one without vessels. Their model suggested the bridging vein should be involved into the modelling when further studying the DAI by the FE method.

Both Willinger et al. (1995), and Ruan and Khalil (1991, 1994), produced FE models with distinguished anatomical features. Ruan set up three 2D models from including initially simple and building up to more complicated anatomical features. The membranes in the advanced model affected the dynamic head response significantly.

Taylor and Miller (2004) used a 2D FE model with the brain/ventricular system to study the non-traumatic injury-hydrocephalus. The well reproduced ventricle helped to predict the strain distribution in hydrocephalic brain associating with the proper material properties.

The other researchers such as Lee et al. (1989) used a 2D FE rhesus monkey model to understand the vein stretch ratio when the subdural haematoma existence, so that the thresholds for SDH could be estimated.

2.7.3. THE BOUNDARY CONDITION

The boundary condition between the brain and the skull modelling is critical to simulating the brain response to the skull by linear and angular loading. Between the brain and skull normally there are several layers such as the dura, subarachnoid space filled with CSF, and bridging veins. Sometimes the scalp and the tentorium or falx is also modelled. There are a few ways to set up the contact situation in a FE model and the results require further validation.

Wittek and Omori (2003) studied the biofidelity of different boundary condition modelling by setting up a 3D FE model with LS-DYNA of a thin sagittal slice of the human head (Figure 2.26). There are three types of modelling; the brain rigidly attached to the skull, frictionless sliding contact between brain and the skull, and the most complex is to create a CSF with fluid like properties, with the element of brain and skull are merged into CSF elements. The first two boundaries gave less accurate result with much noise, while the third one is the most appropriate condition. The correct representation of CSF as a fluid medium is important to get the realistic response of the brain tissue.

Ueno et al. (1995) studied the impact head injury using a 3D FE model with a nonlinear contact surface algorithm for the brain-skull interface in ABAQUS. The pressure distribution of the brain compared favourably with the measured test data.

Aomura et al. (2003) set up a 3D FE head model with two contact conditions, one is the tied-type interface and the other is the slide-type. The model was crashing by an iron block impactor on the occipital region, with the tied-type found out to be a better representation of the skull brain interface.

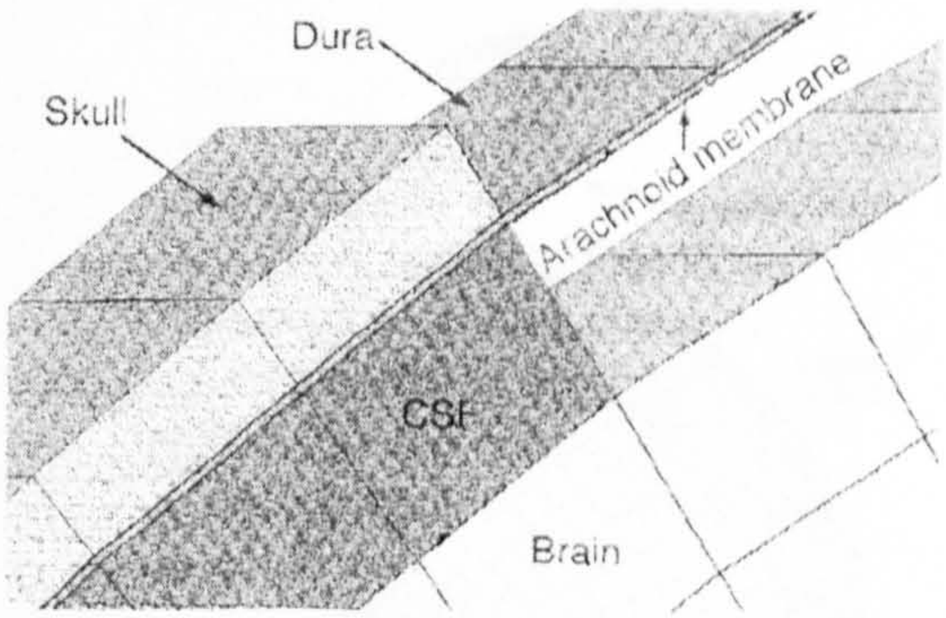

Figure 2.26. *Finite Element Modelling of skull-brain boundary with surface to surface sliding contact between CSF and skull (Wittek and Omori 2003).*

2.7.4. THE PAEDIATRIC MATERIAL PROPERTY APPLIED IN FE MODEL

Modelling of the infant head requires the representation of infant constitutive properties since a scaled material property from adult head is considered less reliable.

Margulies and Thibault (2000) investigated the impact injury by configuring an FE model with infantile structure and material properties (Figure 2.28). The constitutive equations come from a series test on porcine cranial bone, brain and suture (Figure 2.27). A comparable model was produced with adult data. The larger deformation of the

infant model shows the compliant properties of the infant head and suggests any further FE modelling should carefully adopt paediatric properties.

Appendix E demonstrates the development of the biomechanical study of human skull, brain, and vessel. Meanwhile Appendix K tabulates the material properties in different finite element models in the literatures.

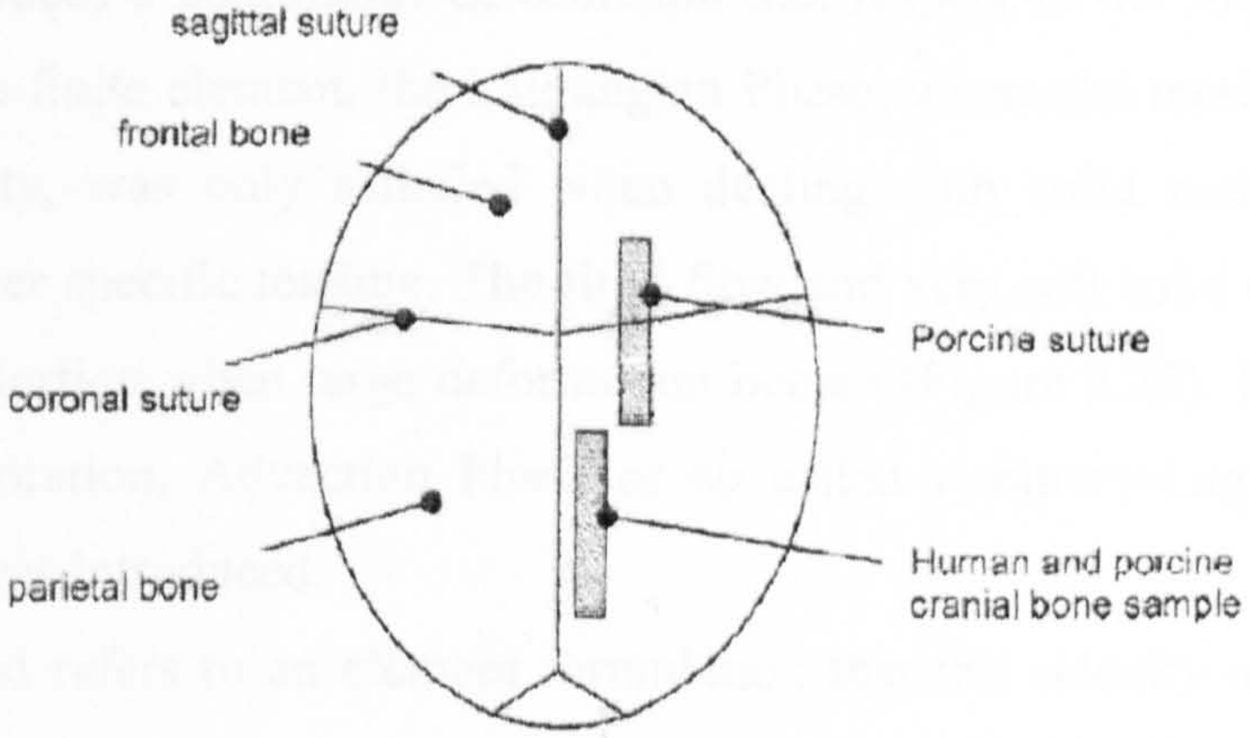

Figure 2.27. *Infant cranial vault: shaded areas represent approximate size and location of skull and suture samples removed (Margulies and Thibault 2000).*

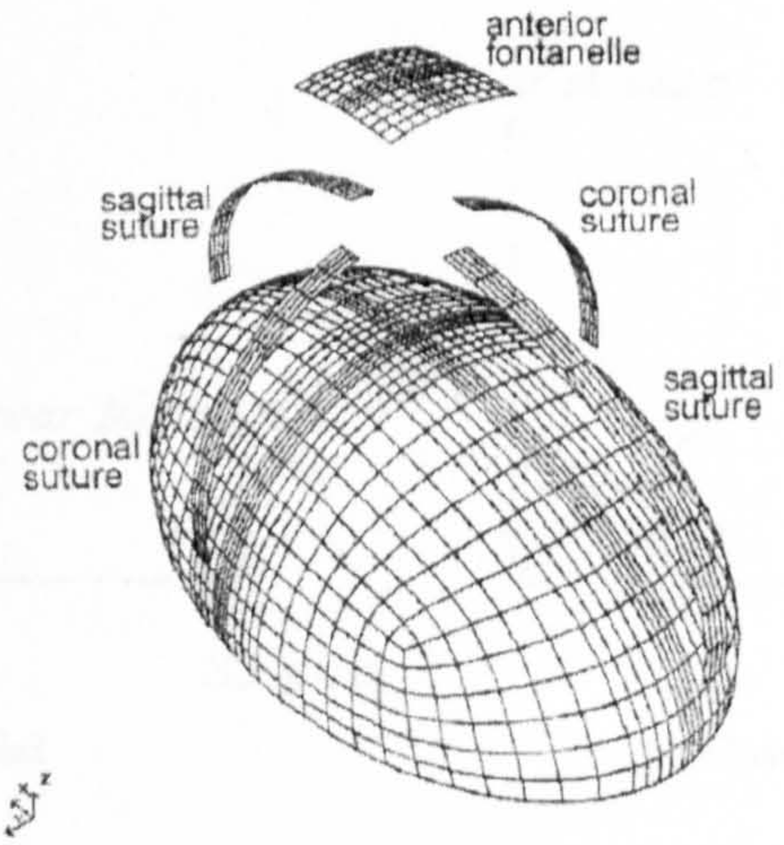

Figure 2.28. *Schematic of finite element mesh of newborn infant head with skull and suture property (Margulies and Thibault 2000).*

2.7.5. THE FLUID STRUCTURE INTERACTION (FSI) (Hallquist 1998; Cook et al. 2002; Hallquist 2003; Moaveni 2003; Olovsson et al. 2003; LSTC 2005)

In solid mechanics, the shear behavior of an element can be represented by the shear stress σ proportional to the shear strain ϵ, the coefficient of proportionality is the shear modulus G with the unit of Pascal (Pa). The displacement gradient is the dependant

variable therefore in the finite element method, the constant shear force produces a finite deformation on an element. In fluid mechanics, the shear behavior on an element is able to be represented by the shear stress σ proportional to the strain rate $\dot{\varepsilon}$, and the coefficient of proportionality is the viscosity μ with units of Pascal·Second (Pa·S). The velocity gradient is the dependant variables in fluid element. Therefore the constant shear force produces a continuous deformation that respect to the time applied to the fluid element. In finite element, the Lagrangian Phase, where the mesh velocity equals the fluid velocity, was only satisfied when dealing with solid material with finite deformation under specific loading. The fluid flow and very soft solid material produce severe mesh distortion when large deformation occurs (Figure 2.29). In order to avoid the mesh deterioration, Advection Phase or so called Arbitrary-Lagrangian-Eulerian (ALE) method was introduced.

The ALE method refers to an element formulation that the velocity of the material is different from the velocity of the background mesh, in other words there is a volume flowing, so called 'Flux', advecting between one element and the adjacent element under the certain force.

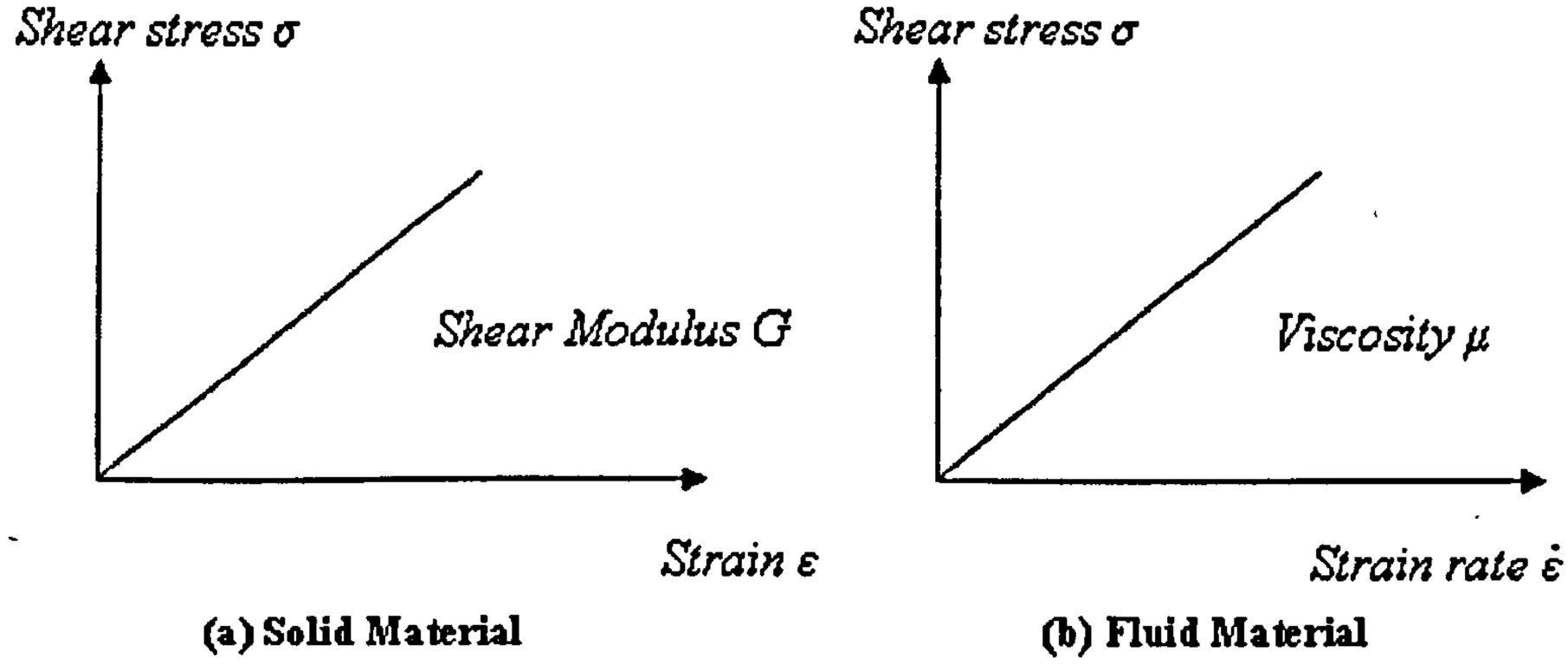

Figure 2.29. *The material property of elastic solid and Newtonian fluid; (a) the relation between shear stress and strain in solid material; (b) the shear stress and strain rate in fluid material.*

The principle of Advection Phase is demonstrated in Figure 2.30. Consider a 'background' mesh with certain material attached into an 'imaginary' mesh, and the two meshes overlap each other. A Lagrangian deformation occurs when all the mesh moves and deforms with the material that the 'imaginary' mesh identical to the background

mesh. An Eulerian deformation occurs when the material deforms with the 'imaginary' mesh as Lagrangian method, and then advects and re-distributes through the static background mesh to the new position. An ALE deformation occurs when the material firstly deforms with the 'imaginary' mesh as the Lagrangian method, and then advects and re-distributes through the moving background mesh to the new position. The ALE method transferred a different amount of flux from the Eulerian method, although both show material flowing. The Eulerian method is normally referred to as a special case of the ALE method where the 'background' mesh velocity is zero. The mass advection is calculated as:

$$\rho_e \cdot V_e = \rho_l \cdot V_l + \sum_{faces} \rho_l^j \cdot Flux_j$$

where ρ_e is density of Eulerian element, V_e is volume of eulerian element, ρ_l is density of Lagrangian element, V_l is volume of Lagrangian Element, ρ_l^j is density of adjacent Lagrangian element j and $Flux_j$ is volume flux through adjacent element j.

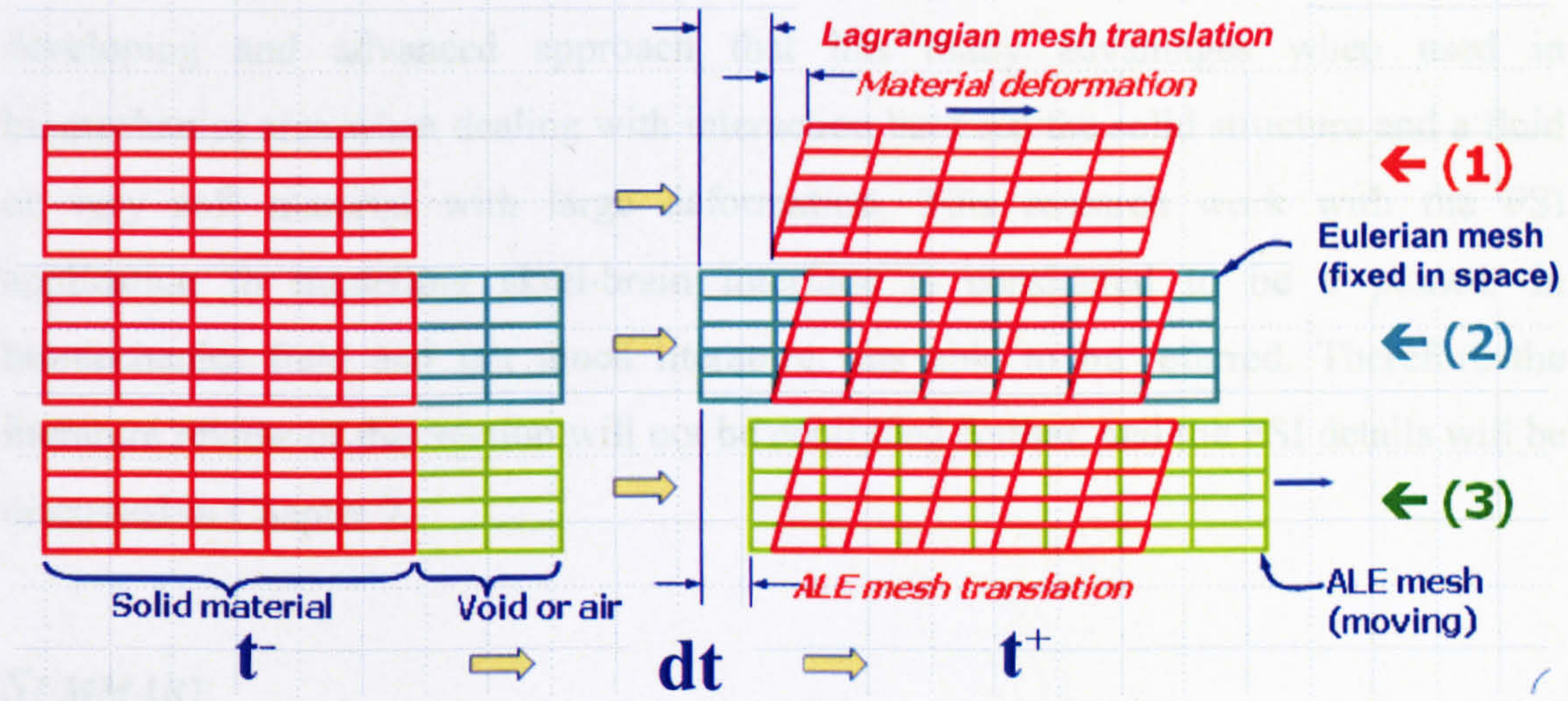

Figure 2.30. *The diagram of (1) Lagrangian, (2) Eulerian and (3) ALE method.*

The Fluid Structure Interaction (FSI) refers to an interaction condition whereby the Lagrangian mesh contacts with the Eulerian or ALE material. The penalty coupling method is normally used between the Lagrangian structure and ALE material. It is based on the procedure that tracks the Lagrangian node and fluid material location in the Eulerian mesh. When intersection happens, the coupling points on the interface between structure and fluid were marked at t^-, then the independent motion of the material over dt is tracked, the penetration distance d is calculated as well as the coupling forces,

finally the structure is re-distributed back onto the Eulerian mesh at t^+. The progress is demonstrated in Figure 2.31 and Equation 2.2.

$$F = -K \cdot d \tag{2.2}$$

where F is penalty force, coefficient K is computed based on the constitutive material model properties and d is the penetration depth.

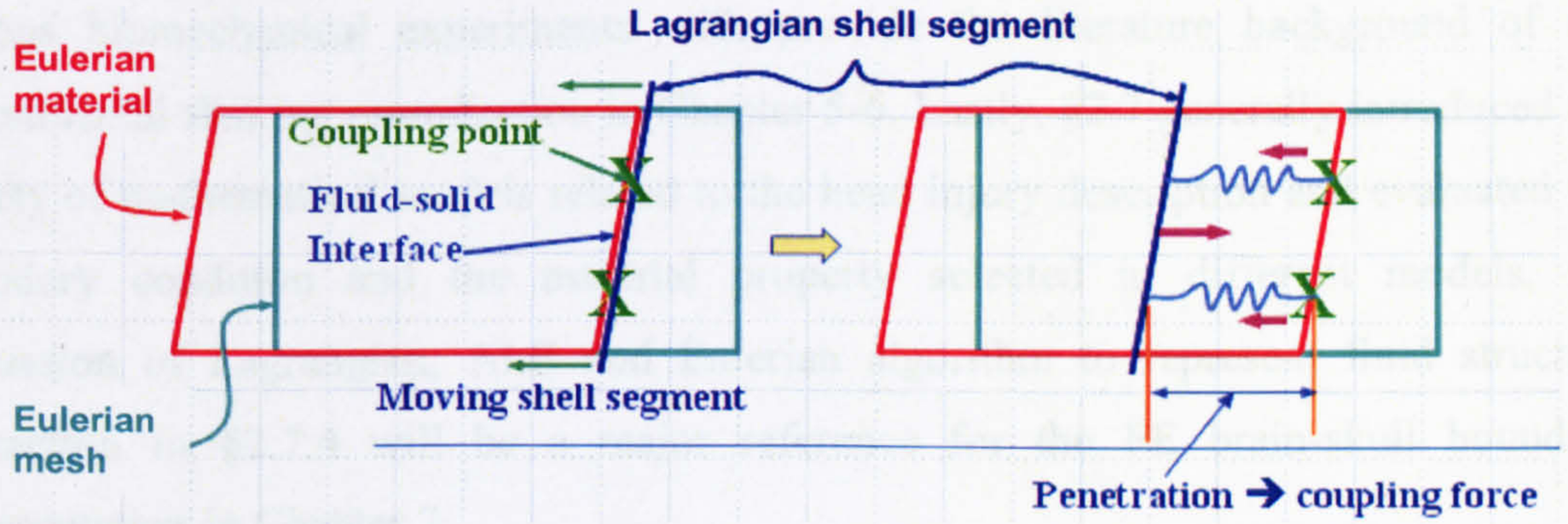

Figure 2.31. *The penalty coupling method in structure and fluid interaction.*

The fluid structure interaction (FSI) with ALE and Eulerian method is considered as a developing and advanced approach that has many advantages when used in biomechanics area when dealing with interaction between the solid structure and a fluid or very soft material with large deformation. This research work with the FSI application in modelling skull-brain interface is considered to be a pioneer in biomechanics field and not much literature was able to be referred. Therefore the literature review of this section will not be continued further, and the FSI details will be discussed in Chapter 7.

SUMMARY

This chapter presents a review, both pathologically and biomechanically, of one type of infantile non-accidental brain injury, the so called shaken baby syndrome (SBS).

The introduction in §2.1 gives the preliminary background of the research in the area of infantile abusive head injury.

§2.2 describe the development of the human head for the geometric shape, skull, brain and the other soft tissue, the difference between infant and adult head structure lends some support for the construction of the experimental and numerical method employed in this work in Chapter 4 and Chapter 7-8 separately.

Further, §2.3 and §2.4 contains the brief history of the development of the research in the infantile head injury, including both the clinical diagnosis and case study which highlight the importance of the biomechanical support in study of SBS.

The dynamic mechanism of various head injury was introduced in §2.5 in order to support the shaking dynamic movement reproduction in Chapter 3. §2.6 summarized various biomechanical experiments with provide the literature background of the experimental shaking reproduction in Chapter 5-6. Lastly, §2.7 generally introduced the variety of mathematical models related to the head injury description and evaluated the boundary condition and the material property selected in different models, the discussion of Lagrangian, ALE and Eulerian algorithm to represent fluid structure interaction in §2.7.4 will be a major reference for the FE brain-skull boundary representation in Chapter 7.

CHAPTER 3: *ANALYSIS OF KINEMATIC MOTION OF HEAD INJURY*

INTRODUCTION

This chapter analyses the motion pattern of violent infant shaking, defines the linear and angular injury parameters associated with it and compares the results with those found in the literature. The motion reconstruction was based on data from a series of tests on an automotive dummy previously undertaken in 2000. The test data was captured by acceleration transducers in the dummy as well as recording from video cameras. Two methods of analysis were set up for the reconstruction; the kinematic equation method and the image analysis method. The chapter contains a detailed description of each of these methods, and discusses the differences between them and the correlation of the data from each. It turns out that there are severe problems with the results of both analyses, problems due not necessarily to the methods themselves, but to the incompleteness of the instrumentation in the TRL dummy. The latter part of the chapter shows how this problem can be partially overcome for the purposes of the present research by using data obtained from analysing the stills in the video output.

3.1. ANTHROPOMORPHIC CONSTRUCTION OF SHAKING INJURY IN INFANTS

In 2000, Dr. A. M. Parsons, a forensic ophthalmologist, organised a set of tests at the Transport Research Laboratories (TRL) in Berkshire to collect data on the kinematic motion associated with the shaking of infants. The tests used the smallest of the available TRL vehicle crash test dummies, modified to be an anthropomorphic surrogate of a 9-month old infant (Brudenell 2000). It consisted of rigid body components for the head, neck, torso and four limbs. The distance between the front of the head and its centre of gravity (COG) was 80 mm, as was that between the rear and the COG. The mass of the dummy was 9.5 kg. Shaking was performed by members of an interdisciplinary team drawn from three Departments of the University of Sheffield; Mechanical Engineering, Medical Physics and Clinical Engineering, and Ophthalmology and Orthoptics. The volunteers ranged from 20 to 50 in age, small to large in size, and poor to high in levels of fitness.

3.1.1. THE COORDINATE SYSTEM FOR THE ANALYSIS

A global Cartesian coordinate system O-X-Y-Z was defined independently of any moving objects in the field (Figure 3.1). The gaze direction of the volunteers in the horizontal plane was taken as the global X axis, with the positive direction as that from the volunteers to the dummy (Figure 3.1(c)). The origin was taken as the position of the centre of gravity of the torso at time t_0=0 (position T in Figure 3.1). The global Z axis is perpendicular to the horizontal plane, with the positive direction being from the dummy to the ground. The Z-X plane defined by the Z and X axes is called the sagittal plane. The global Y axis is perpendicular to the sagittal plane, with the positive direction oriented out of the plane according to the right hand rule.

In addition, two local Cartesian coordinate systems that move with the rigid body segments were defined on the head and torso of the dummy. Their details are shown in Figure 3.1 and set out in Table 3.1. The origin of the local head coordinate system is its centre of gravity (COG) and the local torso coordinate system is centred similarity. The local frames o_C-ξ_C-μ_C-ς_C, and o_T-ξ_T-μ_T-ς_T at time t_0=0 have the same orientation as that of the global coordinate system.

3.1.2. NECK

The weakness of the infant neck muscle allows a significant lag between the head and torso when a movement is imposed on the torso. Since the TRL Dummy was designed to collect data in automotive crash scenarios, the designer used the simplest mechanical connection between the head and the torso that could represent variable stiffness in the joint. This was a hinge, where the stiffness could be adjusted by tightening a nut on a screw. The Sheffield team chose to limit the vast number of potential test parameters by using only three settings of the hinge stiffness; stiff, normal and soft. However, the stiffness of the neck hinge was never measured, so a detailed reconstruction of the motion of the dummy with reference to that of the hands of the shaker is not possible. Observations reveal that the smaller the neck stiffness, the more extreme the head motion, both linear and angular. This is, of course, what mechanical intuition would suggest. In fact, our ignorance of the neck stiffness in these tests is irrelevant to the current research, which needs, as input to the later bio-simulations, a detailed description of the motion of an infant's skull during abusive shaking.

Therefore only the behaviour of the dummy with a soft neck was taken into account in this chapter. The video recordings show that the hinge allows a rotation around the Y axis to begin and continue to develop, following the backwards and forwards input of the shaker. Also the head developed a violent rotation around the Z axis, particularly dangerous clinically. Finally, a side-to-side motion of the head around the X axis can also be seen. All of these secondary motions, of considerable clinical importance, are due to the weakness of the hinge connecting the head and torso.

3.1.3. ACCELEROMETERS

Eight accelerometers (details set out in Appendix A) were mounted on the dummy at the positions marked as A, B, C and T in Figure 3.1; Table 3.1 provides further details. There is no record of the type of the accelerometer used in the test. Three sensors were situated at the T position to measure the acceleration in the local ξ_T, μ_T and ς_T directions. One sensor at the C position measured the acceleration in the local ξ_C direction. Two sensors were mounted at the A position, the front of head, and measured the acceleration in the local μ_C and ς_C directions, and two others were mounted at the B position, the rear of the head, and measured the acceleration in the local μ_C and ς_C directions.

The seven volunteers varied in gender, age and strength. There is no record of each volunteer's age, but all lay between 20-50 years old (Table 3.2).

Accelerometer	Position	Measurement	Direction
T	Torso COG	$a_{T\xi}$	ξ_T
T	Torso COG	$a_{T\eta}$	η_T
T	Torso COG	$a_{T\varsigma}$	ς_T
C	Head COG	$a_{C\xi}$	ξ_C
A	Head front	$a_{A\eta}$	η_C
A	Head front	$a_{A\varsigma}$	ς_C
B	Head rear	$a_{B\eta}$	η_C
B	Head rear	$a_{B\varsigma}$	ς_C

Table 3.1. *The measurements of the accelerometers on the dummy, including the position and orientation in local.*

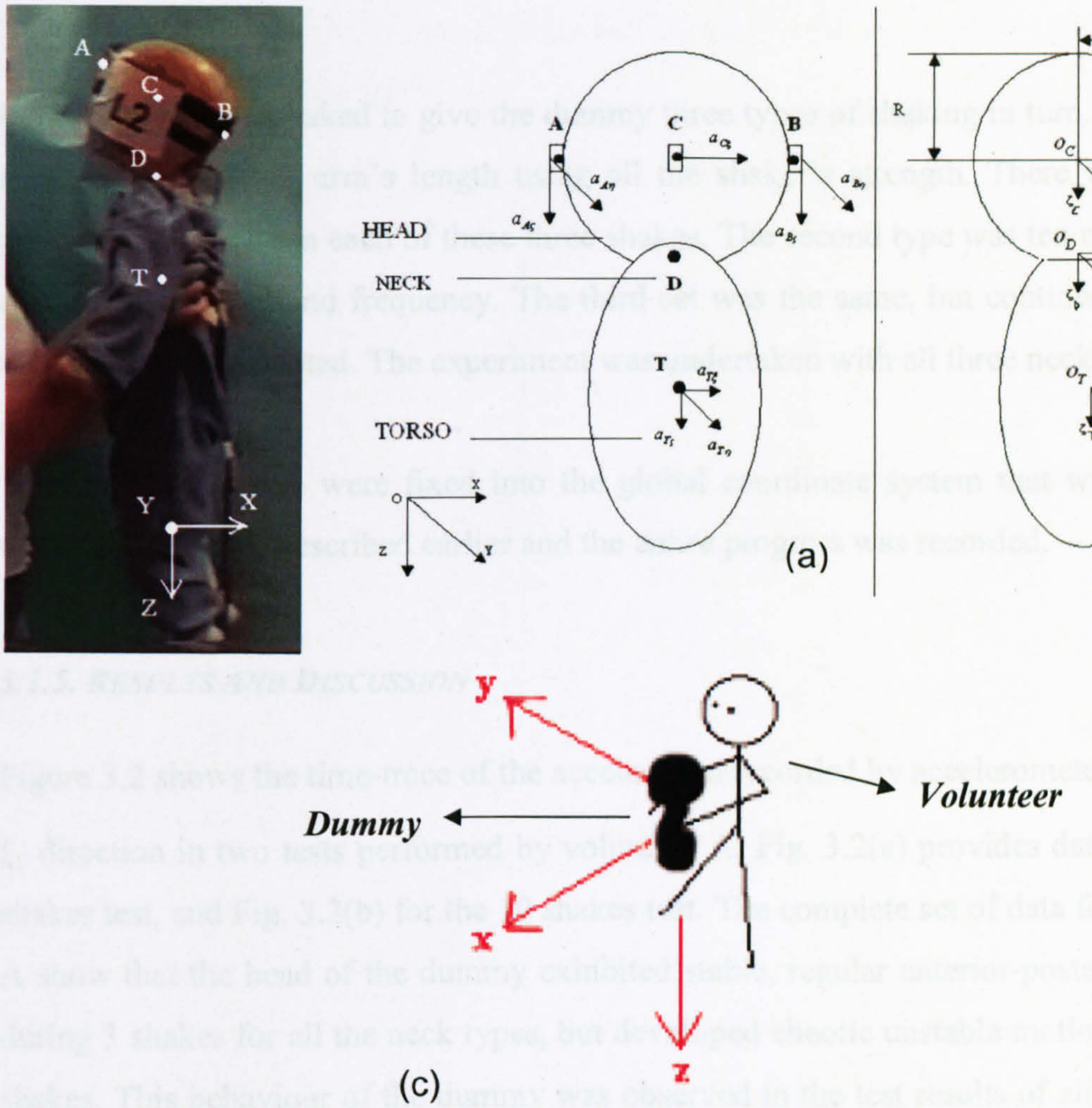

Figure 3.1. *The anthropomorphic dummy in the experiment and the pre-processing for the reconstruction work. The global coordinate is given as X: horizontal direction, Z: vertical direction, and Y: normal to XZ plane direction, which was plot inside the plane for convenience. (a) The accelerometers' position and its measurement. (b) The three local coordinates due to the assumption. (c) Diagram Indicating the Positioning of the Digital Cameras Relative to the Volunteer.*

No.	Gender	Age	Strength
A	Female	Young	Average
B	Male	Young	Average
C	Male	Young	Average
D	Female	Young	Weak
E	Male	Mid age	Strong
F	Female	Mid age	Strong
G	Male	Mid age	Average (left hand)

Table 3.2. *The chosen of the volunteers with the gender, age and strength capacity.*

3.1.4. THE SHAKING

Each volunteer was asked to give the dummy three types of shaking in turn. First, three single shakes at full arm's length using all the shaker's strength. There was a short period of rest between each of these three shakes. The second type was ten rapid shakes at maximum speed and frequency. The third set was the same, but continued until the volunteer was exhausted. The experiment was undertaken with all three neck types: soft, normal and stiff.

Three video cameras were fixed into the global coordinate system that was collinear with the three axes described earlier and the entire progress was recorded.

3.1.5. RESULTS AND DISCUSSION

Figure 3.2 shows the time-trace of the acceleration recorded by accelerometer $a_{c\xi}$, in the ξ_C direction in two tests performed by volunteer A; Fig. 3.2(a) provides data for the 3-shakes test, and Fig. 3.2(b) for the 10 shakes test. The complete set of data for volunteer A show that the head of the dummy exhibited stable, regular anterior-posterior motion during 3 shakes for all the neck types, but developed chaotic unstable motion during 10 shakes. This behaviour of the dummy was observed in the test results of all volunteers, and is consistent with recent physical experiments (Cory et al. 2003).

The accelerometers on the head recorded the accelerations in the local framework that moved with the head during the testing. The maximum acceleration of the head correlated with the perceived strength of the volunteer, in that the stronger volunteers tended to shake the dummy more violently than the weaker ones; the maximum value ranged up to about 20g ($196.2 m/s^2$). For both test types of three slow shakes and rapid repetitive shaking, the average value of acceleration of the torso was about 10g ($98.1 m/s^2$) and that of the head, 15g-20g. This data compares well with previously published results (Duhaime et al. 1987, Wolfson et al. 2005). This confidence in the reliability and consistence of the TRL test data meant that it could be used as input to drive the simulation of both a mathematical rigid body model using the MADYMO software (TNO Automotive, Delft, Holland) with the results reported in Appendix H, and a finite element model using LS-DYNA (Livermore Software Technology Corporation, Livermore, CA, USA) with the results reported in Chapter 8. This required

that the TRL accelerometer data be analysed to provide the full motion of the head, in a coordinate fame fixed in space.

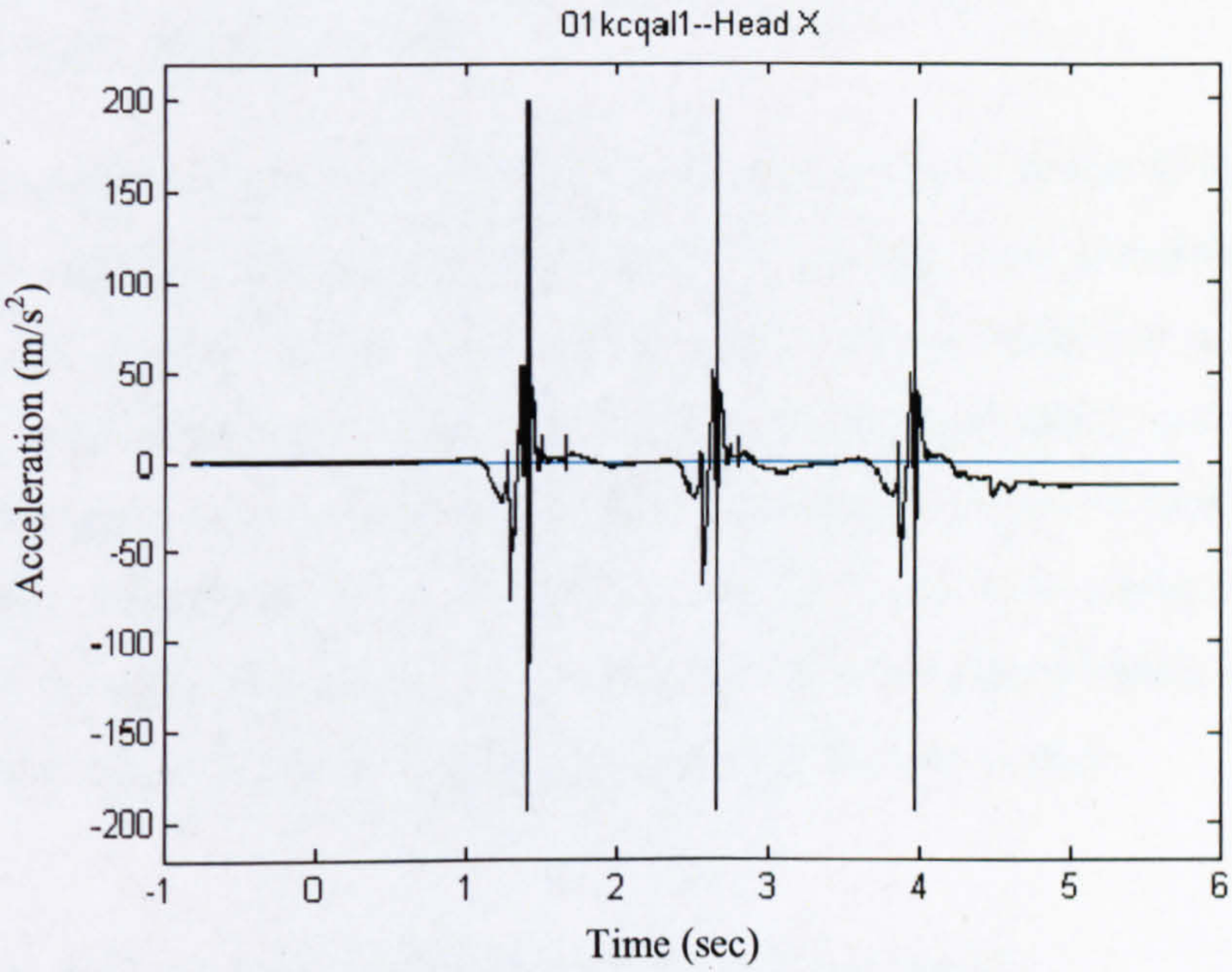

Figure 3.2. *The accelerometer output from TRL shaking test. (a) Volunteer A, 3 shakes, loose neck; (b) Volunteer A, 10 shakes, normal neck.*

3.2. Analytical Model And Shaking Motion Reconstruction (Challis 1994; Woltring et al. 1994; Allard et al. 1995; Van Den Bogert, et al. 1996; Martys and Mountain 1999; Zatsiorsky 2002)

The eight accelerometers recorded the acceleration of the dummy in each local frame. What was required for the planned numerical analysis was a reconstruction of the position and rotation of the head. An analytical model based on a combination of kinematic equations was therefore created to obtain the rotation and position of the head. The output of the model came from a program written in MATLAB 6.5 (The MathWorks, Massachusetts, USA). The coding used two separate mathematical methods to integrate the equations, one based on the Rotational Matrix and the other on Quaternions, These are described in detail in the following section.

3.2.1. The Coordinate System Of The Analytical Model

To reproduce fully the three-dimensional motion of any single rigid segment requires six independent equations to represent the six degrees of freedom. The torso-head system couples together the degrees of freedom of the two components by virtue of the neck-hinge. Hinge D is assumed to be a 3 degree of freedom socket that allows the head to rotate on the torso freely. It therefore removes 3 degrees of freedom from the coupled head-torso system, which can be considered as a 9 (6+6-3=9) degree freedom system. In both principle and practice, 9 independent kinematic equations are needed to reconstruct the motion. There were only 8 channels of recorded data in the TRL experiments and this is not enough to set up 9 independent equations. More information is needed, therefore, and this will come from the assumptions discussed in the following paragraphs.

The first assumption was to consider the local frame of the torso o_T-ξ_T-μ_T-ς_T to be the global frame O-X-Y-Z. The motion of the torso was assumed to be without rotation, so that the acceleration of $a_{T\xi}$, $a_{T\mu}$ and $a_{T\varsigma}$ would be enough to calculate the trajectory of the torso. The neglect of the actual rotational torso motion should not introduce significant error, since it is very small compared with the translational displacement.

There are only five signals available to construct the motion of the head. Another assumption has to be made in order to obtain the sixth variable. So, the bottom of the

head, position D, was given the same motion as that of the torso, position T. These assumptions reduce the head-torso system to one of 8 degrees of freedom for which the 8 available data traces provide the requisite 8 governing equations.

3.2.2. THE KINEMATIC THEORY (Meriam and Kraige 1998)

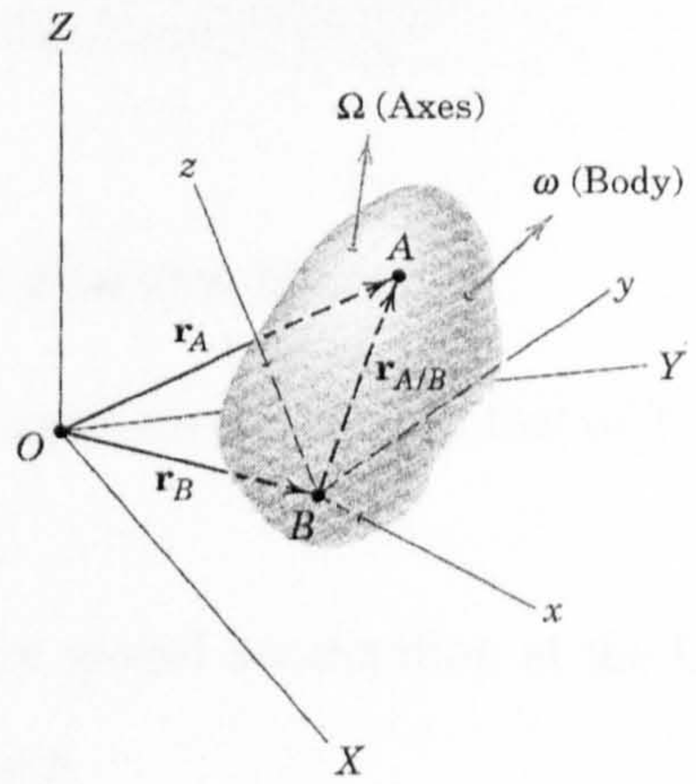

Figure 3.3. *3D dynamics of rigid body.*

Figure 3.3 shows a space described by a set of global coordinate axes OXYZ in which a rigid body moves with an instantaneous absolute angular velocity ω. A local coordinate frame attached to an arbitrary reference point B in the rigid body has an absolute angular velocity Ω that may be different from that, ω, of the body. Expressions for the global velocity v and acceleration a of any other point A in the body in terms of the defined quantities are given below.

$$v_A = v_B + \Omega \times r_{A/B} + v_{rel}$$

$$a_A = a_B + \dot{\Omega} \times r_{A/B} + \Omega \times (\Omega \times r_{A/B}) + 2\Omega \times v_{rel} + a_{rel}$$

where v_{rel} and a_{rel} are the relative velocity and acceleration of point A obtained by an observer who attached to local frame.

$$v_{rel} = \dot{x}i + \dot{y}j + \dot{z}k$$

$$a_{rel} = \ddot{x}i + \ddot{y}j + \ddot{z}k$$

The quantities v_{rel} and a_{rel} will both be zero, and the local absolute angular velocity equal to that of the body, if the local coordinate frame is rigidly attached to the rigid body. In that case, the kinematic equation for velocity v and acceleration a becomes:

$$v_A = v_B + \omega \times r_{A/B}$$

$$a_A = a_B + \dot{\omega} \times r_{A/B} + \omega \times (\omega \times r_{A/B})$$

where $\dot{\omega}$ is the instantaneous angular acceleration of the body.

These equations can be used for the analysis of the linear and angular acceleration of the COG of the head and torso of the dummy.

3.2.3. THE KINEMATIC MODEL FOR THE TORSO

Any point of the torso has the same acceleration as that of T. That is:

$$a_{TG} = a_A \tag{3.1}$$

where $a_{TG} = [a_{TX}, a_{TY}, a_{TZ}]$ is the global acceleration at the COG of the torso, and a_A is the acceleration of any point on it.

a_{TG} can be obtained from the local coordinate measurements:

$$\begin{bmatrix} a_{TX} \\ a_{TY} \\ a_{TZ} \end{bmatrix} = \begin{bmatrix} a_{T\xi} \\ a_{T\eta} \\ a_{T\varsigma} \end{bmatrix} \tag{3.2}$$

where $a_{T\xi}$, $a_{T\mu}$, and $a_{T\zeta}$ are local outputs from each accelerometer.

Then, the velocity $V_{TG} = [V_{TX}, V_{TY}, V_{TZ}]$ and displacement $s_{TG} = [s_{TX}, s_{TY}, s_{TZ}]$ of T in the global coordinate system can be obtained by integrating and double integrating the acceleration $a_{TG} = [a_{TX}, a_{TY}, a_{TZ}]$.

3.2.4. THE KINEMATIC MODEL FOR THE HEAD

According to the assumption set out in the previous section, the relationship between the local acceleration $a_{DL} = [a_{D\xi}, a_{D\mu}, a_{D\varsigma}]$ of the bottom of the head where it attaches to the torso at the neck and the global acceleration $a_{TG} = [a_{TX}, a_{TY}, a_{TZ}]$ at T of the COG of the torso can be represented as:

$$\begin{bmatrix} a_{D\xi} \\ a_{D\eta} \\ a_{D\varsigma} \end{bmatrix} = [R]^T \cdot \begin{bmatrix} a_{TX} \\ a_{TY} \\ a_{TZ} \end{bmatrix} \tag{3.3}$$

where $[R]^T$ is the transverse of the rotation matrix from the local framework to the global framework.

The local linear acceleration $a_{CL} = \left[a_{C\xi}, a_{C\mu}, a_{C\varsigma}\right]$ and local angular acceleration $\varepsilon_{CL} = \left[\varepsilon_{C\xi}, \varepsilon_{C\mu}, \varepsilon_{C\varsigma}\right]$ at position C, the COG of the head, can be represented as:

$$\begin{bmatrix} a_{C\xi} \\ a_{C\eta} \\ a_{C\varsigma} \end{bmatrix} = \begin{bmatrix} a_{C\xi} \\ \dfrac{a_{A\eta} + a_{B\eta}}{2} \\ \dfrac{a_{A\varsigma} + a_{B\varsigma}}{2} \end{bmatrix} \tag{3.4}$$

$$\begin{bmatrix} \varepsilon_{C\xi} \\ \varepsilon_{C\eta} \\ \varepsilon_{C\varsigma} \end{bmatrix} = \begin{bmatrix} \dfrac{a_{D\eta}}{R} + \dfrac{a_{A\eta} + a_{B\eta}}{2R} + \omega_2\omega_3 \\ \dfrac{a_{A\varsigma} - a_{B\varsigma}}{2R} + \omega_1\omega_3 \\ \dfrac{a_{A\eta} + a_{B\eta}}{2R} - \omega_1\omega_2 \end{bmatrix} \tag{3.5}$$

where $\omega = [\omega_1, \omega_2, \omega_3]$ is the instantaneous value of the global angular velocity of the head, and R is its radius; R=AC=BC.

During a calculation based upon these relations, the acceleration and angular vectors above are updated at each time step.

Specifically, equations (3.2), (3.4) and (3.5), provide analytical expressions at each time step for the global linear acceleration $a_{TG} = \left[a_{TX}, a_{TY}, a_{TZ}\right]$ of the torso, and the local linear acceleration $a_{CL} = \left[a_{C\xi}, a_{C\mu}, a_{C\varsigma}\right]$ and local angular acceleration $\varepsilon_{CL} = \left[\varepsilon_{C\xi}, \varepsilon_{C\mu}, \varepsilon_{C\varsigma}\right]$ of the head. They appear in the integration processes described later in §3.2.6.5.

3.2.5. Rotation Matrix Representing 3D Rigid Body Movement

Consider a rigid body moving relative to a global coordinate system, with a local coordinate system attached to the body and moving with it. When the body moves from

the global origin O to a new position o, the motion can be represented by two quantities, the linear translation from O to o and the relative rotation of the local frame with respect to the global one. Figure 3.4 illustrates the details.

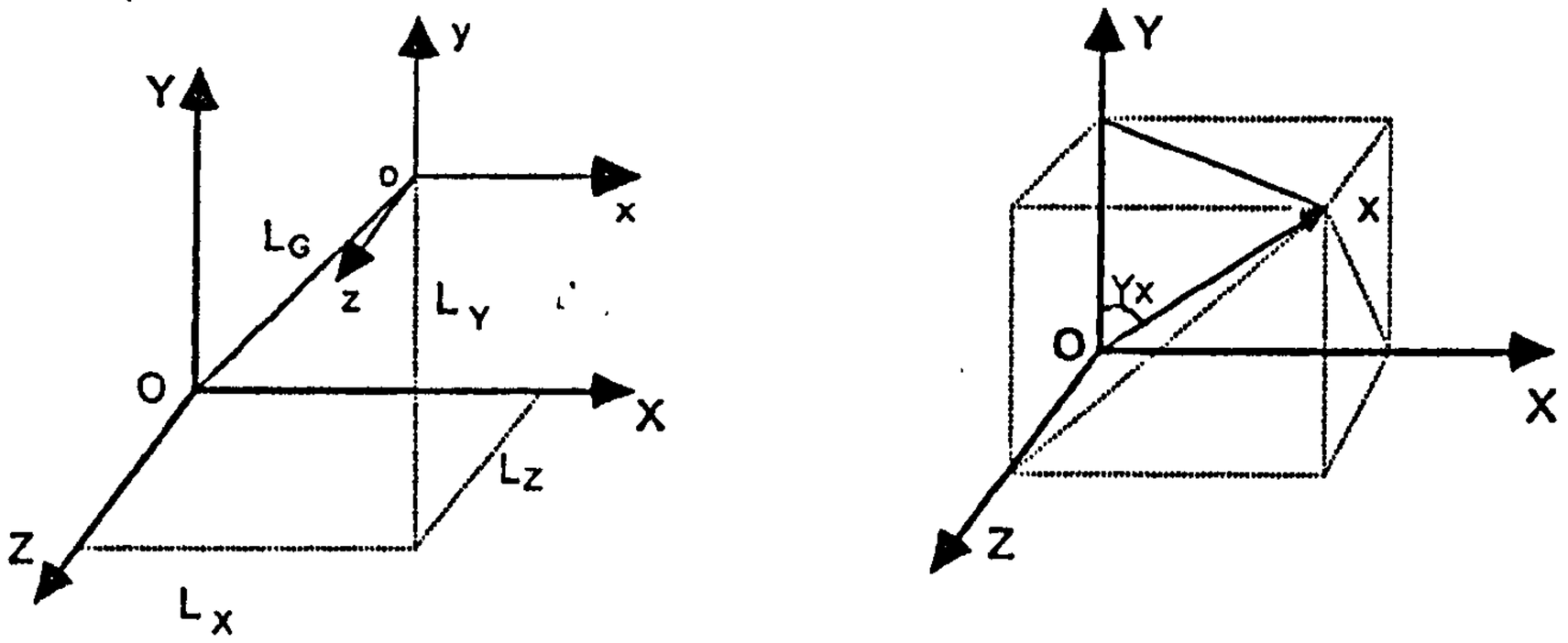

***Figure 3.4.** Left: Relative translation between local coordinate and global coordinate. Right: Relative rotation between local coordinate and global coordinate.*

The quantity L_G, the global vector of the origin o of the local frame, describes the translation of the rigid body, and its components provide the translation matrix:

$$L_G = \begin{bmatrix} L_X \\ L_Y \\ L_Z \end{bmatrix}$$

The local frame moves in the direction of the unit vector Oo. Figure 3.4 also shows a local unit vector x. It has a set of direction cosines, the cosines of the three angles between the direction of x and those of the global coordinate axes.

Each of the three local axis directions has three direction cosines. The resulting 9 elements provide a 3×3 matrix that represents the orientation of the local frame with respect to global axes. This matrix of direction cosines is the rotation matrix.

$$[R] = \begin{bmatrix} \cos_{Xx} & \cos_{Xy} & \cos_{Xz} \\ \cos_{Yx} & \cos_{Yy} & \cos_{Yz} \\ \cos_{Zx} & \cos_{Zy} & \cos_{Zz} \end{bmatrix}$$

where the capital letters X,Y,Z represents the global axes and small letters x,y,z represents the local axes.

Thus the relation between the local vector $P_L = [P_x, P_y, P_z]$ and global vector $P_G = [P_X, P_Y, P_Z]$ of any point P in the rigid body can be expressed as:

$$P_G = L_G + [R] \cdot P_L$$

$$= \begin{bmatrix} 1 & 0 & 0 & 0 \\ L_X & \cos_{Xx} & \cos_{Xy} & \cos_{Xz} \\ L_Y & \cos_{Yx} & \cos_{Yy} & \cos_{Yz} \\ L_Z & \cos_{Zx} & \cos_{Zy} & \cos_{Zz} \end{bmatrix} \cdot P_L$$

$$= [T] \cdot P_L \qquad (3.6)$$

where [T] is the transformation matrix.

3.2.5.1. Distinction Of Direction And Rotation

The matrix of direction cosines gives the direction of the rigid body after transforming from one direction to another direction.

However, the three direction cosines of each local axis are not independent. The identity $\cos^2_{Xx} + \cos^2_{Yx} + \cos^2_{Zx} = 1$ reduces the degrees of freedom of direction cosines from three to two, and their use cannot express the 'change' of the rotation but only its 'result'. In addition, it is inconvenient to obtain the direction angle directly from the raw measurements.

In practice, assembling the rotation matrix invariably uses another type of angle, that has three independent degrees of freedom to represent the rotation, and which can also be obtained directly from the experimental data.

3.2.5.2. Euler Angles

A rotation of a rigid body can be described as a sequence of three successive rotations from an initial position, at which the static, O-X-Y-Z, reference frame and the moving one, o-x-y-z, coincide. The three successive angles of rotation about the pre-set axes are called the Euler's angles (Figure 3.5).

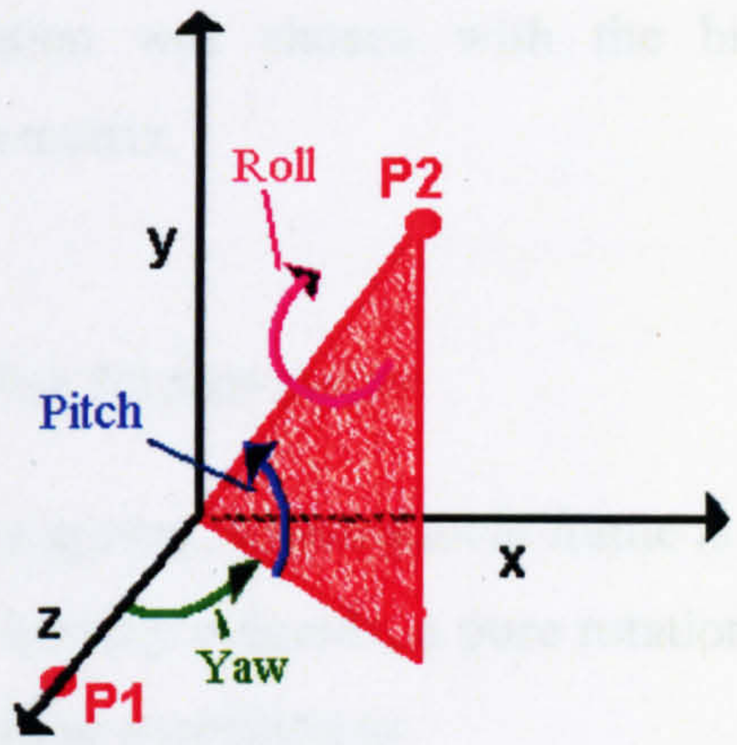

***Figure 3.5**. Euler angle representation for the orientation of a 3D rigid body in a global coordinate frame.*

The two-axis and three-axis systems are two common conventions used in practical analysis. The former, called Euler's convention, being that in which the terminal coordinate axis in the sequence of rotations is identical (e.g., Xy′x″, Zx′z″). The latter called Cardan's convention, is that in which the terminal coordinate axis in the sequence of rotation is different (e.g., Xy′z″, Yx′z″).

The general succession is the same whatever the convention: the first rotation is defined relative to an axis oriented in the global reference frame, the third is defined with respect to an axis fixed within the rotating body and the second is performed relative to the floating axis. The second and the third rotations are about local axes transformed by previous rotations.

The name given each Euler angle depends on the practical situation. For example, yaw, pitch and roll are often used for nautical angles.

When the same body attitude is measured in different conventions, the angular values are different. However, for a given angular convention, the finite angular displacements are independent of sequence.

3.2.6. Convention Used For The Analysis Of The TRL Experiment

The global coordinate system used to described TRL experiment was established in Figure 3.1, in which X and Z and the horizontal and vertical axes, the Y axis is perpendicular to the sagittal plane (XZ plane), and the major whiplash is the rotation to

Y axis. Cardan's convention was chosen with the hierarchy of Xy′z″, for the specification of the rotation matrix.

3.2.6.1. Rotation Matrix For 2D Movement

In a right-handed coordinate system, where a local frame is attached to a rigid body, and the local and global frame initially coincide, a pure rotation of angle α about the Z axis rotates the axes in the XY plane according to:

$$P_G = \begin{bmatrix} P_X \\ P_Y \end{bmatrix} = \begin{bmatrix} \cos\alpha & -\sin\alpha \\ \sin\alpha & \cos\alpha \end{bmatrix} \cdot \begin{bmatrix} P_x \\ P_y \end{bmatrix} = [R] \cdot P_L$$

where [R] is the rotation matrix.

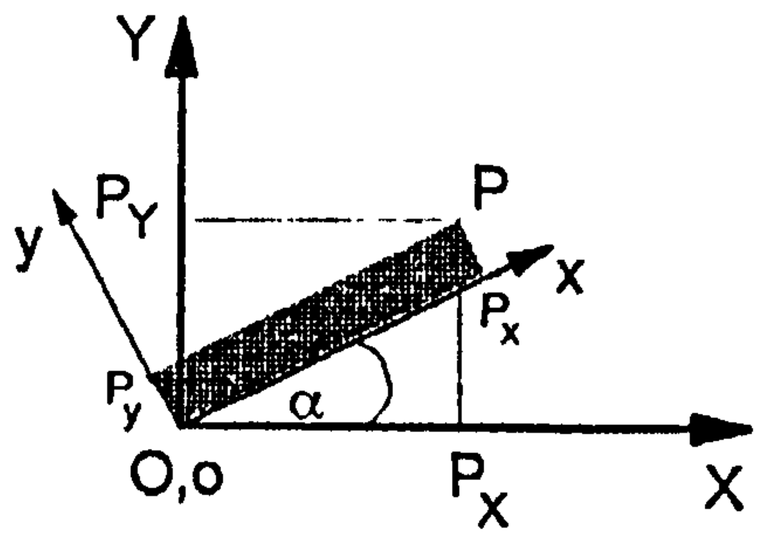

***Figure 3.6.** Local coordinate rotation with global coordinate in plane.*

3.2.6.2. Rotation Matrix For 3D Movement

A 3D rotation matrix comes from the combination of 3 successive rotation matrixes, each of which is an individual rotation with respect to one reference axis.

Cardan's convention Xy′z″ was adopted for analysing the TRL experimental data. The three successive angles φ_1, φ_2, φ_3 were dealt with separately, each one being an individual rotations around the X, y′ and z″ axes, the 2D rotation matrix for each is two dimensional of the form.

$$[R_i] = \begin{bmatrix} 1 & 0 & 0 \\ 0 & \cos\varphi_i & -\sin\varphi_i \\ 0 & \sin\varphi_i & \cos\varphi_i \end{bmatrix} \quad i = 1,3 \qquad (3.7)$$

Then the rotation matrix transferring the vector from local coordinates (attached to the dummy) to global coordinates for the TRL experimental data will be:

$$[R]=[R_1]\cdot[R_2]\cdot[R_3]$$

$$=\begin{bmatrix} \cos\varphi_2\cos\varphi_3 & -\cos\varphi_2\sin\varphi_3 & \sin\varphi_2 \\ \sin\varphi_1\sin\varphi_2\cos\varphi_3+\cos\varphi_1\sin\varphi_3 & -\sin\varphi_1\sin\varphi_2\sin\varphi_3+\cos\varphi_1\cos\varphi_3 & -\sin\varphi_1\cos\varphi_2 \\ -\cos\varphi_1\sin\varphi_2\cos\varphi_3+\sin\varphi_1\sin\varphi_3 & \cos\varphi_1\sin\varphi_2\sin\varphi_3+\sin\varphi_1\cos\varphi_3 & \cos\varphi_1\cos\varphi_2 \end{bmatrix} \tag{3.8}$$

A vector P has the following relation between local and global coordinates.

$$P_G=\begin{bmatrix} P_X \\ P_Y \\ P_Z \end{bmatrix}=[R_1]\cdot[R_2]\cdot[R_3]\cdot\begin{bmatrix} P_x \\ P_y \\ P_z \end{bmatrix}=[R]\cdot P_L \tag{3.9}$$

or

$$P_L=\begin{bmatrix} P_x \\ P_y \\ P_z \end{bmatrix}=[R_3]^T\cdot[R_2]^T\cdot[R_1]^T\cdot\begin{bmatrix} P_X \\ P_Y \\ P_Z \end{bmatrix}=[R]^T\cdot P_G \tag{3.10}$$

3.2.6.3. Defining Position in Two Reference Systems

Whilst the body is changing its orientation, it is also, in general, changing its position. Therefore, a complete description of a change in reference for the body must add that due to translation to that for the orientation. The equation

$$P_G=L_G+[R]\cdot P_L \tag{3.11}$$

describes this.

3.2.6.4. Angular Velocity And Three Successive Angular Rate

In the analysis, the rotation matrix is updated at each time step by obtaining the appropriate rate of change of the angles. The angular velocity of the rigid body $\omega=[\omega_1,\omega_2,\omega_3]$ can be considered as the resultant component of the 3 successive angle rates $\dot{\varphi}=[\dot{\varphi}_1,\dot{\varphi}_2,\dot{\varphi}_3]$. The expression for it is

$$\omega=\begin{bmatrix} \omega_1 \\ \omega_2 \\ \omega_3 \end{bmatrix}=\begin{bmatrix} 0 \\ 0 \\ \dot{\varphi}_3 \end{bmatrix}+[R_3]^T\cdot\left(\begin{bmatrix} 0 \\ \dot{\varphi}_2 \\ 0 \end{bmatrix}+[R_2]^T\cdot\begin{bmatrix} \dot{\varphi}_1 \\ 0 \\ 0 \end{bmatrix}\right)$$

$$= \begin{bmatrix} \cos\varphi_2 \cos\varphi_3 & \sin\varphi_3 & 0 \\ -\cos\varphi_2 \sin\varphi_3 & \cos\varphi_3 & 0 \\ \sin\varphi_2 & 0 & 1 \end{bmatrix} \cdot \begin{bmatrix} \dot{\varphi}_1 \\ \dot{\varphi}_2 \\ \dot{\varphi}_3 \end{bmatrix} \tag{3.12}$$

An inversion of this produces a relation for the angle rates in the form[1]:

$$\begin{bmatrix} \dot{\varphi}_1 \\ \dot{\varphi}_2 \\ \dot{\varphi}_3 \end{bmatrix} = \begin{bmatrix} \dfrac{\cos\varphi_3}{\cos\varphi_2} & -\dfrac{\sin\varphi_3}{\cos\varphi_2} & 0 \\ \sin\varphi_3 & \cos\varphi_3 & 0 \\ -\dfrac{\cos\varphi_3 \sin\varphi_2}{\cos\varphi_2} & \dfrac{\sin\varphi_3 \sin\varphi_2}{\cos\varphi_2} & 1 \end{bmatrix} \cdot \begin{bmatrix} \omega_1 \\ \omega_2 \\ \omega_3 \end{bmatrix} \tag{3.13}$$

In the analysis, new rotation angles come from the integration of the angle rates to produce the new rotation matrix.

3.2.6.5. The Summary Of The Rotation Matrix Method

This section summarises the procedure whereby the simulation of the motion of the head of the dummy can be analysed using the Rotation Matrix method described above using equations (3.1) - (3.13). Figure 3.7 provides a flow diagram illustrating the use of the method to update the motion at time t over the next interval, dt.

Equation (3.2) gives the linear acceleration of the torso in the global frame $a_{TG} = [a_{TX}, a_{TY}, a_{TZ}]$. The assumption of pure linear motion of the torso guarantees that the accelerometer at the T position gave the global linear acceleration in all three directions: $a_{TX} = a_{T\xi}$, $a_{TY} = a_{T\mu}$, and $a_{TZ} = a_{T\varsigma}$.

Equation (3.4) gives the local linear acceleration $a_{CL} = [a_{C\xi}, a_{C\mu}, a_{C\varsigma}]$ of the head, and (3.5) its global angular acceleration $\varepsilon_{CL} = [\varepsilon_{C\xi}, \varepsilon_{C\mu}, \varepsilon_{C\varsigma}]$. The local position of the head can be obtained by integrating equation (3.4) to give $P_L = [P_{C\xi}, P_{C\mu}, P_{C\varsigma}]$, whose value enters equation (3.6) together with the rotation matrix R (equation (3.10)) to obtain the global position of head $P_G = [P_{CX}, P_{CY}, P_{CZ}]$. The rotation angle of the head can be obtained by double integration of the angular acceleration in equation (3.5).

---

[1] A formal singularity would exist when $\varphi_2 = \pm 90^\circ$. It is not difficult to avoid this in the subsequent numerical work.

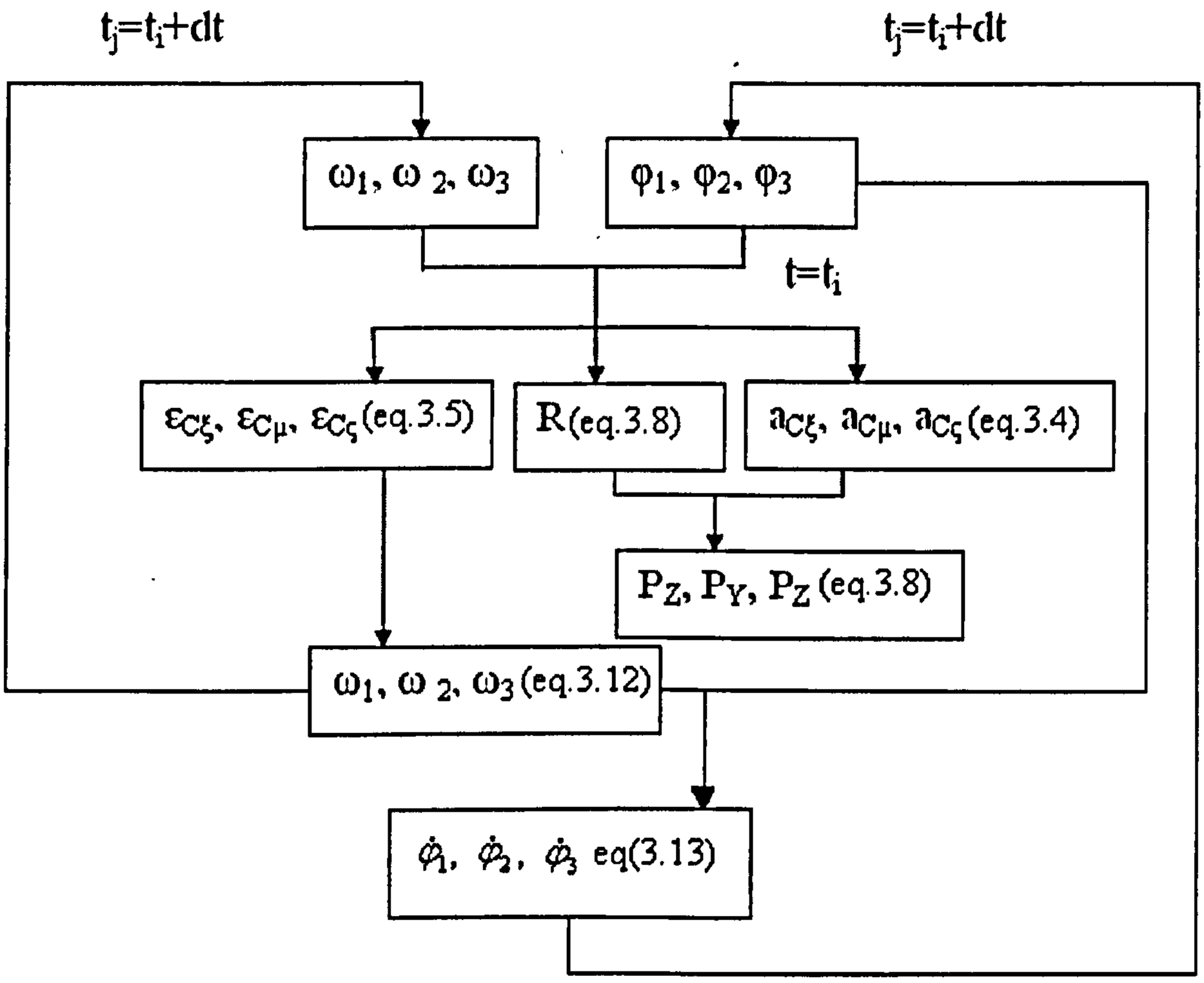

Figure 3.7. *Flow diagram for the analytical model reconstructing the head motion with the use of the Rotation Matrix method.*

The angular acceleration $\varepsilon_{CL}=\left[\varepsilon_{C\xi},\varepsilon_{C\mu},\varepsilon_{C\varsigma}\right]$ is a function of the variables $a_{D\mu}$, $a_{A\mu}$, $a_{A\varsigma}$, $a_{B\mu}$, $a_{B\varsigma}$, and the angular velocity $\omega=\left[\omega_1,\omega_2,\omega_3\right]$. The global position $P_G=\left[P_{CX},P_{CY},P_{CZ}\right]$ is a function of the rotation matrix [R], and the local vector $a_{CL}=\left[a_{C\xi},a_{C\mu},a_{C\varsigma}\right]$. The local linear acceleration, $a_{CL}=\left[a_{C\xi},a_{C\mu},a_{C\varsigma}\right]$, is a function of variables input from the accelerometers; i.e. of $a_{C\mu}$, $a_{A\mu}$, $a_{A\varsigma}$, $a_{B\mu}$, $a_{B\varsigma}$. The rotation matrix [R] is a function of the angles $\varphi=\left[\varphi_1,\varphi_2,\varphi_3\right]$, which may be evaluated by integrating the angle rates $\dot{\varphi}=\left[\dot{\varphi}_1,\dot{\varphi}_2,\dot{\varphi}_3\right]$. These latter quantities can be obtained from equation (3.13), which is a function of the angular velocity, $\omega=\left[\omega_1,\omega_2,\omega_3\right]$, and the values of the three successive angles $\varphi=\left[\varphi_1,\varphi_2,\varphi_3\right]$ from the previous time step.

At time t_0, the local linear acceleration has the output from the accelerometers of $a_{C\mu}$, $a_{A\mu}$, $a_{A\varsigma}$, $a_{B\mu}$, $a_{B\varsigma}$. The angular velocity $\omega = [\omega_1, \omega_2, \omega_3]$ and the angles $\varphi = [\varphi_1, \varphi_2, \varphi_3]$ are zero. Input of these values into equation (3.13) provides data that can then be transferred to equations (3.8), (3.4) and (3.5). Equation (3.6) provides the global position P_G after values from equations (3.8) and (3,4) have been input to it. The new angular velocity $\omega = [\omega_1, \omega_2, \omega_3]$ at time step $t_1 = t_0 + dt$ can be obtained by integrating equation (3.5). The new successive angle $\varphi = [\varphi_1, \varphi_2, \varphi_3]$ at time step $t_1 = t_0 + dt$ can be obtained by integrating the angle rate $\varphi = [\varphi_1, \varphi_2, \varphi_3]$ from previous time step t_0. Thus the simulation at time step t_1 can be started again from equation (3.13) and the simulation continued following the steps outlined above.

Hence the global position and rotation status of a rigid body system can be reconstructed by this rotation angle method from data obtained by simply tracing the discrete signal from accelerometer in each time step. The results, and a discussion of their value and meaning, is provide in §3.2.8 in combination with those for the Quaternion method.

3.2.7. The Introduction Of Quaternions And Their advantages (Hamilton 1853, Worden 1990; Lewis and Stevens 2003; Weisstein 2004)

A quaternion is a mathematical structure of algebraic geometry that is widely used in computer graphics as an alternative way of representing 3D rotations of objects and their orientation in a scene.

When a large number of objects is simulated, the use of quaternions, each encoding rotations by 4 real numbers, will save significant space compared with using the Euler angle rotation matrix, which requires 9 components.

In practice, during the very large umber of increments of integration in the numerical work, there is a problem due to drifting from small errors accumulating from the 'sin' and 'cos' computations and round-off errors introduced from many multiplications and divisions. These can be eliminated by re-normalizing the resultant quaternion if it becomes non-unitary. The analogous procedure for rotation matrices when the orthogonal matrix becomes non-orthogonal needs a Gram-Schmidt orthogonalization algorithm, but its implementation is very much more difficult.

When representing an object orientation in two consecutive animation frames, interpolation between two unit quaternions is much easier to process than the equivalent using rotation matrices, since the unit quaternion is constrained to the surface of a four dimensional hyper-sphere of radius unity, and so the intermediate interpolated quaternion just lies on the smallest great hyper-arc between the two values.

3.2.7.1. THE PRINCIPLES OF QUATERNIONS

A quaternion is a four-dimensional mathematical structure, composed of 4 hyper-complex numbers to represent one real axis and three orthogonal imaginary axes. It is represented as a quadruplet of real numbers in the form:

$$Q = [q_0, q_1, q_2, q_3] = q_0 + iq_1 + jq_2 + kq_3 = [s, \vec{v}]$$

where $s = q_0$ is the scalar component, and $\vec{v} = [q_1, q_2, q_3]$ is the vector component.

Quaternions obey the normal laws of algebra, except that multiplication is not commutative. Given two quaternions $Q_1 = [s_1, \vec{v}_1]$, $Q_2 = [s_2, \vec{v}_2]$, the basic operations are defined as follows.

1. Addition

$$Q_1 + Q_2 = (s_1 + s_2) + (\vec{v}_1 + \vec{v}_2)$$

2. Dot Product

$$Q_1 \cdot Q_2 = s_1 s_2 + \vec{v}_1 \cdot \vec{v}_2$$

3. Multiplication

$$Q_1 Q_2 = (s_1 s_2 - \vec{v}_1 \cdot \vec{v}_2) + (s_1 \vec{v}_2 + s_2 \vec{v}_1 + \vec{v}_1 \times \vec{v}_2)$$

4. Conjugate

$$\overline{Q} = \overline{s_1 + \vec{v}_1} = s_1 - \vec{v}_1$$

$$\overline{Q_1}\,\overline{Q_2} = \overline{Q_1 Q_2}$$

5. Modulus

$$|Q_1|^2 = s_1^2 + q_1^2 + q_2^2 + q_3^2$$

$$|Q_1 Q_2|^2 = |Q_1|^2 |Q_2|^2$$

6. Inverse

$$Q_1^{-1} = \frac{\overline{Q}_1}{|Q_1|^2}$$

7. Normalization

$$Q_{1n} = \frac{Q_1}{|Q_1|}$$

A quaternion with modulus equal to unity ($|Q_1| = 1$) is called a unit quaternion. Any arbitrary three-dimensional vector $v(R^3)$ can be represented as a pure quaternion that has zero real part $q = [0, v]$. Any unitary vector in R^3, such as a normalized vector can be represented as a pure unit quaternion.

The inverse of a unit quaternion is equal to its conjugate, which in turn can be computed by negating its imaginary part:

$$Q_{1n}^{-1} = \overline{Q}_{1n}$$

3.2.7.2. Axis Angles And Quaternions

The rotation of any rigid body can always be represented in the frame of the observer by a unit vector and an angle of revolution about that vector. This is called the "axis angle representation", and uses the notation $[u, \theta]$, where $u_x = [u_x, u_y, u_z]$ is the unit magnitude vector of rotation axis and θ is the rotation angle of that axis.

The identities

$$\sin^2\left(\frac{\theta}{2}\right) + \cos^2\left(\frac{\theta}{2}\right) = 1$$

$$u_x^{\,2} + u_y^{\,2} + u_z^{\,2} = 1$$

$$q_0^{\,2} + q_1^{\,2} + q_2^{\,2} + q_3^{\,2} = 1$$

for trigonometric functions, unit vectors and quaternions allow us to represent any rigid body rotation in an observed frame by the unit quaternion

$$q = \begin{bmatrix} q_0 \\ q_1 \\ q_2 \\ q_3 \end{bmatrix} = \begin{bmatrix} \cos\left(\frac{\theta}{2}\right) \\ u_x \sin\left(\frac{\theta}{2}\right) \\ u_y \sin\left(\frac{\theta}{2}\right) \\ u_z \sin\left(\frac{\theta}{2}\right) \end{bmatrix}$$

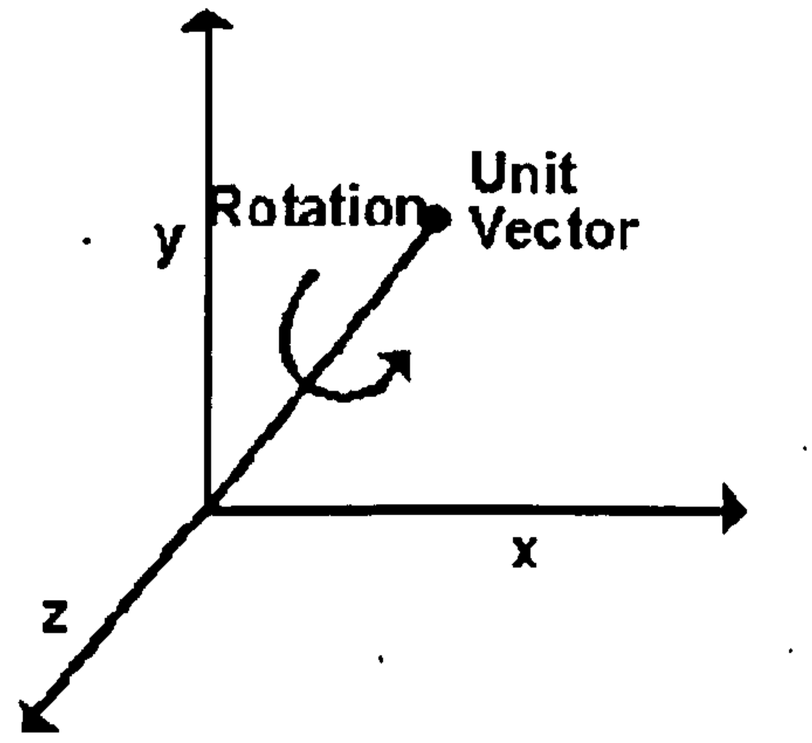

Figure 3.8. *Euler angle representation for 3D orientation of a rigid body in a global coordinate system.*

This formulation is a guarantee that there is a unique quaternion for every value of θ in the range of ±180°; it encompasses all possible rotations without any singularity.

3.2.7.3. Rotation Representation By Quaternions

A quaternion can represent a rigid body transformation by multiplication by a vector. A Euclidean quaternion is compatible with this multiplication:

$$q_p = [0, v]$$

where q_p is called a pure quaternion.

Hence if a right hand rotation of a rigid body by an angle θ around an axis u (u>0), takes the orientation vector $v_1 = \left[0, v_{1x}, v_{1y}, v_{1z}\right]$ to $v_2 = \left[0, v_{2x}, v_{2y}, v_{2z}\right]$, the relation between v_1 and v_2 can be represented by:

$$v_1 = q_p^{-1} \cdot v_2 \cdot q_p$$

or

$$v_2 = q_p \cdot v_1 \cdot q_p^{-1}$$

The quaternion q_p may be updated at each time step in a procedure to reconstruct the rotation from the local frame back to the global frame. This is the basis of the quaternion integration method.

3.2.7.4. TIME UPDATE OF THE ROTATION

The time-update of the rotation can be obtained by continuously updating the quaternion matrix. This takes the form of a differential equation for the quaternion, with angular velocity for the determined coefficients:

$$\begin{bmatrix} \dot{q}_0 \\ \dot{q}_1 \\ \dot{q}_2 \\ \dot{q}_3 \end{bmatrix} = \frac{1}{2} \begin{bmatrix} 0 & -\omega_1 & -\omega_2 & -\omega_3 \\ \omega_1 & 0 & \omega_3 & -\omega_2 \\ \omega_2 & -\omega_3 & 0 & \omega_1 \\ \omega_3 & \omega_2 & -\omega_1 & 0 \end{bmatrix} \begin{bmatrix} q_0 \\ q_1 \\ q_2 \\ q_3 \end{bmatrix} \tag{3.14}$$

The derivation of the equation is not given here due to the space constraints (LEWIS 2003).

3.2.7.5. FROM ROTATION MATRIX TO QUATERNION

As a result, the transformation due to a rotation between vectors v_1 and v_2 can be represented by:

$$v_1 = q_p^{-1} \cdot v_2 \cdot q_p$$

$$= \begin{bmatrix} 1-2q_2^2-2q_3^2 & 2q_1q_2-2q_0q_3 & 2q_1q_3+2q_0q_2 \\ 2q_1q_2+2q_0q_3 & 1-2q_1^2-2q_3^2 & 2q_2q_3-2q_0q_1 \\ 2q_1q_3-2q_0q_2 & 2q_2q_3+2q_0q_1 & 1-2q_1^2-2q_2^2 \end{bmatrix} \begin{bmatrix} v_{2x} \\ v_{2y} \\ v_{2z} \end{bmatrix}$$

$$= Rv_2 \tag{3.15}$$

where R is the rotation matrix from local coordinates to global coordinates. So the Rotation Matrix can be given in terms of values from the quaternion as:

$$R = \begin{bmatrix} 1-2q_2^2-2q_3^2 & 2q_1q_2-2q_0q_3 & 2q_1q_3+2q_0q_2 \\ 2q_1q_2+2q_0q_3 & 1-2q_1^2-2q_3^2 & 2q_2q_3-2q_0q_1 \\ 2q_1q_3-2q_0q_2 & 2q_2q_3+2q_0q_1 & 1-2q_1^2-2q_2^2 \end{bmatrix} \tag{3.16}$$

3.2.7.6. *FROM EULER ANGLE TO QUATERNION*

The relations above between the rotation matrix and quaternion components, and the rotation matrix and the Euler angles, provide a new relationship between a quaternion and the Euler angles in the form

$$q = \begin{bmatrix} q_0 \\ q_1 \\ q_2 \\ q_3 \end{bmatrix} = \begin{bmatrix} c_1c_2c_3 - s_1s_2s_3 \\ s_1c_2c_3 + c_1s_2s_3 \\ c_1s_2c_3 - s_1c_2s_3 \\ s_1s_2c_3 - c_1c_2s_3 \end{bmatrix} \tag{3.17}$$

where

$$\begin{bmatrix} c_1 \\ c_2 \\ c_3 \end{bmatrix} = \begin{bmatrix} \cos\left(\frac{\varphi_1}{2}\right) \\ \cos\left(\frac{\varphi_2}{2}\right) \\ \cos\left(\frac{\varphi_3}{2}\right) \end{bmatrix} \tag{3.18}$$

and

$$\begin{bmatrix} s_1 \\ s_2 \\ s_3 \end{bmatrix} = \begin{bmatrix} \sin\left(\frac{\varphi_1}{2}\right) \\ \sin\left(\frac{\varphi_2}{2}\right) \\ \sin\left(\frac{\varphi_3}{2}\right) \end{bmatrix} \tag{3.19}$$

3.2.7.7. *THE SUMMARY OF THE QUATERNION METHOD*

This section provides a summary of the procedure for the simulation of the motion of a body using the Quaternion method set out in equations (3.14) to (3.19). Figure 3.9 is a flow diagram for the Quaternion method.

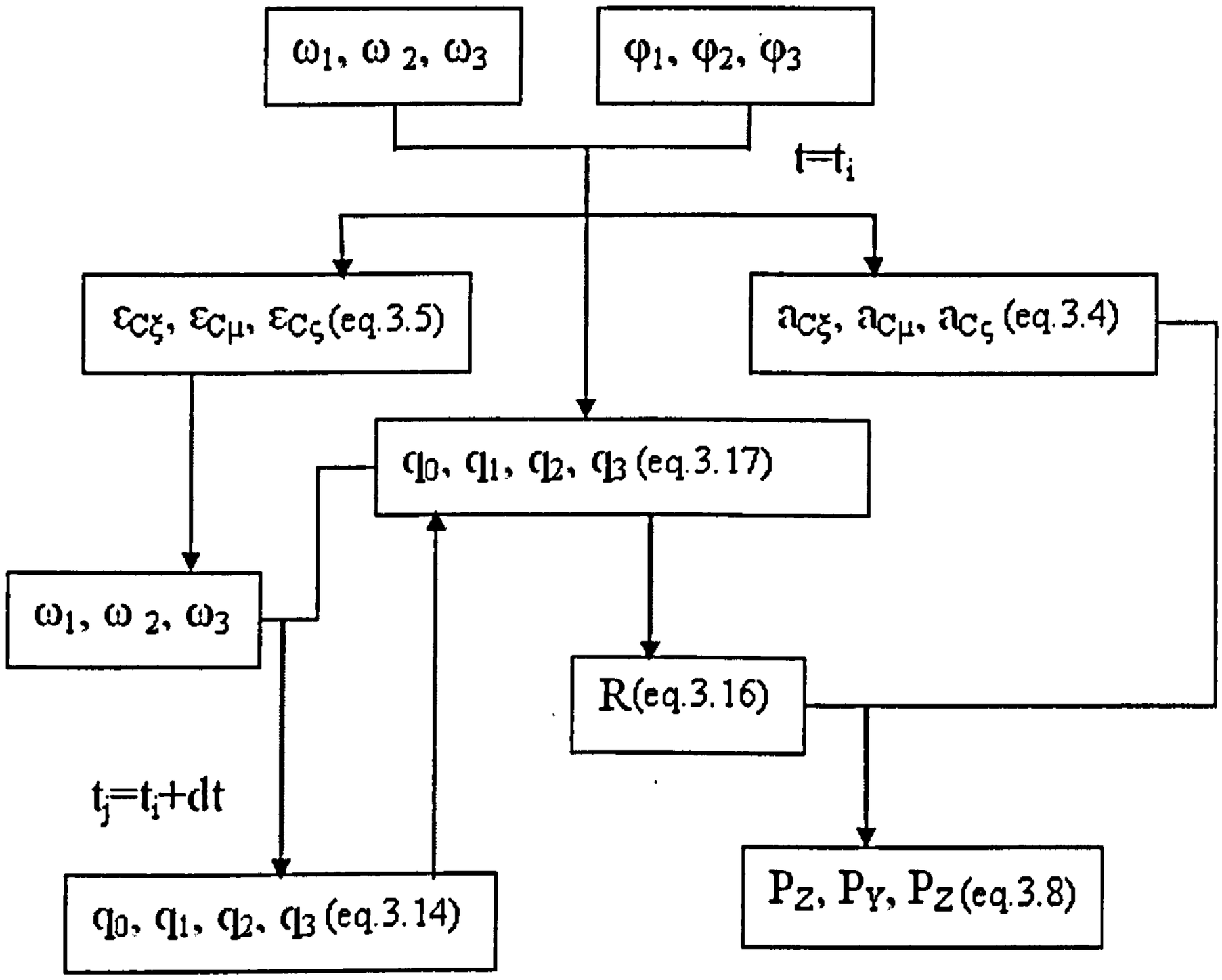

Figure 3.9. *Flow diagram of the analytical model to reconstruct the head motion using the Quaternion method.*

The angular velocity $\omega = [\omega_1, \omega_2, \omega_3]$ and three successive angles at time t_0 contribute to equations (3.19), (3.18), and (3.17). Therefore the rotation matrix in quaternion form can be obtained via equation (3.16). As a result, the global head position P_G can be obtained from equation (3.4), and the rotation matrix (3.16). The angular acceleration can be obtained via equation (3.5) and the angular velocity at t_0, which can be integrated to the value of the angular velocity $\omega = [\omega_1, \omega_2, \omega_3]$ at time step $t_1 = t_0 + dt$. At the same time, the differential form of the quaternion in equation (3.15) can be obtained, thus allowing a new quaternion at time step $t_1 = t_0 + dt$ to be obtained by integrating the differential format of equation (3.15). Finally the simulation at time $t_1 = t_0 + dt$ can be repeated from the rotation matrix (3.16) directly with the new quaternion result.

3.2.8 RESULTS AND DISCUSSION

A major assumption of the analysis is that, due to the tight gripping, the torso of the dummy can be described by linear motion along three directions (Figure 3.10(b)) in tests driven by anterior-posterior shaking. There might, in truth, have been small amounts of imposed rotation in the vertical direction due to different forces applied by the two hands, but even if there were, they were small enough not to be noticed by the numbers of the team, and they have been neglected in the current simulation. An example of the results of the simulation is provided in Figure 3.10, which gives the torso trajectory in tests driven by volunteer A with the dummy set with a loose neck, Figure 3.10 (a & b) are for the 3 shake test, and Figure 3.10 (c & d) are for the 10 shake test. The output is consistent with the input, and physically realistic. However, that is not the case for the simulation of the head motion.

An unexpected error seriously distorted the results during the reconstruction analysis of the head motion. The problem is most clearly illustrated by Figure 3.12(a), output data from a special test run designed to identify the source. The output begins to diverge from what it should be after about 4½ shakes, the error increases violently thereafter, with the motion soon becoming chaotic. There are two possible sources of the error: first, accumulating numerical round-off error during the loop of calculation; secondly, the assumption that the bottom of the head followed precisely the motion of the torso. An attempt was made to identify the source of the errors by giving an artificial motion as input to the analytical model (Figure 3.11-Figure 3.12).

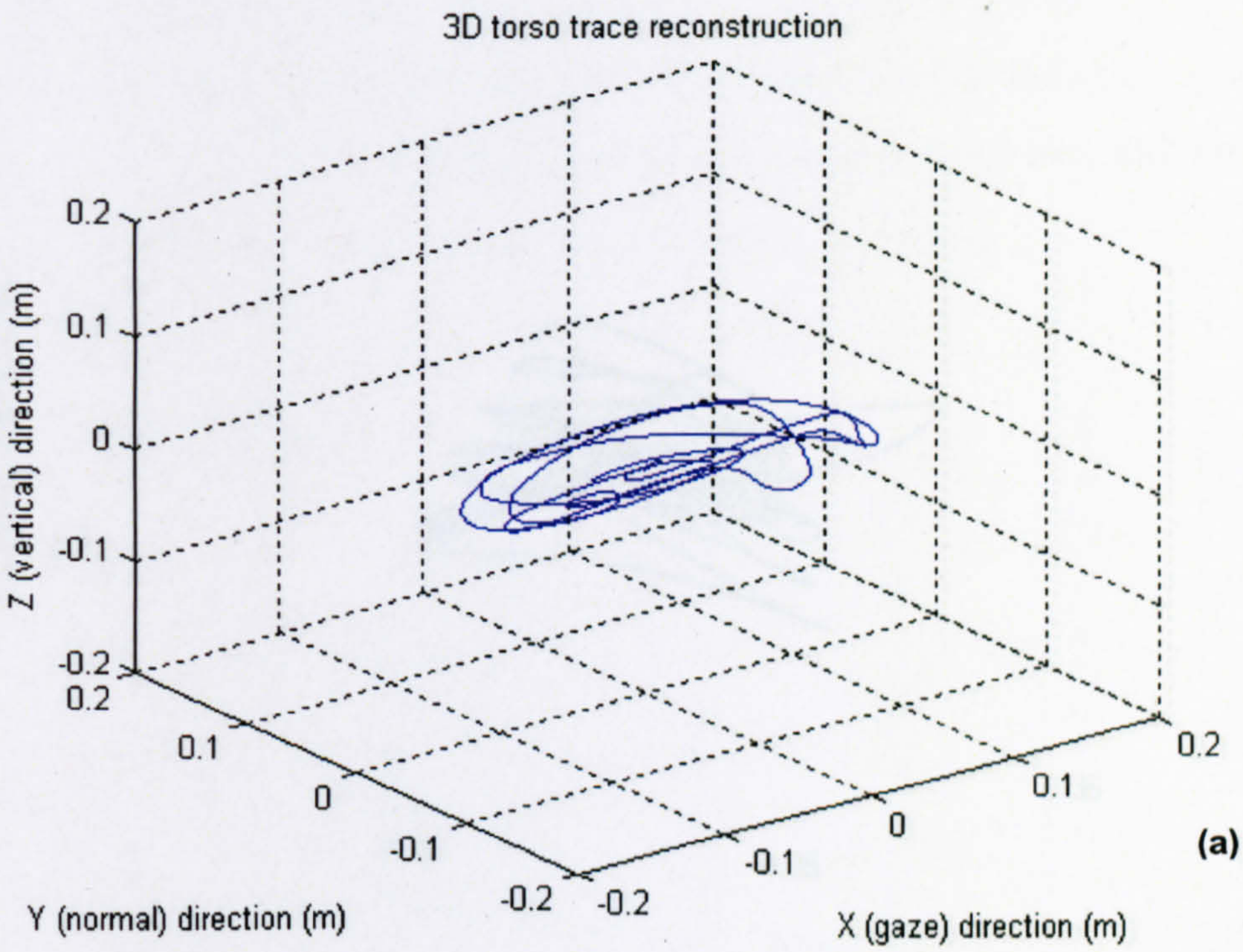
3D torso trace reconstruction
Z (vertical) direction (m)
0.2
0.1
0
-0.1
-0.2
0.2
0.1
0
-0.1
-0.2
Y (normal) direction (m)
0.2
0.1
0
-0.1
-0.2
X (gaze) direction (m)

(a)

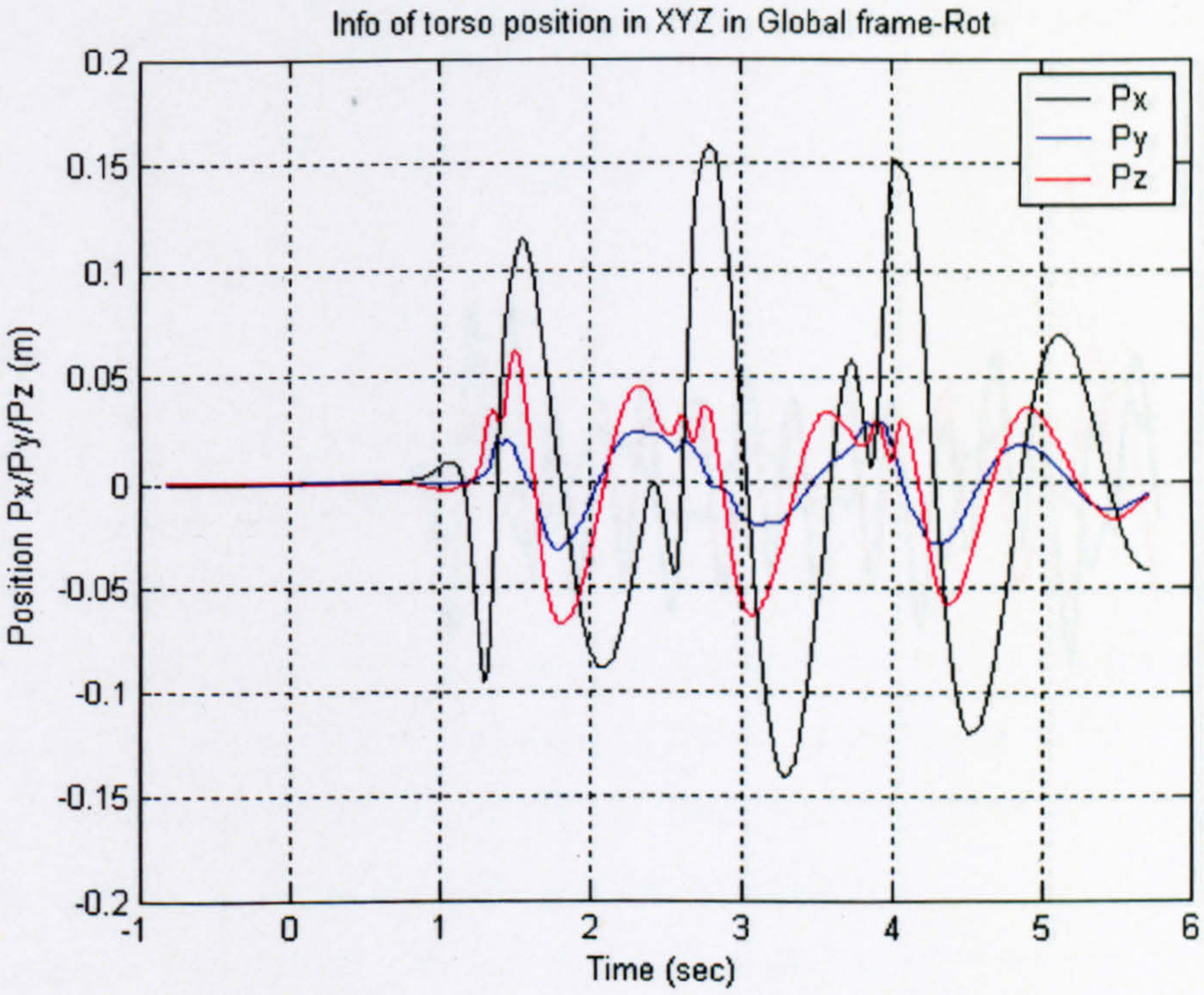
Info of torso position in XYZ in Global frame-Rot
Position Px/Py/Pz (m)
0.2
0.15
0.1
0.05
0
-0.05
-0.1
-0.15
-0.2
-1
0
1
2
3
4
5
6
Time (sec)
Px
Py
Pz

(b)

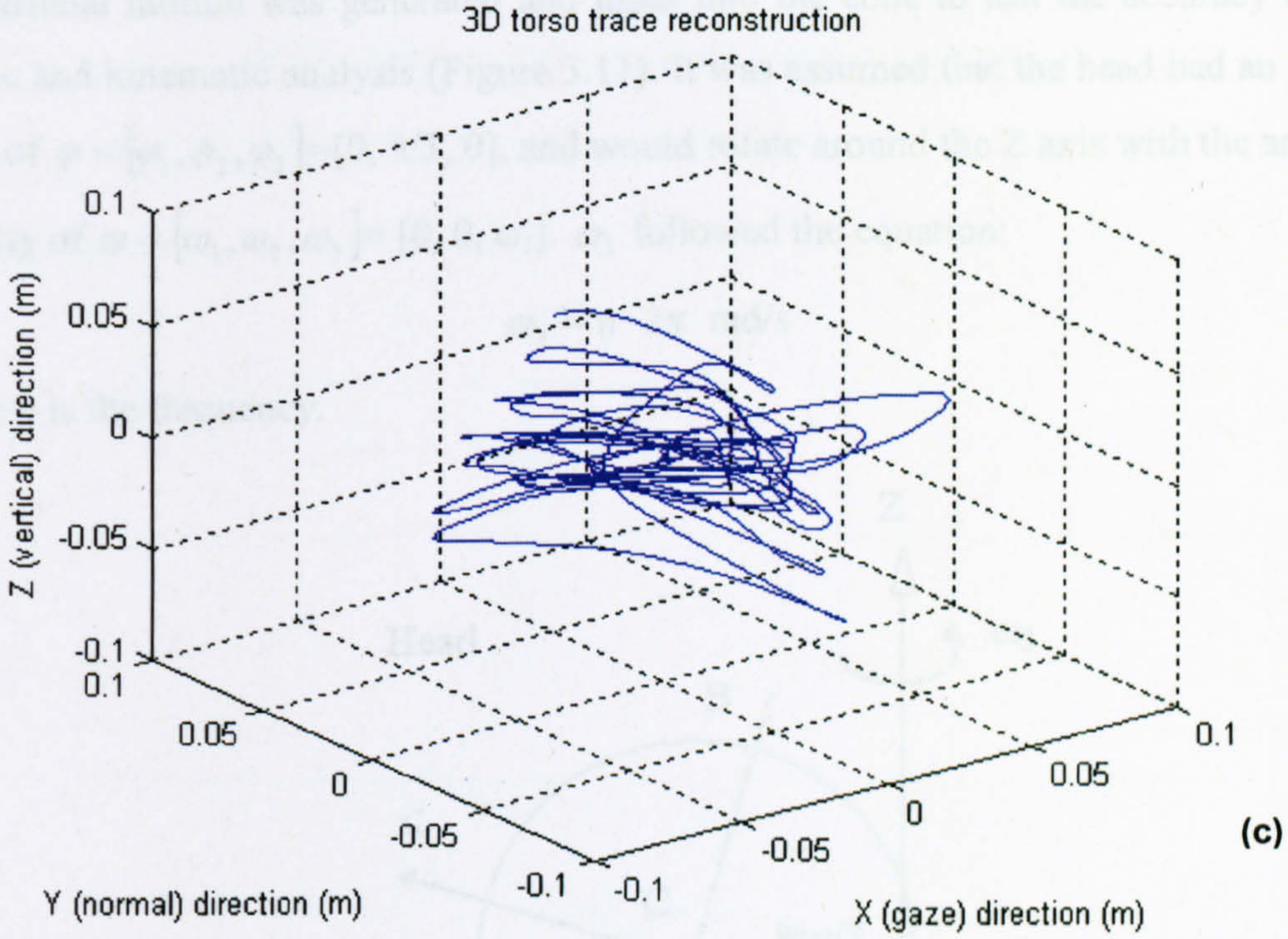

(c)

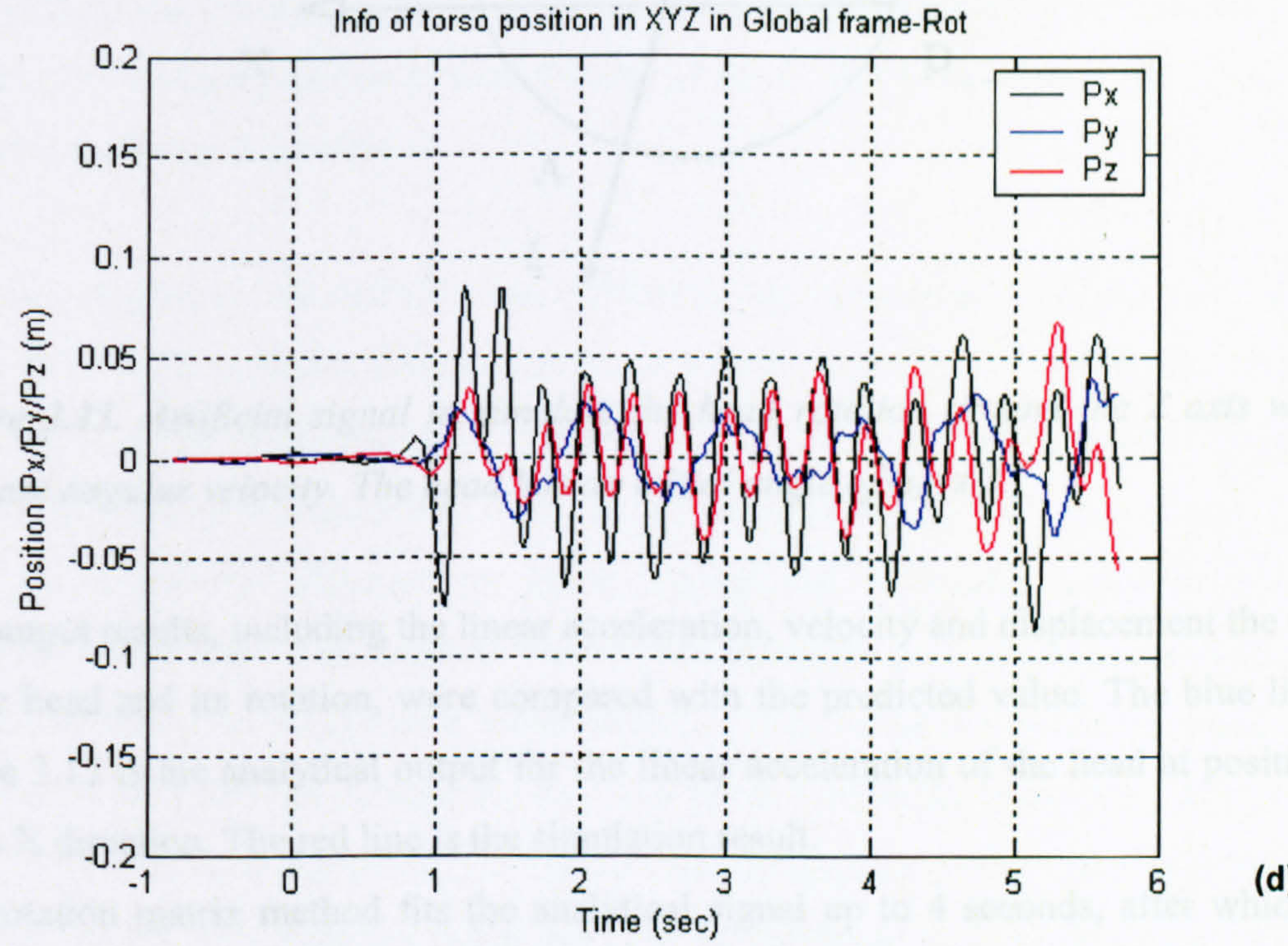

(d)

***Figure 3.10**. The trajectory of the dummy with loose neck shaken by volunteer A with 3 shakes and 10 shakes respectively. (a)-(b) the 3 shakes displacement, (c)-(d)) the 10 shakes displacement(Figure 3.2 in page54).*

An artificial motion was generated and input into the code to test the accuracy of the routine and kinematic analysis (Figure 3.11). It was assumed that the head had an initial angle of $\varphi = [\varphi_1, \varphi_2, \varphi_3]$=[0, π/3, 0], and would rotate around the Z axis with the angular velocity of $\omega = [\omega_1, \omega_2, \omega_3]$= [0, 0, ω_3]. ω_3 followed the equation:

$$\omega_3 = n \cdot 2\pi \text{ rad/s}$$

where n is the frequency.

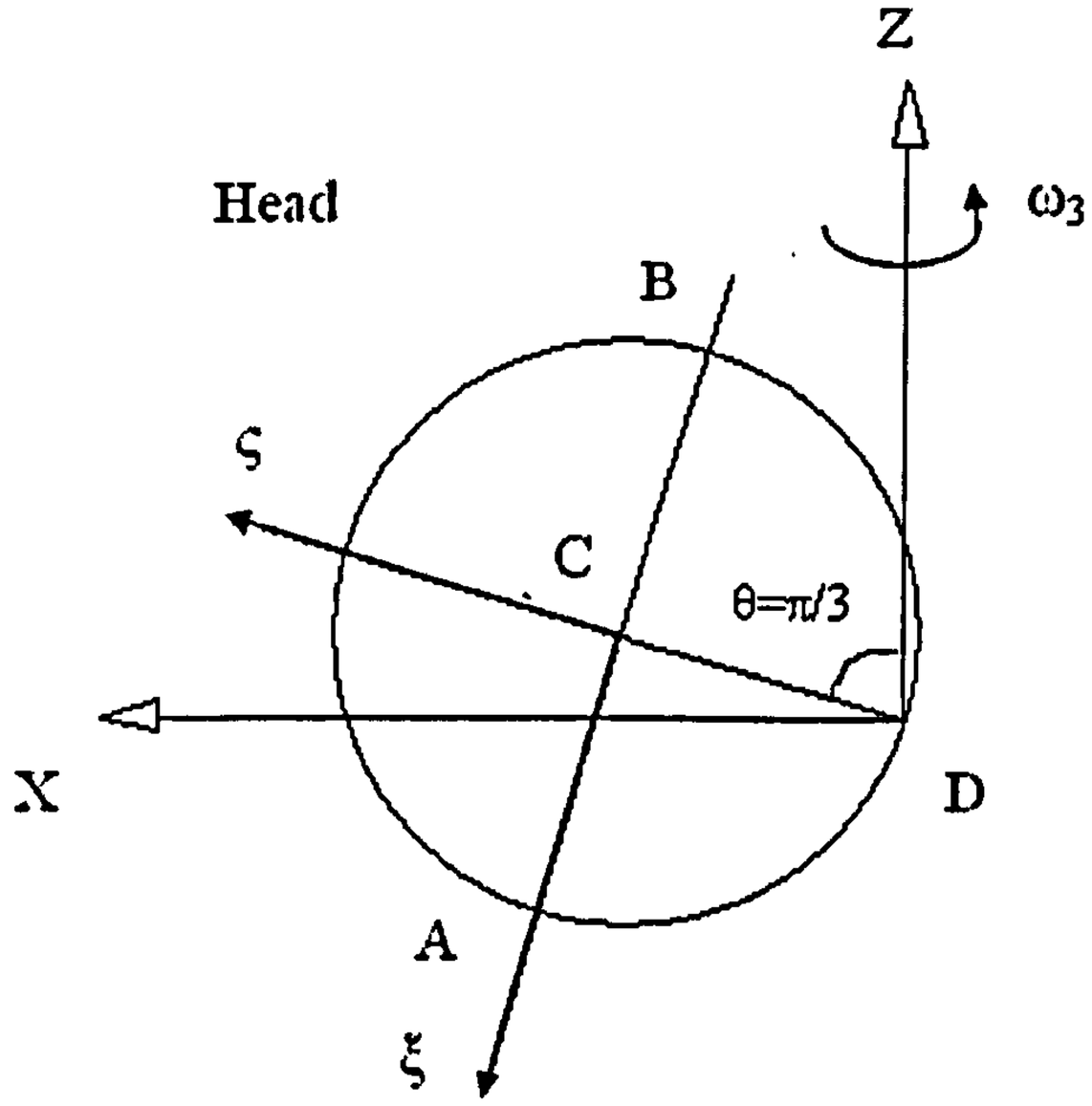

Figure 3.11. Artificial signal to simulate the head rotation around the Z axis with a constant angular velocity. The head has an initial angle of $\phi_2=\pi/3$.

The output results, including the linear acceleration, velocity and displacement the COG of the head and its rotation, were compared with the predicted value. The blue line in Figure 3.12 is the analytical output for the linear acceleration of the head at position C in the X direction. The red line is the simulation result.

The rotation matrix method fits the analytical signal up to 4 seconds, after which the simulated signal deteriorates. It cannot represent rotation at higher frequency (e.g.10Hz) rotation because of the rounding error. The quaternion method, on the other hand, was introduced to avoid the rounding error, the existence of a formal singularity and to reduce the processing time. Its results for the artificial signal are consistent with the predicted output even in very high frequency motion (e.g. 500 Hz), which also means that there is no mistake in the matrix algorithm.

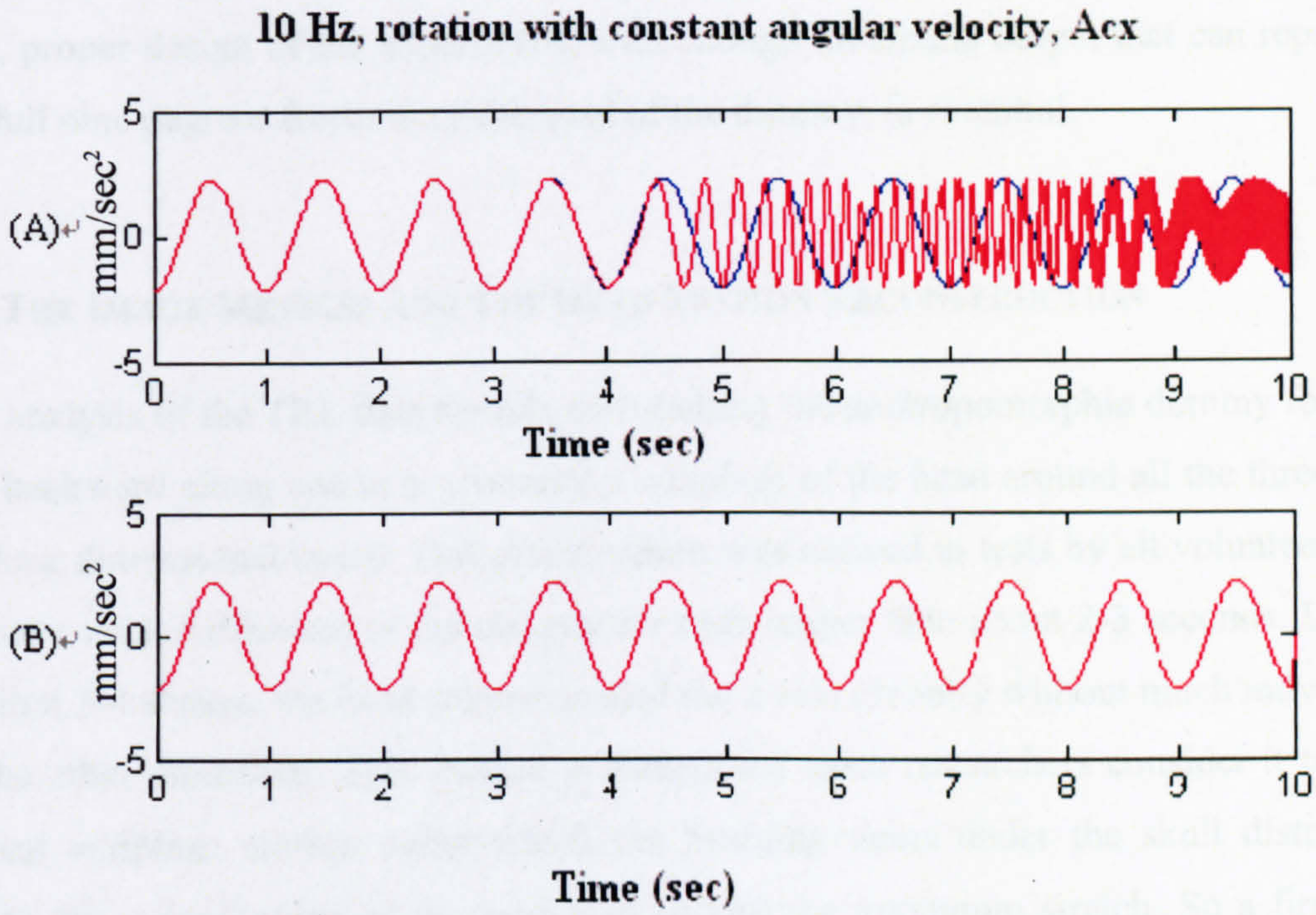

Figure 3.12. *The trace of dummy's head representation, the Y-axis represents the linear acceleration of head position C with the unit of mm/sec². (A) rotation matrix algorithm and (B) quaternion algorithm.*

However, neither of the methods can eliminate, nor compensate for, the error which comes from the insufficient information about the mechanics of the connection between the torso and the head and the resulting use of possibly inappropriate kinematic assumptions during reconstruction of the angular motion for the TRL data (Figure 3.17). Also, the kinematic assumptions made during the kinematic analysis probably contribute to the error. The simplest way of processing the data was to assumes that the motions of the torso and the neck were identical. This, of course, is not accurate, since the torso actually follows the anterior-posterior pattern under the heavy shaking in many cases due to a lack of control by the shaker. The assumption works quite well in linear torso motion but will introduce larger errors to the rotational motion. Having eliminated the possibility of the time interval during the integration affecting the results, one is left with the conclusion that the simplified assumption about the kinematics of the head and torso is the source of the errors in the computed results.

This work demonstrates very clearly that a reasonable reconstruction of the motion of the head of the dummy for more than a 4 or so shakes is impossible using the TRL accelerometer data. Simply, the data is insufficient, and there is no way to compensate

for its inadequacy. A conclusion is that, in any future attempt at producing more useful data, proper design of the experiment, with enough kinematic output that can represent the full nine degrees freedom of the head of the dummy, is essential.

3.3. The Image Method And The Head Motion Reconstruction

The analysis of the TRL data reveals that shaking the anthropomorphic dummy forward and backward along one axis produced a whiplash of the head around all the three axes of three dimensional space. This phenomenon was noticed in tests by all volunteers and all three neck stiffnesses of the dummy for tests longer than about 2-3 seconds. During the first 3-4 shakes, the head rotated around the z axis globally without much movement in the other directions. This motion is dangerous, since researchers consider it to be a typical whiplash motion under which the bridging veins under the skull distributed inside the sagittal plane of the head will sustain the maximum stretch. So a first step towards accurate reconstruction of the head motion was to begin a programme of study examining this in detail. In this, the 6 degrees of freedom of the head motion can be reduced to three, including translation in the X-Z plane (sagittal plane), and rotation around the Y axis. Data for the angular movement as well as the position of the head can be acquired by analysing the video camera output (Figures 3.13-3.14).

From all the motions shown in the full set of volunteer video clips, the tests by volunteer A on the dummy with a soft neck were chosen for the analysis, since they were relatively the most stable and severe shaking in the 2D plane. Work in the future can, if needed, deal with all the video clips to compare the variation in shaking pattern of all the volunteers.

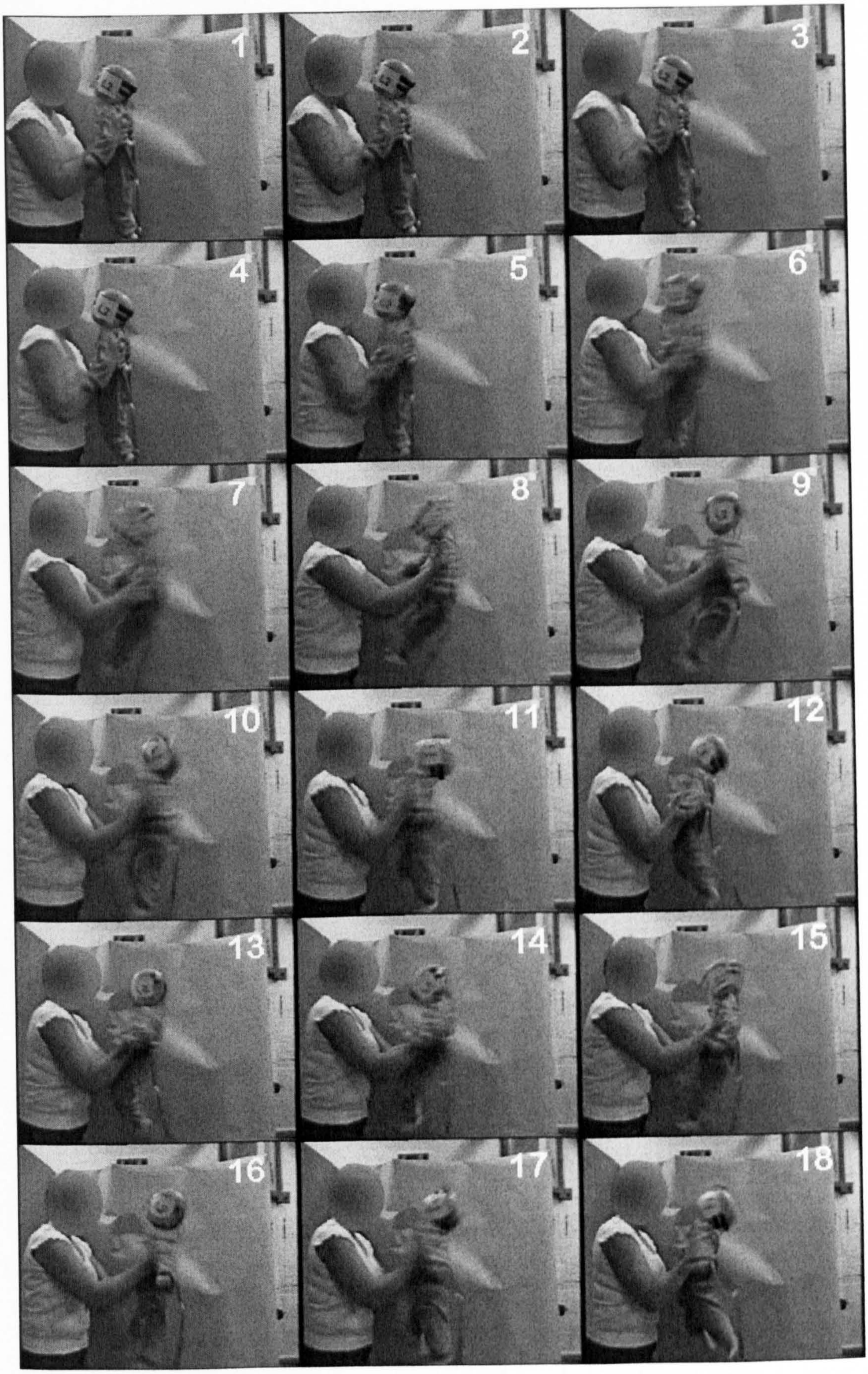
1
2
3
4
5
6
7
8
9
10
11
12
13
14
15
16
17
18

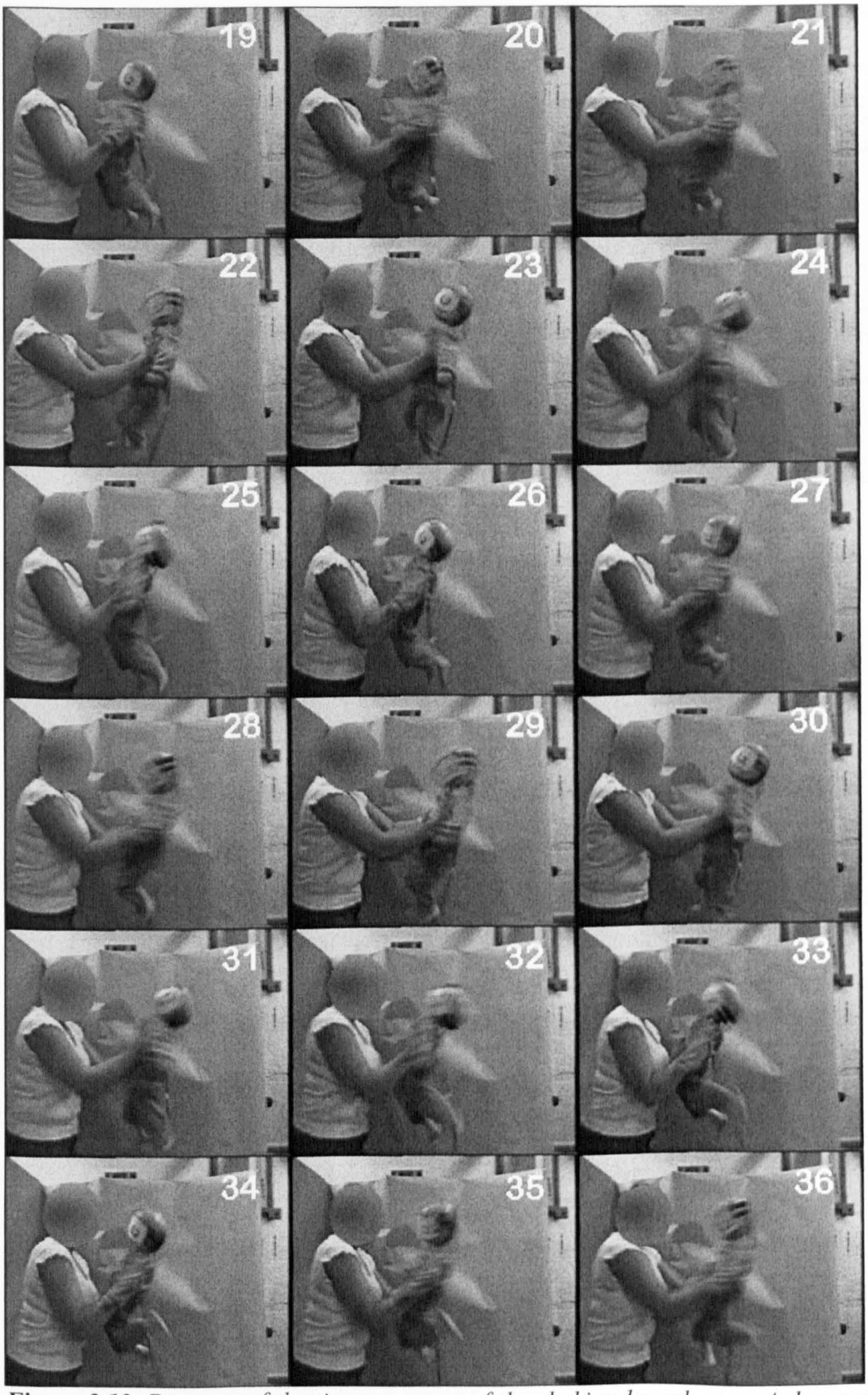

Figure 3.13. *Diagram of the time sequence of the shaking by volunteer A, loose neck. The time step between each adjacent picture is 0.038 sec.*

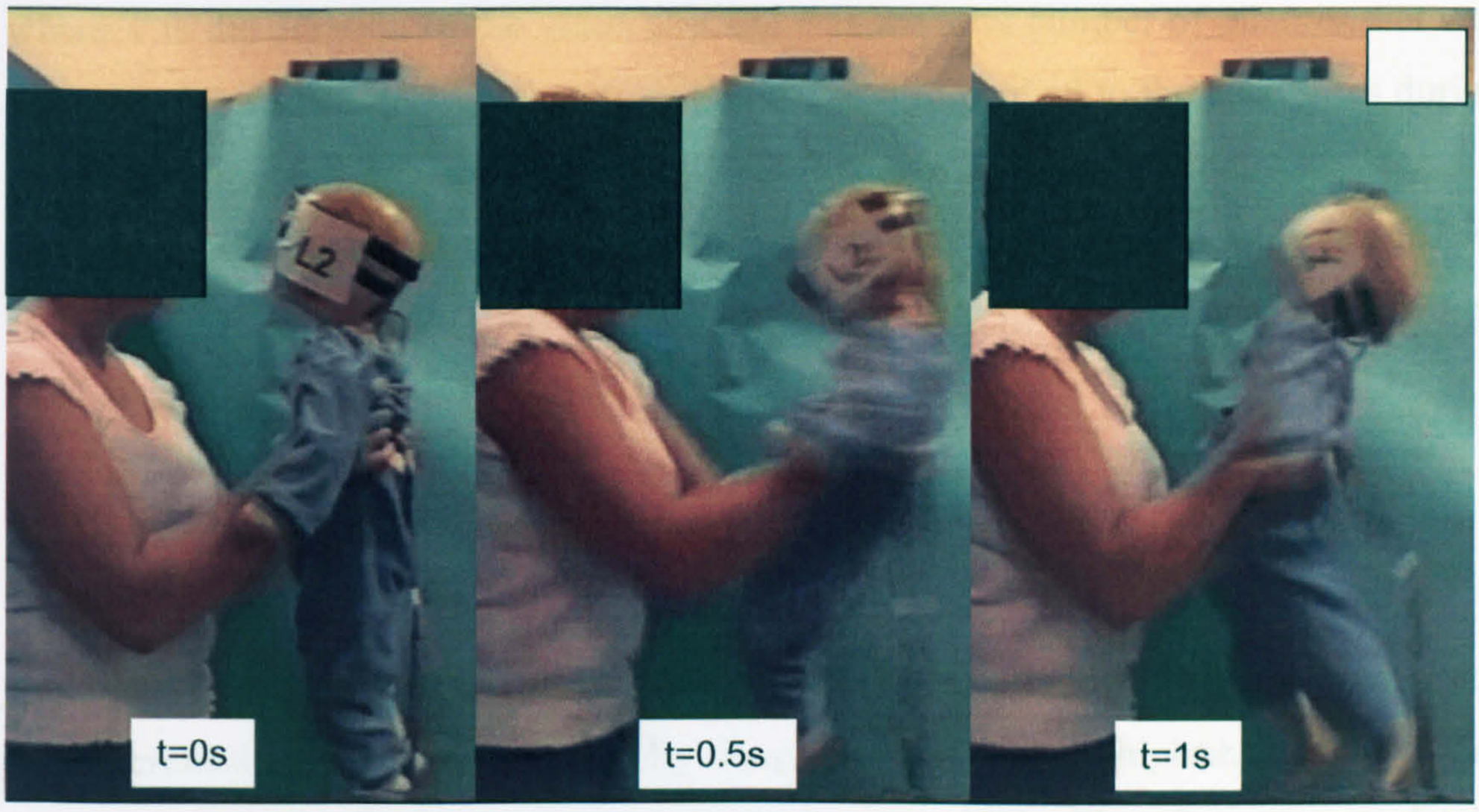

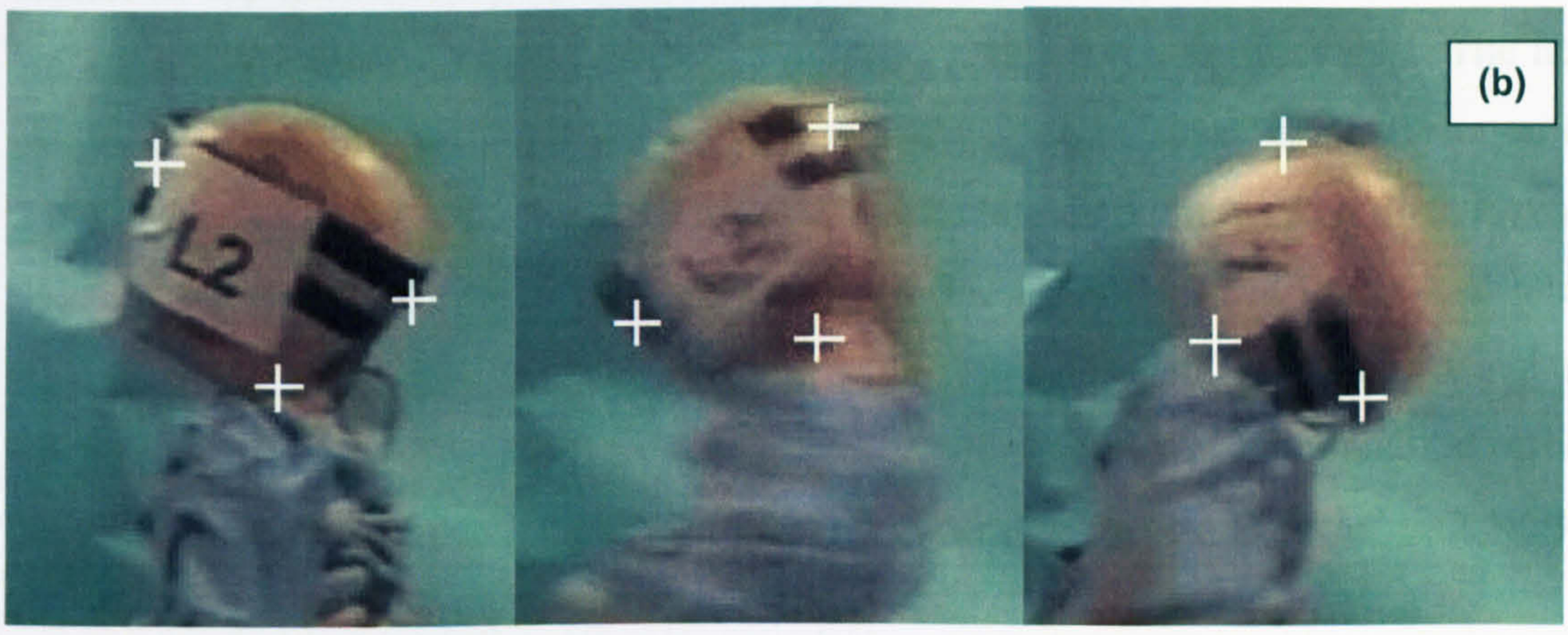

Figure 3.14. *The Image method to reconstruct the head rotation motion. The video clip is that for constant shaking by volunteer A with loose neck dummy. (a) the shaking progress, (b) the image method, picking up three positions on the head.*

3.3.1. THE METHOD

A video clip of approximately 1.2 seconds was chosen from the 10-shake test by volunteer A on the loose neck dummy. The software used to discretise into the pictures (Figure 3.13) was VirtualDub-1.6.11. The time interval *dt* between each adjacent picture equals the video clip duration divided by the picture number minus 1.

$$dt = \frac{T}{(n-1)} = \frac{1.11}{(30-1)} = 0.038\,\text{sec} \qquad (3.20)$$

where T is the duration of the video clip and n is the total number of pictures that was discretised from the video clips. Interpolation was also applied to the data series during the differentiation from the displacement to the velocity and acceleration.

In each picture, the pixels in the A, B and D positions were picked up using ImageTool (UTHSCSA). The angular motion of the head as well as its position was calculated by Matlab 6.5.

3.3.2. THE RESULTS

Figure 3.15 (a) shows the changing rotation of the head with time. The data from which it was created was picked up image by image. However, the whiplash induced in this shaking motion has frequency components higher than 30Hz. Therefore accurate details cannot be captured directly by a normal video camera (the type used in the TRL tests). As a result, the analysis used Matlab 6.5 to interpolate on the sampled data. The head rotates between -40° and 100° during violent shaking, and a loose neck setting on the dummy guaranteed that the potential rotation reached the maximum of all three types of neck setting. Figure 3.15(b) shows the linear movement of the head in the X-Z plane, Figures 3.15(c) and (d) give the components in the horizontal (X) and vertical (Z) directions separately. The maximum horizontal displacement is 150mm, and the vertical displacement ranges over 25mm-30mm during rotation. The velocity reaches 2.5m/s in the X direction and 0.5m/s in the Z direction.

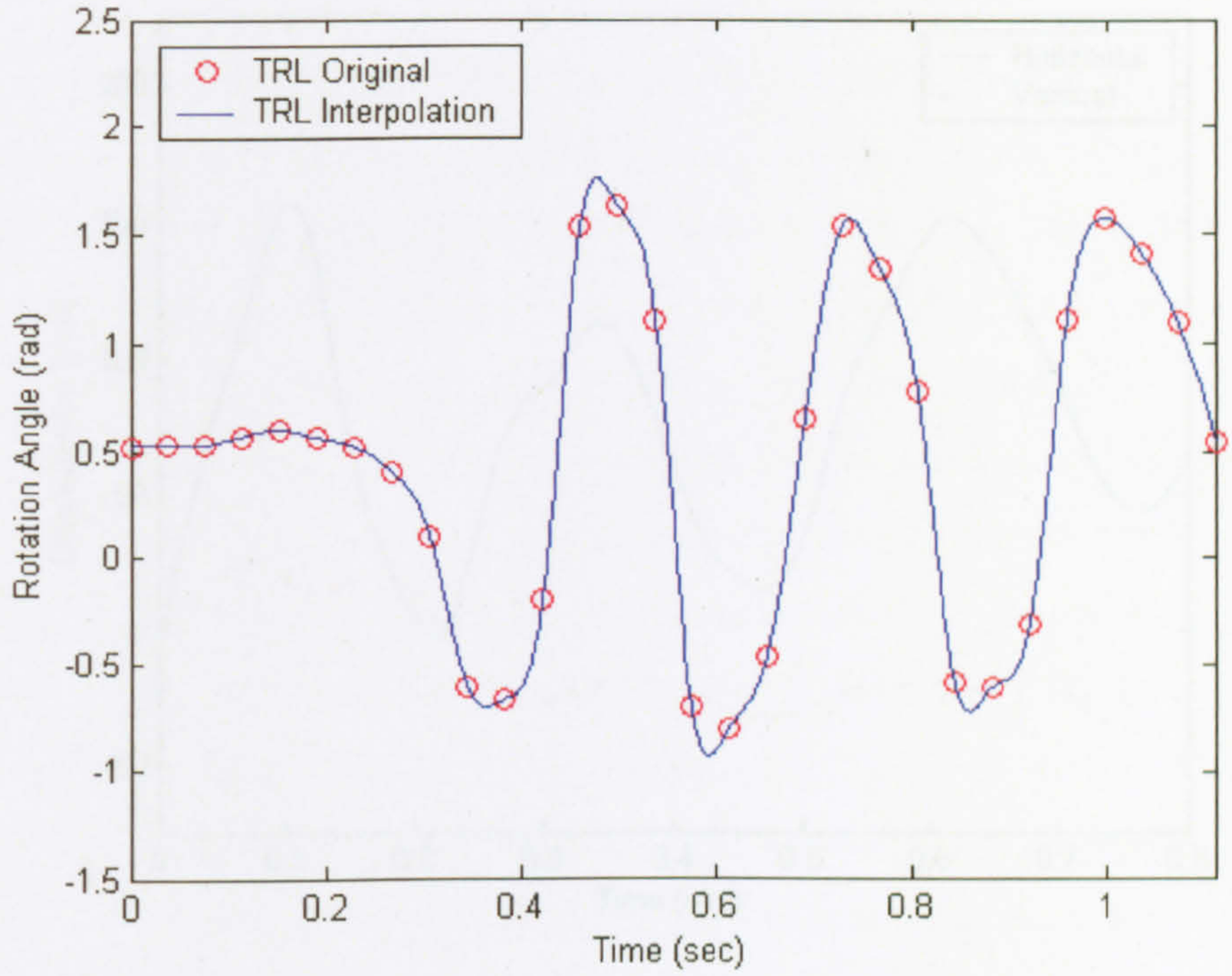
TRL Original
TRL Interpolation
Rotation Angle (rad)
Time (sec)

(a)

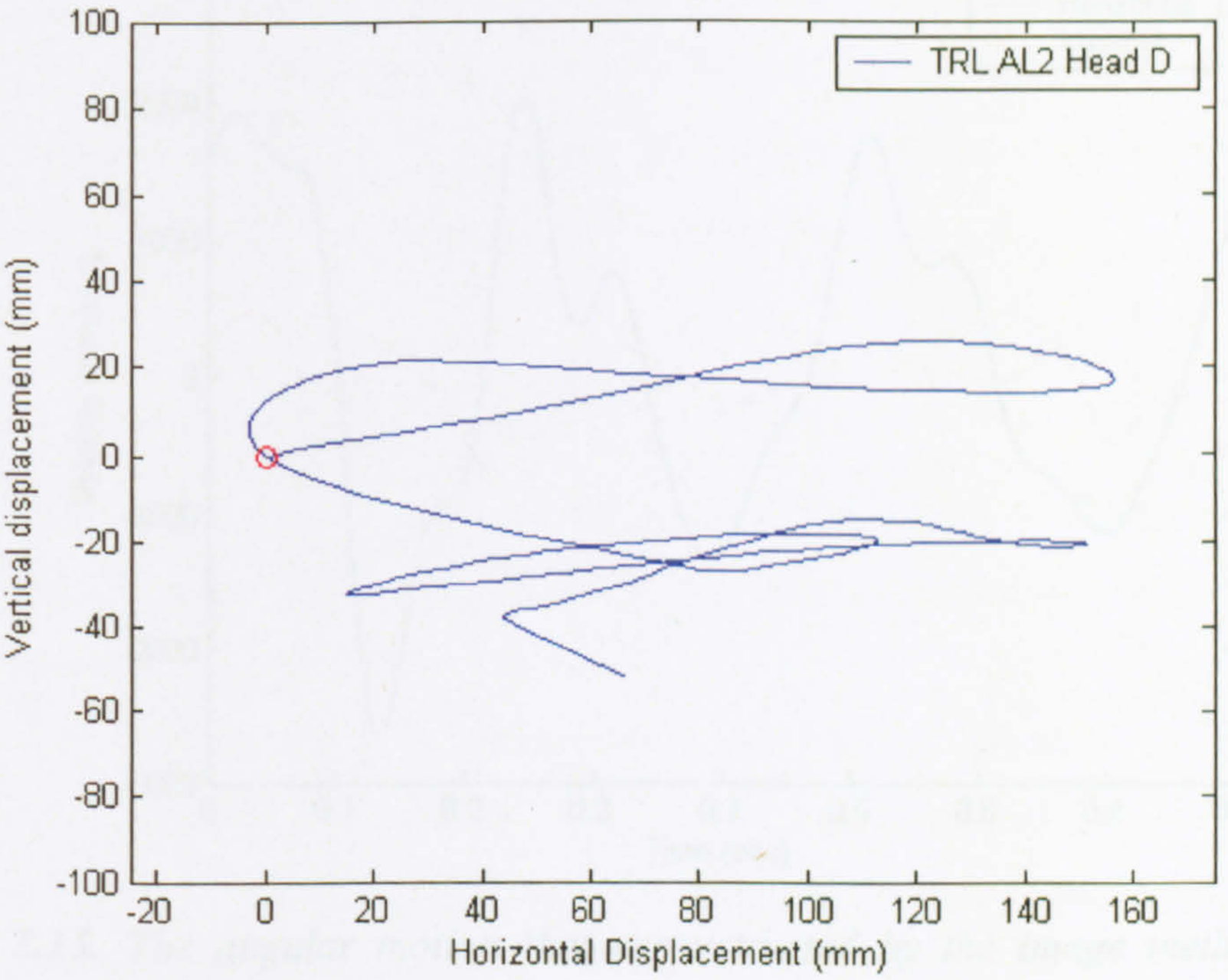
TRL AL2 Head D
Vertical displacement (mm)
Horizontal Displacement (mm)

(b)

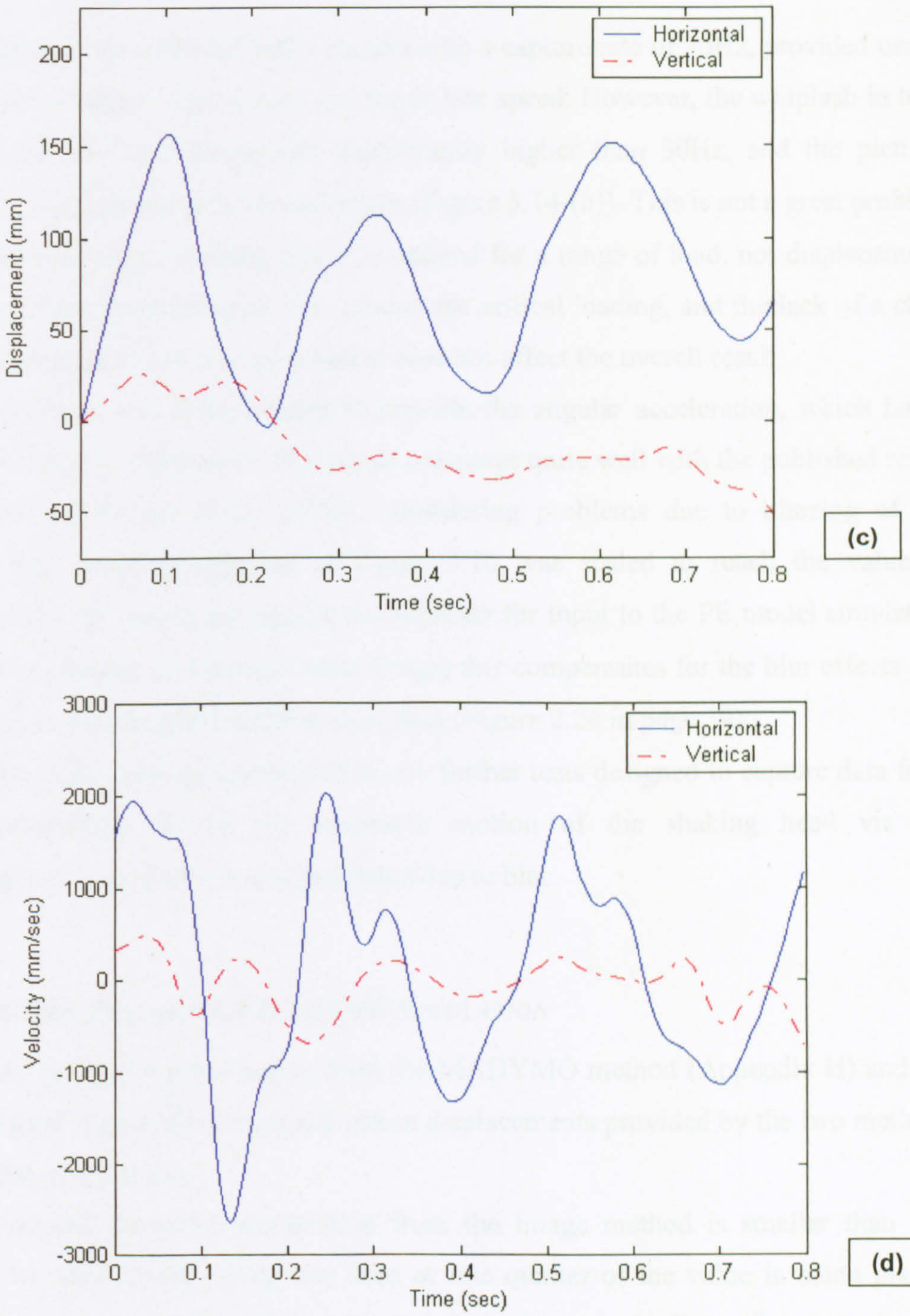

Figure 3.15. *The angular motion that reconstructed by the image method. (a) the rotation angle in the X-Z plane was created by image method with its original data and the interpolation; (b) The displacement of C position on head in X-Z plane; (c) the displacement of C position on head in X and Z direction separately; (d) the velocity shown in the X and Z directions were created by differentiation of the function found by interpolating the displacement data.*

3.3.3. PROBLEMS DUE TO BLUR

Motion captured by a normal video camera with a capture rate of 30Hz, provided useful information when the dummy was moving at low speed. However, the whiplash in tests at maximum load has frequencies significantly higher than 30Hz, and the pictures captured by the camera have blurred edges (Figure 3.14-(b)). This is not a great problem here, since in practice, shaking injury is defined for a range of load, not displacement. The aim of the current analysis is to predict the critical loading, and the lack of a clear edge in reconstructing the actual position does not affect the overall result.

The angular data was differentiated to provide the angular acceleration, which had a maximum value of 2000rad/s^2. This result compares quite well with the published result (2640rad/s^2) of Prange et al. (2003), considering problems due to blurring of the pictures. The resulting data set in Figure 3.16 was scaled to reach the value of 2600rad/s^2 for the maximum angular acceleration for input to the FE model simulation described in Chapter 8. Amongst other things, this compensates for the blur effects and relates the analysis to published literature data (Figure 2.24 in page 39).

Three high speed cameras are needed in any further tests designed to capture data for a full reconstruction of the 3D kinematic motion of the shaking head via the photogrammetry method to avoid problems due to blur.

3.3.4. THE TRL TEST AND ITS MADYMO SIMULATION

Figure 3.17 compares some output from the MADYMO method (Appendix H) and the image method. The X (horizontal) direction displacements provided by the two methods have similar magnitudes.

The Z (vertical) direction acceleration from the image method is smaller than that provided by MADYMO, being one third or one quarter of the value in some places. This discrepancy is probably due to the fact that, although the linear forces applied to the torso are similar in the two methods, the consequences of the shaking for the head also depend on the neck properties. Since there was no tuning of the mechanics of the experimental dummy and the MADYMO model, the results derived from it, can, as seen in Figure 3.17 differ from those observed. As we have seen, this difference is stronger in the vertical than the horizontal direction. Even so, there is reasonable qualitative agreement between the MADYMO simulation and the results from the

image analysis of the TRL data, enough to give some confidence in using that data (suitably scaled) to drive the FE simulation that will be discussed in Chapter 8.

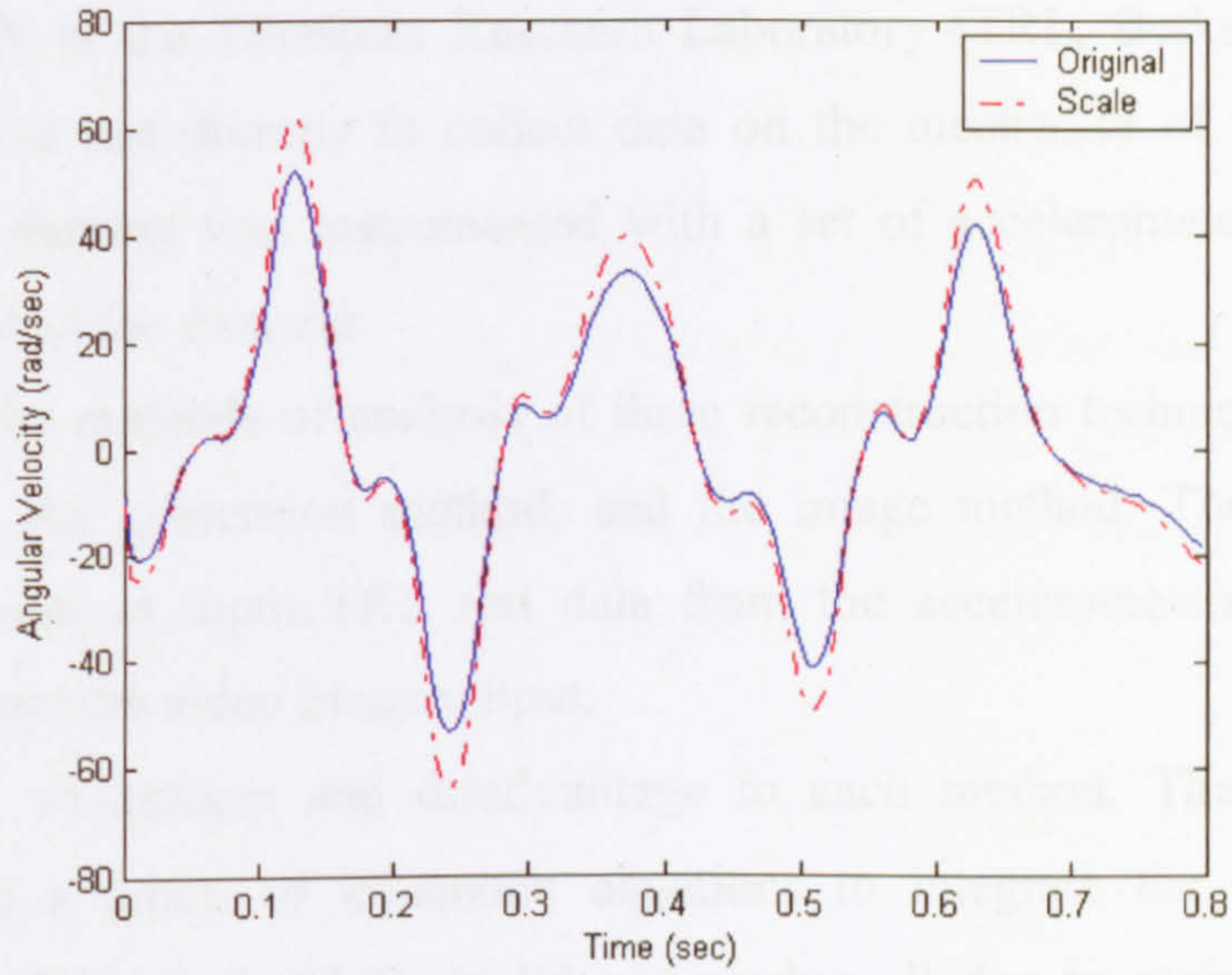

Figure 3.16. *The rotation angle of the head of both original result and scaled result with the angular velocity that differentiated from the angle.*

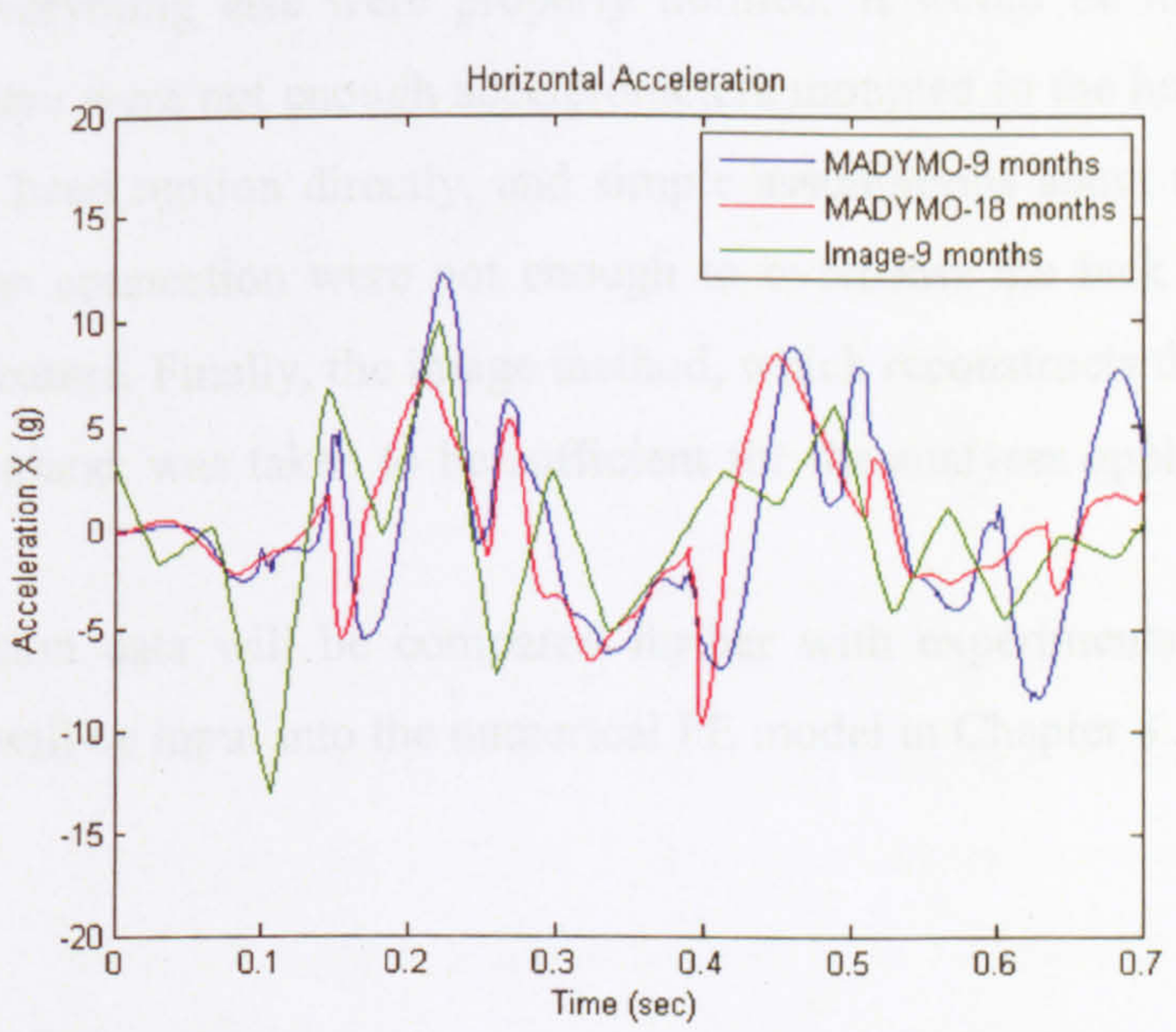

Figure 3.17. *The comparison of horizontal acceleration of the head motion in the MADYMO simulation and data from the image analysis of the TRL data.*

SUMMARY

This chapter began by describing the experiments conducted in 2000 by the Soft Structure Group (Department of Mechanical Engineering, Sheffield University) (Brudenell 2000) at the Transport Research Laboratory (TRL, Berkshire) using a 9-month automotive test dummy to collect data on the mechanics of the shaken baby syndrome. The dummy was instrumented with a set of accelerometers, and the tests were recorded on video cameras.

It then set out the methods of analysis of three reconstruction techniques, the rotation matrix method, the quaternion method, and the image method. The first two were designed to accept as input TRL test data from the accelerometers. The third had digitised data from the video images input.

There are both advantages and disadvantage to each method. The rotation matrix method sets up a group of kinematic equations to integrate the output from the accelerometers (Chapter 3, §3.2). It did not work well due to rapidly accumulating numerical rounding error during the calculation (Figure 3.12(a)). The quaternion method avoided the numerical error (Figure 3.12(b)) and speeded up the calculation time, and, if everything else were properly defined, it would be the choice for the analysis. But there were not enough accelerometers mounted in the head of the dummy to integrate the head motion directly, and simple assumptions about the kinematics of the head-to-torso connection were not enough to overcome the lack of knowledge of this important feature. Finally, the image method, which reconstructs the head motion in the 2D sagittal plane, was taken to be sufficient for the analyses applied in Chapters 6 and Chapter 8.

The reconstruction data will be compared further with experimental test rig data in Chapter 6, and will be input into the numerical FE model in Chapter 8.

CHAPTER 4: *EXPERIMENTAL APPARATUS AND ANTHROPOMORPHIC MODELLING*

INTRODUCTION

This chapter describes an experimental test rig that was designed by the author, and built under her guidance by the staff of the Department of Mechanical Engineering at the University of Sheffield. The purpose of the rig was to simulate the shaking of mechanical models of biological systems, especially those related to the shaken baby phenomenon. In particular, the object of the research reported here was a model of the infant skull, and its soft tissue contents, the design of which was undertaken after that of the test apparatus had been finalised. A set of material property tests was essential in providing data to aid the choice of inert soft material to mimic the properties of the infant brain tissue and the other essential mechanical components of the infant head. Furthermore, accurate determination of the mechanical properties of the materials actually chosen for the model tests would be essential for input to the computational model whose development is described later in Chapter 7. The model was assembled onto the rig and provides the testing apparatus for the shaking test which will be described later in Chapter 5 and Chapter 6.

4.1. THE DESIGN OF THE LOADING CELL

The machine designed for the reconstruction of the shaking phenomenon was required to create repetitive linear motion under the whiplash load within the range of 5g-15g, and a 5Hz reversal motion. The pneumatic power was chosen to drive the experimental rig to provide the stable, repetitive motion by the air compressor in our laboratory. The air, which can be compressed easily, is able to produce a cushioning effect to represent the motion of the human limb.

4.1.1. THE AIR FLOW IN PNEUMATIC CYLINDER

The compressed air contributes to the primary system and reaches the pneumatic actuator, or pneumatic cylinder (ram) via the pneumatic circuit. The double-acting

pneumatic cylinder is a pneumatic component that conducts stroke in two directions by extending and retracting the mechanical piston driven by the pneumatic power. Figure 4.1 gives a typical double acting pneumatic cylinder with the piston using wear compensating and pressure energized U cup seals to provide low friction sealing and smooth chatter-free movement of this cylinder. The end plates use ribbed aluminium alloy to provide strength while minimizing weight. Self-aligning Buna-N seals provide a positive leak proof cushion with check valve action which reverts to free flow upon cylinder reversal. The cushion adjustment, which uses a tapered self-locking needle at each end, provides positive control over the stroke.

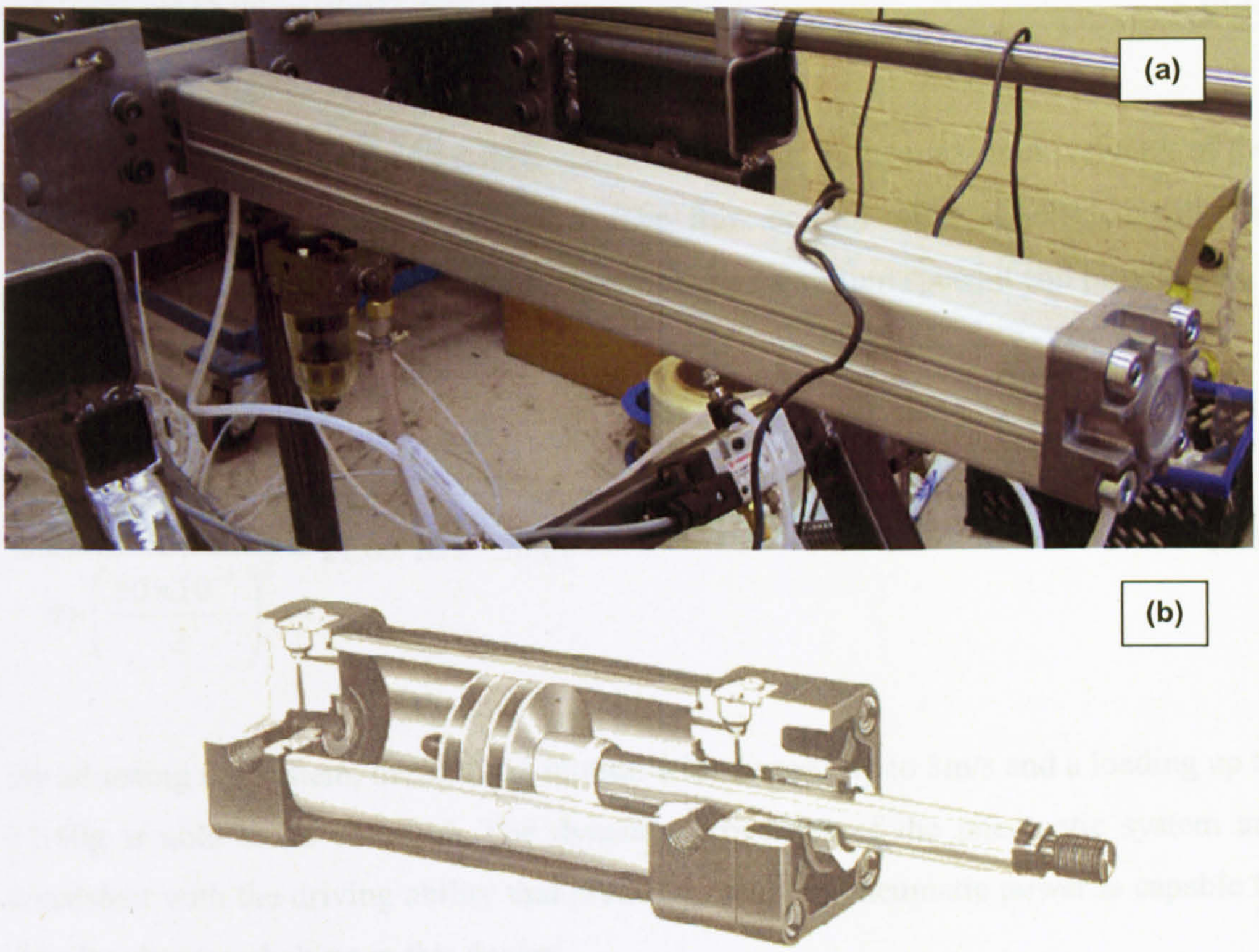

Figure 4.1. *Pneumatic cylinder: (a) in the lab; (b) diagram of the internal structure (Esposito 1980).*

By analyzing the air flow to the pneumatic components, the acquired speed and loading for the dynamic system can be defined.

The maximum air pressure of the air compressor is 6 bars, and the diameter of the selected pneumatic cylinder is 50mm, therefore the maximum loading the whole system can drive is:

$$F_{ram} = P_{ram} \times S_{ram} = P_{ram} \times \pi \times \left(\frac{d_{ram}}{2}\right)^2 \tag{4.1}$$

The actual acceleration a_{real} by current system is:

$$a_{real} = \frac{F_{ram}}{m_{\max}}$$

$$= \frac{1178.1}{10.53} = 111.88 \text{ m/s}^2 = 11.40\text{g} \tag{4.2}$$

According to the TRL data described earlier in Chapter 3, the maximum velocity of the linear shaking is up to 3m/s, or 360l/s. The flow control valve is selected with the maximum flow rate ability of 2600l/s, therefore the maximum speed it can provided is:

$$v = \frac{v_{fr}}{S_{ram}}$$

$$= \frac{2600 \times \frac{10^{-3}}{60}}{\pi \times \left(\frac{50 \times 10^{-3}}{2}\right)^2} = 21.65 \text{ m/s} > 3\text{m/s} \tag{4.3}$$

By adjusting the system, the shaking motion with a speed up to 3m/s and a loading up to 11.40g is able to be obtained. The dynamic properties of the pneumatic system are consistent with the driving ability that predicted, and the pneumatic power is capable to simulate human shaking in this design.

4.1.2. THE PNEUMATIC CIRCULATION (Esposito 1980; Norgren 1998; Parr 1998)

The design of the pneumatic circulation is shown schematically in the Figure 4.2. It consists of a pneumatic cylinder, a direction control valve of solenoid 3/2, and a direction control valve of solenoid 5/2, a filter regulator, a lubricator, a flow control valve and some nylon tubes to conduct air (Table 4.1, Figure 4.2, Figure 4.3 (b)).

The regulator uses a spring loaded diagram and features balanced valves for superior regulation characteristics. Large main valve seats and precisely positioned aspirator tubes provide for excellent flow characteristics and minimal pressure drop. The regulator contains an adjustable upper spring which allows the valve to hold a given pressure on the downstream side.

The function of the filter is to remove contaminants from the air before it reaches pneumatic components such as valves and actuators.

The lubricator ensures proper lubrication of internal moving parts of pneumatic components. It inserts every drop of oil leaving the drip tube, directly into the air stream. These drops of oil are transformed into an oil mist prior to their being transported downstream. These oil mist particles are created when a portion of the incoming air passes through the centre of the variable orifice and enters the mist generator, mixing with the oil delivered by the drip tube. This air-oil mixture then rejoins any air that has bypassed the centre of the variable orifice and continues with that air toward its final destination.

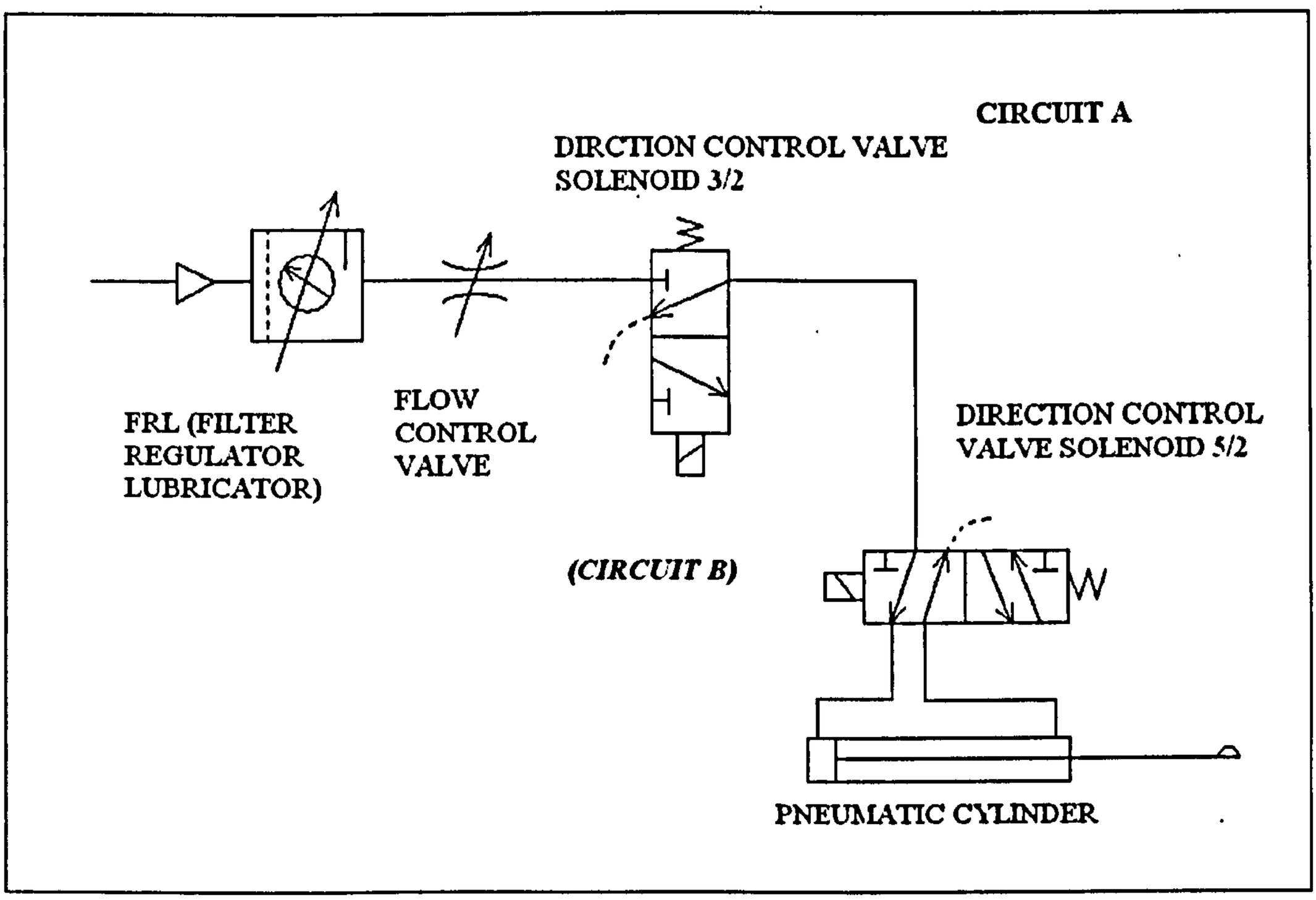

Figure 4.2. *The pneumatic circulation and the logical control.*

The air control valves are used to control the pressure, flow rate, and direction of air in pneumatic circuits. Two directional control valves were applied into the circuit. One is a two-position, three-way valve and the other one is a five-way, two-position valve. Both

of them are solenoid-actuated with 24DC voltage. The single-solenoid operator shown moves the spool when energized, and a spring will return the spool when the solenoid is de-energized. It helps to change the position of the valve in order to control the direction of the air. A 3/2 valve conducts the air from the filer-lubricator-regulator (FLR) into the 5/2 valve. The 5/2 valve changes the direction of the air that into of the pneumatic cylinder to control the stroke direction of the piston.

On the control valve, several pneumatic exhaust silencers (mufflers) are used to control the noise caused by a rapidly exhausting air stream flowing into the atmosphere.

Each piece of pneumatic component was connected by nylon tubes to construct a closed pneumatic circulation.

No.	Component	Quantity	Order Type
1	Pneumatic cylinder 2000, 600mm stroke, D=50mm 2600l/s G3/8'' 8-10bar	1	PRA/182050/M/600
2	3/2 single solenoid	1	V61B417AA2000
3	5/2 Solenoid 24V	1	V61B517AA2000
4	Flow valve (V60-V63)	2	TRE028
5	Coils 24V	2	QM135/21
6	Lubricator	1	NOEGEN 10 bar
7	Regulator	1	NORGEN B13-A3 mk II 0.4-10bar
8	Nylon tube	-	-

Table 4.1. The components of the pneumatic circuit, the supplier of the pneumatic component is Norgren (Norgren 1998).

4.1.3. THE FRAME

The frame was designed to support both loading and moveable parts of the system. The whole structure was fabricated using weldable 40×40 square section, and Figure 4.3 (a) shows the concept design of the structure. The main frame was constructed by two truncated A section, and welded parallel with five identical square steel bars (Figure 4.3 (b)). The beam in the middle of the truncated A sections was constructed to support each side of the leg, and they are set free only to support the four legs with the 40×40 square section welded between the central beam and each legs. The whole structure was

bolted on the ground by a clevis mounting in each of the four leg. Two 80×80 square sections were welded on the top, parallel beams, in order to assembly the linear guidance system. Between the 80 square section beams, an aluminium plate was fixed by two custom designed steel corner. Hence the pneumatic cylinder can then be mounted on the centre of the plate. The other components of the pneumatic circuit, as well as the logical control cell, were also fixed on this frame.

4.2. The Design Of The Motion Cell (Martin 1969; HepcoMotion 2004)

The linear guidance system transmits the dynamic movement from the pneumatic cylinder to the platform and conducts linear, steady motion to the platform. The linear guidance system consists of one double edge spacer slides, four standard bearings, one flat track and four narrow track rollers (Figure 4.4). The spacer slide was mounted on the top square section beam. The standard bearing was attached to the spacer slides with two on each side to grip the platform tightly on the rail. The flat track was mounted on the other side of the top square section beam, and parallel with the spacer slide. Four narrow track rollers were attached on the flat track with two on each side. The design of the four parts of the system is chosen from the Hepco Manufacture's Manual (HepcoMotion 2004), a tolerance analysis was undertaken to find out the maximum distance the system can tolerate before assembly in situ. The detail of the design is described in the Appendix I.

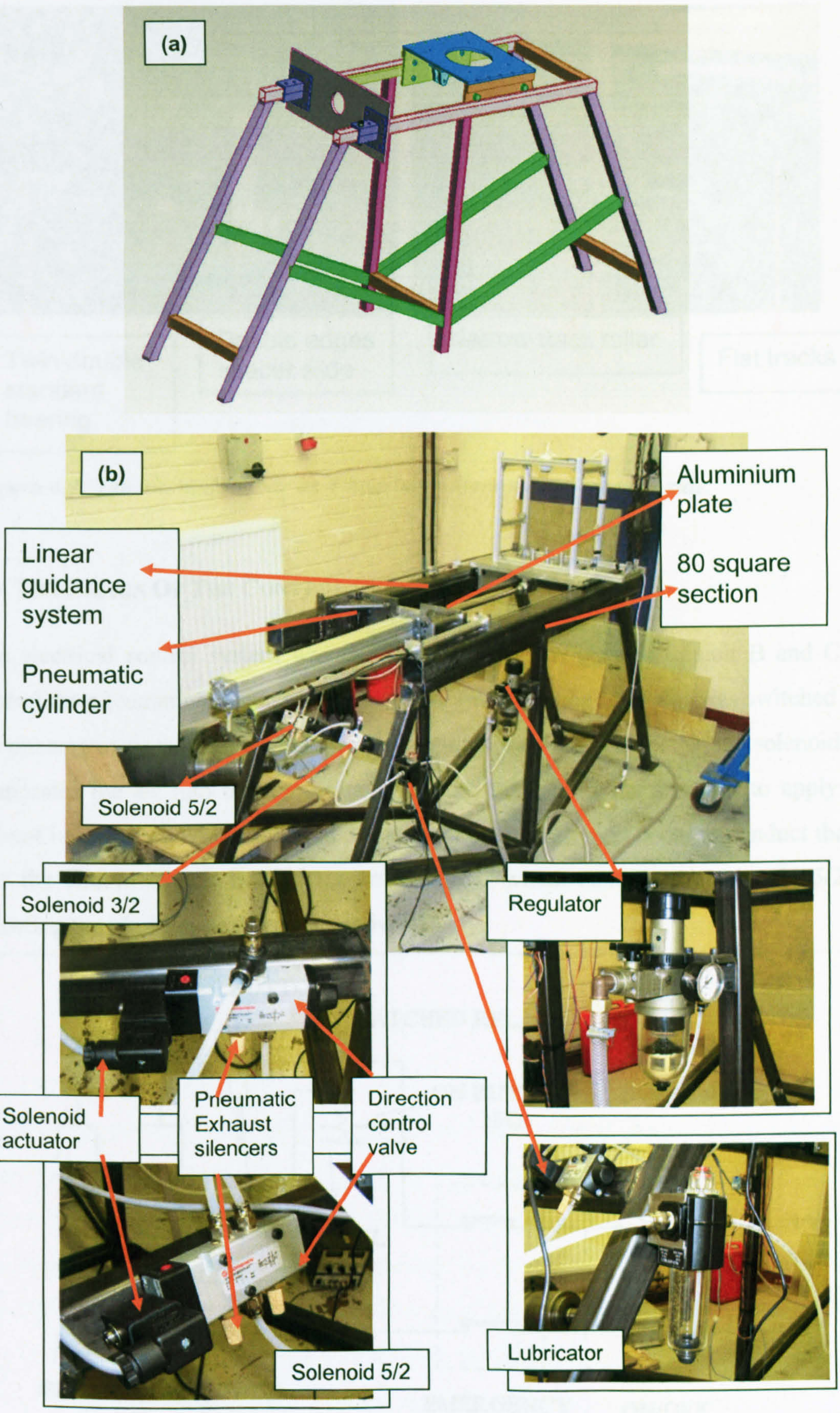

Figure 4.3. *The ProEngineer design of the frame and the frame in situ. (a) ProEngineer design, (b) the frame in situ.*

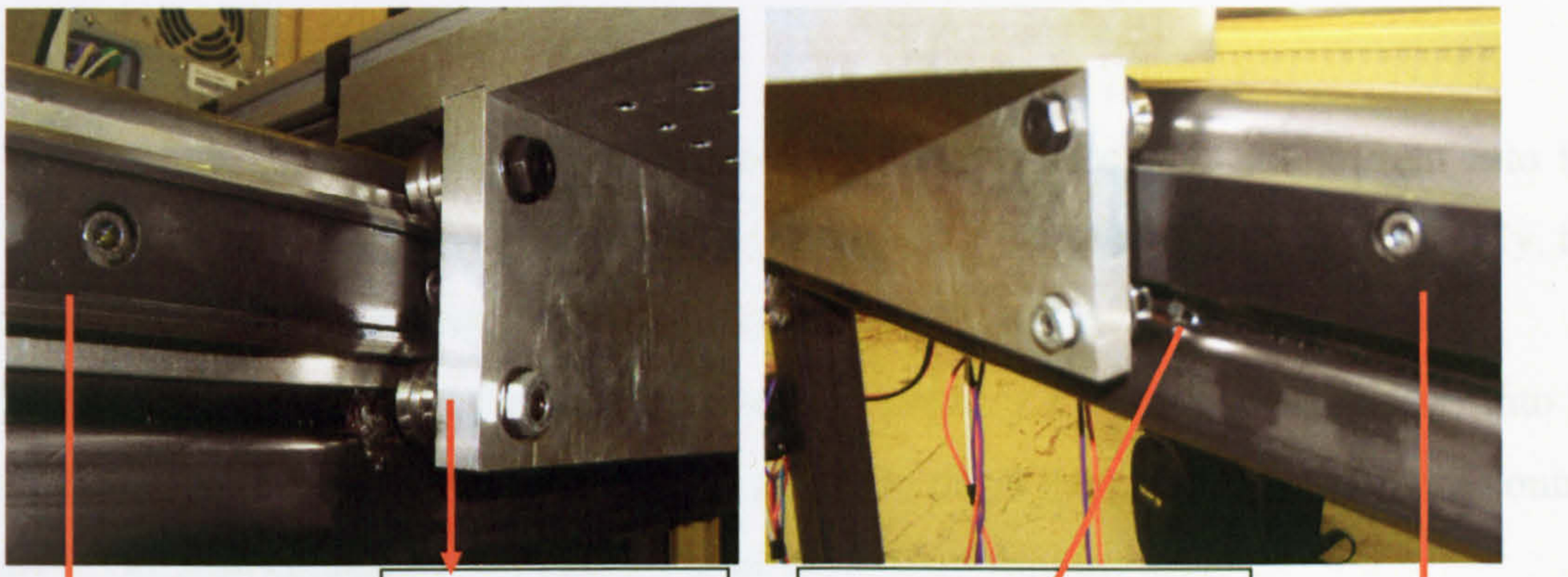

Figure 4.4. *The aluminium bar as 4 bearing/rollers mount on each side.*

4.3. The Design Of The Control Cell

The electrical control system was constructed with two circuits (circuit B and C) to control the pneumatic circuit. At the start position, when the regulator was switched and the pneumatic air was conducted into the pneumatic circuit (circuit A), the solenoid 3/2 evaporates the air into the atmosphere. Circuit B set up a main circuit to apply the current into the coil of the solenoid 3/2 to switch its position in order to conduct the air into the circuit. Circuit B also triggers circuit C which controls the solenoid 5/2 by detecting the platform position interactively.

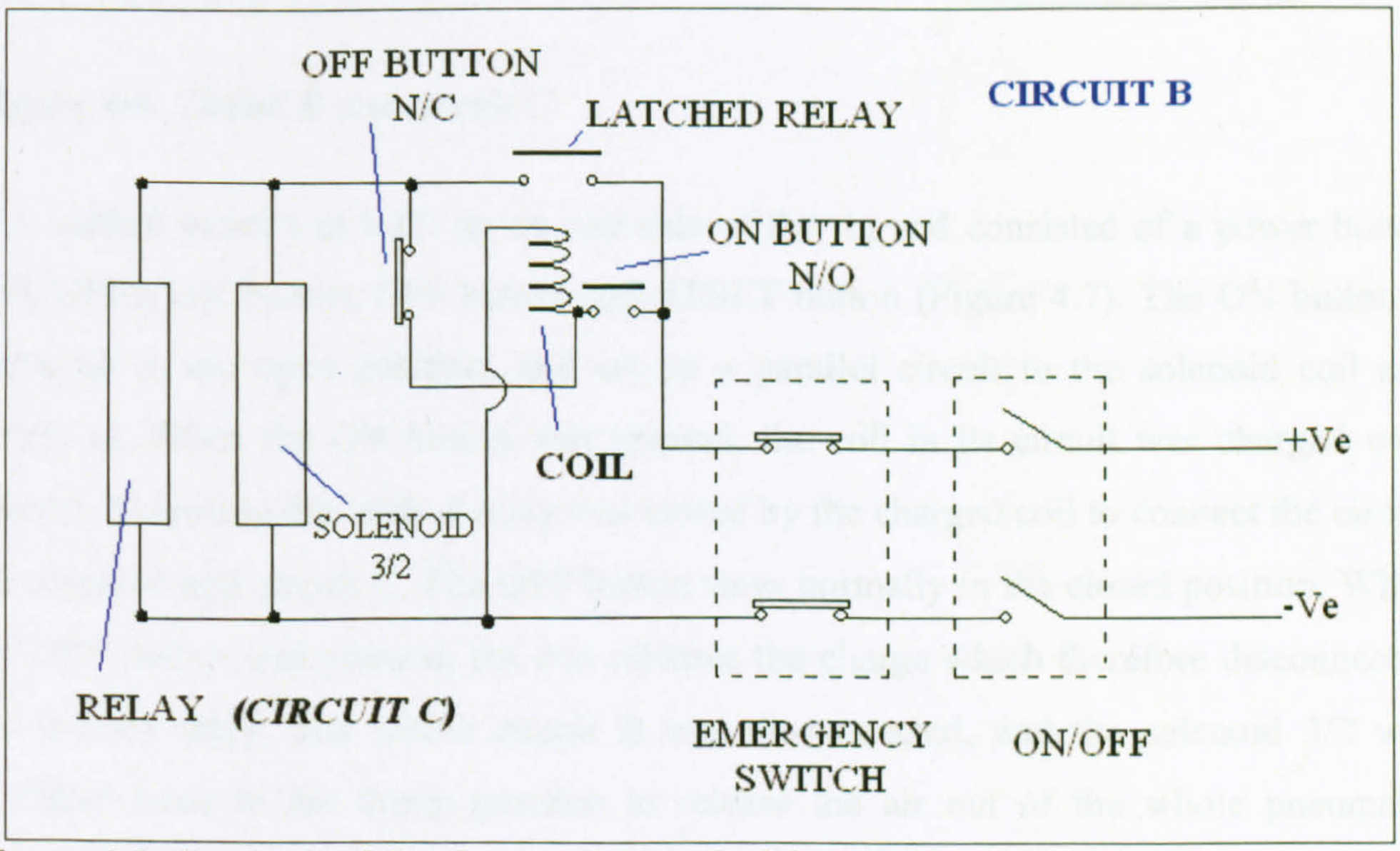

Figure 4.5. *Circuit B of the electrical control of the logical system.*

4.3.1. THE DESIGN OF THE CIRCUIT B

The circuit B set up a direct electrical control circuit to conduct the current into the whole system (Figure 4.5, Figure 4.6). It consists of a 24 voltage DC power supply, the ON/OFF bottom to connect and disconnect the circuit, and an emergency switch.

The 24 voltage DC power supply converted the industry 220 voltage AC power into 24 voltage DC power, which is the standard power to drive the pneumatic solenoid control valve. The low voltage power keeps the whole system running safely.

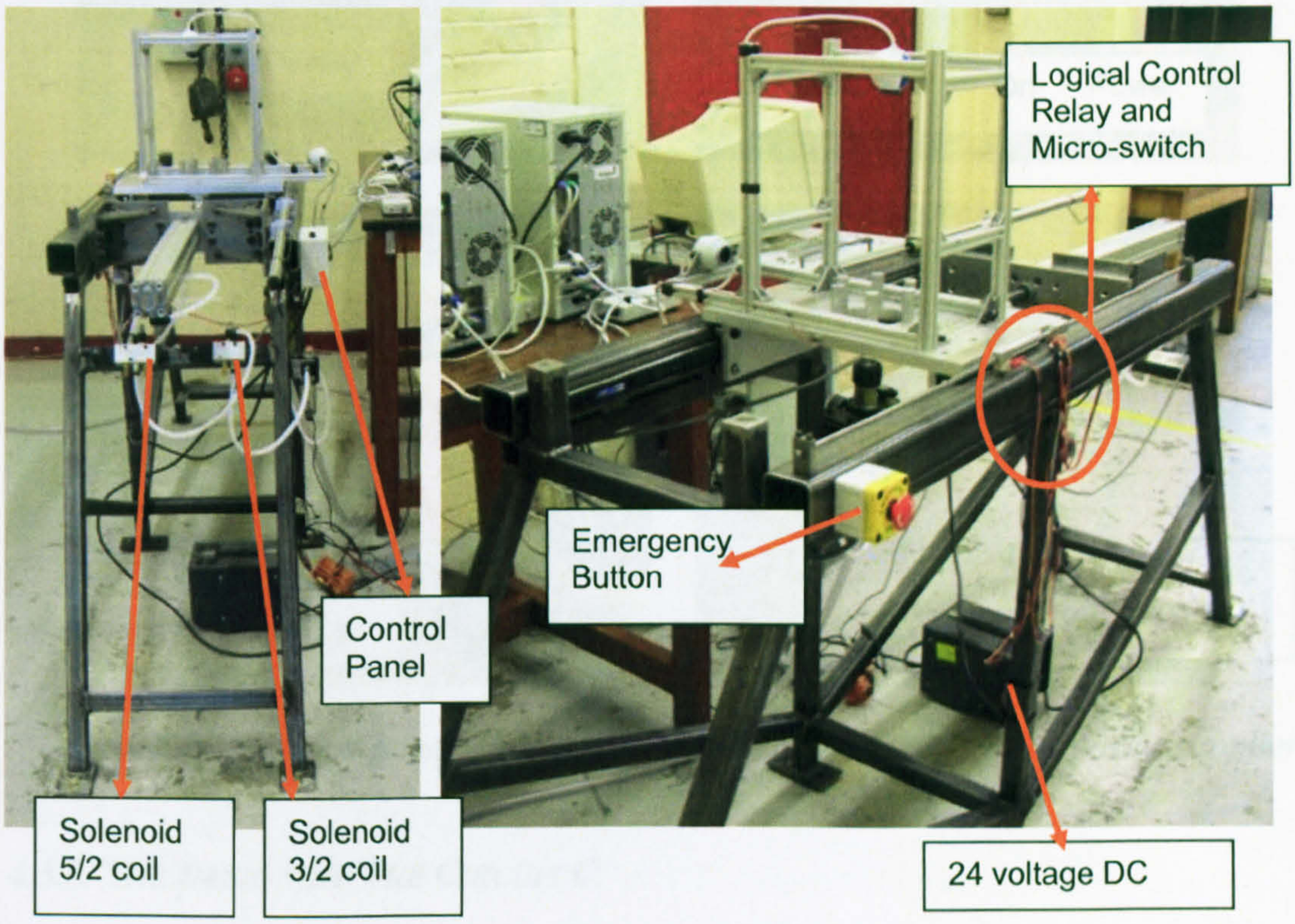

Figure 4.6. *Circuit B and circuit C*

The control panel was built up on one side of the rig and consisted of a power button (ON/OFF), ON button, OFF button and RESET button (Figure 4.7). The ON button is normally in the open position, and set up a parallel circuit to the solenoid coil and circuit C. When the ON button was pressed, the coil in its circuit was charged with current. Therefore the latched relay was closed by the charged coil to connect the circuit for solenoid and circuit C. The OFF button stays normally in the closed position. When the OFF button was pressed, the coil releases the charge which therefore disconnected the latched relay. The whole circuit B was disconnected, and the solenoid 3/2 was switched back to the dump position to release the air out of the whole pneumatic system. The emergency switch was built up on the other side of the rig in comparison to

the control panel. It is used to disconnect the whole circuit anytime if required, if the operator is not able to approach the control panel.

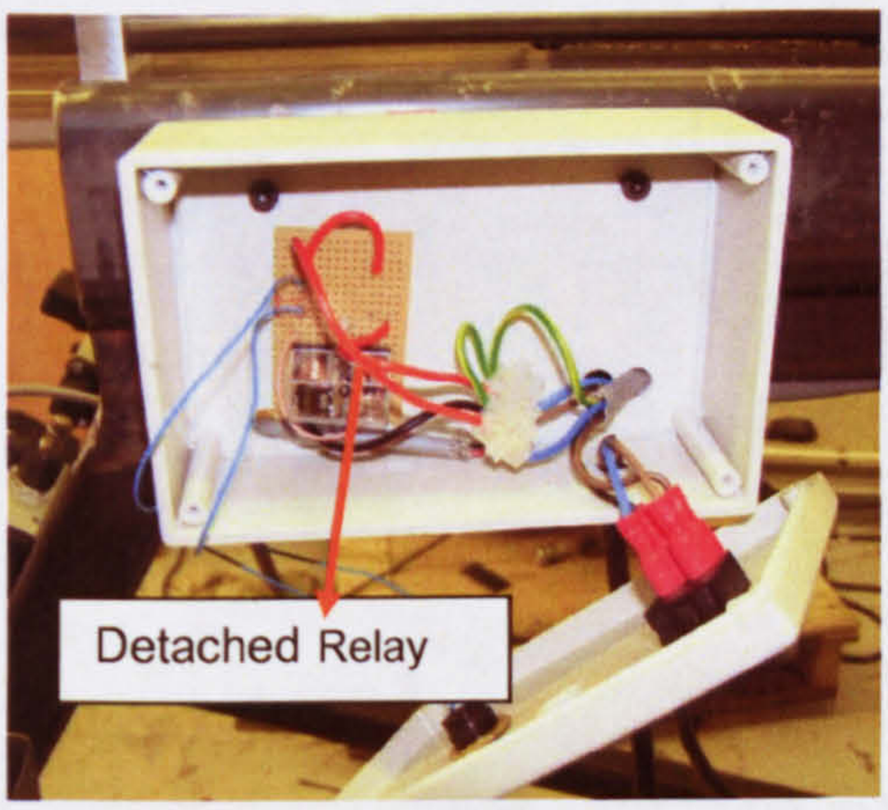

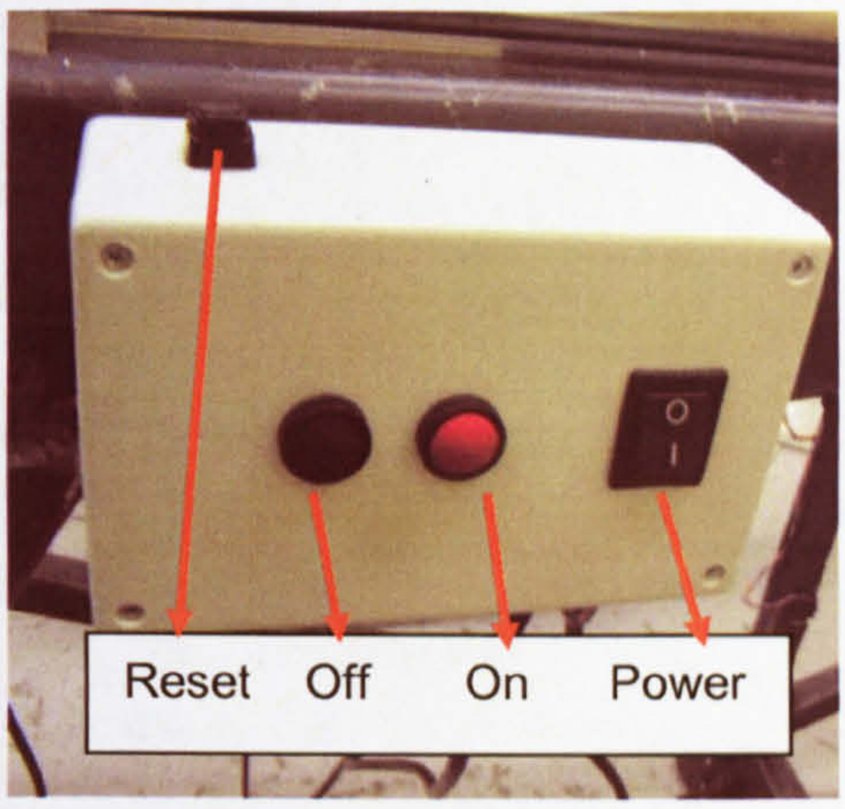

Figure 4.7. *Control panel, Emergency button, and 24 voltage DC power supplier.*

4.3.2. THE DESIGN OF THE CIRCUIT C

The circuit C gives the logical control for repetitive motion of the platform. It consists of one relay, two micro-switches, and one Nylon 66 ramp trigger mounted on the aluminium platform (Figure 4.8, Figure 4.9). The micro-switches are both set as normal open condition (N/O). The ramp trigger was mounted on the platform and triggers one of the micro-switch each time when passing through the defined position. The relay controls the 5/2 solenoid valve with the two position associated with the two micro-switches. The micro-switches are fixed on an aluminium rail mounted on one of the 80×80 square sections, hence the distance of the reversal motion can be defined by setting the two micro-switches in different positions.

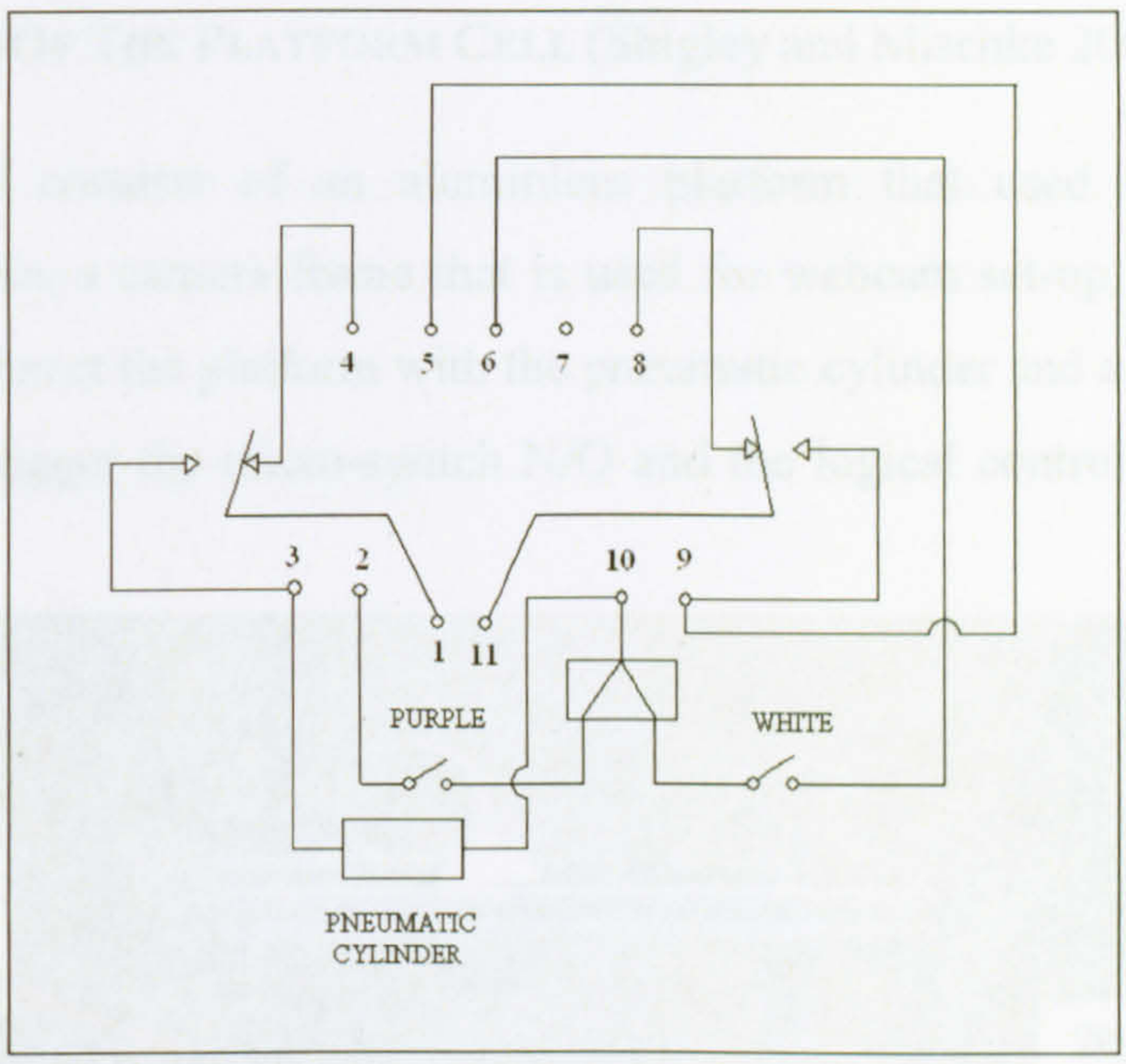

Figure 4.8. *Circuit C of ramp trigger, micro-switch controlled repetitive motion with logical circuit in Logical control Relay.*

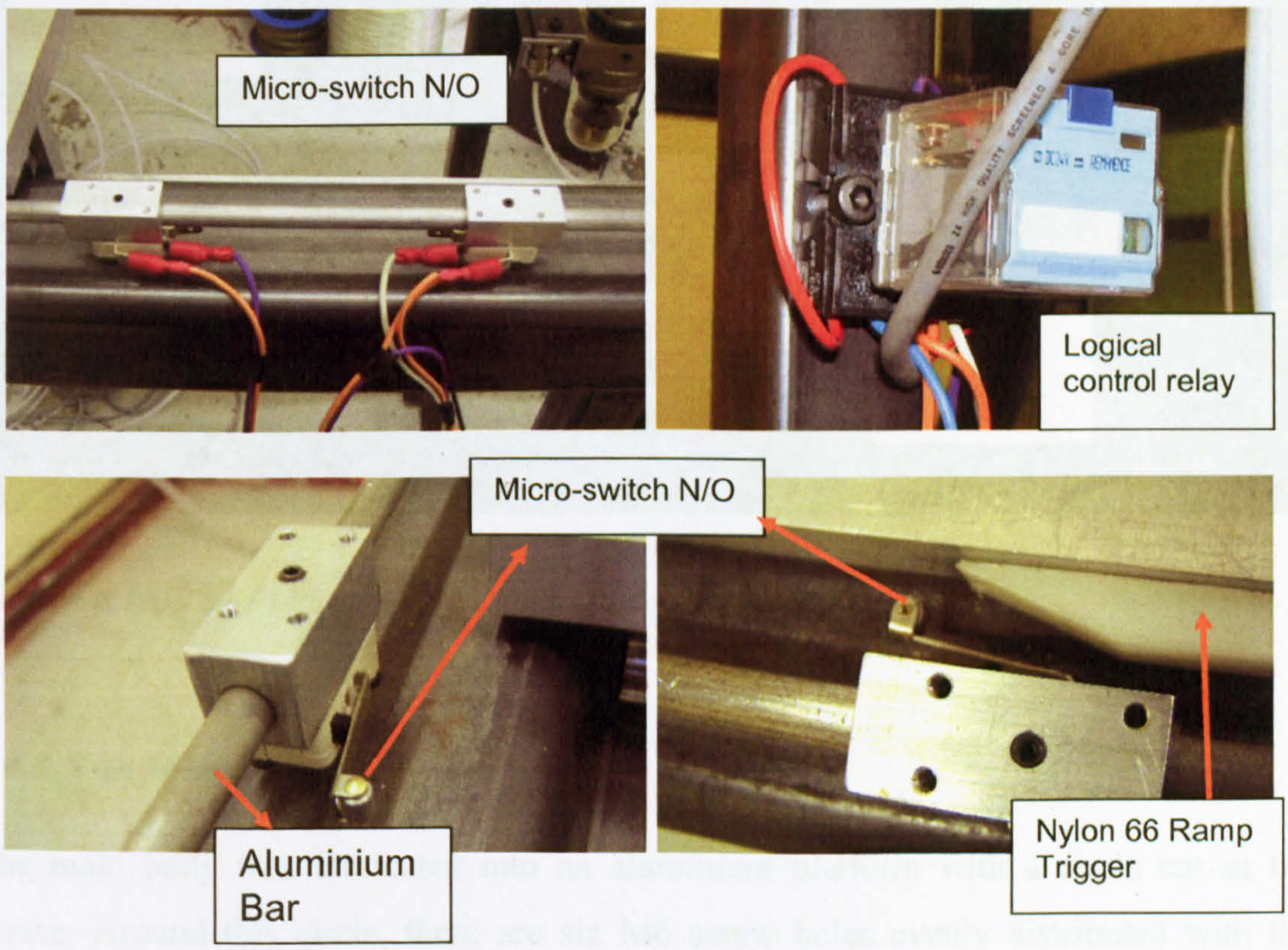

Figure 4.9. *The construction of the circuit C by Relay, two micro-switches, one Nylon 66 ramp trigger.*

4.4. THE DESIGN OF THE PLATFORM CELL (Shigley and Mischke 2001)

The motion cell consists of an aluminium platform that used for mounting the experimental mode, a camera frame that is used for webcam set-up, a connection port that is used to connect the platform with the pneumatic cylinder and a piece of Nylon 66 ramp trigger to trigger the micro-switch N/O and the logical control relay in C circuit (Figure 4.10).

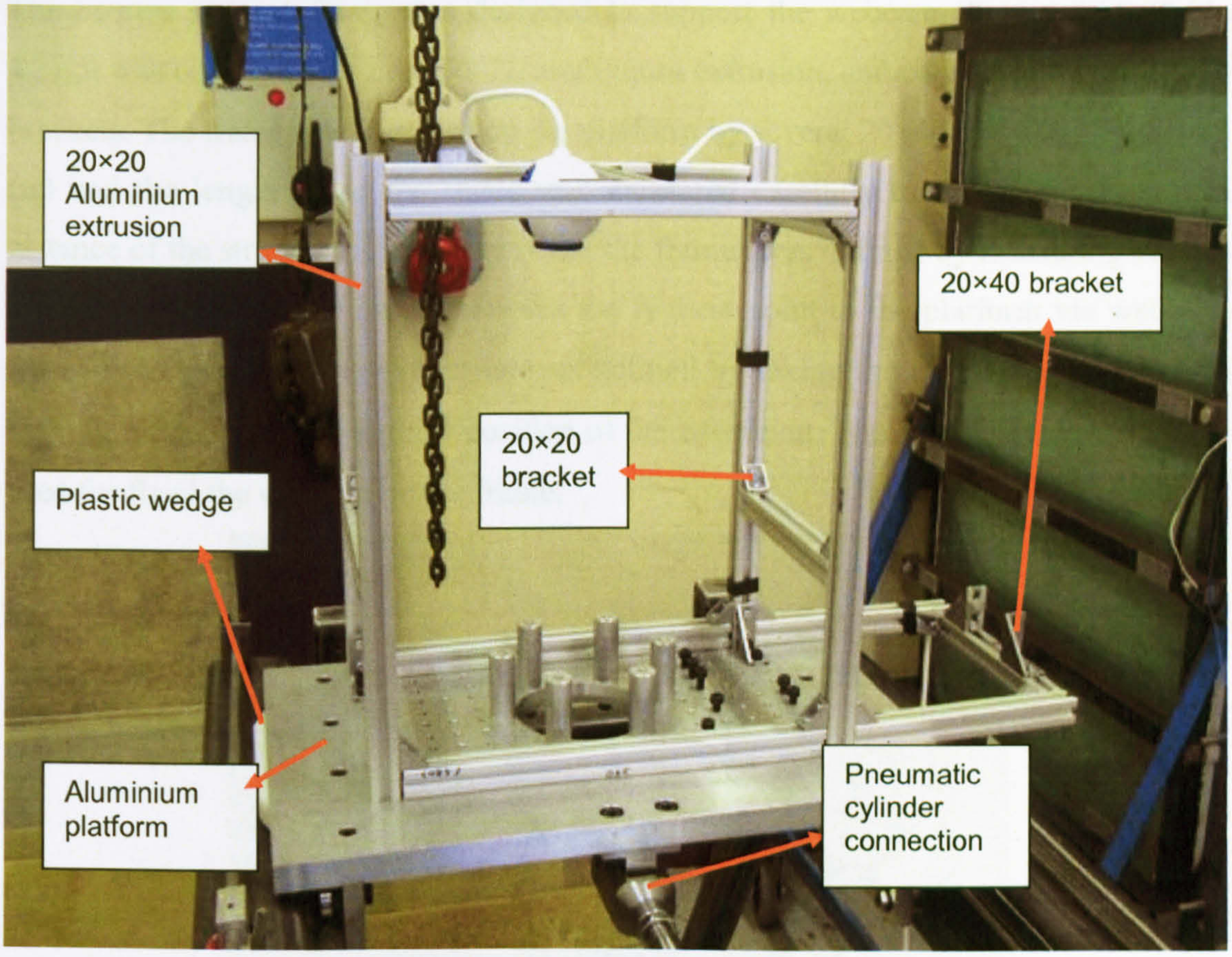

Figure 4.10. *The Platform cell as well as its components*

4.4.1. THE MAIN BODY

The main body was fabricated into an aluminium platform with a circle cut in the centre. Around this circle, there are six M6 screw holes evenly distributed with the pinch circle diameter of 120mm. On each side of the centre, there are 11×5 M6 screw holes matrix distributed with a 20mm distance in between to enable the fixing of other structures.

4.4.2. THE CONNECTION

The pneumatic cylinder connection between the platform and the pneumatic cylinder was fabricated by an aluminium bar to connect the rod with the platform.

4.4.3. THE CAMERA SUPPORT FRAME

The camera support frame was designed to support the webcam (Figure 4.11, Table 4.2). It was constructed by the 20×20 aluminium extrusion, and connected by the 20×20 brackets. The frame was mounted on the platform by several 20×40 brackets. The width (w) and the length (l) of the frame was measured carefully to obtain the maximum distance of the structure. The height (h) of the frames was defined by measuring the full top view of the 150mm model between the highest point to the platform via webcam. An extra extension (l_1) of the frame was defined by taking the full lateral view of the 150mm model from the farthest position of the extension. The 20×40 brackets are also used for fixed the webcam on the frame.

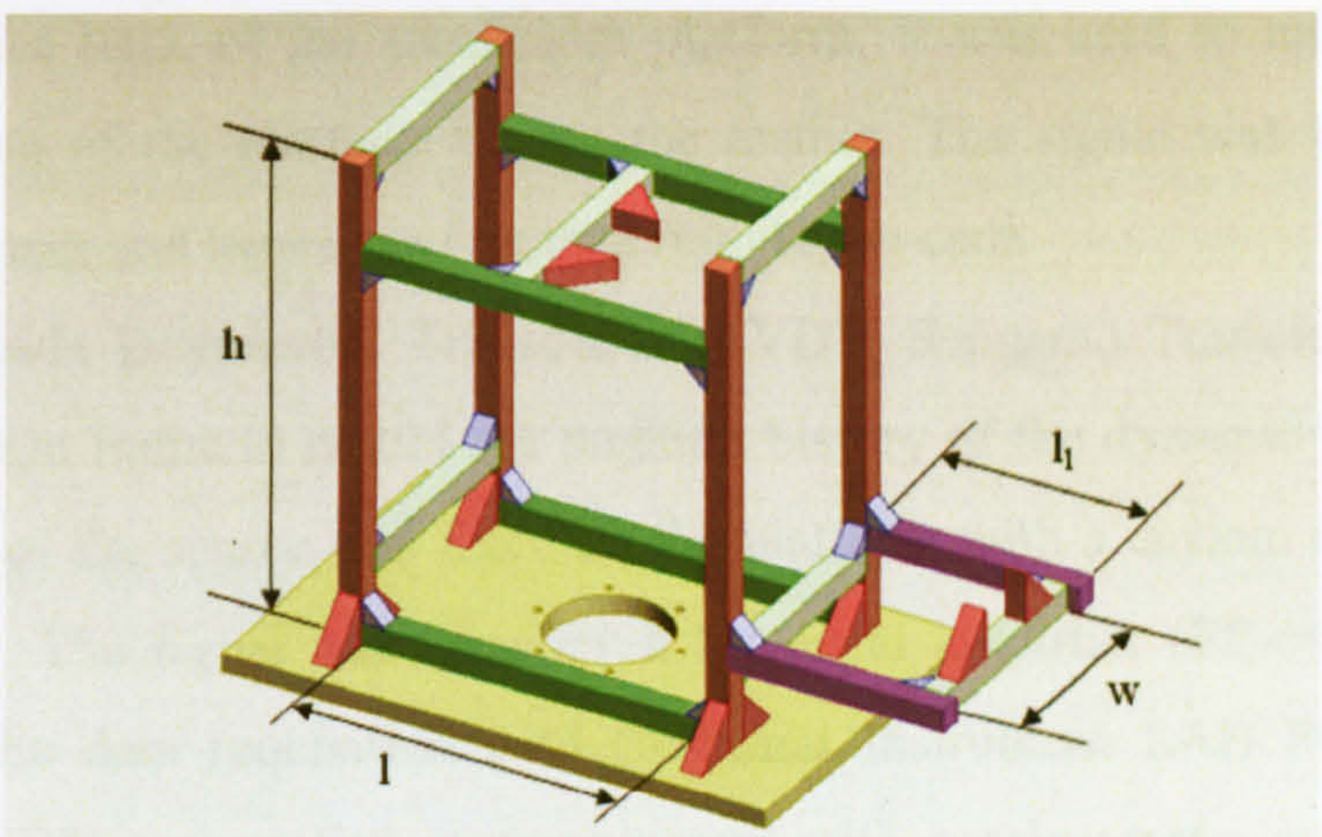

Figure 4.11. *The concept design of the camera support frame via ProEngineer.*

No.	Component	Parameter (mm)	Quantity
1	h	400	4
2	l	290	4
3	l_1	180	2
4	w	180	6
5	Bracket	20×20	22
6	Bracket	20×40	6

Table 4.2. *The component of the camera support frame*

The total weight of the frame was calculated by the multiplying the length with a scale factor from the user's manual (Bosch Rexroth AG 2005). The scale factor for the 20×20 aluminium extrusion is 0.4.

$$l_{frame} = h \times 4 + l \times 4 + l_1 \times 2 + w \times 6$$

$$= 400 \times 4 + 290 \times 4 + 180 \times 2 + 180 \times 6 = 4200 \text{ mm} \quad (4.17)$$

Where l_{frame} is the overall length of the

Therefore the weight of the frame is:

$$m_{frame} = 0.4 \times length = 0.4 \times l_{frame} = 0.4 \times 4200 \times 10^{-3} = 1.68 \text{kg} \quad (4.18)$$

4.4.4. THE TRANSDUCER

Three transducers were mounted on the motion cell to derive the positional information of the dynamic platform and relative motion within the experimental model (Figure 4.12).

A piezoelectric accelerometer (ISOTRON 4416B, Endevco Sanjuan Capistrano, LA) was fixed on the back of the aluminium platform. It was used to measure the linear dynamic loading of the platform during the testing. The signal was transferred to an Isotron conditioner and hence read by data requisition card.

A Linear Variable Differential Transducer (LVDT, Sangamo Transducer 43428) was fixed on the main frame to record the position history of the dynamic platform (Figure 4.13). The top of the sensor was fixed on the platform with a custom designed angular aluminium bar. The signal was transferred to carrier amplifier (FE-641-CA) and later was read by the data requisition card (National Instrument LAB PC+). During the testing, the LVDT was applied in combination with accelerometer and collected both the loading and the position information at the same time. The redundancy set up is designed for the further complex tests, when more than one motion information are required. The accelerometer will be able to measure the local acceleration. The accelerometer is not considered during this stage of the research.

Two webcams (QuickCam®, Logitech) were mounted on the camera support frame using 20×40 brackets, one has a view perpendicular to the horizontal plane of the model, and one has a view that parallel to the horizontal plane and perpendicular to the lateral plane of the model. The distance between the webcam and model can be adjusted by moving the aluminium extrusion where the webcams sits.

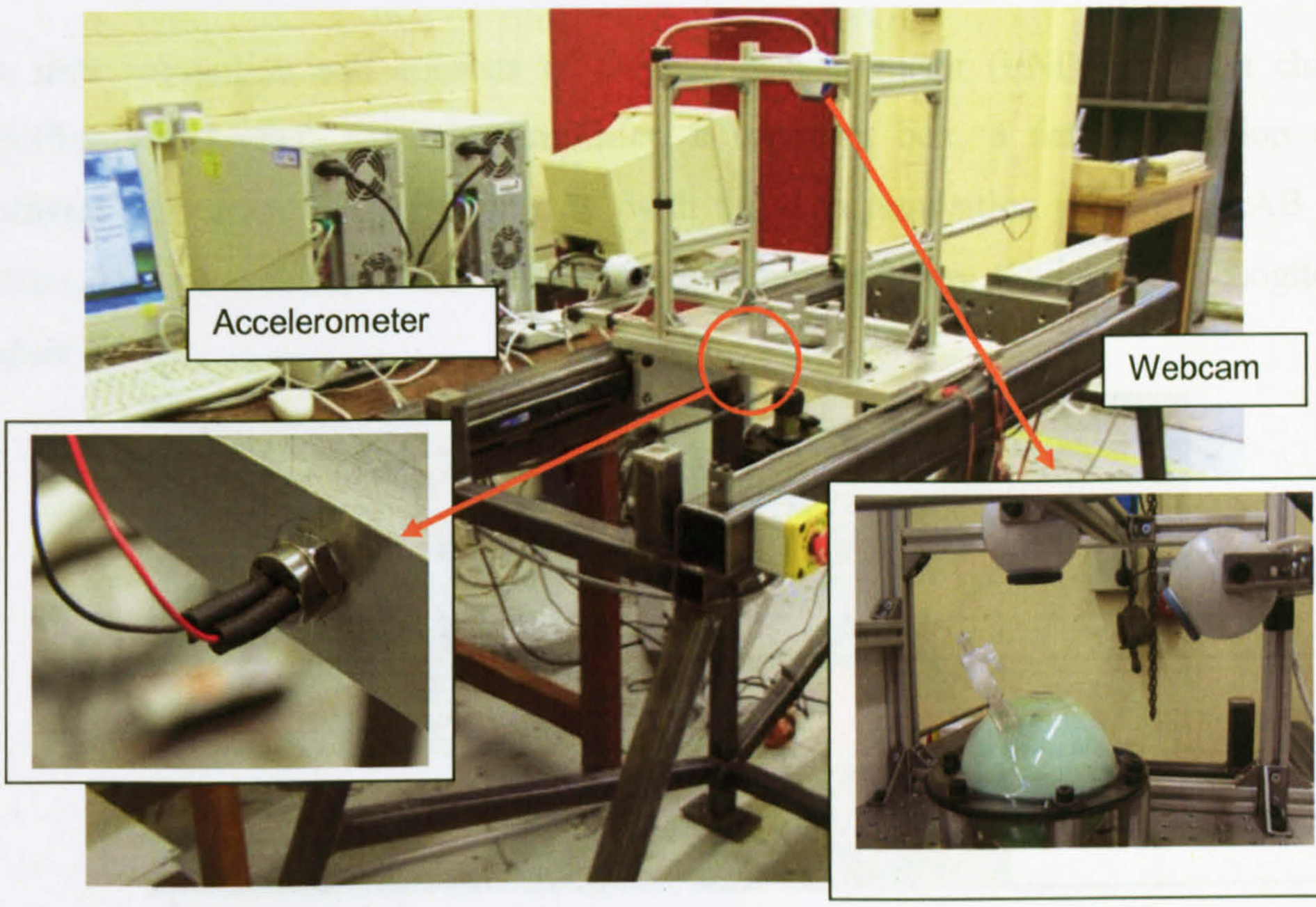

Figure 4.12. *The platform cell with accelerometer and webcam.*

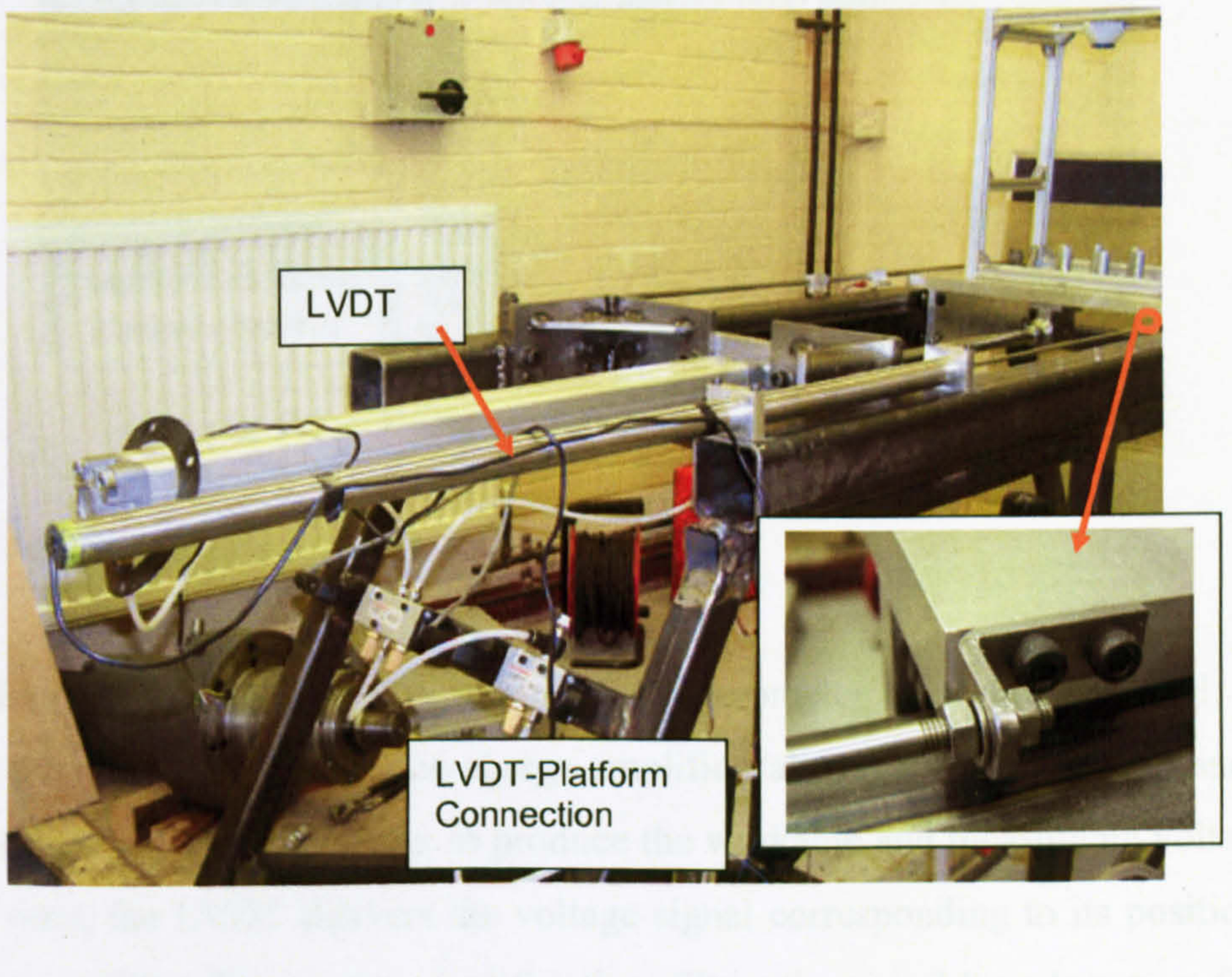

Figure 4.13. *The LVDT and its connection with platform.*

4.5. THE DESIGN OF DATA REQUISITION CELL

The data requisition cell consists of a piezo accelerometer (ENDEVCO), a charge amplifier, the LVDT, a carrier amplifier, a breakout box, a data requisition card (National Instrument LAB PC+), a PC with the data requisition software (LAB Tec Notebook), two webcams, and the video requisition software (QuickCam®, Logitech) (Figure 4.14).

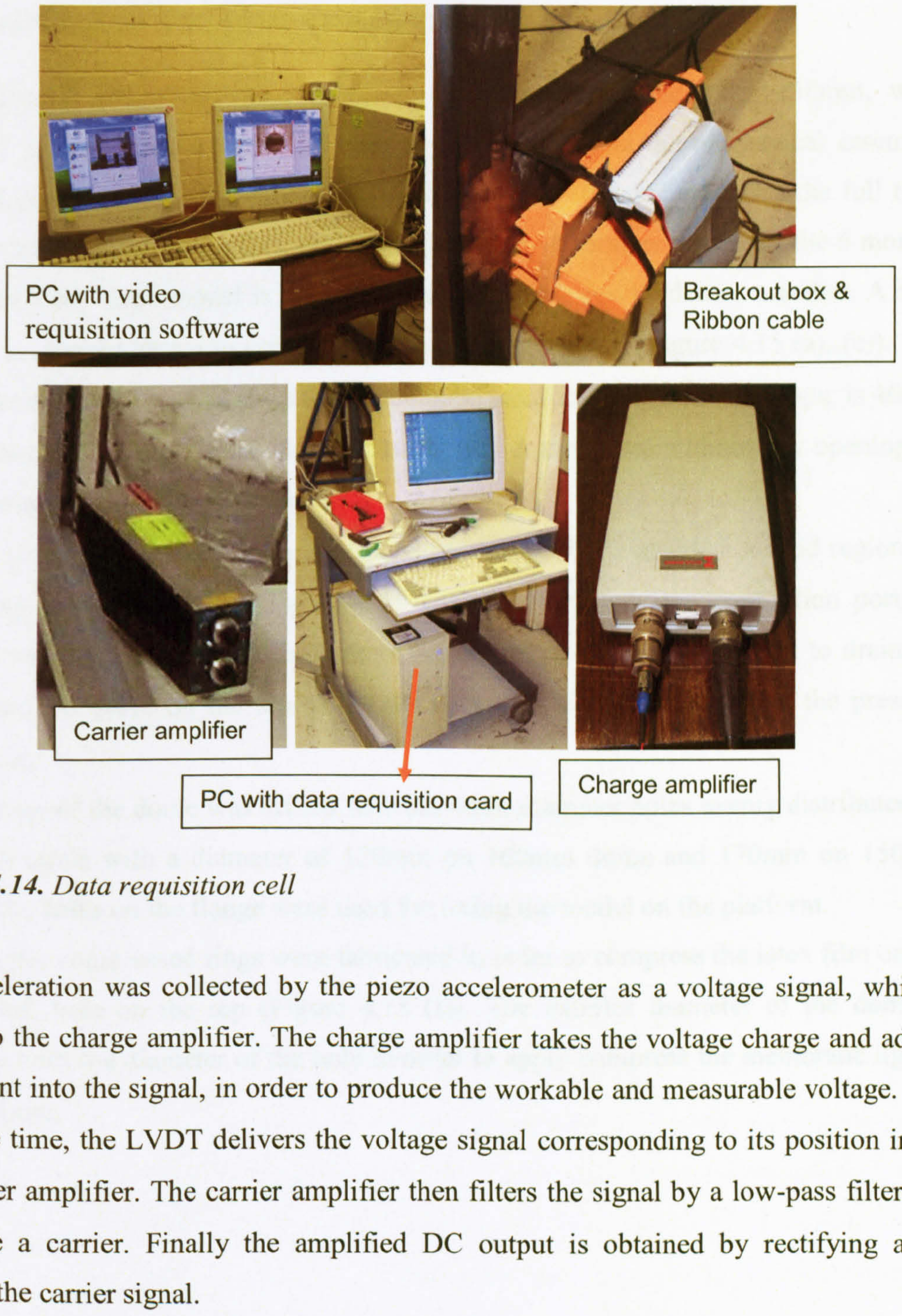

Figure 4.14. *Data requisition cell*

The acceleration was collected by the piezo accelerometer as a voltage signal, which goes into the charge amplifier. The charge amplifier takes the voltage charge and adds the current into the signal, in order to produce the workable and measurable voltage. At the same time, the LVDT delivers the voltage signal corresponding to its position into the carrier amplifier. The carrier amplifier then filters the signal by a low-pass filter to modulate a carrier. Finally the amplified DC output is obtained by rectifying and filtering the carrier signal.

Both measurable signals that come out of the charge amplifier and carrier amplifier were collected by data requisition card (National Instrument LAB PC+) via the breakout box with ribbon cable. The PC records and stores the data via LAB TEC Notebook.
The video information was captured by two webcams via the video requisition software (QuickCam®, Logitech).

4.6. The Design Of The Anthropomorphic Model

Two sizes of anthropomorphic models, one 100mm and the other 150mm, were designed with simplified biofidelic paediatric structures and the mechanical assembly structure (Figure 4.15). The model with a diameter of 100mm represents the full term newborn infant head, and the model with a diameter of 150mm represents the 6 months old infant head. Each model is made by combining two acrylic domes together. A hole was cut on the top dome to represent the anterior fontanelle (Figure 4.15 (a), (c)). The diameter of the hole, scaled from the histological structure of a diamond shape, is 40mm for 100mm model, and 36mm for 150mm model. A top dome without any opening on the top was prepared for comparison.

Several acrylic bases were made and glued on the model to establish a rigid region for setting up the medical luer (Figure 4.15 (d), (e)), which is the connection port for medical valve. The valves on the bottom were used as a drainage system to drain the water, and the valve on the top of the dome is used for a connection to the pressure transducer.

Each flange of the dome was drilled with six 6mm diameter holes evenly distributed on the pitch circle with a diameter of 120mm on 100mm dome and 170mm on 150mm dome. The holes on the flange were used for fixing the model on the platform.

Two acrylic compressed rings were fabricated in order to compress the latex film on the dome with hole on the top (Figure 4.15 (f)). The exterior diameter of the dome is identical with the diameter of the hole in order to apply compress the membrane tightly on the dome.

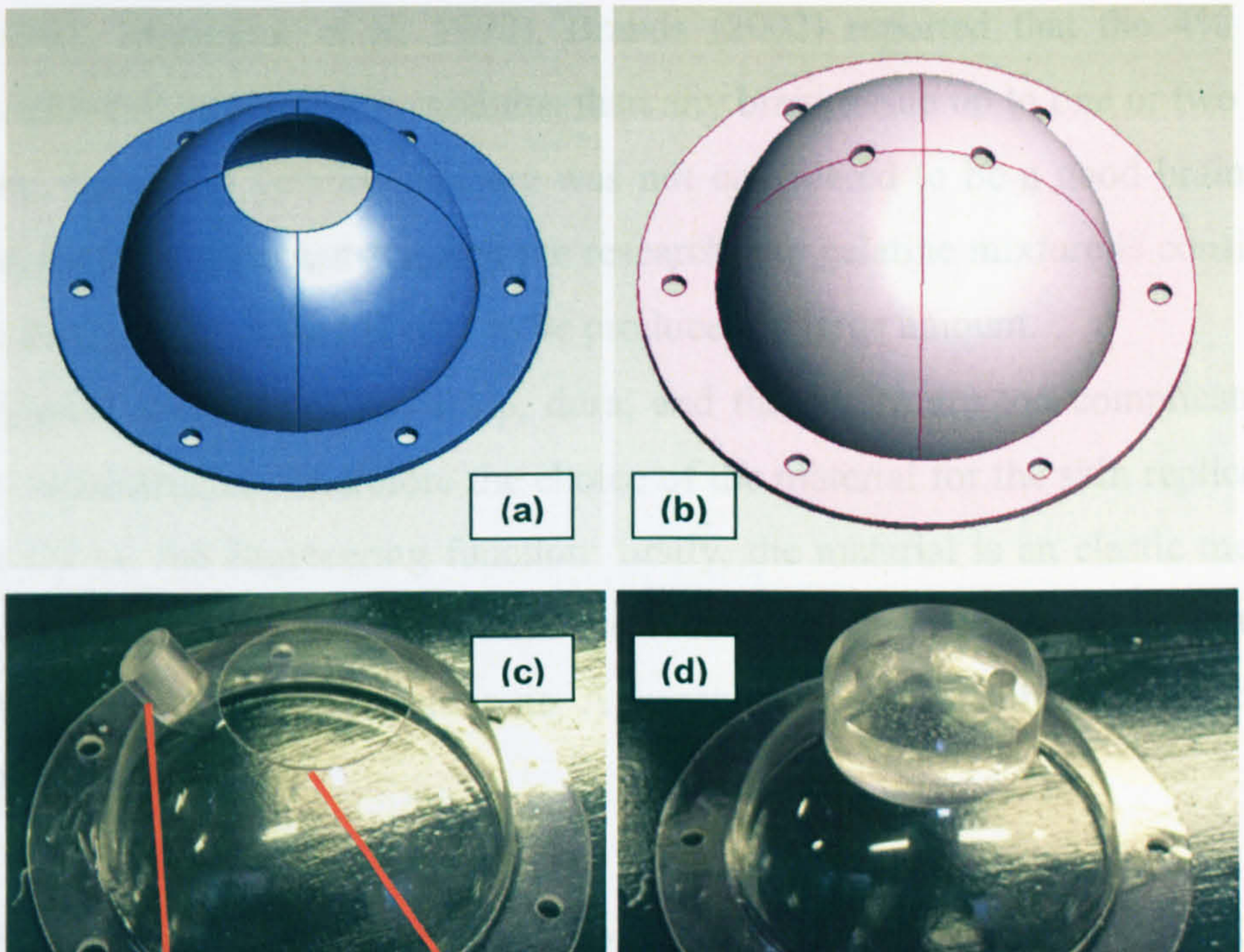

Figure 4.15. *The design and the fabrication of the model. (a),(b) The concept design by ProEngineer of Top and Bottom dome; (c),(d) The fabrication of the Top and Bottom dome; (e),(f) acrylic base and compression ring.*

4.6.1. The Choosing Of The Soft Structure

The candidate materials, which represent the brain and the skin, are tested to obtain the material properties for the computational model. In the earlier biofidelic modelling, both the silicone gel (Dow Corning Sylgard® 527 A&B) (Dow Corning Corporation 2008) and the gelatine mixture were used to simulate the brain tissue. The silicone gel (Dow Corning Sylgard® 527 A&B) which has viscoelastic properties in the low frequency, is considered to be a proper model for brain tissue in the literature (Bradshaw et al. 2001,

Brands 2002, Margulies et al. 1990). Brands (2002) reported that the 4% gelatine mixture exhibited larger elastic modulus than any brain tissue up to one or two order of magnitude, hence the gelatine mixture was not considered to be a good brain replica. However, during the current stage of the research, the gelatine mixture is considered to be a cost saving product and is easy to be produced in large amount.

The biological structure of the scalp, dura, and the suture are too complicated to be precisely reconstructed. Therefore the choice of the material for the skin replica mainly concentrated on the engineering function: firstly, the material is an elastic membrane; secondly, the material is transparent that the camera is able to detect the internal motion inside the dome through the membrane. A transparent latex membrane was chosen for the material testing.

4.6.2. THE MATERIAL PROPERTY TEST (Dally and Riley 1991; Fung 1993; Gere and Timoshenko 1997)

The material test was carried out on the VISCOANALYZER VA2000 in University of Sheffield (Figure 4.16). VA2000 is a material testing machine that can provide harmonic/dynamic test, relaxation test, creep/retardation test on various materials including the elastic viscoelastic solid and the viscous fluid. Dynamic test was chosen for the current material testing (Appendix F).

The VISCOANALYZER is used to apply a displacement $d(\omega)$ at the upper end of a sample and measures the force $F(\omega)$ transmitted to the fixed lower end (or conversely, to measure the displacement required at a constant force). $F(\omega)$, $d(\omega)$, δ, and f are values which can be obtained using sensors. Both the gelatine and the latex are going to be tested with tension-compression dynamic loading.

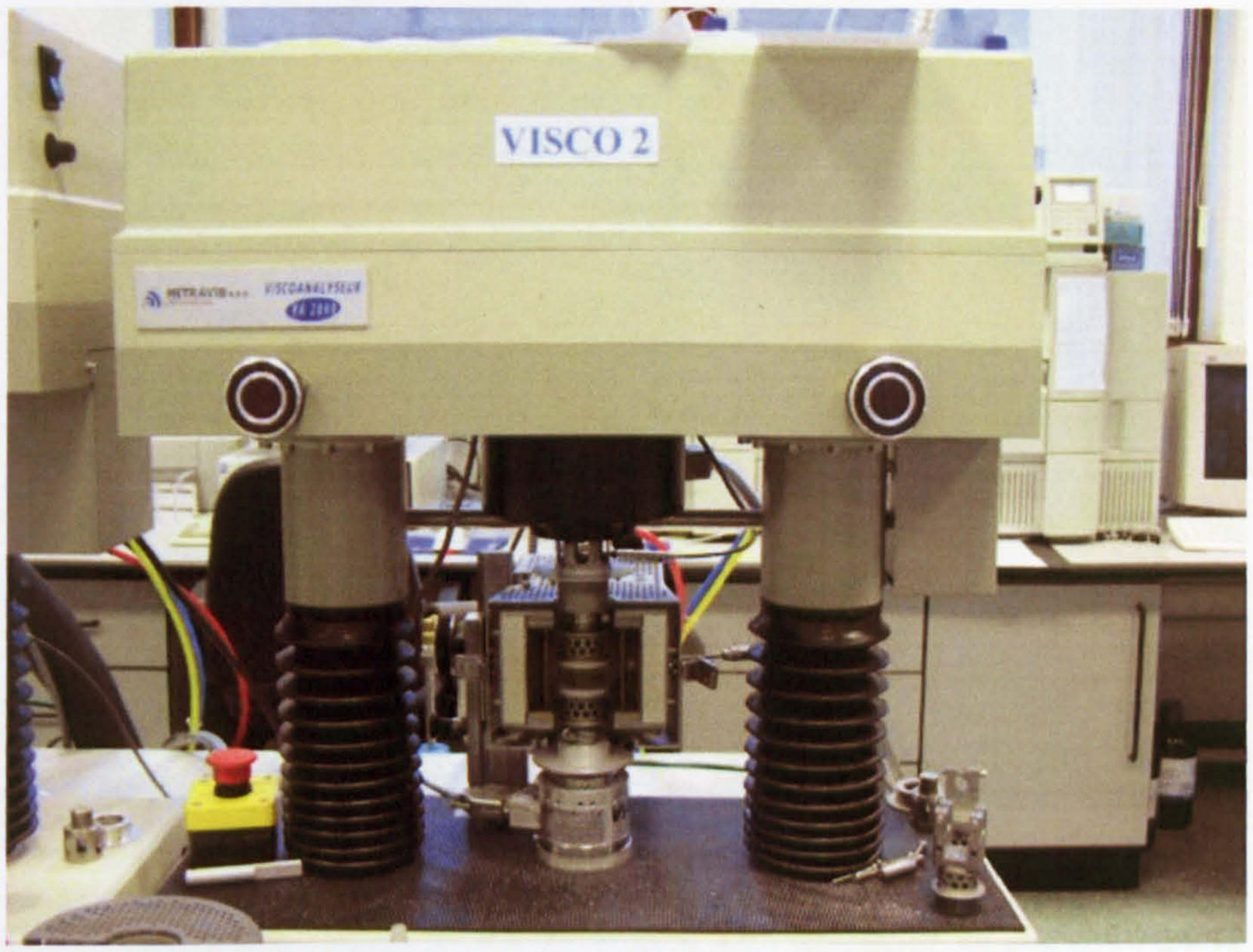

Figure 4.16. *The platform and sample of VISCOANALYZER 2000.*

Four gelatine mixture samples of 20%, 10%, 4% and 1% were solidified into the syringes and cut into cylindrical pieces with the same diameter of 11.8mm, and the length is different in the various tests (Figure 4.17). The sample was mounted on the parallel plate sample holders (Figure 4.18). The top surface of the cylinder sample was glued onto the top plate of the sample holder by super glue (cyanoacrylate), while the bottom plate of the holder was covered with glue. The top plate then moved downwards until bottom of the sample stick on the bottom plate tightly. The glue cured after 20 minutes, and then the top plate moved upwards to eliminate any pre-compressed pressure inside the sample.

Figure 4.17. *The sample of gel in the syringes. The diameter of the syringe is 11.8mm, the sample was cut directly from the tube to make the diameter identical. From bottom to top: 20%, 10%, 4%, 1%.*

A dynamic loading with strain span between 0 and 0.01 was applied to the 20% gelatine, with the frequency of 1Hz, 2.5Hz, 5Hz, 10Hz, and 20Hz. A dynamic loading with strain span between 0 and 0.05 was applied to the 10% gelatine, with the frequency of 1Hz, 2.5Hz, and 5Hz.

The sample of the transparent latex was cut and clamped by the film clamp sample holders (Figure 4.19). The width of the sample is 15.9mm with the length variable in different tests. The top clamp always moves upward for a certain distances to apply some pre-tensile force to avoid sample buckling during the sinusoidal displacement. The height of the sample is the distance between two clamps after the pre-displacement. A dynamic loading was given with the strain span between 0 and 0.05 with the frequency of 1Hz, 2.5Hz, and 5Hz separately.

The temperature during the test was kept at 21 °C all the time.

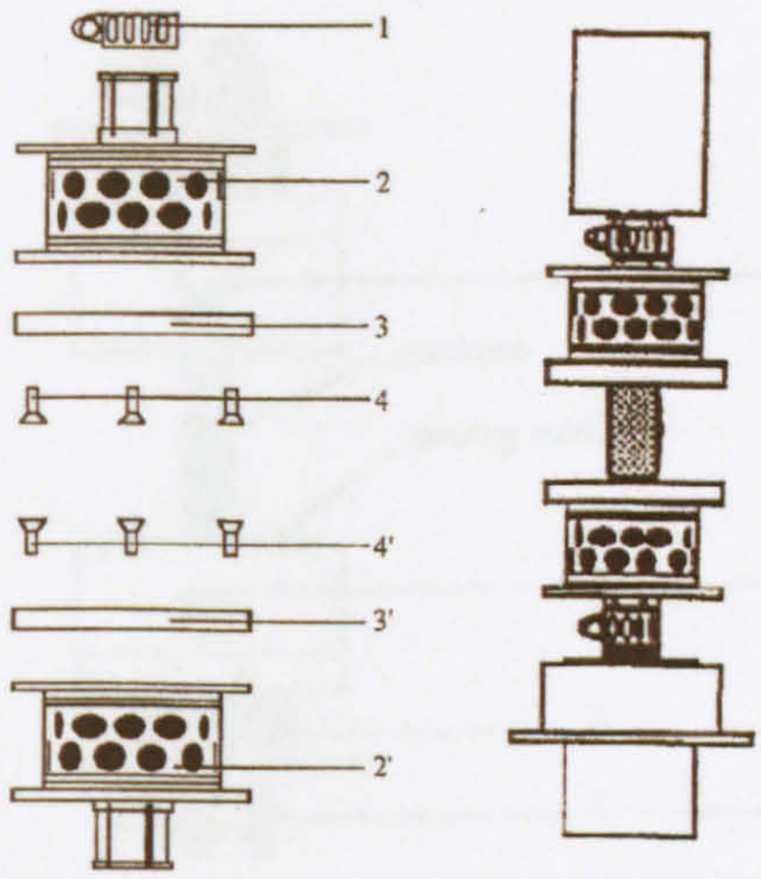

1. Stainless steel ring used to attach the head on the measurement column mechanically.
2. Thermal barrier.
3. Consumable plate treated to adherence and equipped with concentric circles for centring the specimen.
4. Screw attaching plate onto thermal barrier.

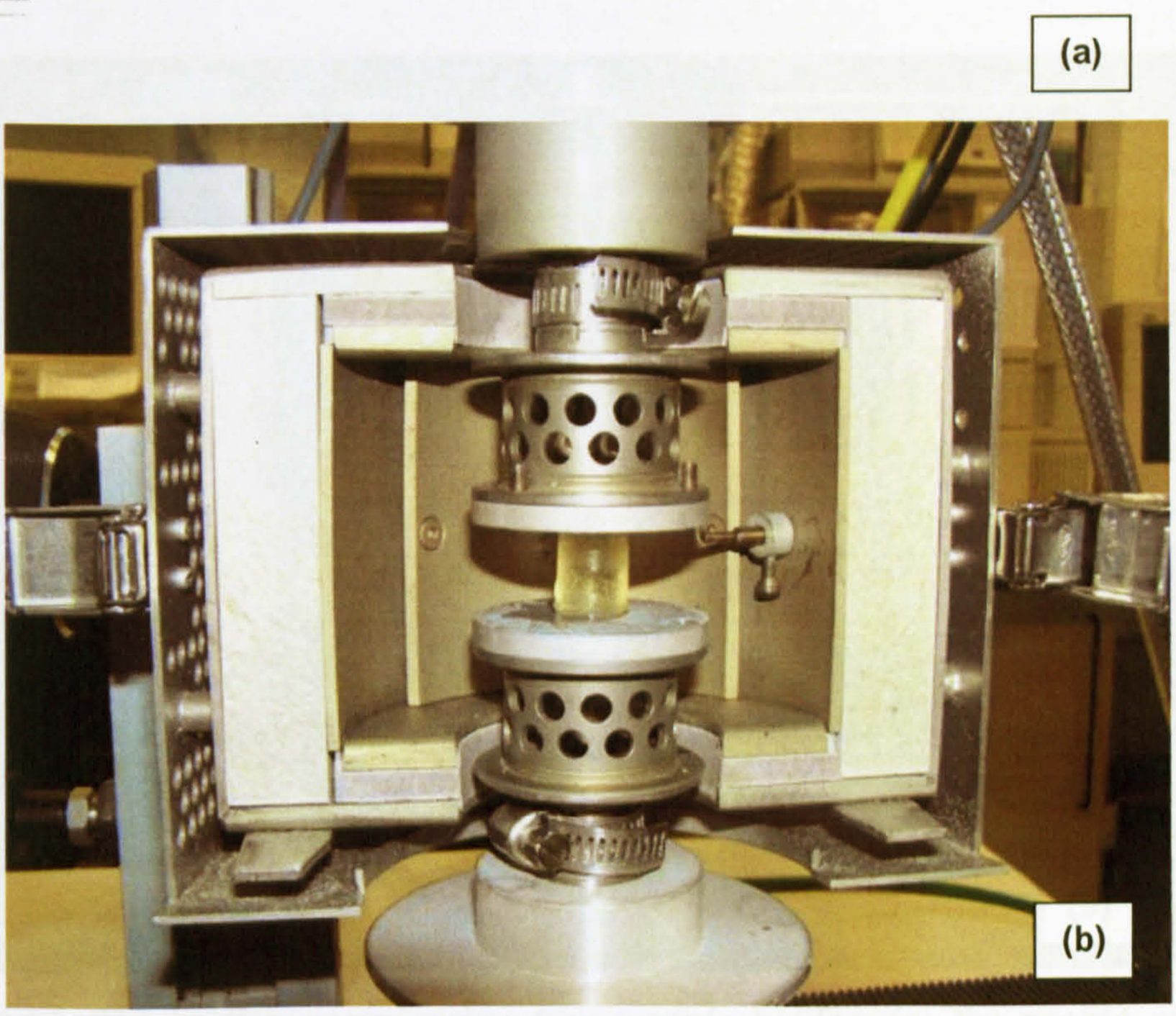

Figure 4.18. *The tension-compression solid sample holder. (a) the profile of parallel plate for solid cylindrical sample; (b) the solid cylindrical sample in situ.*

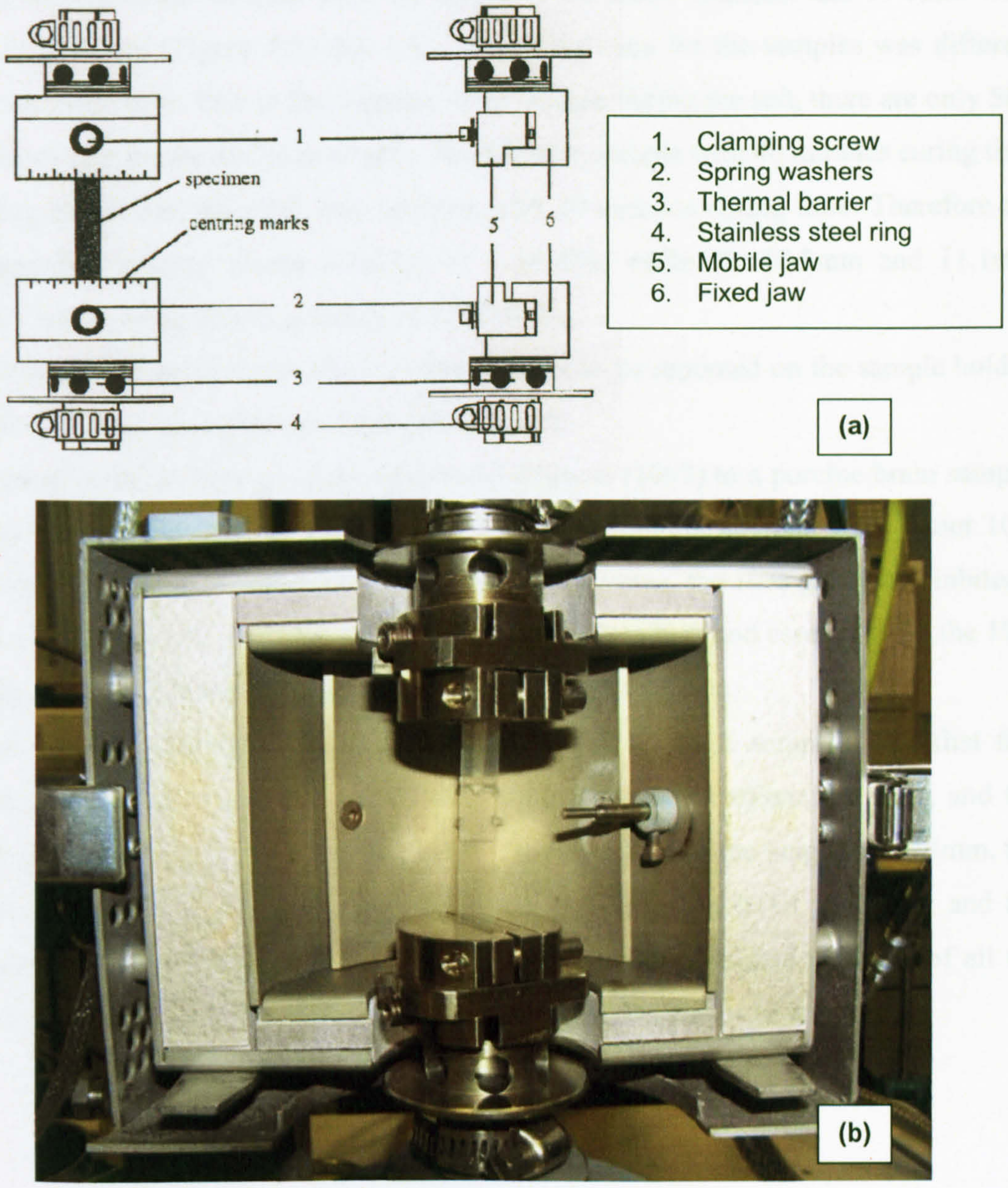

Figure 4.19. *The tension-compression film sample holder. (a) the profile of the film clamp for parallelepipeds film sample; (b) the latex film sample in situ.*

4.6.3. RESULT

The strain-stress curve from the dynamic test of gelatine 20% and 10% are plotted in Figure 4.20.

The 20% gelatine sample with the height of 14.6mm had average elastic modulus of 2.0MPa in the strain ranges between 0.001 and 0.01, and the frequency span between 1Hz and 5 Hz does not influence its elasticity (Figure 4.20 (a), (c)).

Three 10% gelatine samples with the height of 18.3mm, 10.2mm, and 11.1mm were tested separately (Figure 4.20 (b), (c)). The curing time for the samples was different between each other. Due to the fracture of the sample during the test, there are only 5Hz frequency test for the 10.2mm sample. The 18.3mm sample with 40 minutes curing time became stiffer than the other two samples with 20 minutes curing time. Therefore the 18.3mm had average elastic modulus of 1.34MPa, while the 10.2mm and 11.1mm sample had average elastic modulus of 0.0272MPa.

The 4% and 1% gelatine sample are very difficult to be mounted on the sample holder, therefore no test were given on these two samples.

Compared with the tests given by Miller and Chinzei (1997) to a porcine brain sample, the elastic modulus of 2.5×10^{-3}MPa reported in their literature is one tenth to our 10% gelatine with the elastic modulus of 0.0272MPa. However, the 10% gelatine exhibited a good visibility inside the water, and is convenient to produce and assembly. So the 10% gelatine was used during this research to mimic the brain tissue.

Figure 4.21 demonstrated the stress-strain curves of six latex samples. The first five samples were tested with various heights under the same frequency of 5Hz, and the strain span is between 0.001 and 0.01. The sixth sample with the height of 26.4mm, the width of 15.0mm, was tested under the strain span between 0.001 and 0.05, and the frequency of 1Hz, 2.5Hz, and 5Hz separately. The average elastic modulus of all the tests is 0.424MPa, which is independent to the length, frequency or strain.

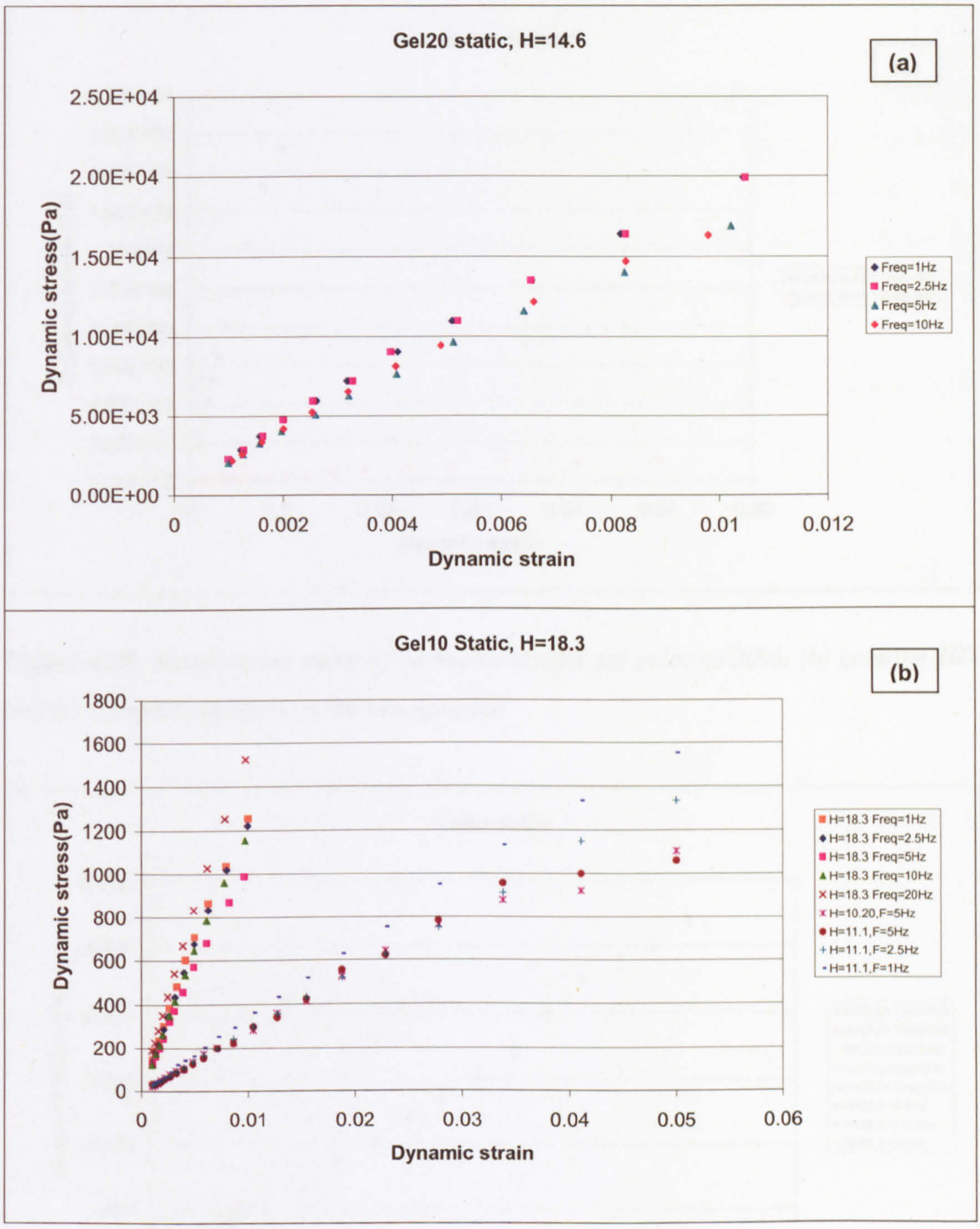
Gel20 static, H=14.6
(a)
2.50E+04
2.00E+04
1.50E+04
1.00E+04
5.00E+03
0.00E+00
Dynamic stress(Pa)
0
0.002
0.004
0.006
0.008
0.01
0.012
Dynamic strain
Freq=1Hz
Freq=2.5Hz
Freq=5Hz
Freq=10Hz
Gel10 Static, H=18.3
(b)
1800
1600
1400
1200
1000
800
600
400
200
0
Dynamic stress(Pa)
0
0.01
0.02
0.03
0.04
0.05
0.06
Dynamic strain
H=18.3 Freq=1Hz
H=18.3 Freq=2.5Hz
H=18.3 Freq=5Hz
H=18.3 Freq=10Hz
H=18.3 Freq=20Hz
H=10.20,F=5Hz
H=11.1,F=5Hz
H=11.1,F=2.5Hz
H=11.1,F=1Hz

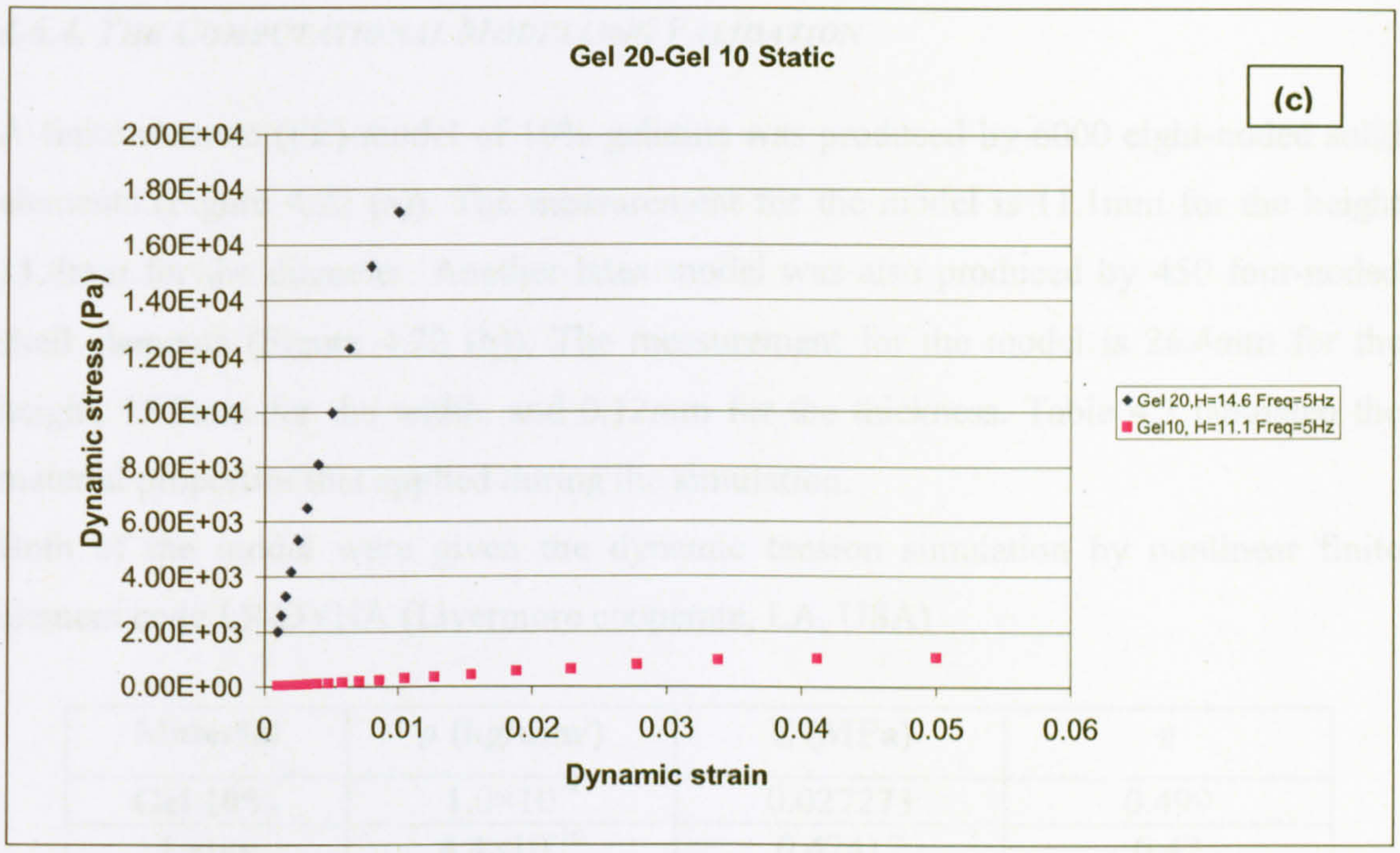

Figure 4.20. *Strain-stress curve of harmonic test for (a) gelatine 20%; (b) gelatine 10% and (c) comparison between the two samples.*

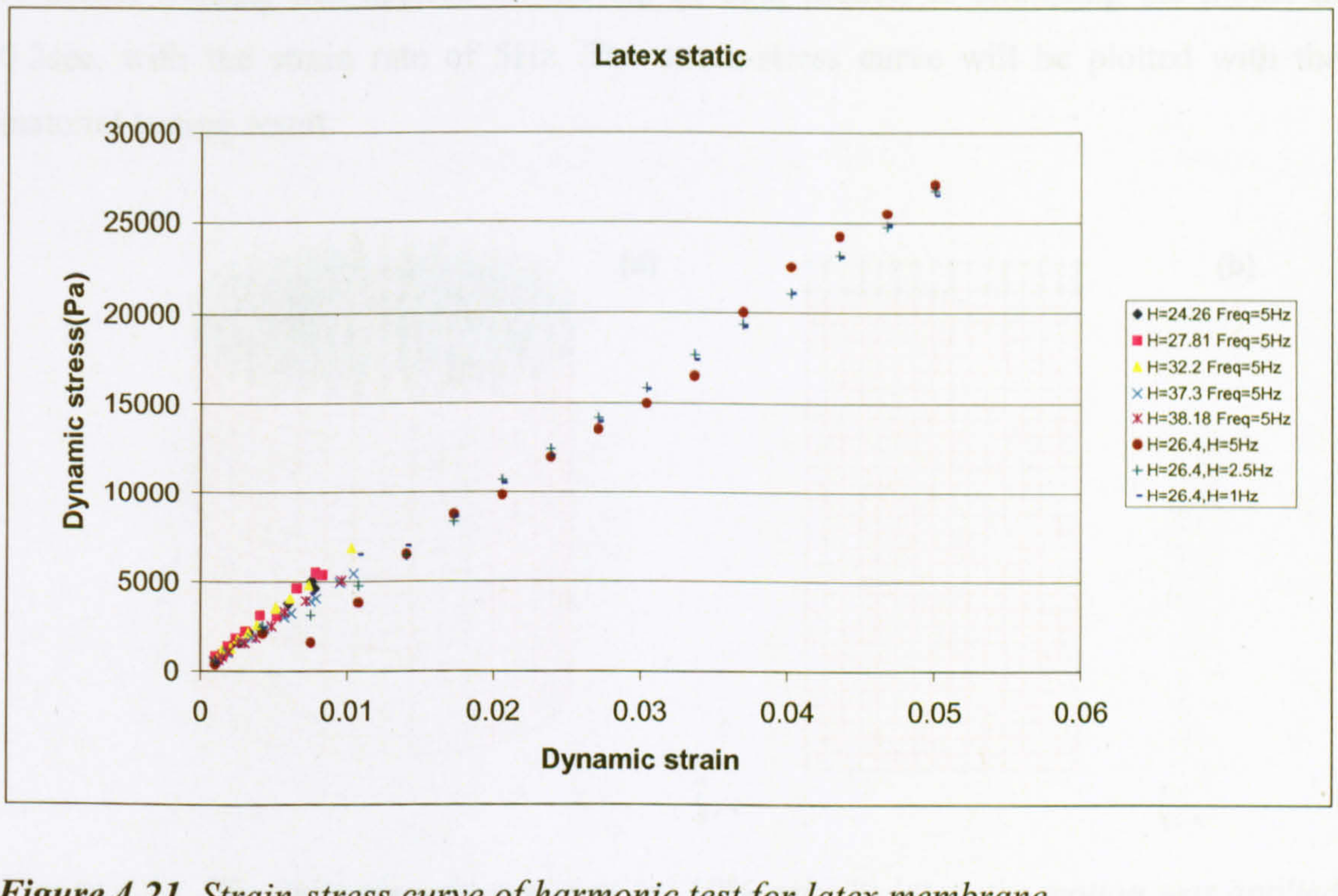

Figure 4.21. *Strain-stress curve of harmonic test for latex membrane.*

4.6.4. THE COMPUTATIONAL MODELLING VALIDATION

A finite element (FE) model of 10% gelatine was produced by 6000 eight-noded solid elements (Figure 4.22 (a)). The measurement for the model is 11.1mm for the height 11.8mm for the diameter. Another latex model was also produced by 450 four-noded shell elements (Figure 4.22 (b)). The measurement for the model is 26.4mm for the height, 15.9mm for the width, and 0.12mm for the thickness. Table 4.3 tabulated the material properties that applied during the simulation.

Both of the model were given the dynamic tension simulation by nonlinear finite element code LS-DYNA (Livermore cooperate, LA, USA)

Material	**ρ (kg/mm^3)**	**E (MPa)**	**v**
Gel 10%	1.0×10^{-9}	0.027273	0.499
Latex	4.4×10^{-10}	0.42417	0.42

Table 4.3. *Material properties of the testing output and DYNA input.*

A tensile loading was applied on the top of both models to stretching the model in 0.2sec, with the strain rate of 5Hz. The strain-stress curve will be plotted with the material testing result.

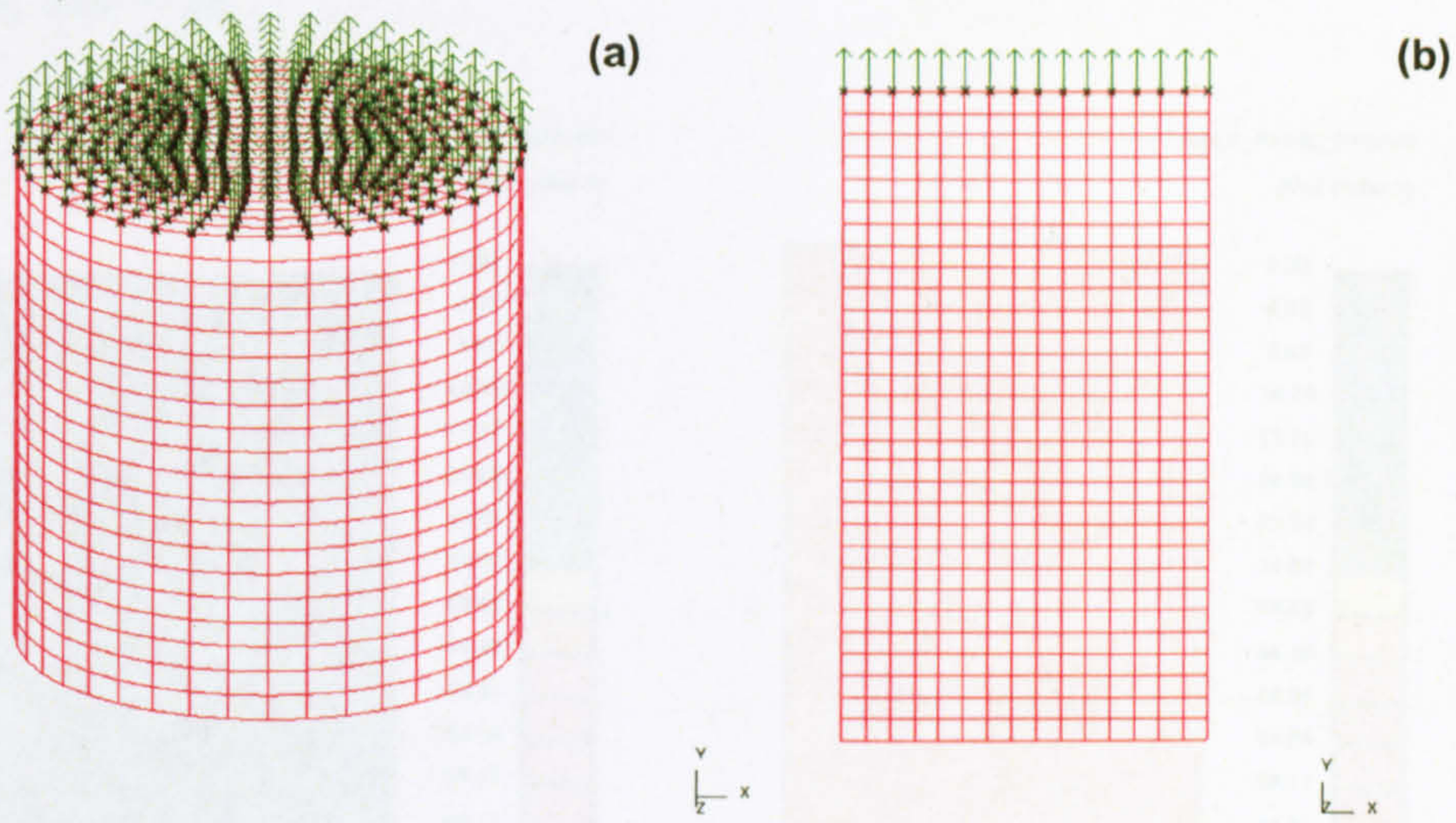

Figure 4.22. *The finite element model of (a) 10% gel; (b) latex, the motion was applied on the top surface of the gel and top edge of the latex, with the frequency of 5 Hz.*

4.6.5. RESULT

Figure 4.23-4.24 gave the contour for the maximum principle strain of the two models at 0 and 0.2 seconds separately. Figure 4.25-4.26 plotted the stress-strain curves of the two models. The simulation of the 10% gelatine and the latex are consistent with the tests under 5 Hz strain rate, and therefore the material properties are ideal to be used into the FE modelling in Chapter 7.

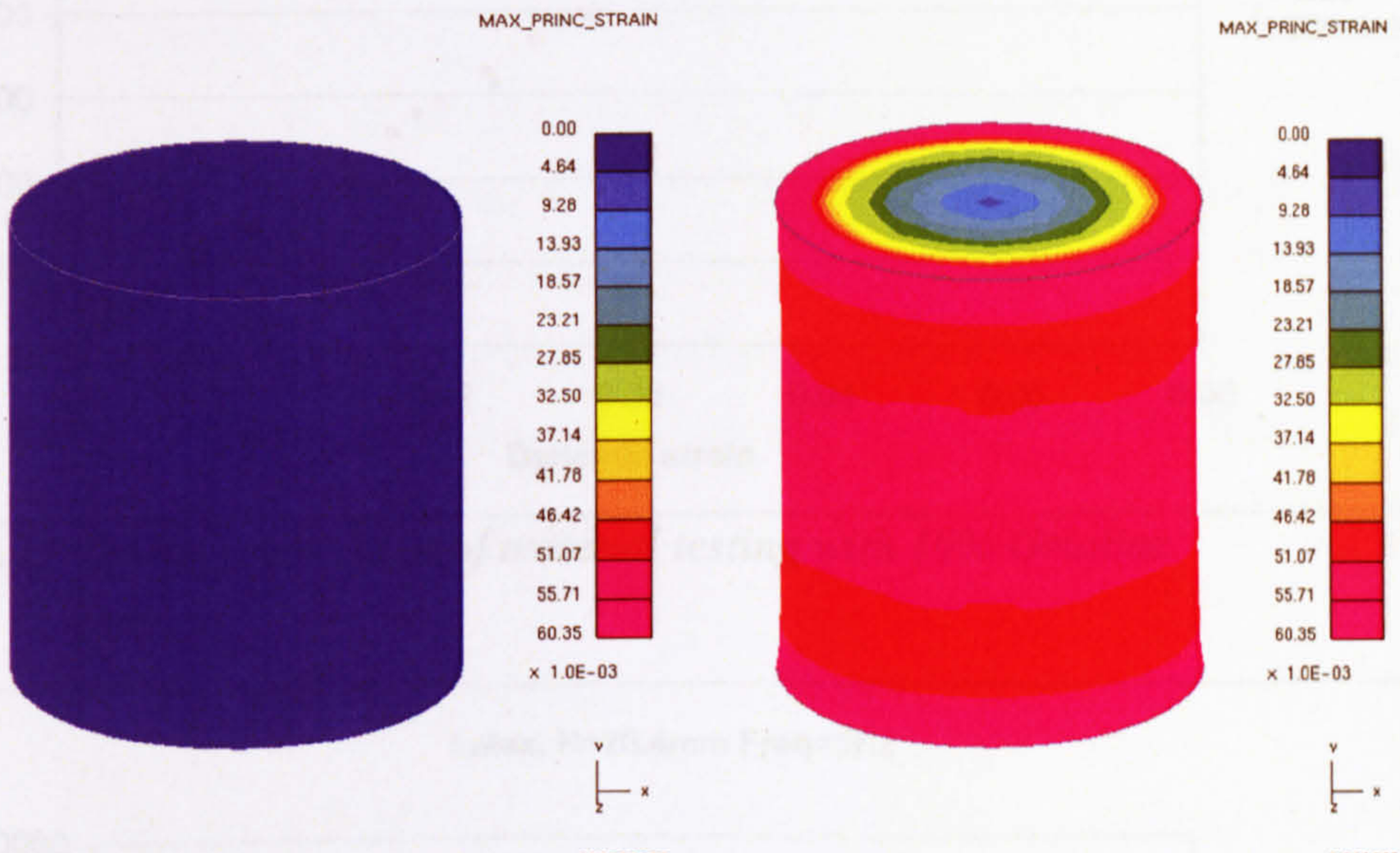

Figure 4.23. *3D contour of, stress distribution on gel 10% d=11.8, h=11.1 under 5 Hz tension at 0s, and 0.2s.*

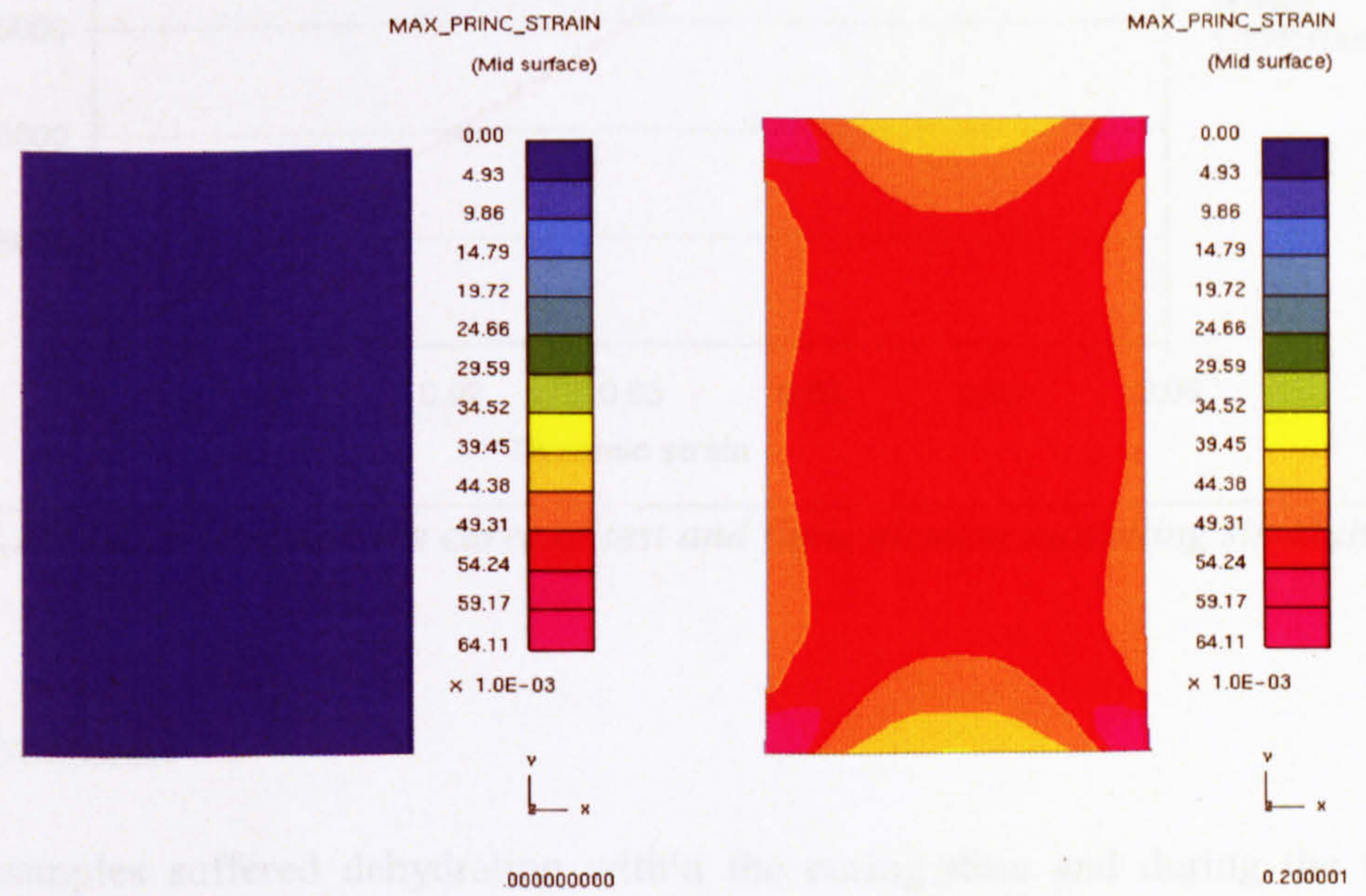

Figure 4.24. *Stress distribution of latex in tension test with strain frequency 5Hz at 0s, and 0.2s.*

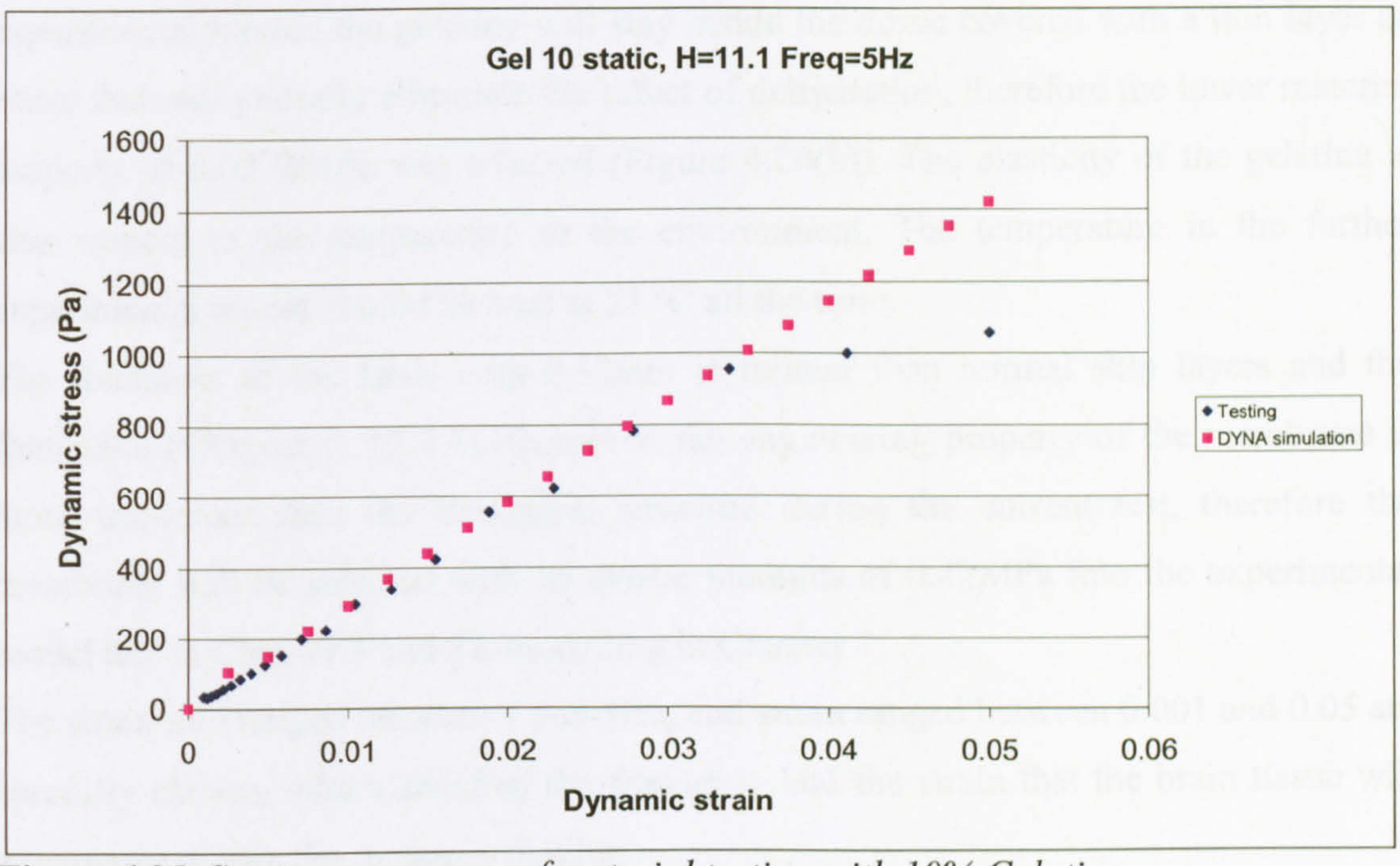

Figure 4.25. *Strain-stress curve of material testing with 10% Gelatine.*

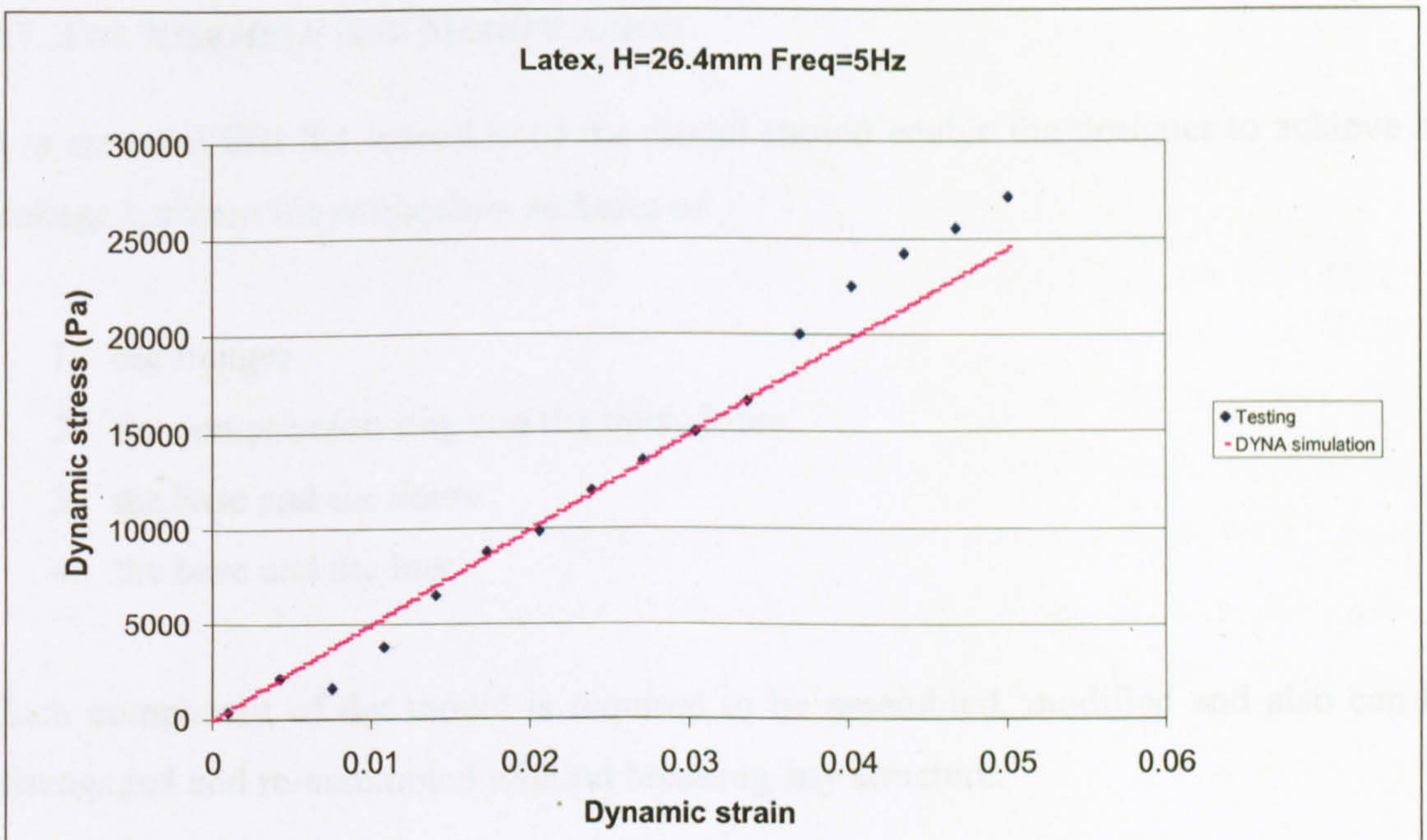

Figure 4.26. *Latex strain-stress curve of test and finite element modelling simulation.*

4.6.6. DISCUSSION

All the samples suffered dehydration within the curing time and during the testing progress. The 10% gelatine that had larger elastic modulus had more curing time than

the other two groups that had lower elastic modulus. During the test of shaking the experimental model, the gelatine will stay inside the dome covered with a thin layer of water that will partially eliminate the effect of dehydration, therefore the lower material property of 0.0272MPa was selected (Figure 4.20(b)). The elasticity of the gelatine is also respect to the temperature in the environment. The temperature in the further experimental model should be kept at 21 ℃ all the time.

The thickness of the latex with 0.12mm is thinner than normal skin layers and the fontanelle (Chapter 2, §2.2.4). However, the engineering property of the membrane is more important than the biological structure during the current test, therefore the membrane will be selected with its elastic modulus of 0.42MPa into the experimental model test in Chapter 5 and FE modelling in Chapter 7.

The strain rate ranged between 1 and 5Hz, and strain ranged between 0.001 and 0.05 are carefully chosen, which satisfied the frequency and the strain that the brain tissue will experience during the dynamic shaking.

4.7. The Assembly And Modification

It is essential that the assembly of the model should enable the designer to achieve no leakage between the connection surfaces of:

1. the flanges
2. the compression ring and the open dome
3. the base and the dome
4. the base and the luer

Each component of the model is required to be assembled, modified and also can be disengaged and re-assembled without breaking any structure.

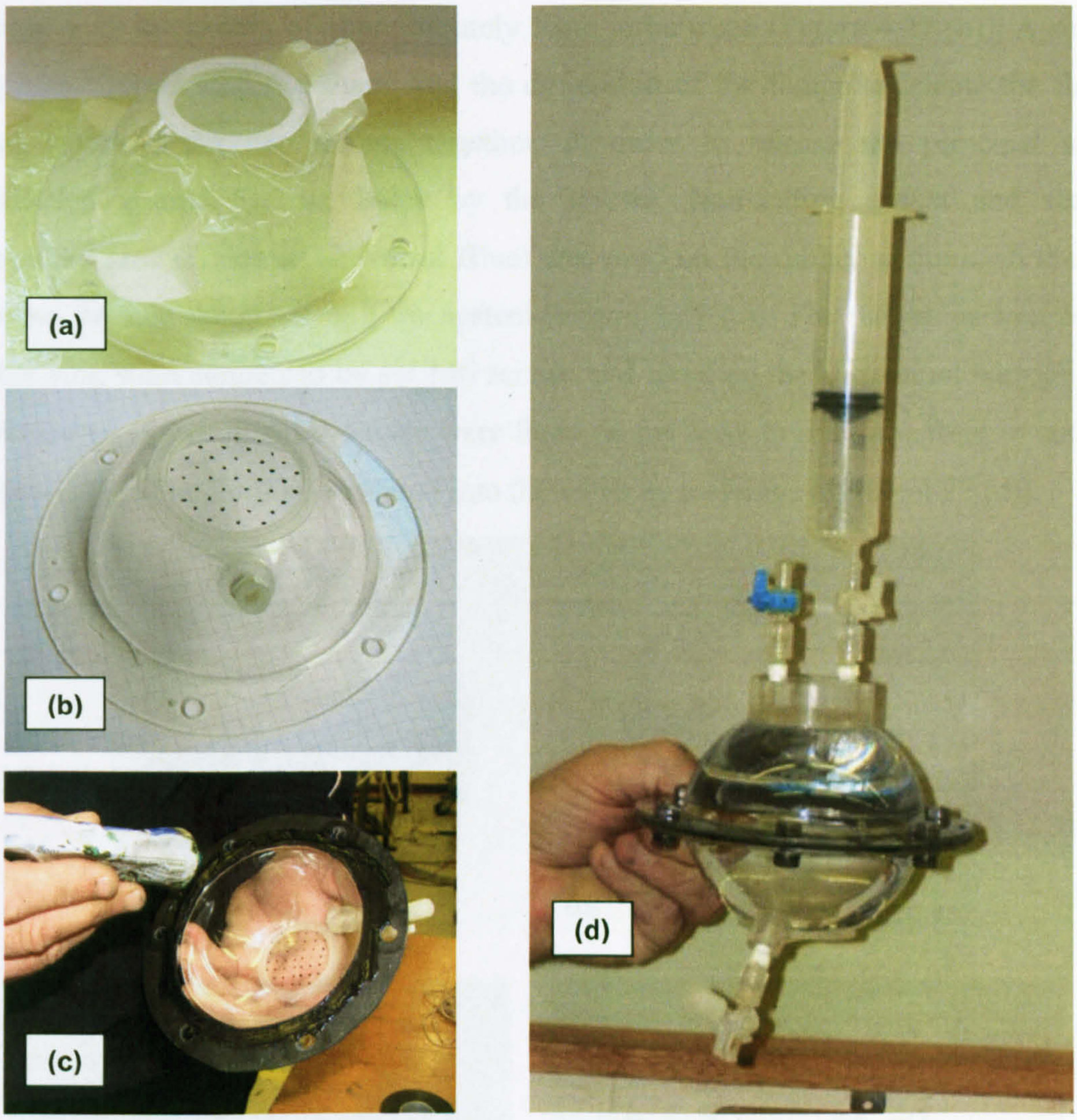

Figure 4.27. *The procedure of model assembly. (a) lay the latex covering the top of the dome; (b) compress the latex by compression ring and plot the ink on the membrane for grid, the luer was screw into the base covered by PVC insulation tape; (c) attach the rubber ring on the dome and glue (Hylomar Universal Blue) to stick the contact surfaces; (d) fix the valve on the luer to set up a drainage system, and use epidemic syringe to inject the water into the globe.*

The procedure of the model assembly can be divided into four steps (Figure 4.27 (a)-(d)). The latex was carefully lay on the top of the open dome, and then the compression ring compressed the latex into the hole that represented fontanelle (Figure 4.27 (a)). The force applied on the latex from the ring was adjusted manually to reduce any extra tension or fold. The medical luer was wrapped with PVC tape and screwed into the acrylic base, in order to seal the base tightly without leakage. The latex membrane was

marked with dot matrix of approximately 5mm in between (Figure 4.27 (b)). A rubber ring was clipped with the shape and the dimension of the flange to isolate the flange when combine the two domes together, in order to release the principal stress distributed around the six holes by the screws. Non-setting gasket and sealing compound glue (Hylomar Universal Blue) was used on the rubber to diminish the gap between the two flanges to seal the system (Figure 4.27 (c)). The flanges as well as the rubber ring were connected by six M6 screws and fixed on the aluminium bars (Figure 4.28 (a)-(b)). Three medical valves were fixed on the luers to drain the fluid in and out of the system. The fluid was pressed into the valve by a syringe (Figure 4.27 (d)).

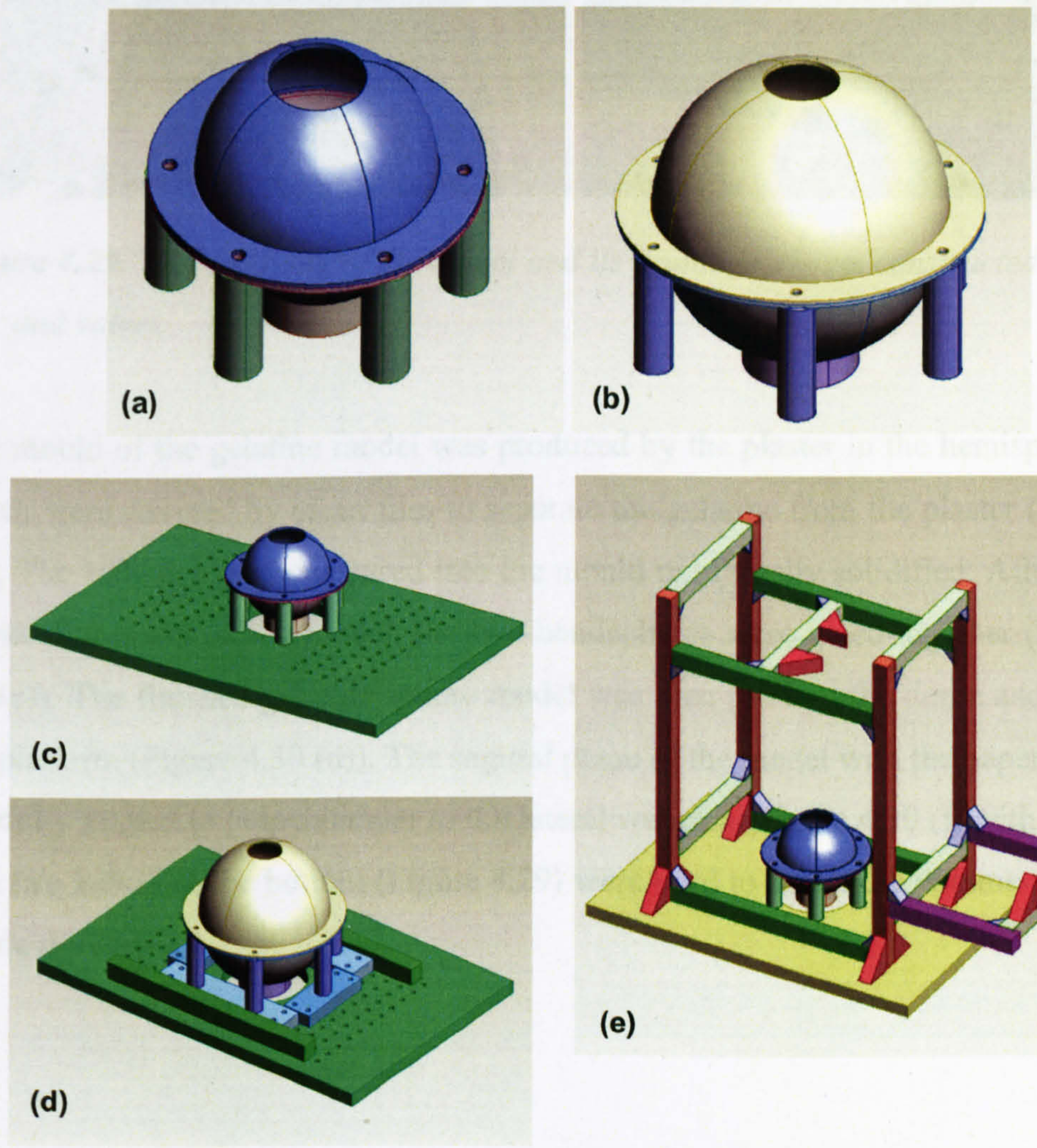

Figure 4.28. *(a)-(e): The concept design of the assembly of acrylic dome onto the platform by ProEngineer. (a) the 100mm dome assembly onto the aluminium bars, (b) the 150mm dome assembly onto the aluminium bars, (c) the 100mm dome mounting onto the platform, (d) the 150mm dome mounting onto the platform, (e) the full view of 100mm dome mounting on the platform with camera support frame.*

The 100mm dome was fixed on the platform direction by six aluminium bar (Figure 4.28 (c)), while the 150mm dome with the larger pitch circle was fixed by six aluminium bar sitting on another four aluminium bases on the platform (Figure 4.28 (d)).

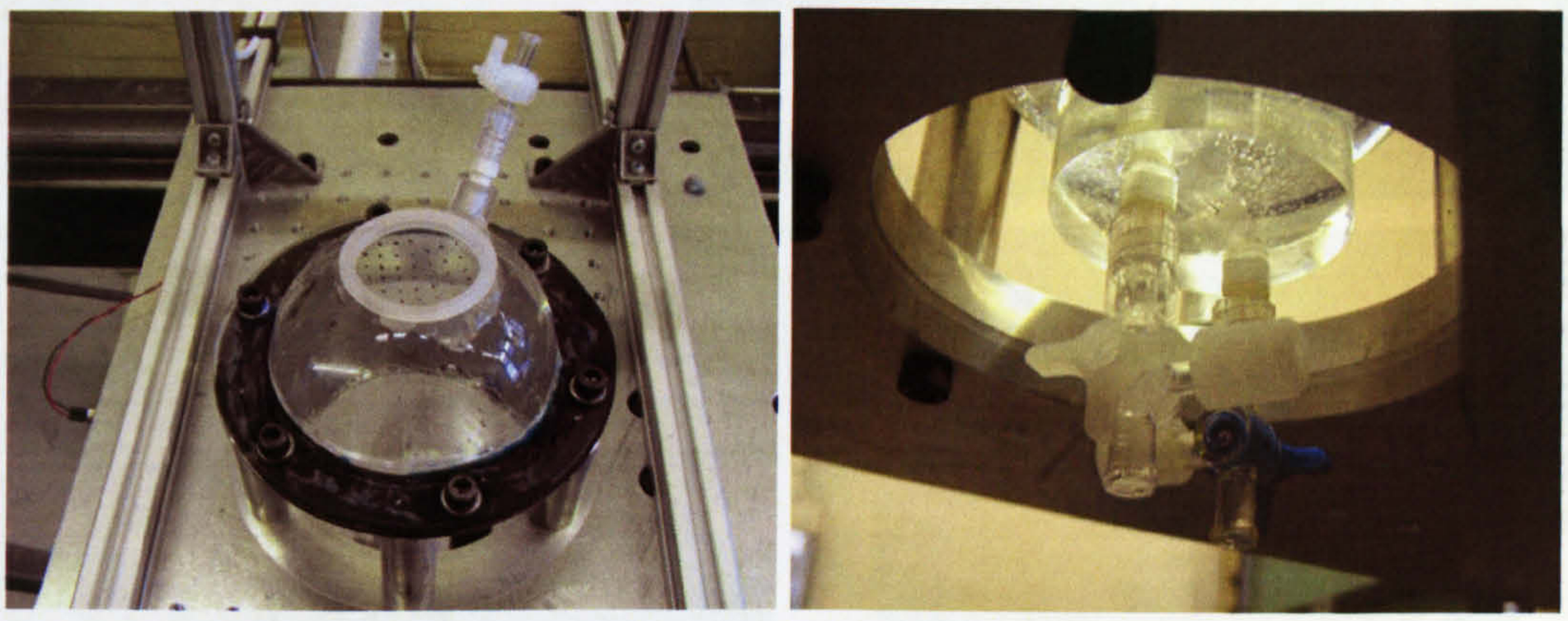

Figure 4.29. *The assembly of the model and its drainage system constructed by medical luer and valves.*

The mould of the gelatine model was produced by the plaster in the hemisphere shape, which were covered by clean film to separate the gelatine from the plaster (Figure 4.30 (a)). The 10% gelatine was cured into the mould until totally solidified. After the paper marks was glued on the model, the two hemispheres were glued together (Figure 4.30 (b)-(c)). The finished gelatine sphere model was then put into the dome and fixed onto the platform (Figure 4.30 (d)). The sagittal plane of the model with the paper marks was carefully rotated to perpendicular to the lateral webcam (Figure 4.30 (f) with red arrow). The two valves in the bottom (Figure 4.29) were used to adjust the volume of the water inside the dome.

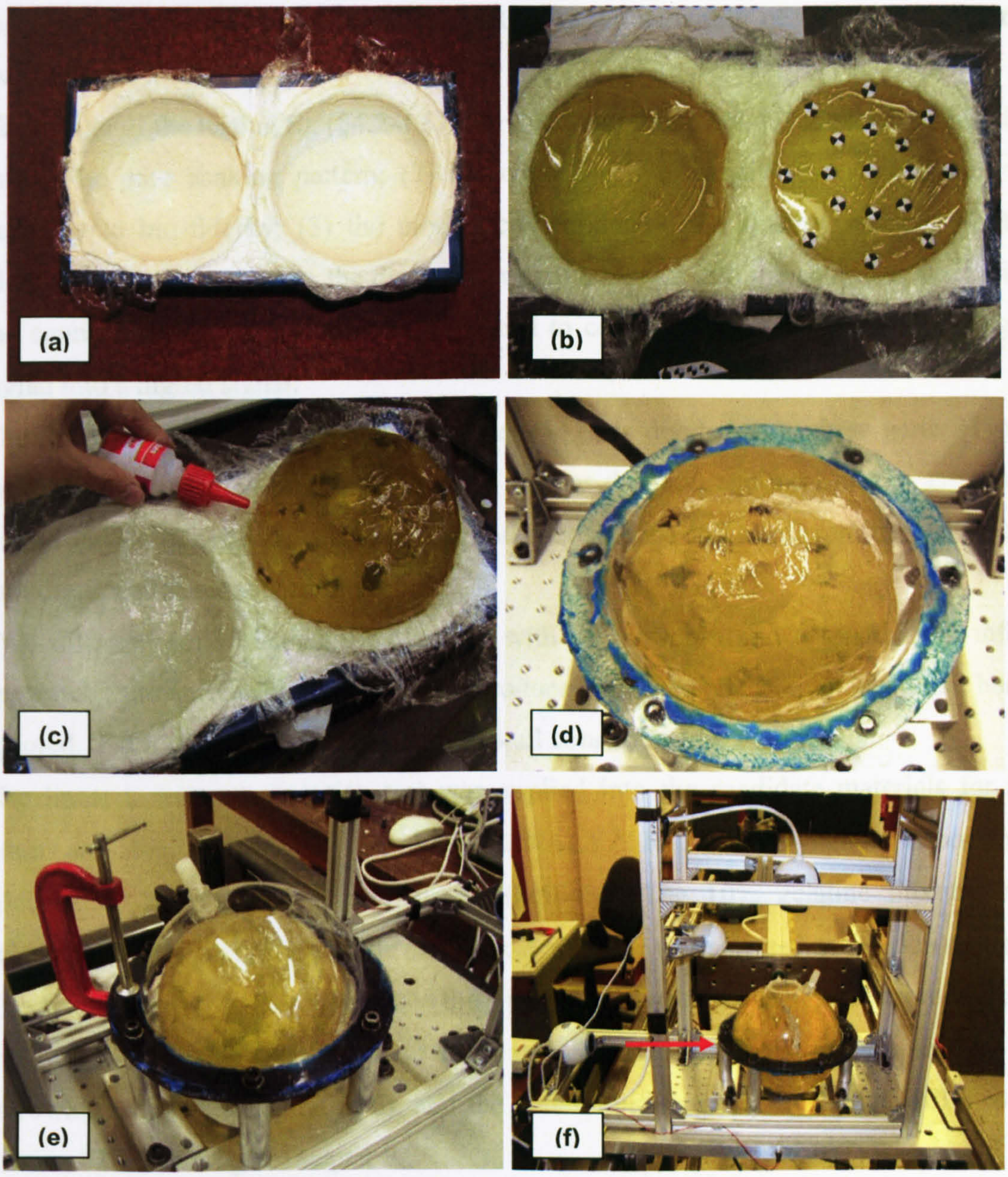

Figure 4.30. *Gelatine model production and assembly. (a) plaster mould, (b) cured 10% gelatine with paper mark, (c) glue the hemisphere together, (d) put the model into the dome, (e), fix the dome with screw on the bar, (f) filling with water and set up the webcam for the motion capturing.*

SUMMARY

Based on the shaking motion reconstruction from the laboratory test contained in the previous chapter, this chapter describes the detail and progress of the design of testing apparatus. The progress includes the design and construction of the test rig, the choosing and fabricating of the anthropomorphic head models, the material test of the

inert material for soft tissue replica, and finally the assembly of the test rig and the experimental model.

The design of the testing rig (§4.2-4.5) is divided into five parts: (1) the loading cell that inputs the pure shaking pattern; (2) the control cell to modify the simulation with accuracy to bio-fidelity; (3) the motion cell producing the shaking motion; (4) the platform cell which outputs the direct and relative motion into the computer (including the counter); and (5) the data acquisition cell to convert the output from the analogue signal into a digital signal.

The design of the experimental head model (§4.6) is divided in to three parts: (1) the production of the rigid mechanical part as well as the joint and base for the assembly, mount and fix transducer; (2) the testing and choosing the soft tissue replica; and (3) the mounting, and the modification.

Two different head diameters were used with the newborn and 6 months old infant separately; the anterior fontanelle was reproduced with the other biological detail being ignored. Each group had the rigid closed skull constructed for comparison.

The linear tension/compression test was applied into the candidate materials for the brain and the scalp (§4.6) by VISCOANALYZER 2000 (Dynamic Laboratory, Mechanical Engineering, University of Sheffield). The 10% gelatine mixture was selected as the brain replica, while one latex membrane was selected as the skin replica.

The final section (§4.7) demonstrated the assembly between the experimental model and the test rig. The chapter provided the basic shaking apparatus for the test in the following chapters (Chapter 5, 6), and the data output from the apparatus will also be used in FE modelling in Chapter 7.

CHAPTER 5: *THE EXPERIMENTAL SHAKING MOTION RECONSTRUCTION*

INTRODUCTION

The previous Chapter discussed the design of the experimental test rig and the model of the infant skull. This chapter first describes the methodology, in rig-proving tests, of reproducing the shaking pattern by double-differentiation of the displacement data from the LVDT on the test rig. Once confidence in the rig was established, it could be used for testing models related to the shaking baby phenomenon. There were six head models studied in these tests, and the results from them are compared with those from the TRL experiments, specifically those presented earlier in Chapter 3 (§3.4, Figure 3.17). A discussion of these comparisons is presented later in this chapter.

The head models were of two sizes, and either contained only water (a model of the CSF), or a gelatine (a model of the brain tissue) sphere suspended in a thin layer of water. Some models were run with an open part at the top to represent the effect of the fontanelles. There tests were performed using the maximum airflow permissible into the pneumatic component. The deformation of the gelatine and the soft membrane over the fontanelle were captured using web cameras. The analyses of the data captured in these tests are described in chapter 6 and chapter 7.

5.1. RIG CALIBRATION

Two micro-switch pins were fixed at the centre of the track with a spacing of approximately 200mm. The control valve was set to the medium airflow setting of the system. There was no experimental model mounted on the rig, which was set running with a repetitive motion. The displacement recorded by the LVDT was collected in parallel using the LABTECH software in a PC fitted with a data acquisition card (National Instrument LAB PC+). Figure 5.1 (a) shows the position of each transducer. Figure 5.1 (b) illustrates how the acquisition system was set up. The tests were performed over a 10 second interval, the first 3-4 seconds being the interval before stable results emerged. Although in real life, the shaking could last from three shakes up to regular repetitive shaking (Chapter 2, §2.4), the TRL results were obtained with three

or ten shakes in tests lasting from 1 to 10 sec. Therefore a 10 second test interval in this rig was judged to be enough for the current research. The data was saved as separate files of time (seconds), acceleration (mm/s^2) and position (mm).

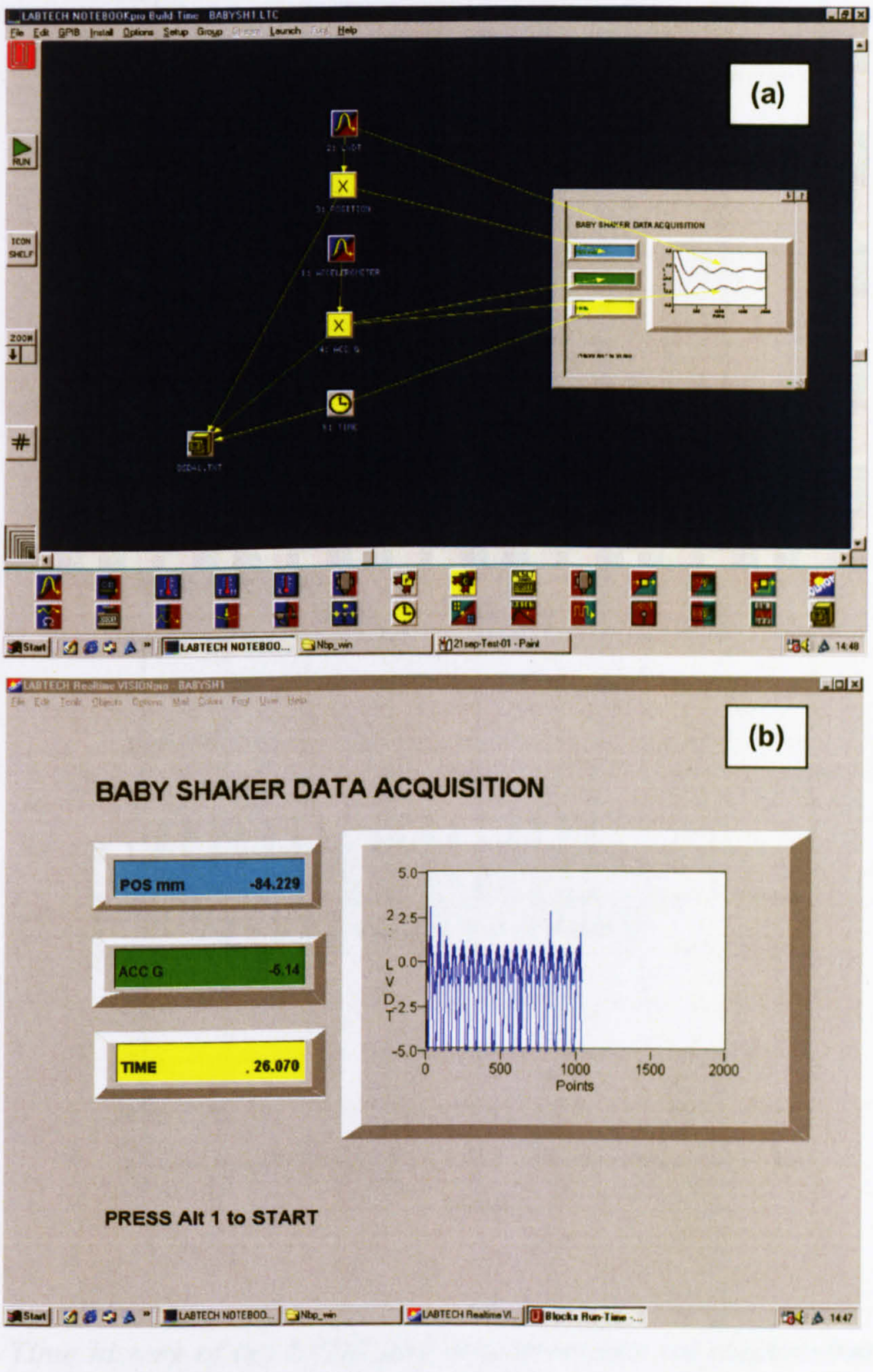

Figure 5.1. *An output from the LabTech software showing the software diagram (a) to collect and save the LVDT and acceleration data, (b) the position, acceleration and time during the testing.*

Figure 5.2 presents the results of the displacement measurement obtained from the LVDT. The displacement on the track was from -125mm to 95mm. The acceleration

was obtained by differentiating the displacement data twice, resulting in a range from -0.75g to 1.5g (g=9.81m/s^2) during a period of 12 seconds.

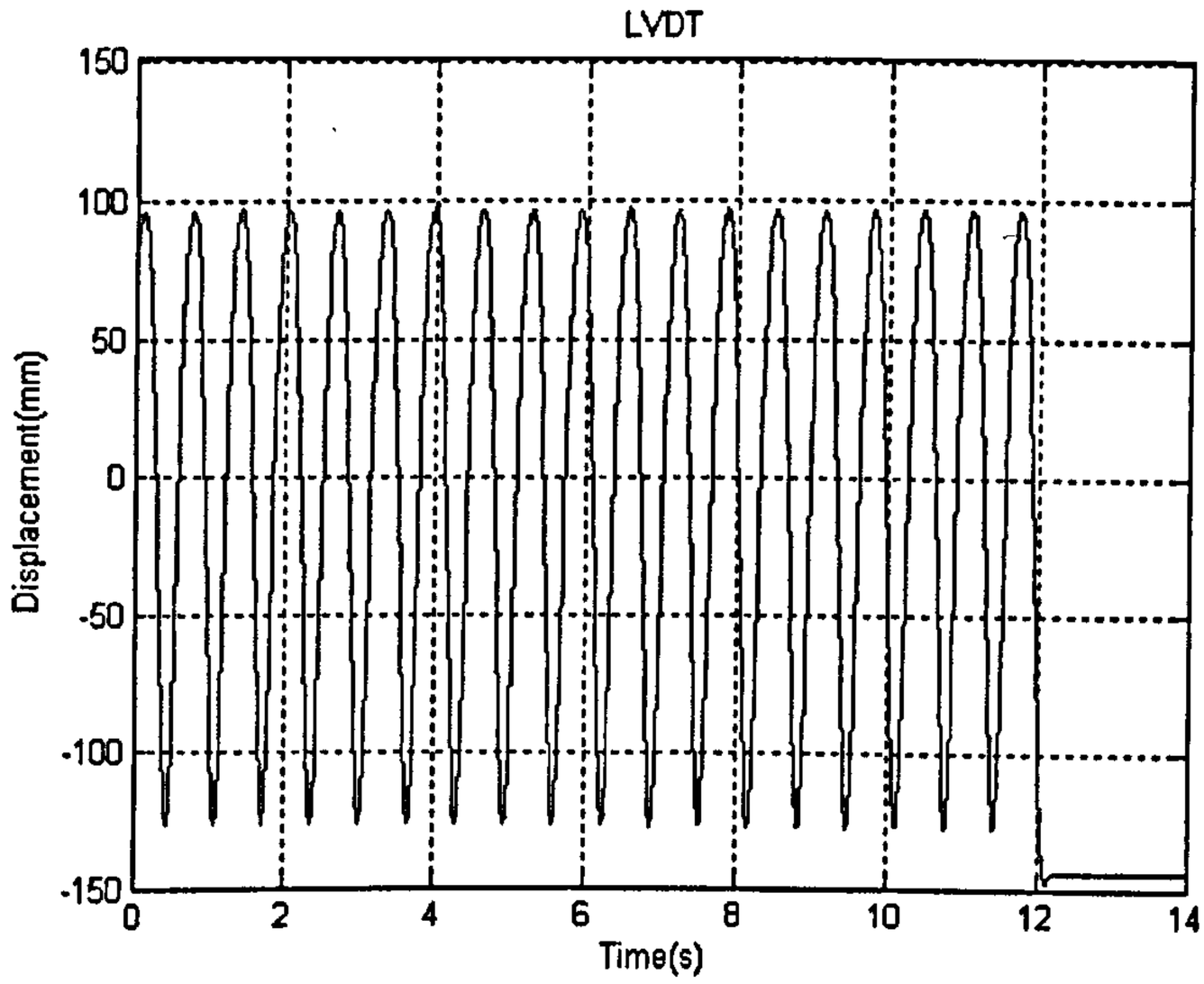

(a)

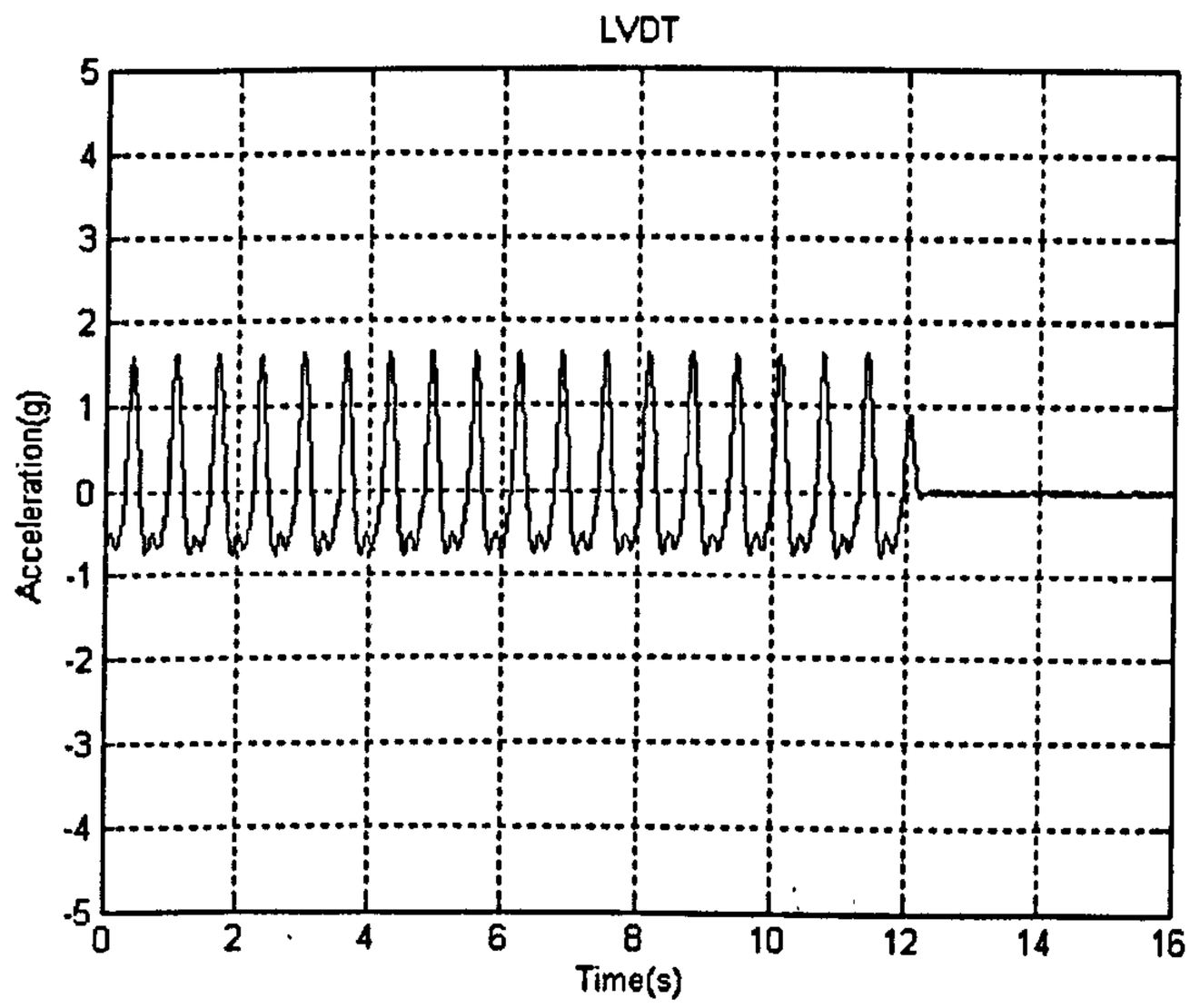

(b)

Figure 5.2. *Time history of the LVDT and accelerometer. (a) displacement in mm, (b) acceleration differentiated from (a) in g.*

5.2. EXPERIMENTAL MODEL TESTING

Six tests (Table 5.1) were conducted with the experimental model. These tests were divided into two groups one with a 100mm and the other with a 150mm diameter head.

Three experiments were performed in each group, specifically (a), an open top structure model filled only with water; (b) an open top structure model filled with a gelatine sphere surrounded by a water layer; and (c) a closed structure filled with a gelatine sphere and water layer, as in (b). Each model was subjected to 10 seconds of shaking on the rig. The distance between the two micro-switches was 100mm, and the airflow of the system was adjusted to the maximum capacity. The construction and the assembly of the experimental model followed that described in Chapter 4 (§4.6-§4.7). The water used in Tests 1 and 4 (Table 5.1) was dyed with a colourant (Figure 5.4, Figure 5.6) to improve the visibility of the particle drawn on the membrane over the open top.

The webcams were fixed on the support frame to capture the top view, the angle view of the membrane and the top and lateral view of the whole model (Figure 5.3 (b)). All three directional views were in the plane OXY shown in Figure 5.3 (a). The linear motion of the rig was in the direction of the X axis.

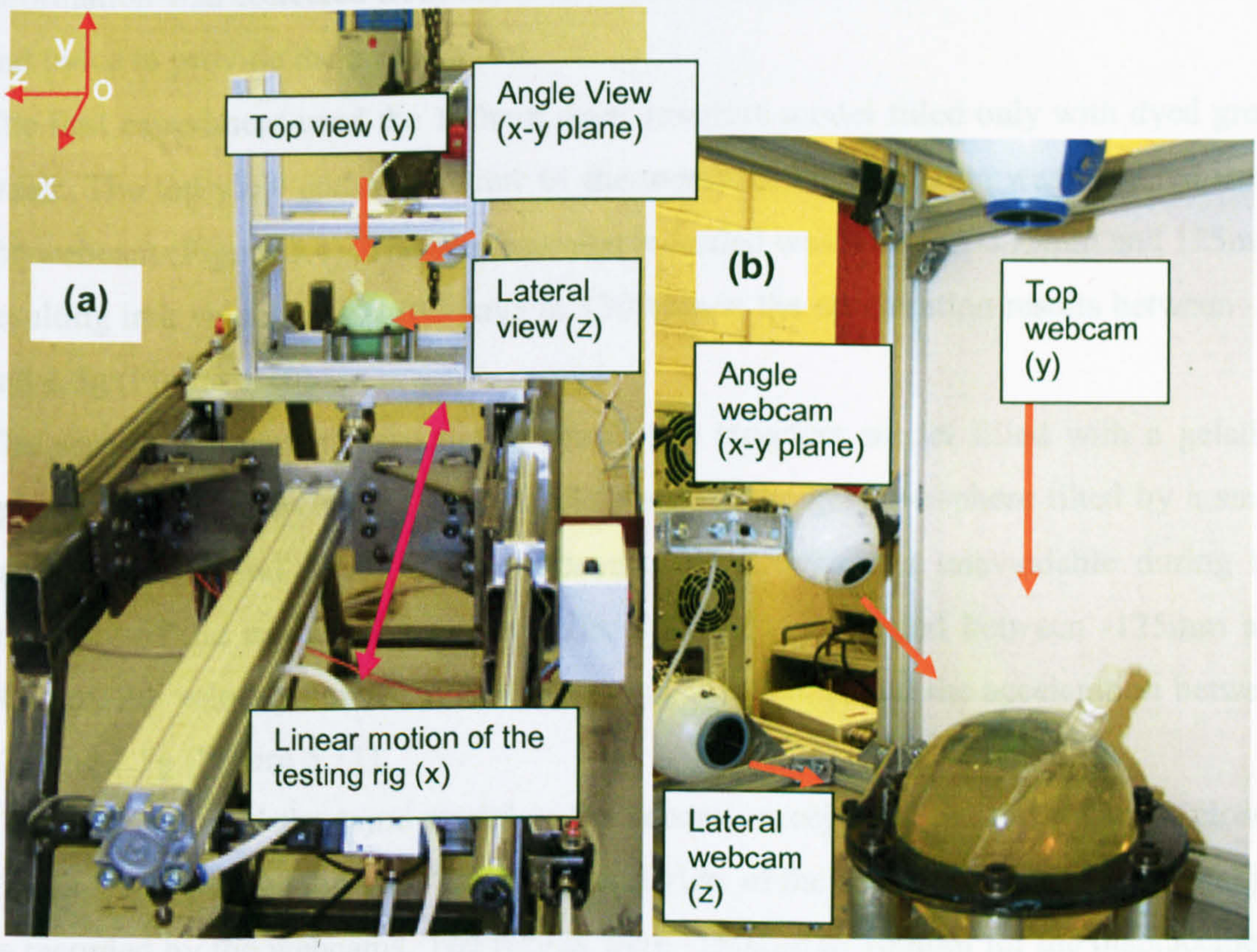

Figure 5.3. *The 100mm model of water; (a) the model, (b) mounting on the rig and prepared for shaking.*

5.13 shows that the displacement ranged from -125mm to 100mm, the velocity from -1200mm/s to 1300mm/s and the acceleration from -1.5g to 2.5g.

The fifth test was on the 150mm model, now with an open top, and filled with the gelatine sphere and surrounding water layer. The top view, angle view of the membrane and the lateral view of the model were captured. The fact that the middle plane of the gelatine sphere tilted from the lateral plane can be seen from the top view shown in Figure 5.9. The displacement values ranged from -125mm to 100mm, resulting in a velocity between -1250mm/s and 1250mm/s, and an acceleration between 1.8g and 2.5g (Figure 5.14).

The sixth and final model was the fifth, but now with a closed top. The top and lateral view of the model was recorded. As can be seen in Figure 5.18, the middle plane of the gelatine sphere was tilted by a small angle from the lateral plane. The results showed a displacement ranging from -130mm to 100mm, a velocity from -1200mm/s to 1200mm/s, and an acceleration from -1.8g to 2.5g (Figure 5.15).

Table 5.2 sets out the approximate peak values of the displacement, velocity and acceleration the rig produced during the testing of each model.

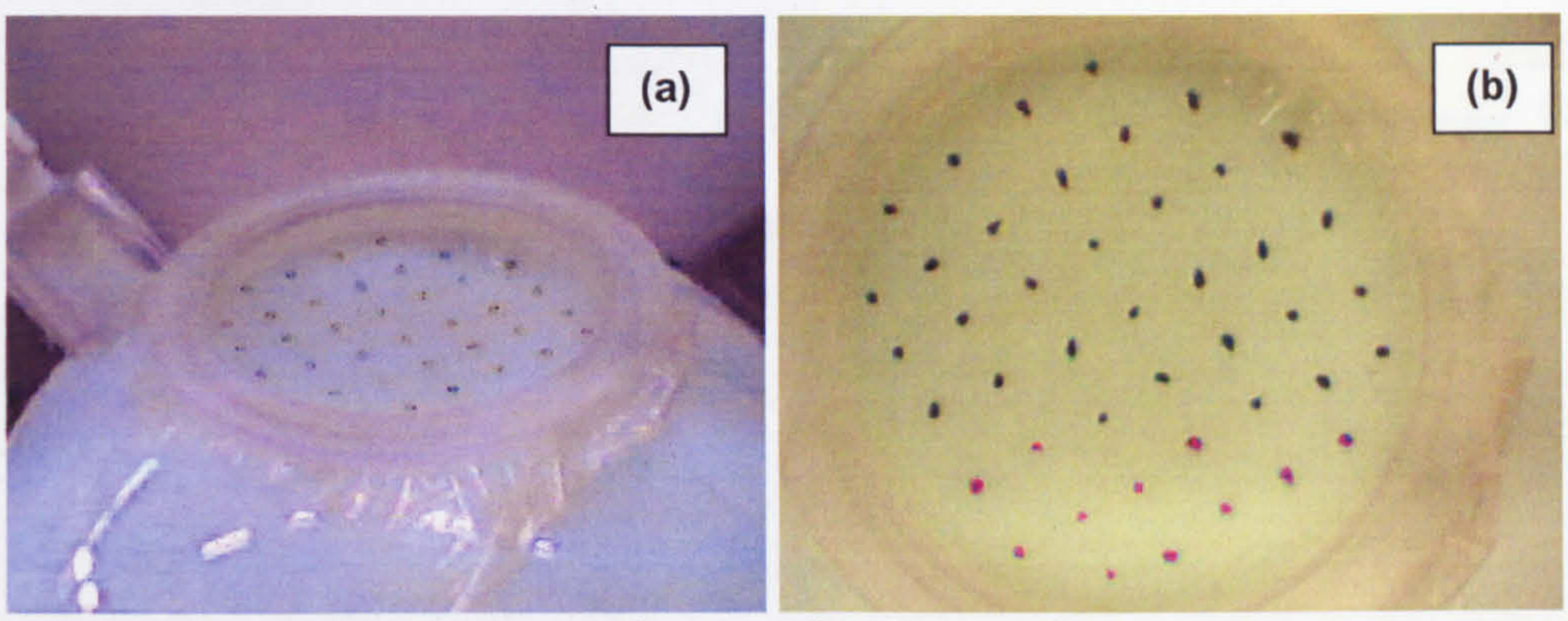

Figure 5.4. *Water 100mm. (a) view from angle, (b) view from top.*

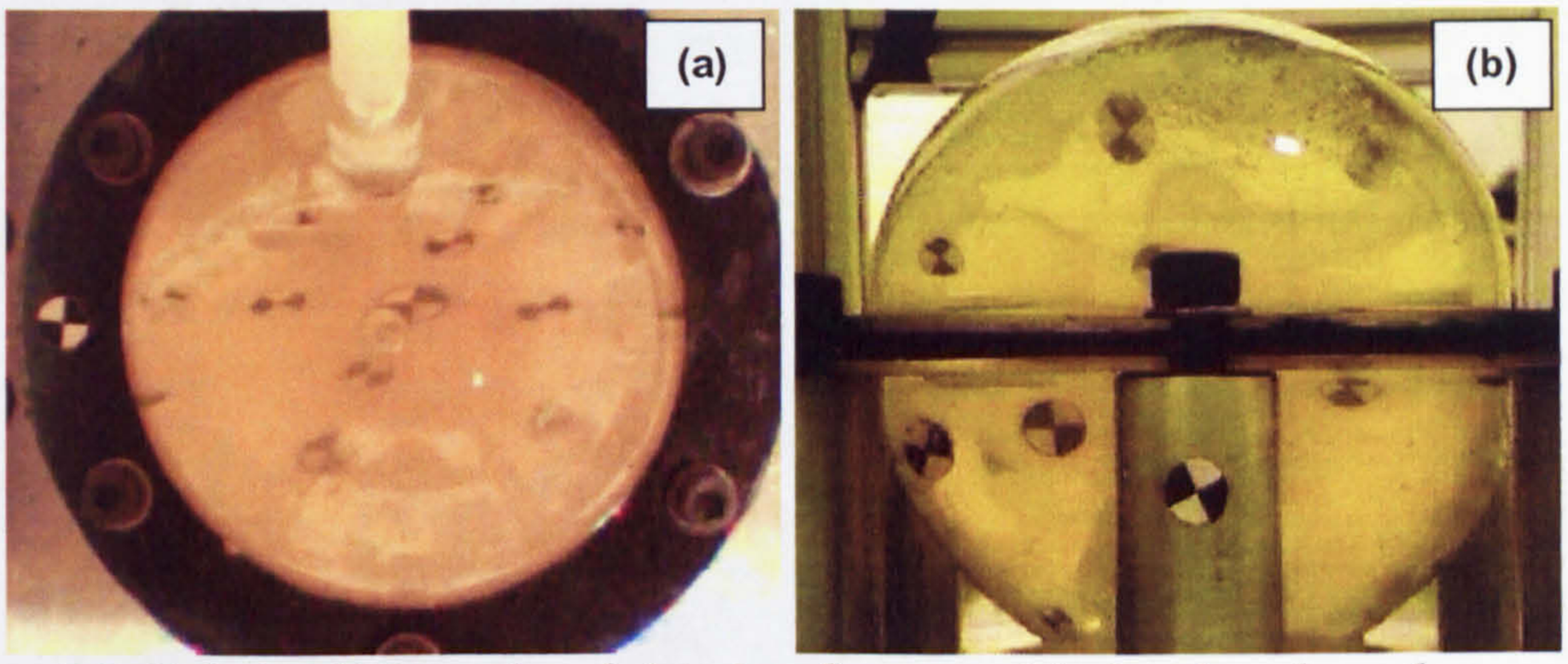

Figure 5.5. *Gelatine 100mm closed. (a) view from top, (b) view from lateral.*

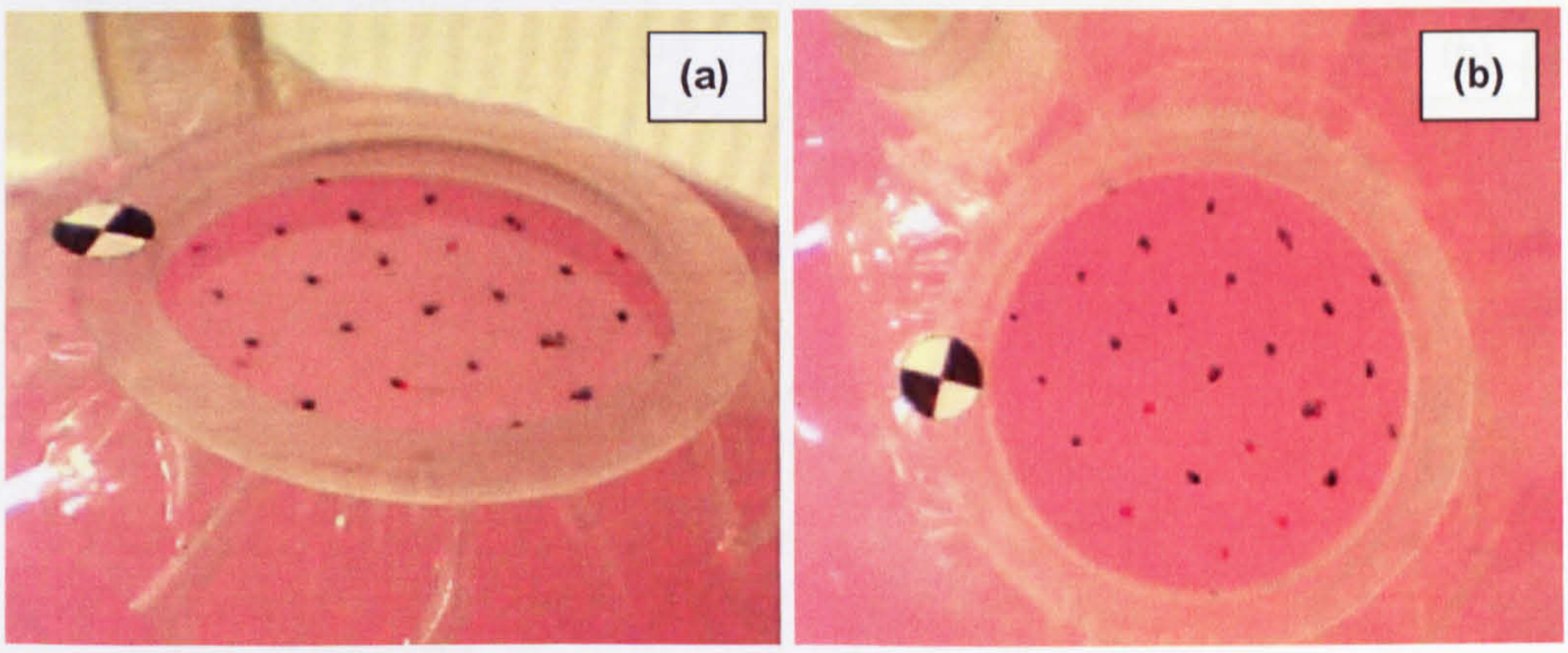

Figure 5.6. *Water 150mm open. (a) view from angle, (b) view from lateral.*

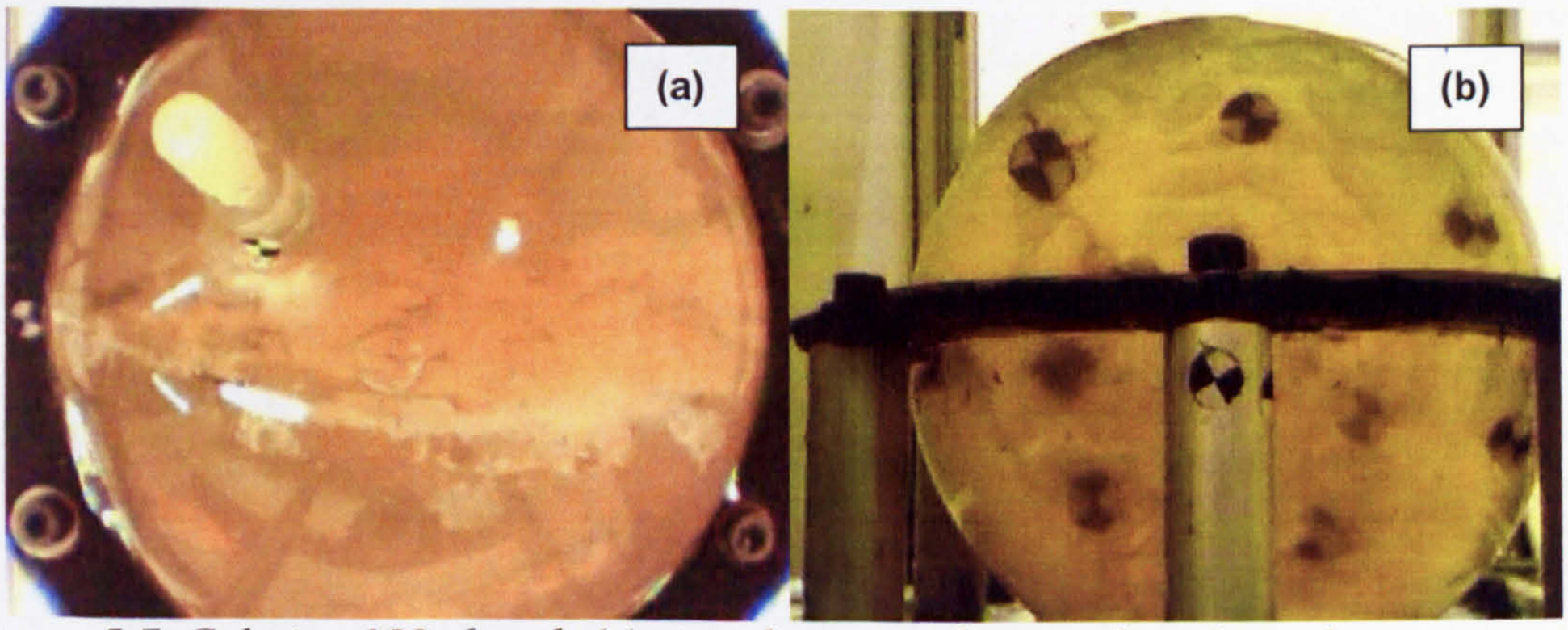

Figure 5.7. *Gelatine 150 closed. (a) view from top, (b) view from lateral.*

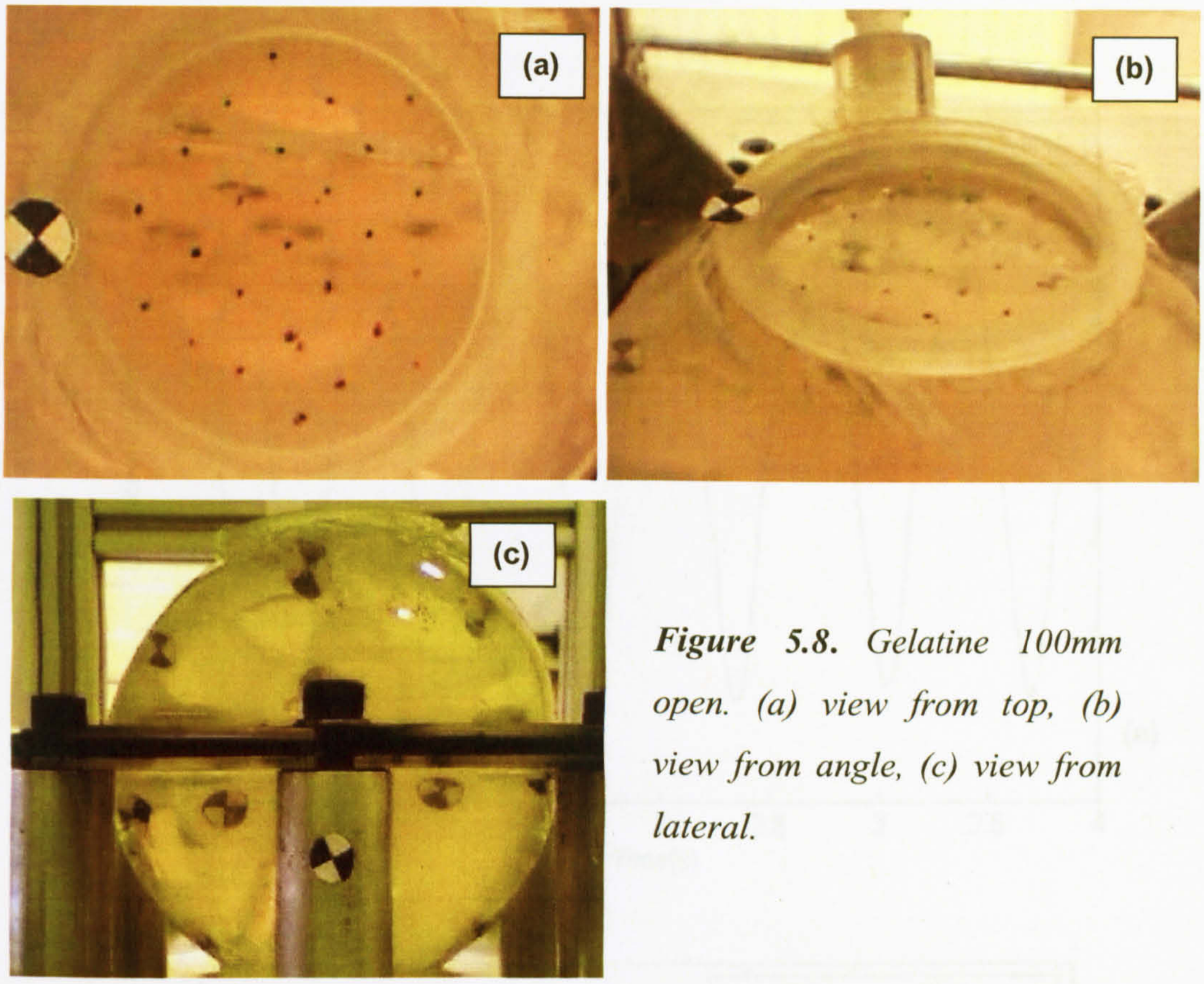

Figure 5.8. *Gelatine 100mm open. (a) view from top, (b) view from angle, (c) view from lateral.*

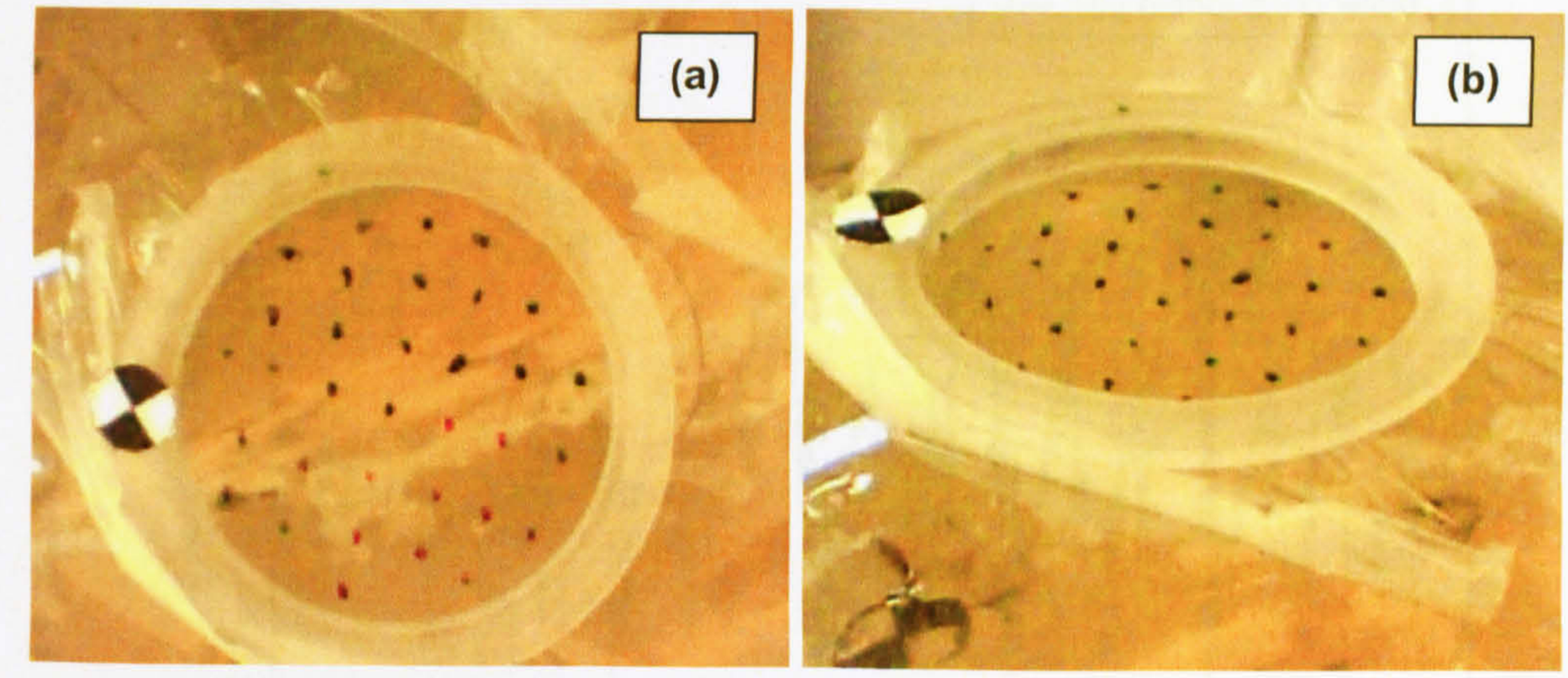

Figure 5.9. *Gelatine 150mm open. (a) view from top, (b) view from angle, (c) view from lateral.*

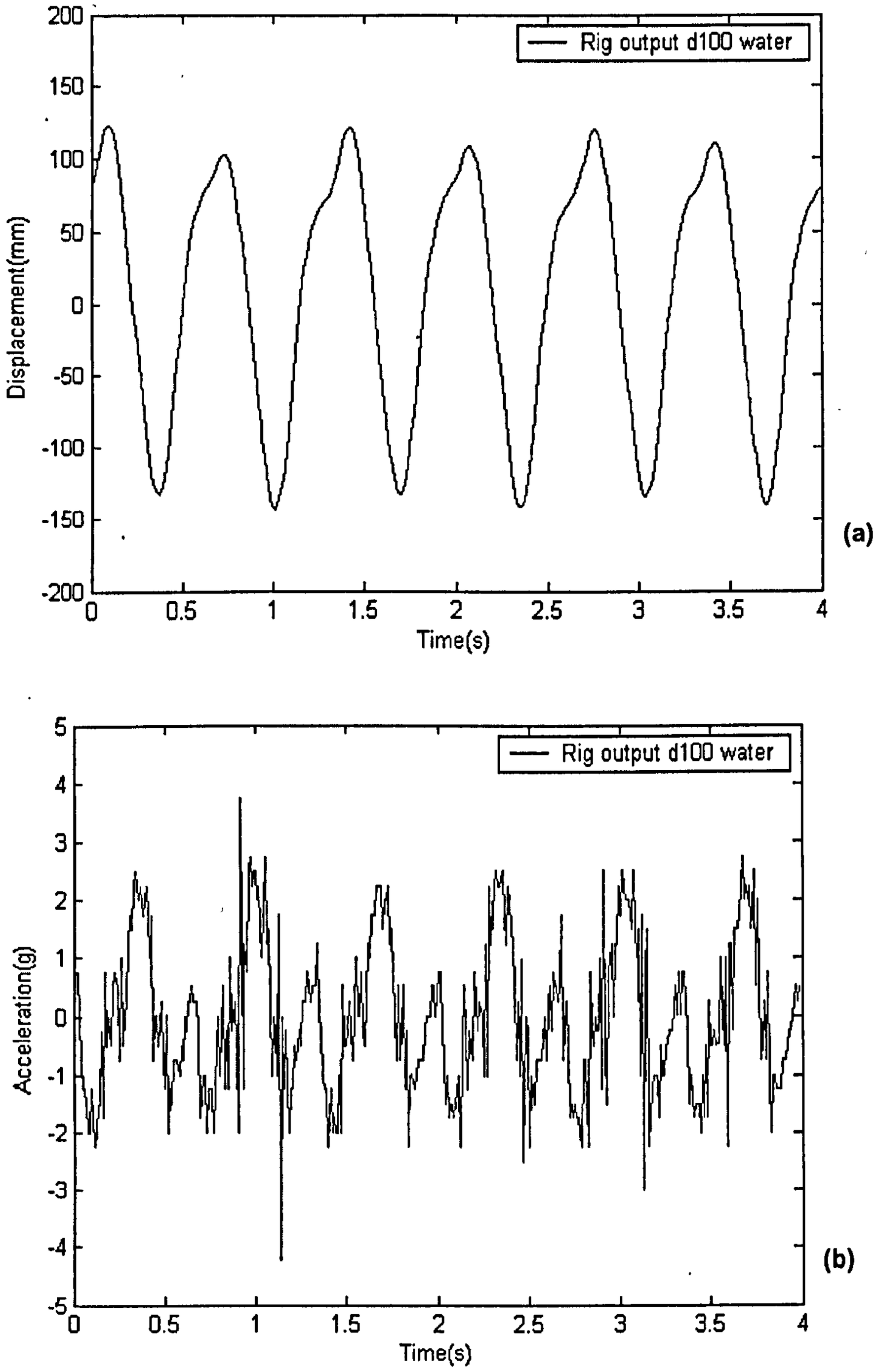

Figure 5.10. *The LVDT data of water 100mm model testing, (a) displacement in mm, (b) acceleration double differentiated from displacement in g.*

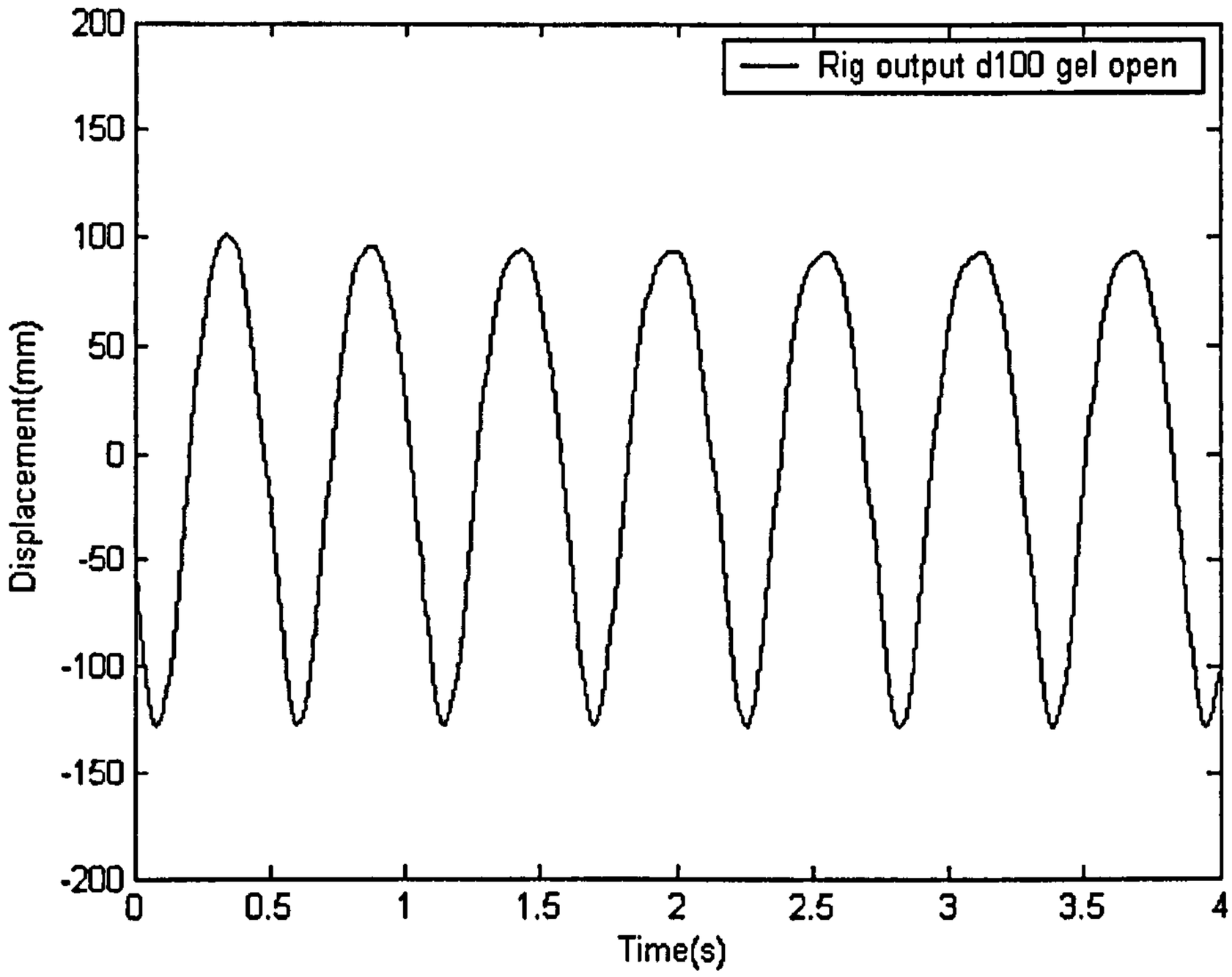

(a)

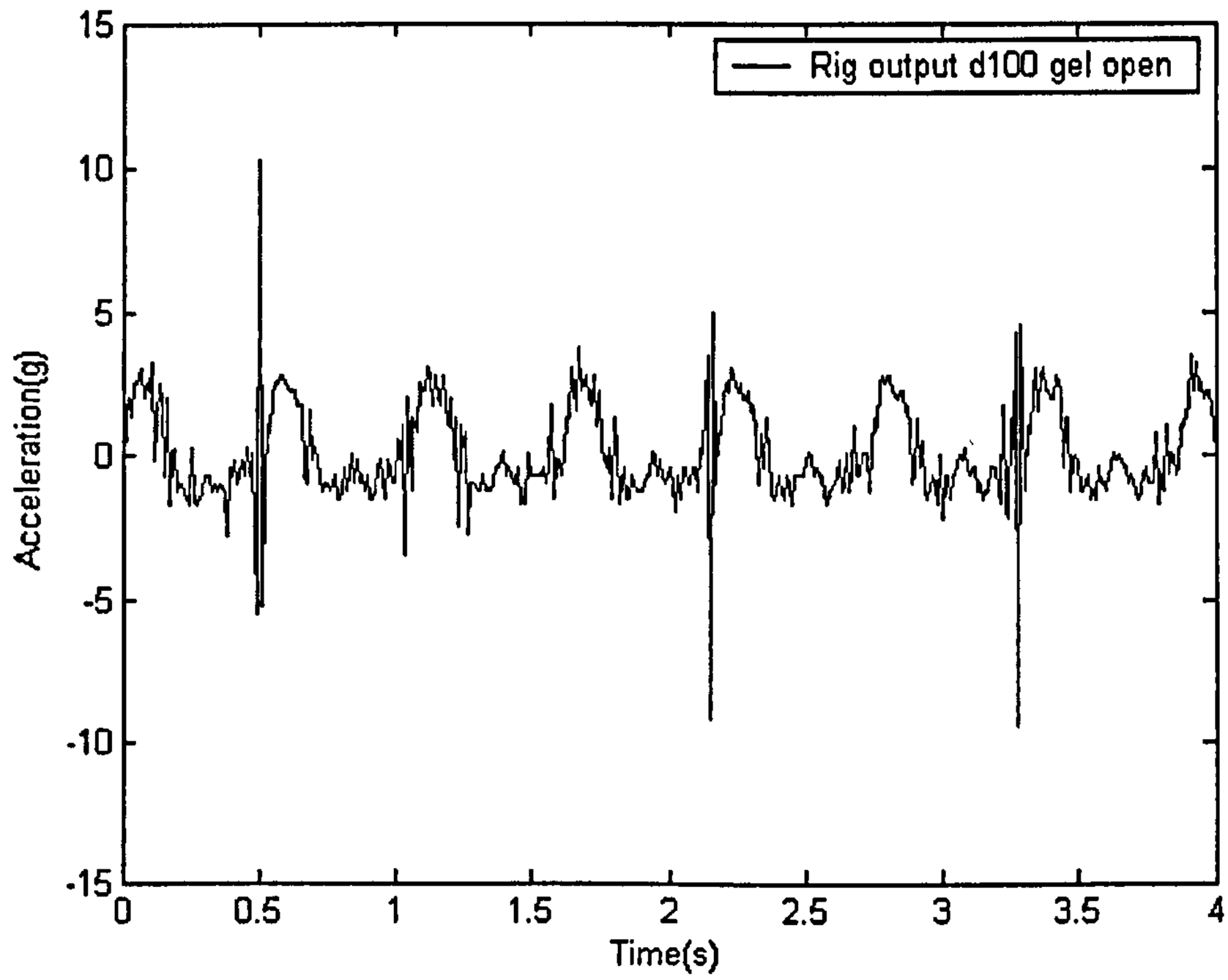

(b)

Figure 5.11. *The LVDT data of gelatine 100mm open model testing, (a) displacement in mm, (b) acceleration double differentiated from displacement in g.*

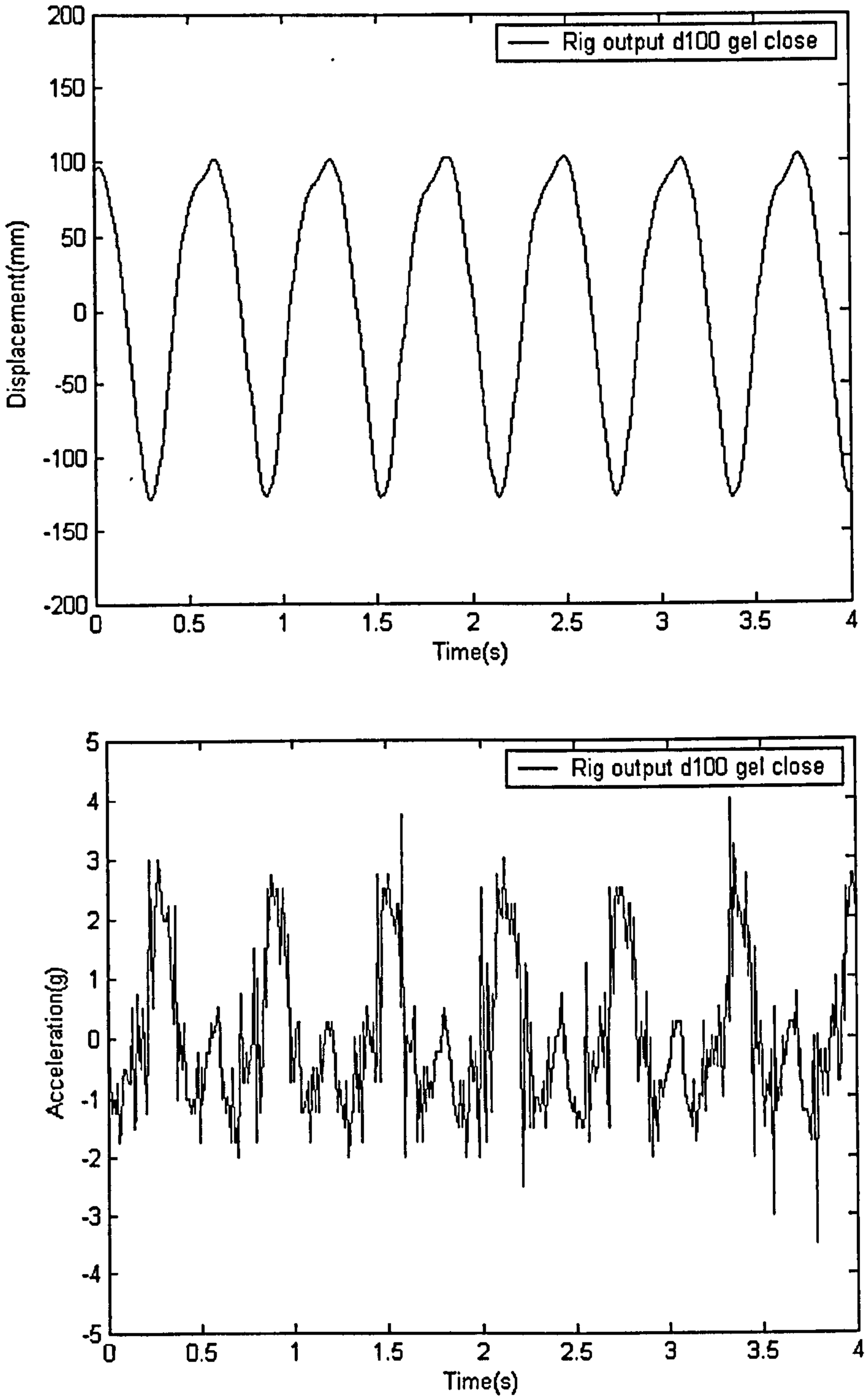

Figure 5.12. *The LVDT data of gelatine 100mm closed model testing, (a) displacement in mm, (b) acceleration double differentiated from displacement in g.*

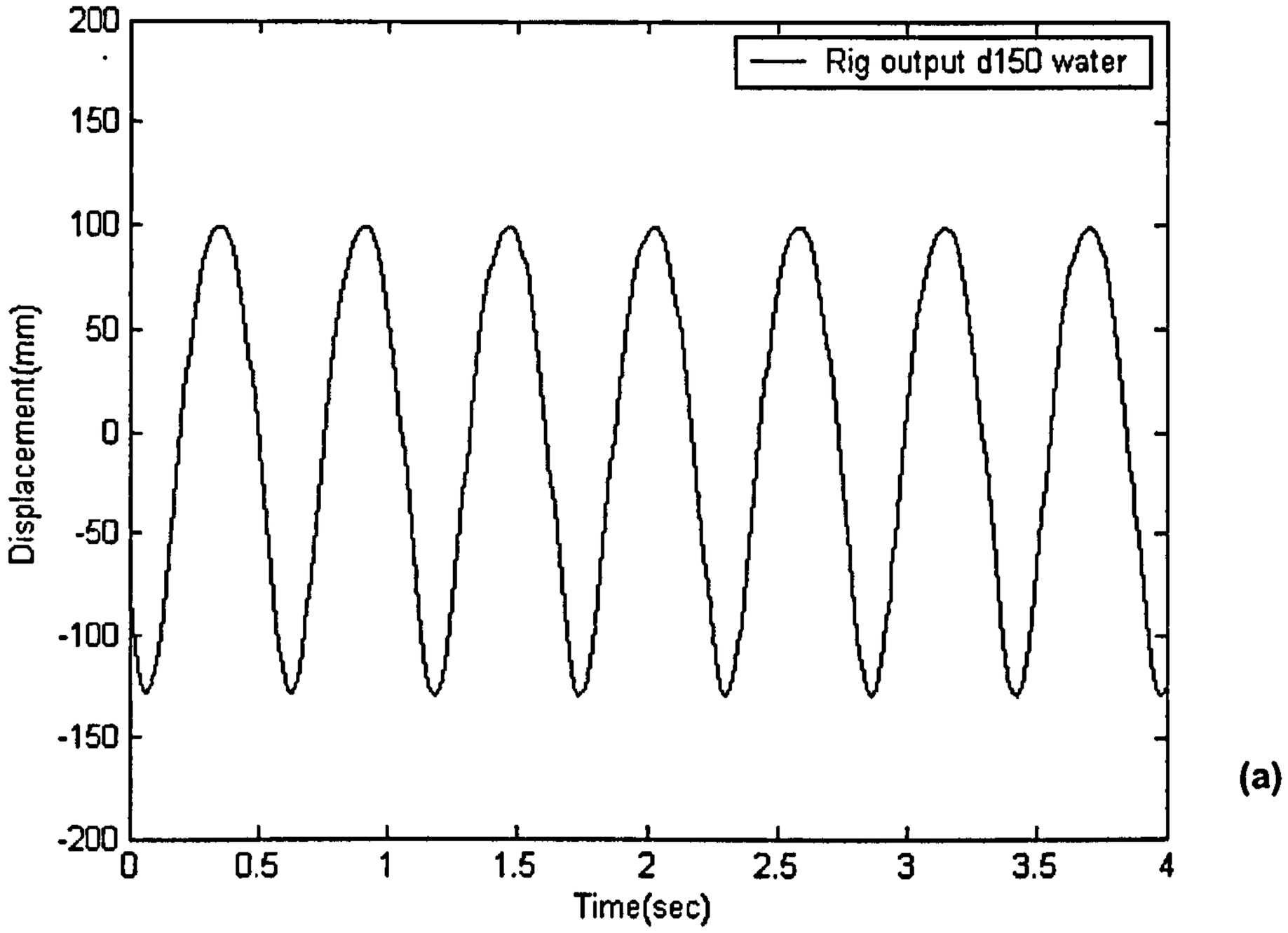

(a)

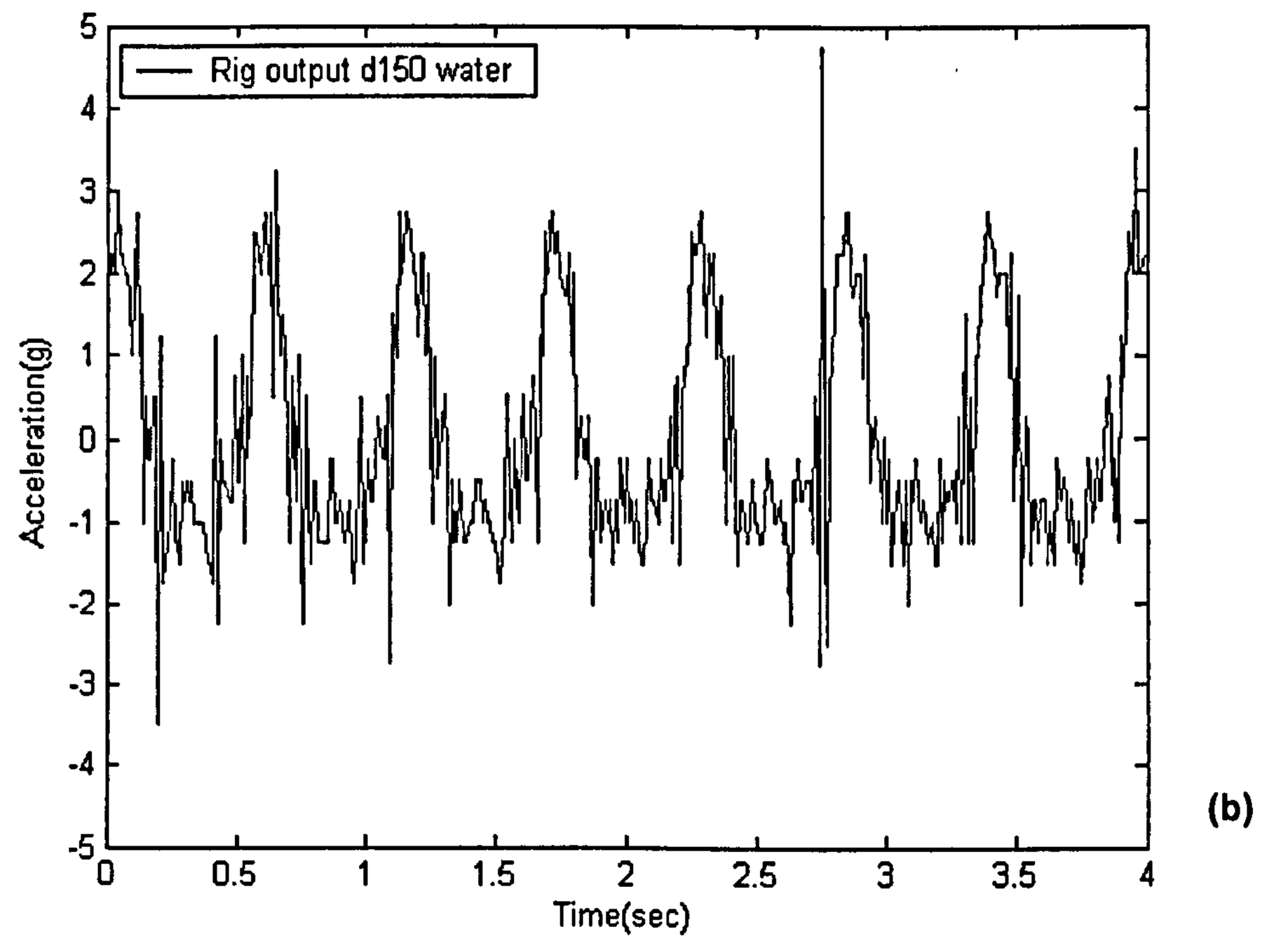

(b)

Figure 5.13. *The LVDT data of water 150 open model testing, (a) displacement in mm, (b) acceleration double differentiated from displacement in g.*

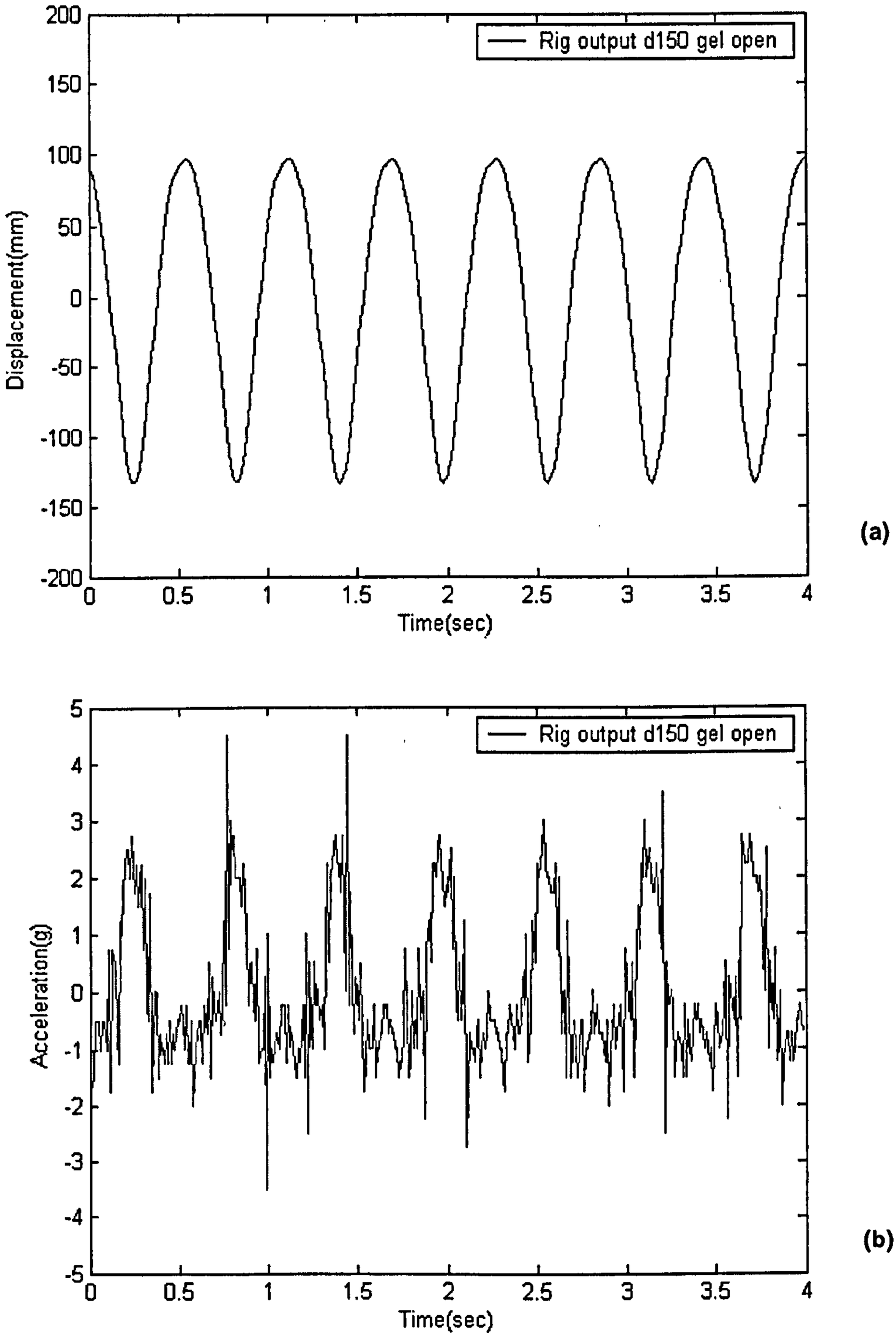

Figure 5.14. *The LVDT data of gelatine 150 open model testing, (a) displacement in mm, (b) acceleration double differentiated from displacement in g.*

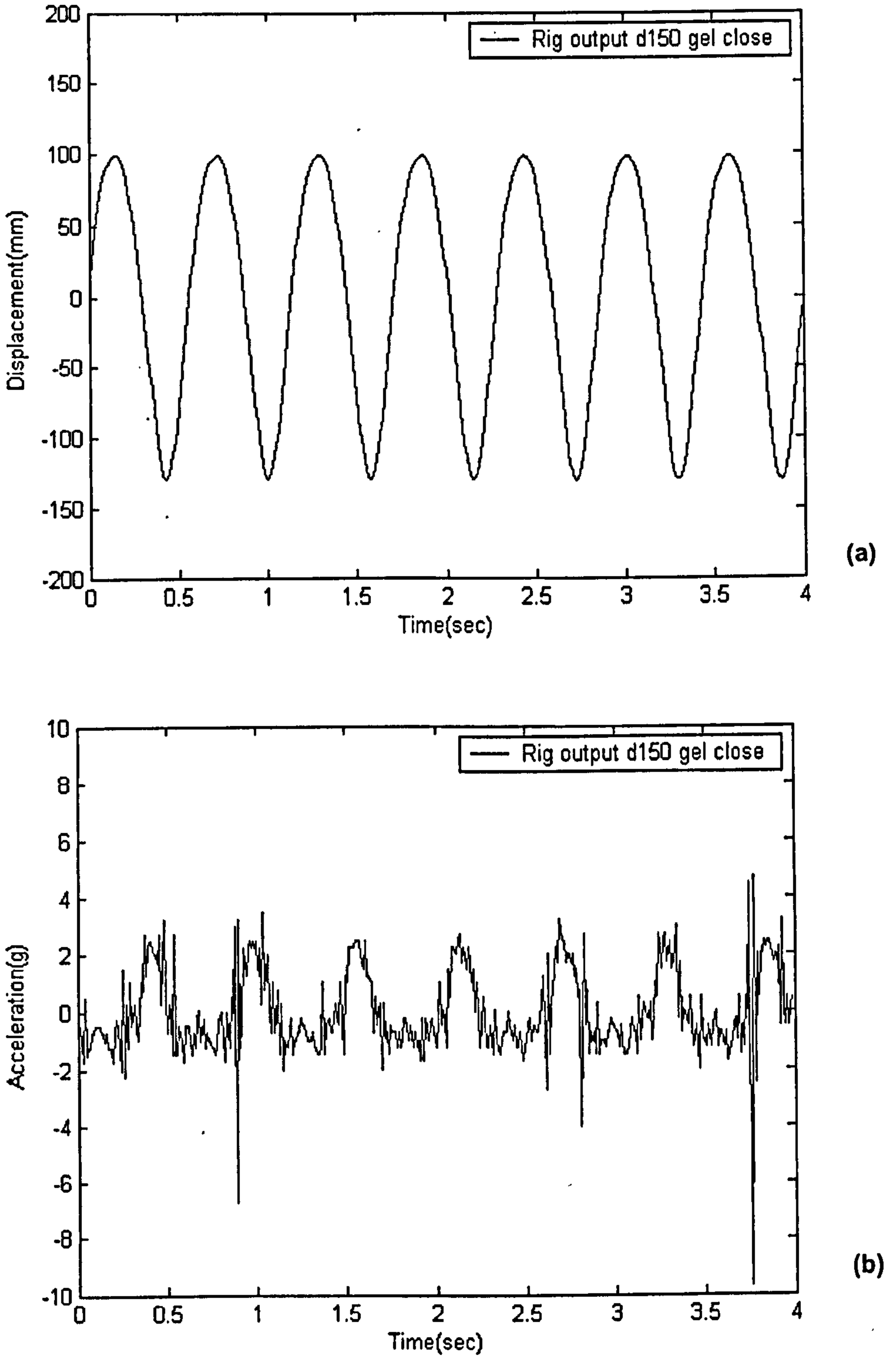

Figure 5.15. *The LVDT data of gelatine 150 closed model testing, (a) displacement in mm, (b) acceleration double differentiated from displacement in g.*

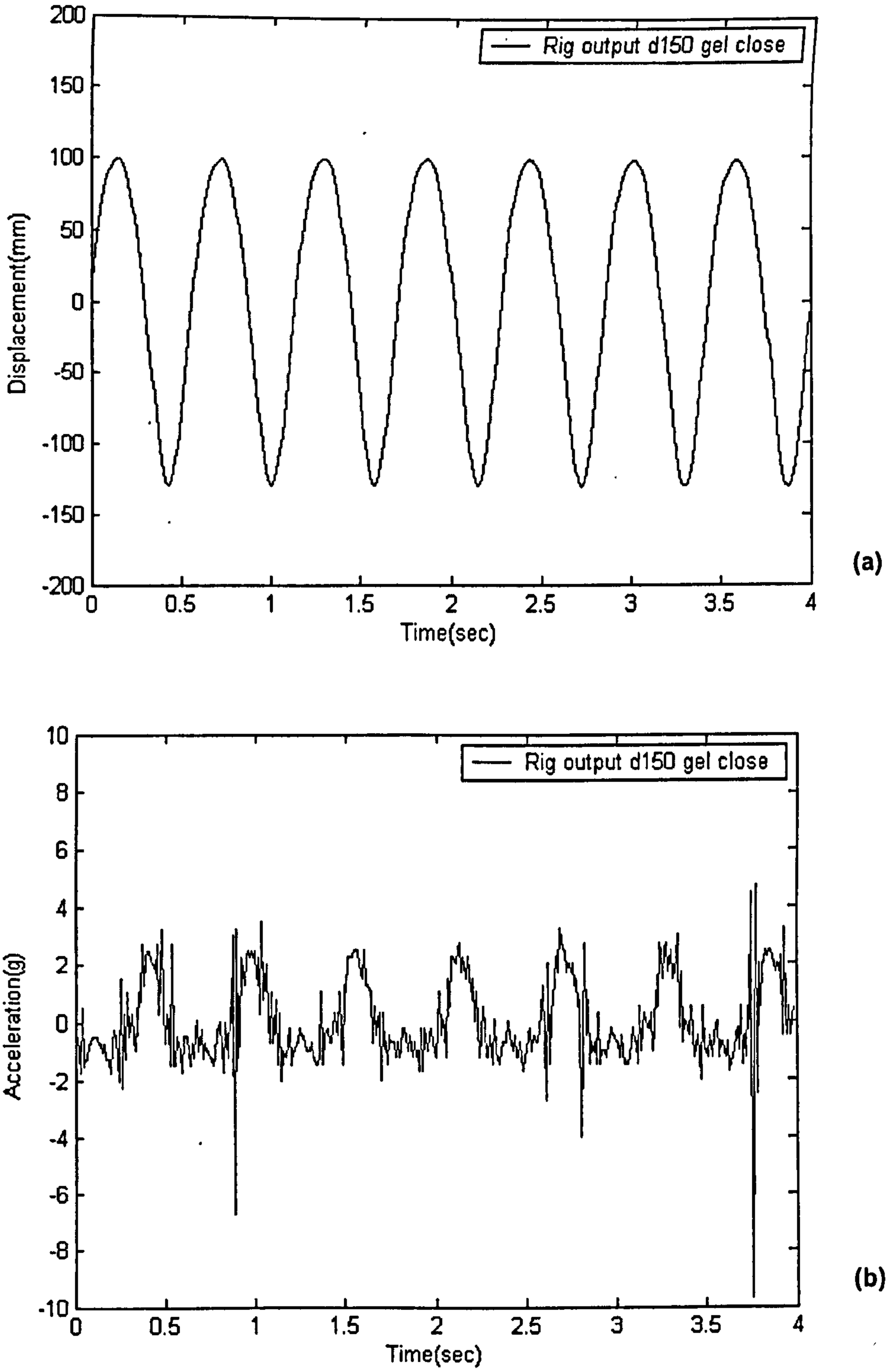

Figure 5.15. *The LVDT data of gelatine 150 closed model testing, (a) displacement in mm, (b) acceleration double differentiated from displacement in g.*

Test No.	Displacement (mm)		Velocity (mm/s)		Acceleration (g)	
	from	to	From	to	from	to
1	-175	125	-1200	1300	-2	2.5
2	-125	100	-1250	1500	-2	2.5
3	-150	100	-1300	1500	-1.7	3
4	-125	100	-1200	1300	-1.5	2.5
5	-125	100	-1250	1250	-1.8	2.5
6	-130	100	-1200	1200	-1.8	2.5

Table 5.2. The peak value of displacement, velocity and acceleration of the rig produced on each model during the testing.

5.4. The Synchronization Of The Transducer

Synchronization of the results from the webcams and the LVDT would have enabled quantitative reconstruction of the membrane deformation. In fact, during the tests reported here, the webcam and LVDT data streams entered the PC separately, with no common origin of time. The current results therefore only give a qualitative reconstruction of what happened. Further development will be focused on the design of the synchronization of different transducers (Chapter 10, §10.3). A LED panel will be used to produce a clear record of a digital counter inside the view of the webcam. The panel will then be triggered from the starting of the rig. This improvement will be built into the rig in future work.

5.5. The Discussion Of Results

In Chapter 3 (§3.1.2) the neck were divided into loose (L), normal (N), and stiff (S) types, the loose neck of all the tests produced the largest rotation of the dummy's head about its torso. Furthermore, the analysis of the all the volunteer's data is irrelevant to the research in this stage as long as the shaking is stable. Among all the volunteers, volunteer A provided the motion in the gaze direction (§3.1.3 Figure 3.1) that was the most stable and hence closest to the simulated conditions of the test rig. Therefore, two sets of TRL linear shaking data were chosen from the results from volunteer A with the

soft neck setting of the dummy (Figure 5.16) in order to compare the results of these experiments with those in the TRL tests. Set AL1 refers to slow, long distance shaking and AL2 to rapid, short distance shaking. The horizontal torso displacement during the first 3.5 seconds was selected for comparison with the output data of the pneumatic rig. The AL1 displacement data ranged from -150mm to 150mm and, for AL2 it was from -50 to 50mm with 3 Hz frequency, whilst for the rig, it was from -125 to 100mm with the frequency of 2Hz. The AL1 velocity ranged between -1000 and 1700mm/s and the AL2 data from -1000 to 1000mm/s: this should be compared with that from the pneumatic rig, a velocity from -1250 to 1500mm/s. The AL1 acceleration was from -7g to 10g and the comparative AL2 values from -8g to 10g, while the rig gave a maximum whiplash value of 2.5g.

The above shows that the pneumatic rig produced a repetitive displacement that lay between those of the AL1 and AL2 TRL tests. It can, therefore, mimic the shaking profile generated by a human volunteer on an automotive test dummy. In addition, the rig velocity was comparable with the TRL values, sometimes exceeding it by a modest proportion. However, the magnitude of the rig acceleration was lower than the maximum results in the TRL tests, partly explainable by the longer time of the rig test. This could be improved in future work by reducing the distance of the micro-switches and increasing the airflow inside the circuit.

In conclusion, the pneumatic technique has proved to be appropriate for the simulation of the shaken baby syndrome. The rig needs further development if it is to mimic tests like those done at TRL accurately. Despite that the rig output displacement data was used as an input in the finite element model which is discussed in Chapter 7. This is because, at this stage, we can regard the rig and rig model as an experimental test bed to generate data for the validation of the finite element model to be discussed later.

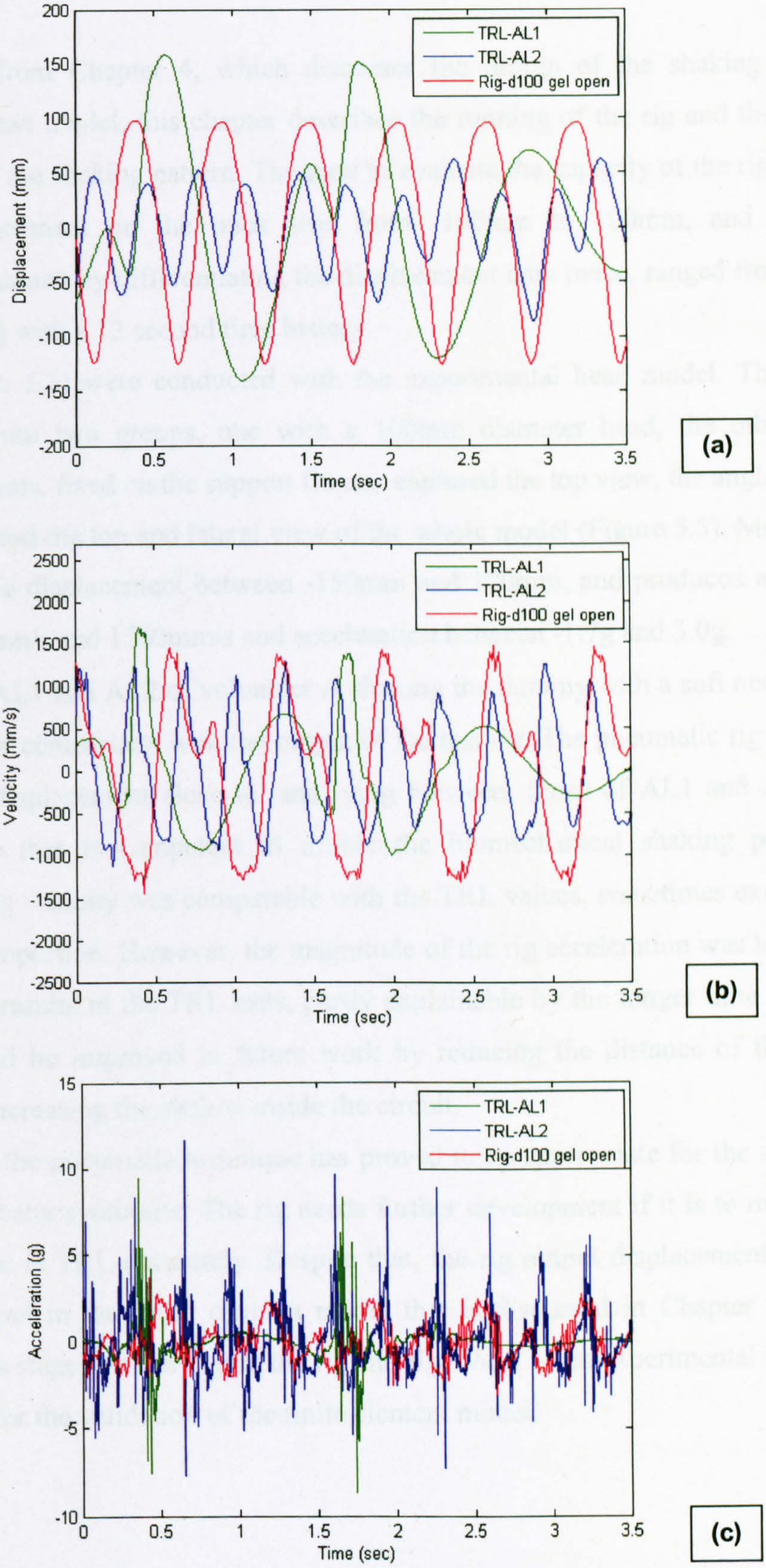

Figure 5.16. *The result and comparison by human shaking on torso and the experimental rig shaking on the model. (a) displacement, (b) velocity, (c) acceleration*

SUMMARY

Following on from Chapter 4, which discusses the design of the shaking rig and experimental head model, this chapter describes the running of the rig and the motion reproduction of the shaking pattern. The tests to evaluate the capacity of the rig showed that the displacement on the track was from -150mm to 100mm, and that the acceleration obtained by differentiating the displacement data twice, ranged from -3g to 3g ($g=9.81m/s^2$) with a 12 second time history.

Six tests (Table 5.1) were conducted with the experimental head model. These tests were divided into two groups, one with a 100mm diameter head, the other being 150mm. Webcams, fixed on the support frame, captured the top view, the angle view of the membrane and the top and lateral view of the whole model (Figure 5.3). Most of the tests, involved a displacement between -150mm and 100mm, and produced a velocity between 1300mm/s and 1500mm/s and acceleration between -1.7g and 3.0g.

TRL test data AL1 and AL2 of volunteer A shaking the dummy with a soft neck setting were chosen for comparison with the output of the test rig. The pneumatic rig produces the repetitive displacement close to, and lying between, those of AL1 and AL2, and thereby shows that is competent to mimic the biomechanical shaking profile. In addition, the rig velocity was comparable with the TRL values, sometimes exceeding it by a modest proportion. However, the magnitude of the rig acceleration was lower than the maximum results in the TRL tests, partly explainable by the longer time of the rig test. This could be improved in future work by reducing the distance of the micro-switches and increasing the airflow inside the circuit.

In conclusion, the pneumatic technique has proved to be appropriate for the simulation of the shaken baby syndrome. The rig needs further development if it is to mimic tests like those done at TRL accurately. Despite that, the rig output displacement data was sued as an input in the finite element model that is discussed in Chapter 7. This is because, at this stage, we can regard the rig and rig model as an experimental test bed to generate data for the validation of the finite element model.

CHAPTER 6: *PHYSICAL SHAKING RECONSTRUCTION*

INTRODUCTION

The previous chapter discussed the reproducing of the shaking pattern by the rig-proving tests with six head models. The displacement of the test rig output lies in between the two TRL samples, which was proved to be appropriate for the reproducing shaken baby phenomenon. The rig displacement and the image of the head model were recorded and prepared for the analysed in this chapter.

This chapter discusses the analysis of the motion of the gelatine sphere inside the experimental model. The different consequences between the dome structure and the size are discussed. The movement of the gelatine between the open structure and closed structure was traced and compared, which provided the experimental data to support the FE analysis discussed in Chapter 7.

6.1. METHOD

Four video clips were chosen corresponding to the rig acceleration output described in the last chapter. All are lateral views (Chapter 5, Figure 5.5(b), Figure 5.7(b), Figure 5.8(c), and Figure 5.9(c)) from the webcam that was perpendicular to the sagittal plane of the model. The videos chosen were four types of experimental model; the dome 100mm with open top, dome 100mm with closed top, dome 150mm with open top, and dome 150mm with closed top. Each video clip was differentiated into a series of images with the minimum time step of 0.0664 seconds using VirtualDub 1.6.11. On each image, six paper markers were picked up on the sagittal plane of the gelatine sphere (Figure 6.1) that experienced whiplash movement inside the dome along the shaking direction (Chapter 5, Figure 5.3(a)) during the test. The markers were listed from a1 to a7 for the open structure model, and b1 to b7 for the closed structure model. Markers a5 and b5 were attached to the aluminium bar as the reference and the origin for the local frame. The position of the markers was collected and saved by software ImageTool 3.0 as a pixel vector [x,y].

The distance measured in pixels can then be converted into mm by measuring the diameter of a reference marker on aluminium bar. The paper marker has diameter of 7mm in the 100mm dome test and 9mm in the 150mm dome test. Hence the scale

factor k_{100} and k_{150} can be defined as a ratio of the marker dimension in mm and image coordinates in pixels.

$$k_{100} = \frac{7}{dia_{100}} \tag{6.1}$$

$$k_{150} = \frac{9}{dia_{150}} \tag{6.2}$$

The time history of horizontal position dx_p of each marker was found by subtracting the pixels vector of reference marker 5 from the pixel vector of gelatine marker 1-4, 6 and 7, and multiplying the scale factor k (k_{100} in dome the 100mm test and k_{150} in dome the 150 test).

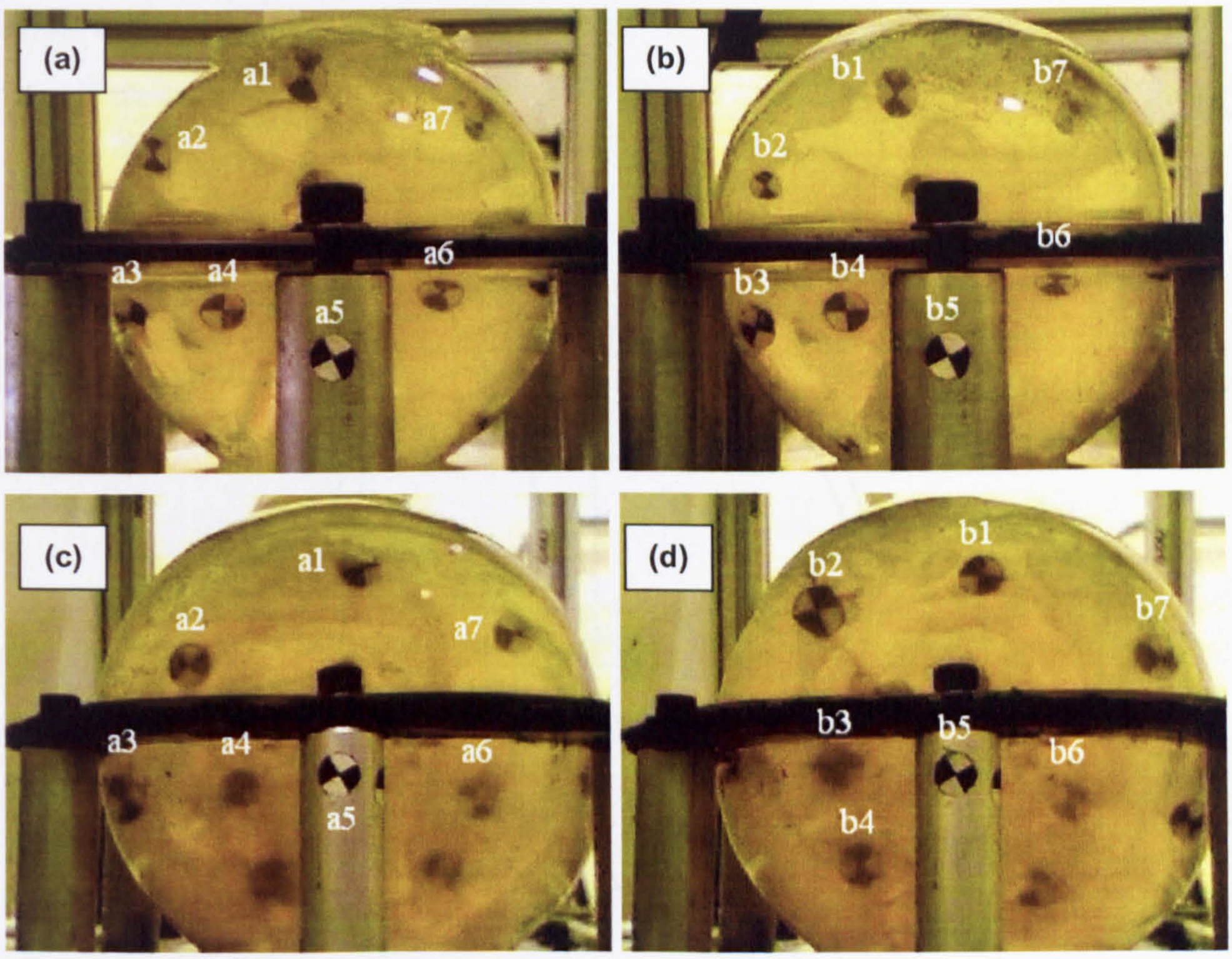

Figure 6.1. *The lateral and top view of the model from two webcam. (a) dome 100mm open; (b) dome 100mm closed; (c) dome 150mm open; (d) dome 150mm closed. The marker position was shown on the pictures. The direction of shaking refers to Chapter 5 (Figure5.4)*

The relative movement dx of each marker can then be found by taking the first data out of the series data dx_p. The rotational movement of the gelatine sphere can be

determined by calculating the rotation angle θ, which represents the rotation of the marker 1-4, 6, 7 on gelatine subjected to the reference marker 5 on the aluminium bar.

$$dx = k \times \left| x_{gel} - x_{Al} \right| \text{ mm} \tag{6.3}$$

$$dx_p = dx - dx_0 \text{ mm} \tag{6.4}$$

$$dy = k \times \left| y_{gel} - y_{Al} \right| \text{ mm} \tag{6.5}$$

$$dy_p = dy - dy_0 \text{ mm} \tag{6.6}$$

The angle θ can be obtained from the horizontal distance dx and vertical distance dy between the gelatine marker and reference marker (Figure 6.2, Equation 6.7). The time history of the first 7 seconds motion was reconstructed out of the approximately 40 seconds test.

$$\theta = tg^{-1}\left(\frac{dx}{dy}\right) \text{ rad} \tag{6.7}$$

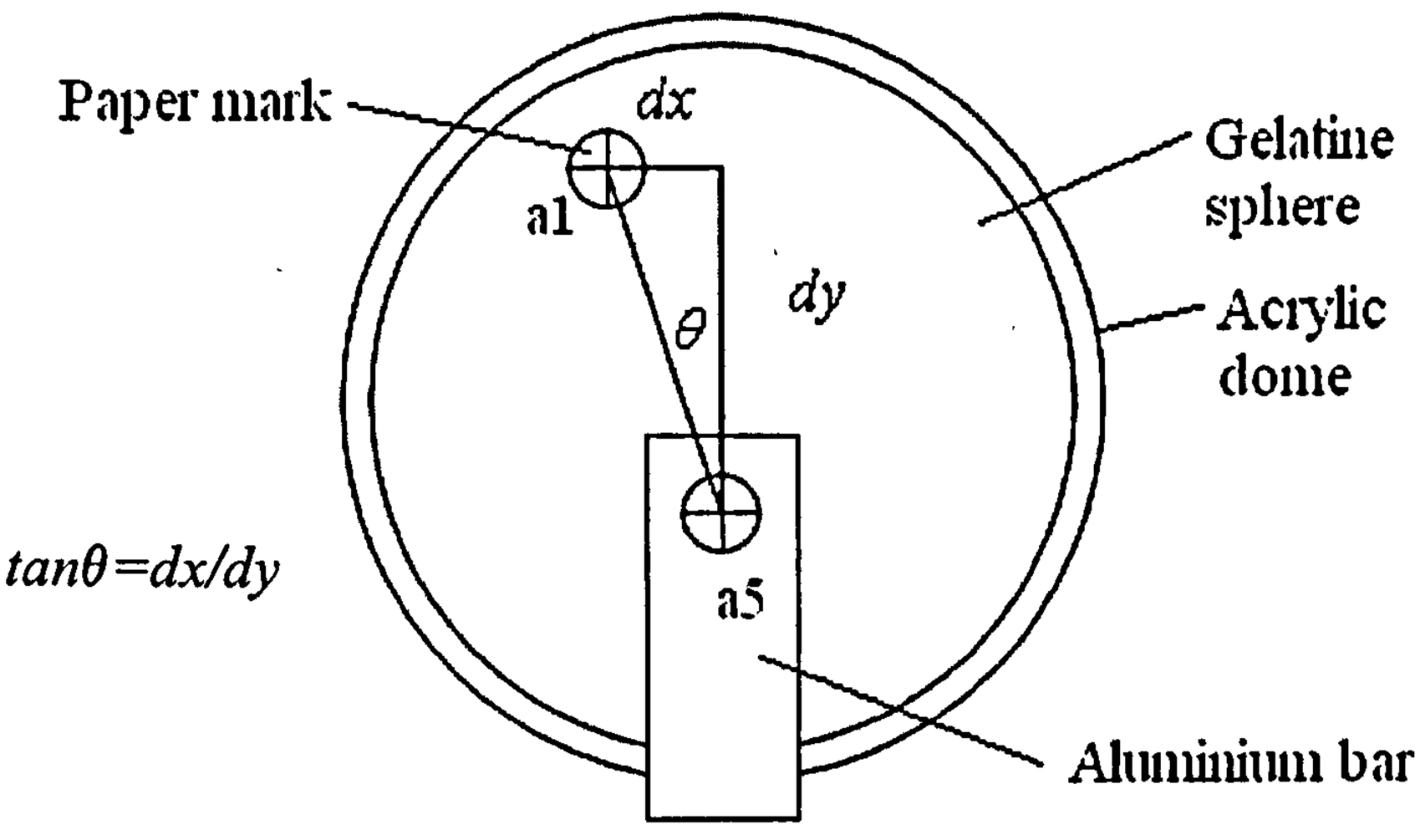

Figure 6.2. *The diagram of getting the linear and rotational motion of gelatine. dx is the distance between a1 and a5, dy is the distance between a1 and a5, the angle θ comes from tgθ when the angle is small.*

6.2. RESULT

During the testing, the whiplash of the gelatine sphere suspended inside water can be observed from the webcams. The difference in the membrane displacement between two types of dome is too small to be differentiated directly but has to be analysed via the method introduced further in Chapter 10 (§10.3). Figure 6.3-6.6 shows the result of gelatine movement from all four models, with comparison between the dome 100mm of the open and closed structure into one diagram, and dome 150mm of open and closed structure into another diagram. Figure 6.7-6.8 shows the time sequences of the dome 100mm open structure and the 150mm closed structure.

For the dome 100mm (Figure 6.3), the motion of all six markers was compared between the open and closed structures according to their position similarity. Marker a1 and b1, where the bridging veins situated in the real human brain, shows similar horizontal movement on the open structure model to the closed model. Marker a1 & b1 in closed model gives regular sinusoidal whiplash around the original position, with a magnitude of -2mm to 2mm for peak value.

Figure 6.4 shows the rotational angle of each marker position in the 100mm dome. The gelatine sphere in the open and closed dome rotates around the reference point b5 in regular sinusoidal profile with the magnitude of -3 degree to 4 degree.

For the dome 150mm (Figure 6.5), marker 1, 2, 7 (Figure 6.1 (c)-(d)) were compared and discussed between the open and closed structure model because of the similarity of the position of all six markers on the gelatine. The difference according to the structure variation gives no significant discrepancy on the gelatine movement according to the motion analysis in first 7 seconds. The magnitude of linear motion for both models is between -2mm to 2mm, and the angle is between -3 degree to 3 degree (Figure 6.6).

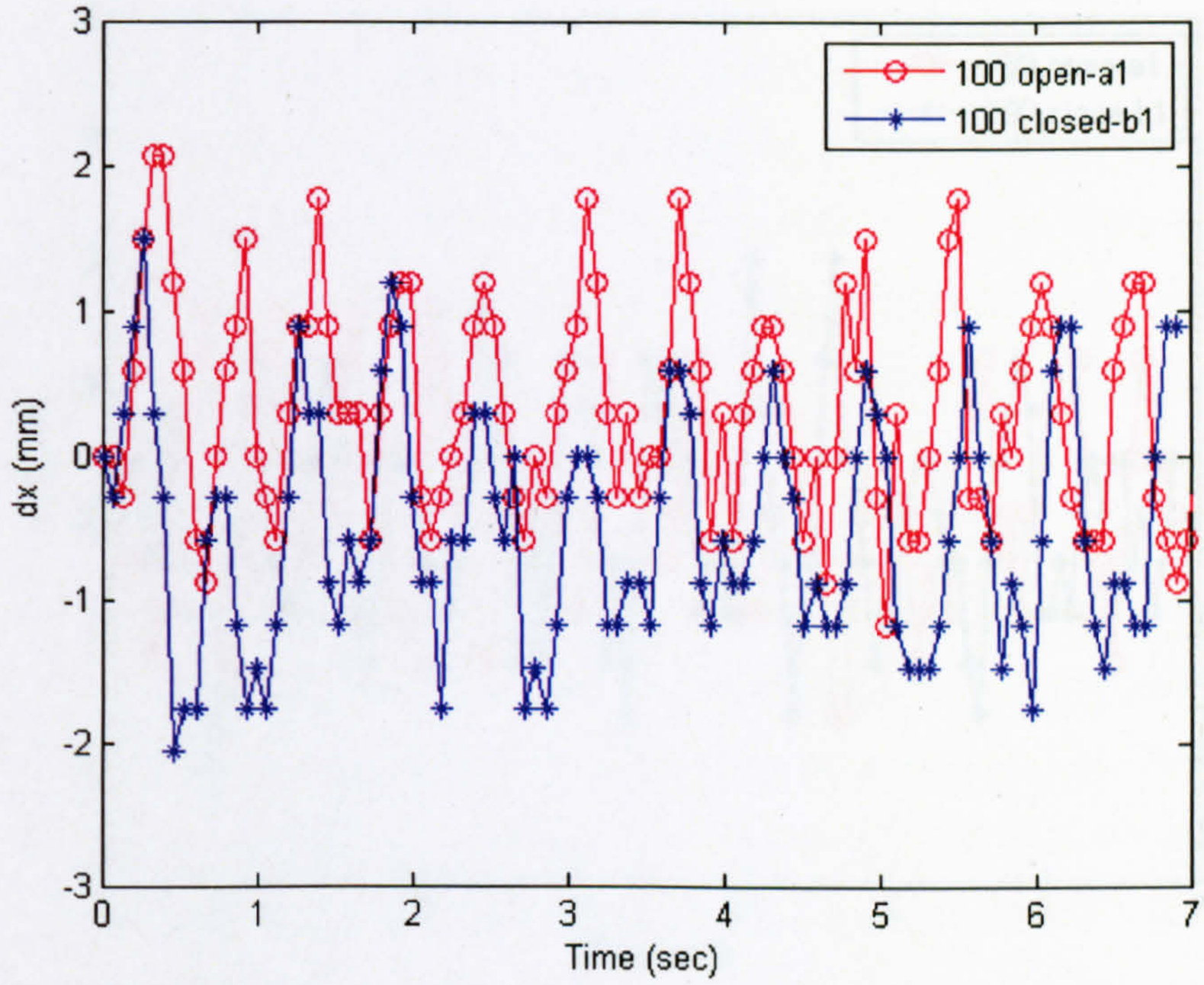

Figure 6.3. *Linear dx of dome 100mm, paper marker a1 & b1.*

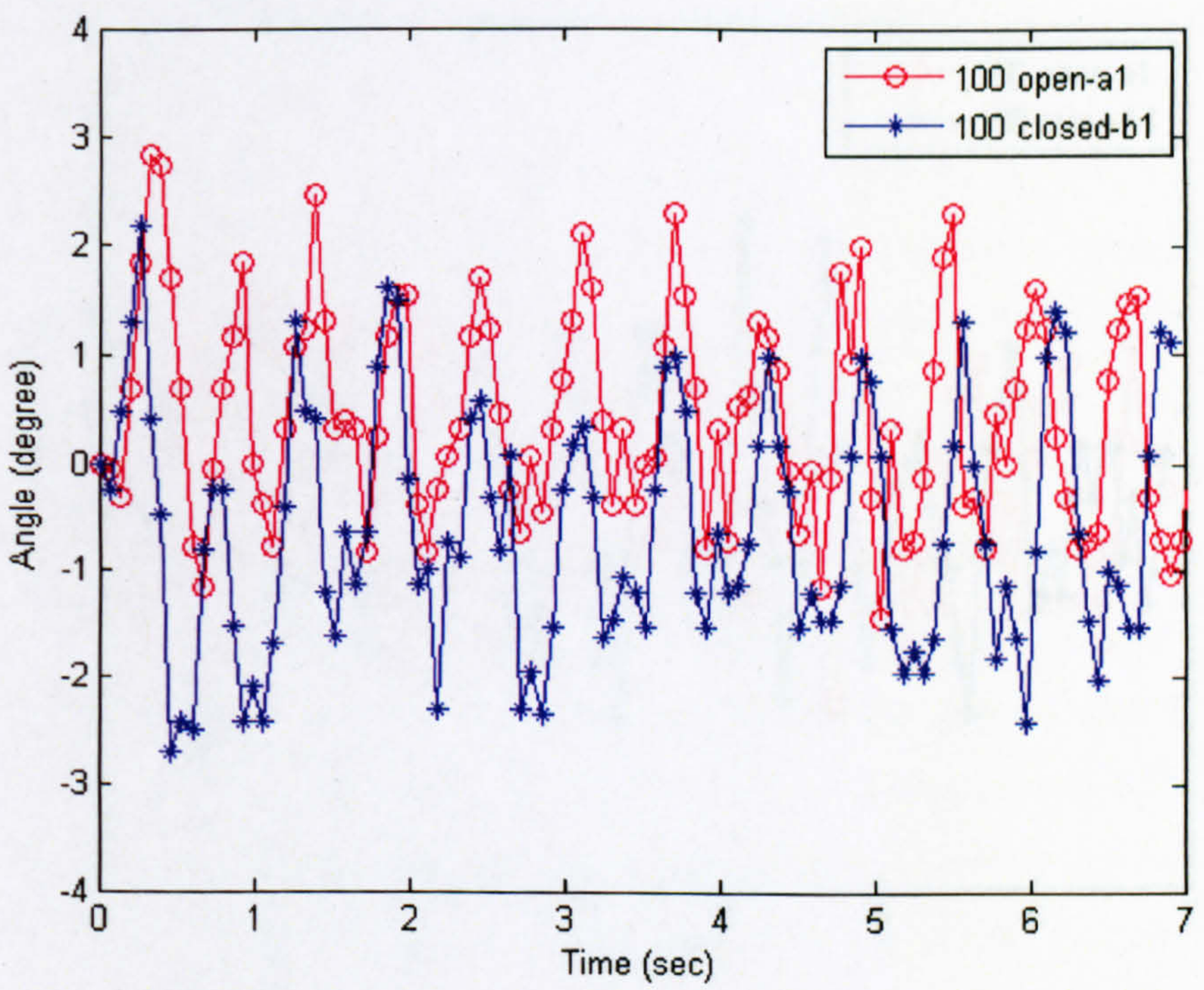

Figure 6.4. *angle θ of dome 100mm, paper marker a1 & b1.*

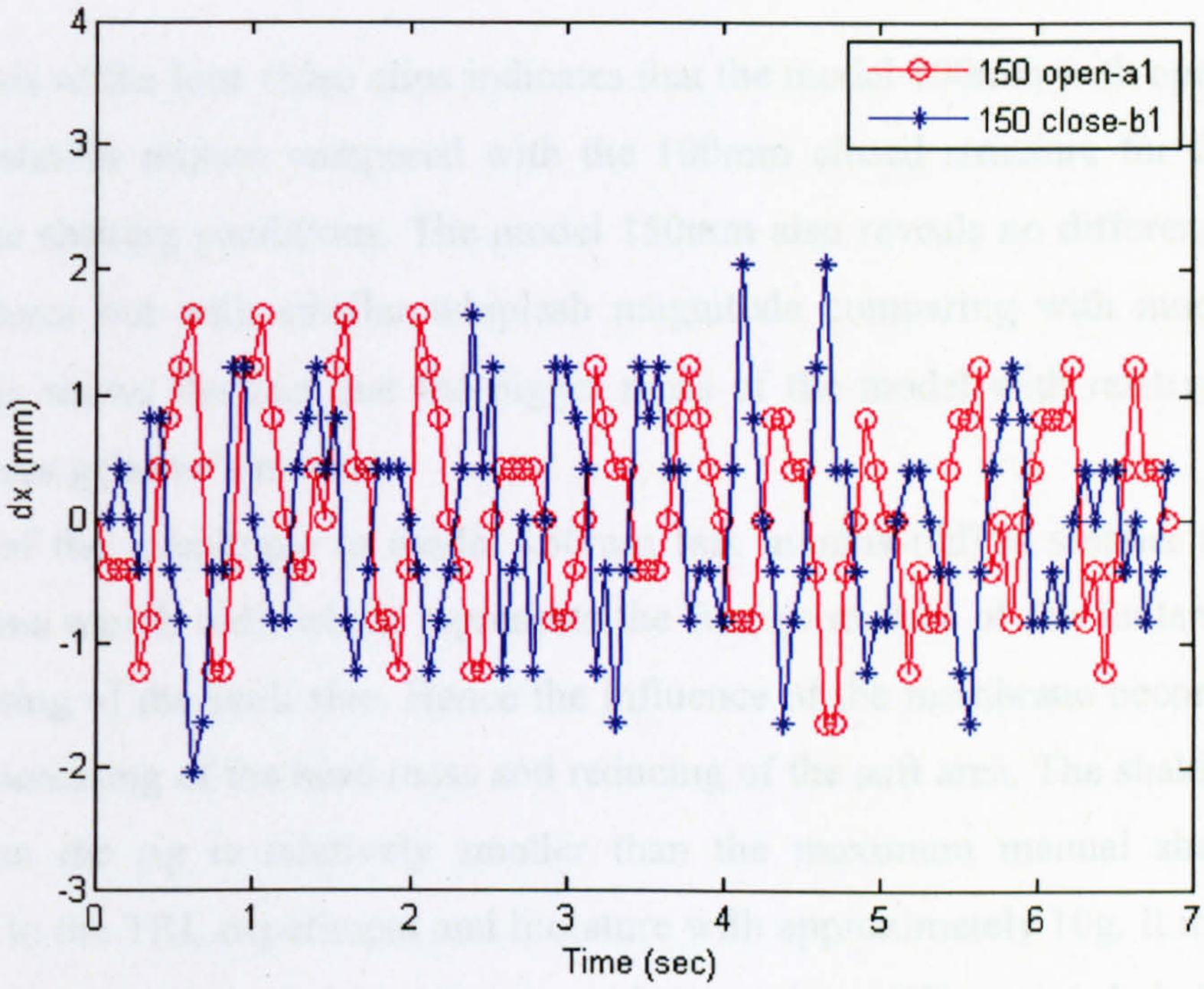

Figure 6.5. *Linear dx dome 150mm, paper marker a1 & b1.*

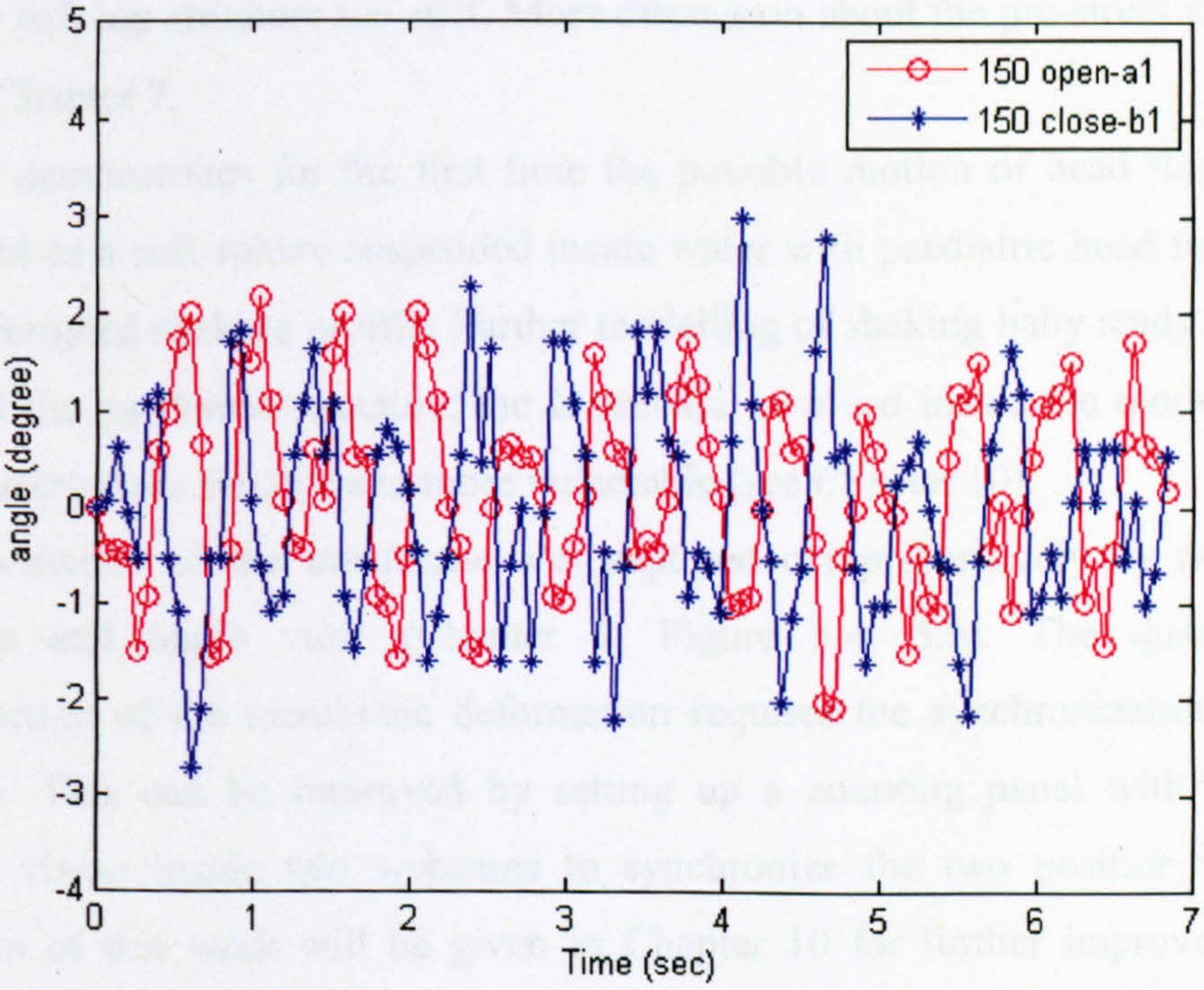

Figure 6.6. *Angle θ dome 150mm, paper marker a1 & b1.*

6.3. DISCUSSION

The analysis of the four video clips indicates that the model 100mm with open structure brings in similar motion compared with the 100mm closed structure for the gelatine under same shaking conditions. The model 150mm also reveals no difference between two structures but with smaller whiplash magnitude comparing with model 100mm dome. This shows the fact that the bigger mass of the model with relatively smaller force reduces gelatine's motion.

The area of the membrane in model 150mm (six months old) is smaller than model 100mm (one month old), which represents the fuse procedure of the fontanelle during the increasing of the skull size. Hence the influence of the membrane becomes weaker with the increasing of the head mass and reducing of the soft area. The shaking force of 2g-3g from the rig is relatively smaller than the maximum manual shaking force according to the TRL experiment and literature with approximately 10g. It may indicate the lack of proper force that is strong enough to produce differentiated shaking effects inside the model. Another reason for the similarity is possibly due to the engineering design of the compression ring that brought into extra stress on the membrane, and made the soft top structure too stiff. More discussion about the pre-stress effect will be given in Chapter 7.

This test demonstrates for the first time the possible motion of head tissue which is considered as a soft sphere suspended inside water with paediatric head features under custom designed shaking profile. Further modelling of shaking baby study requires full details of the paediatric structure; the fontanelle involved inside the model makes the whole system more flexible and more vulnerable (see Chapter 10).

The deformation of the membrane was captured comprehensively by two webcams from top and angle view (Chapter 5, Figure 5.4, 5.6). The quantitative 3D reconstruction of the membrane deformation requires the synchronization of the two webcams. This can be improved by setting up a counting panel with LED digital counting vision inside two webcams to synchronize the two position images. The discussion of this work will be given in Chapter 10 for further improvement of the experimental rig.

SUMMARY

Following by the shaking test in Chapter 5, this chapter analyzed the internal movement of the gelatine within the 100mm and 150mm for both closed and open structures. Four video clips were chosen and each video clip was differentiated into a series of images with the minimum time step of 0.0664 second via VirtualDub 1.6.11. During the testing, the whiplash of the gelatine sphere that suspended inside water can be observed from webcams. Figure 6.7 and Figure 6.8 gives the time sequence of gelatine movement in one pair of 100mm dome. The analysis of the four video clips indicates that the model 100mm with open top brings in similar motion compared to the gelatine in the 100mm closed model under same shaking conditions. The area of the membrane in model 150mm (6 month old infant) is smaller than model 100mm (newborn infant). The similarity motion of gelatine between the two different structures indicated the possibility of insufficient loading, and the possibly of extra strain induced by the engineering design and the assembly of the model. The latter would be given more discussion in Chapter 7. The analysis of shaking the custom designed physical model, for the first time, demonstrates the possibility of the brain movement inside the skull experimentally during shaking. The results provided the validation for the numerical analysis in Chapter 7.

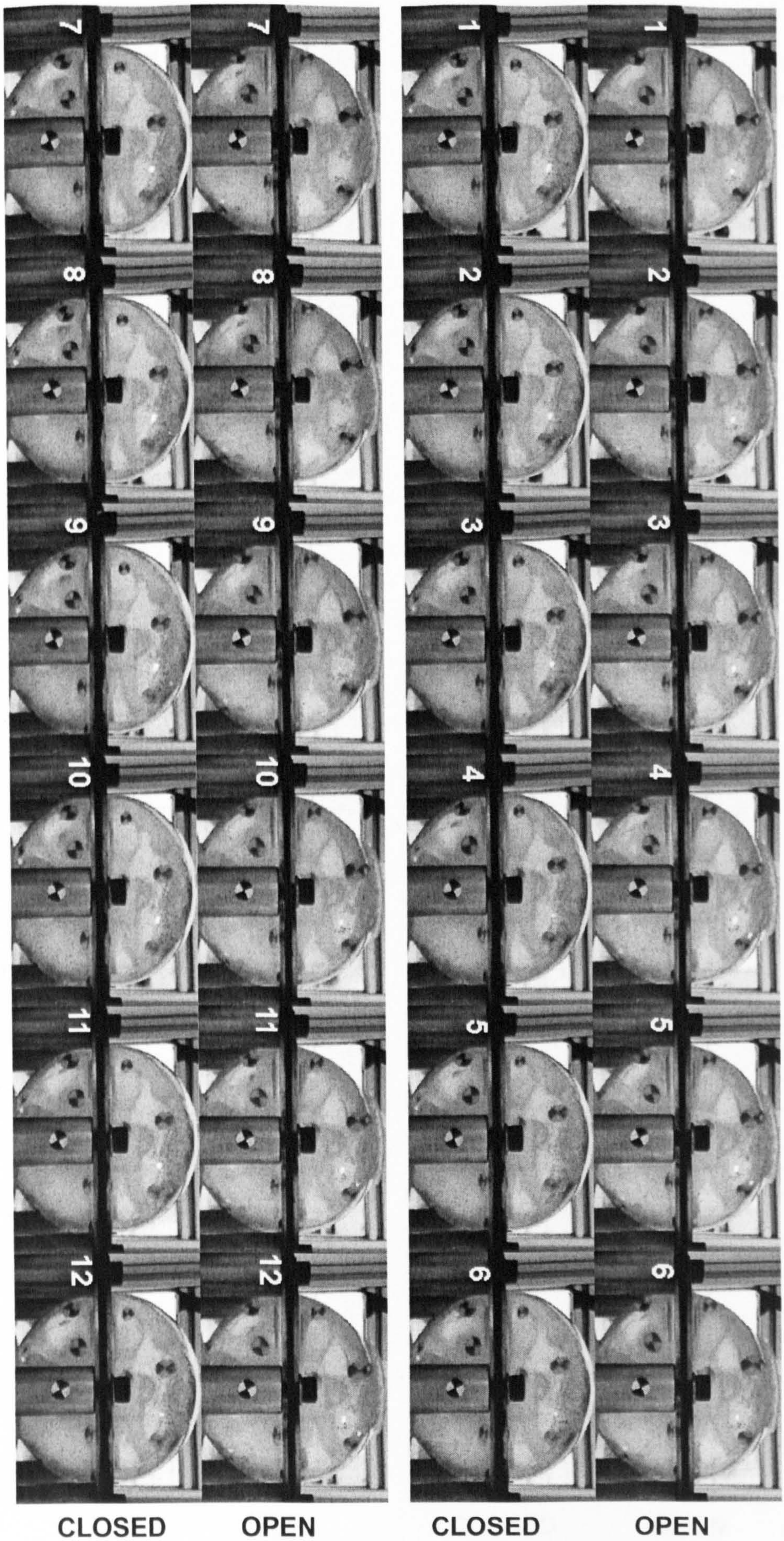
CLOSED
OPEN
CLOSED
OPEN

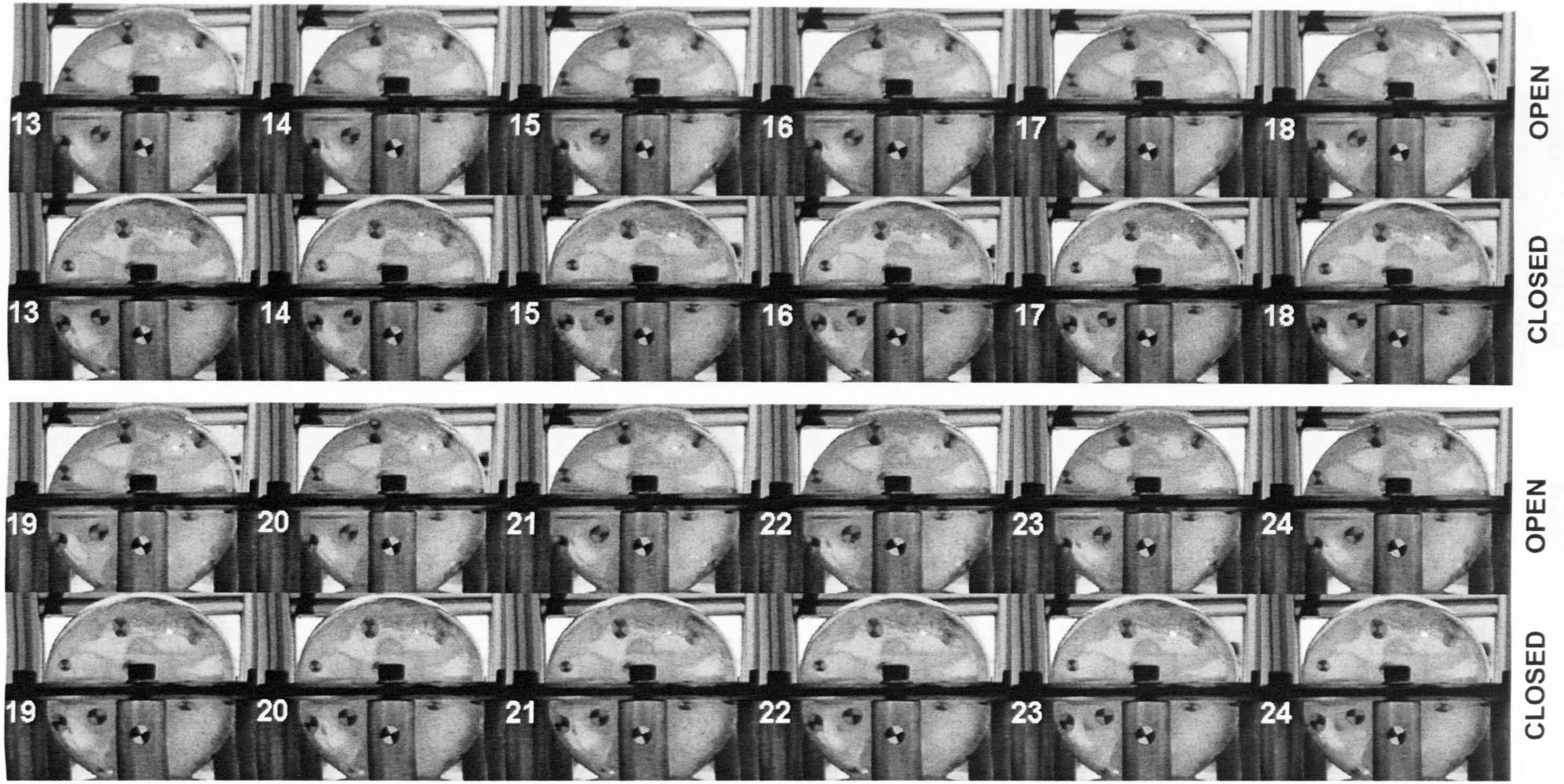

Figure 6.7. *Diagram of time sequence of experimental 100mm dome shaking. Each row: top-open, bottom-closedl. Each model was demonstrated by 24 pictures, approximately 2.5 shaking, lasts 1.60sec. The time step between each adjacent picture is 0.066sec.*

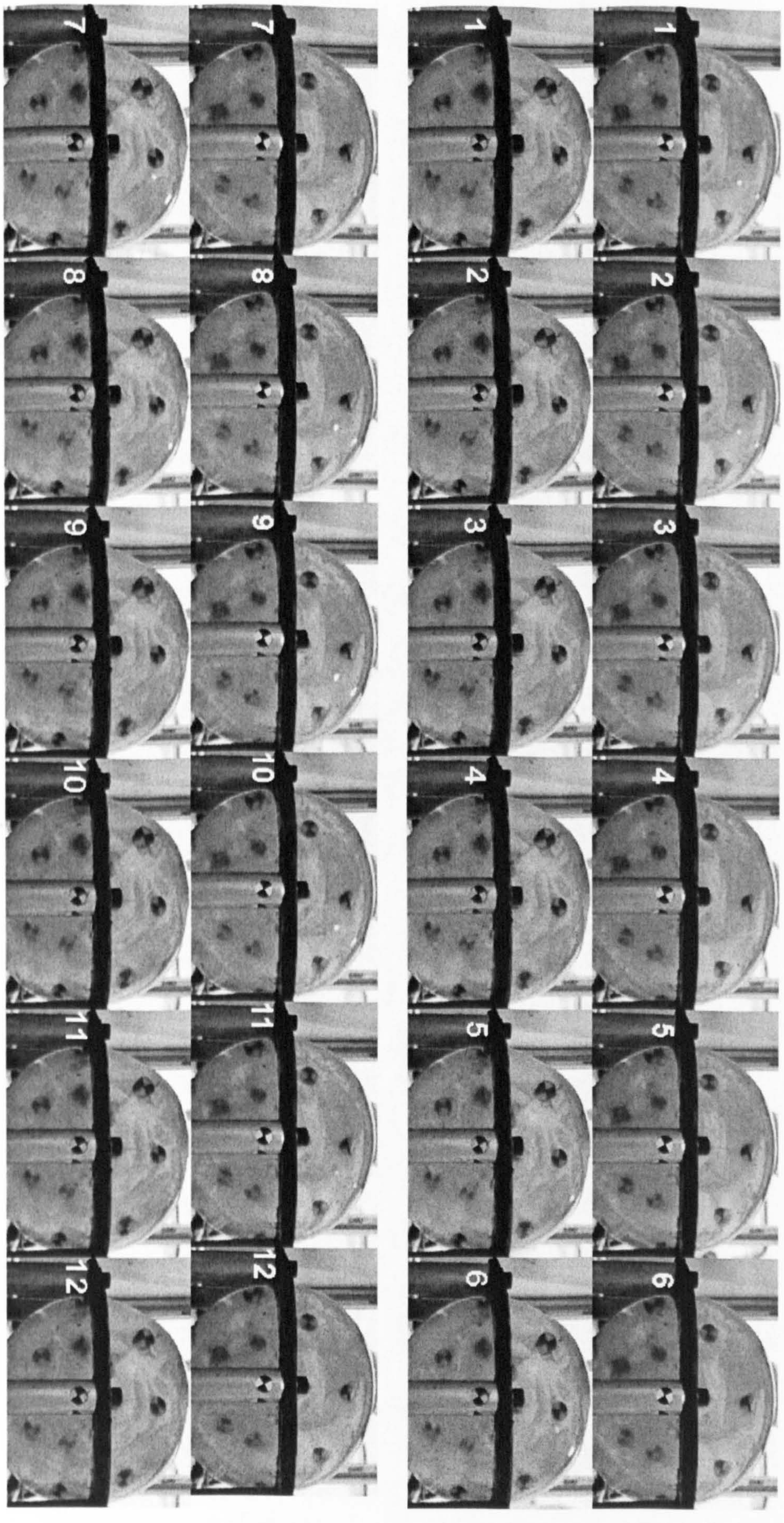

CLOSED OPEN CLOSED OPEN

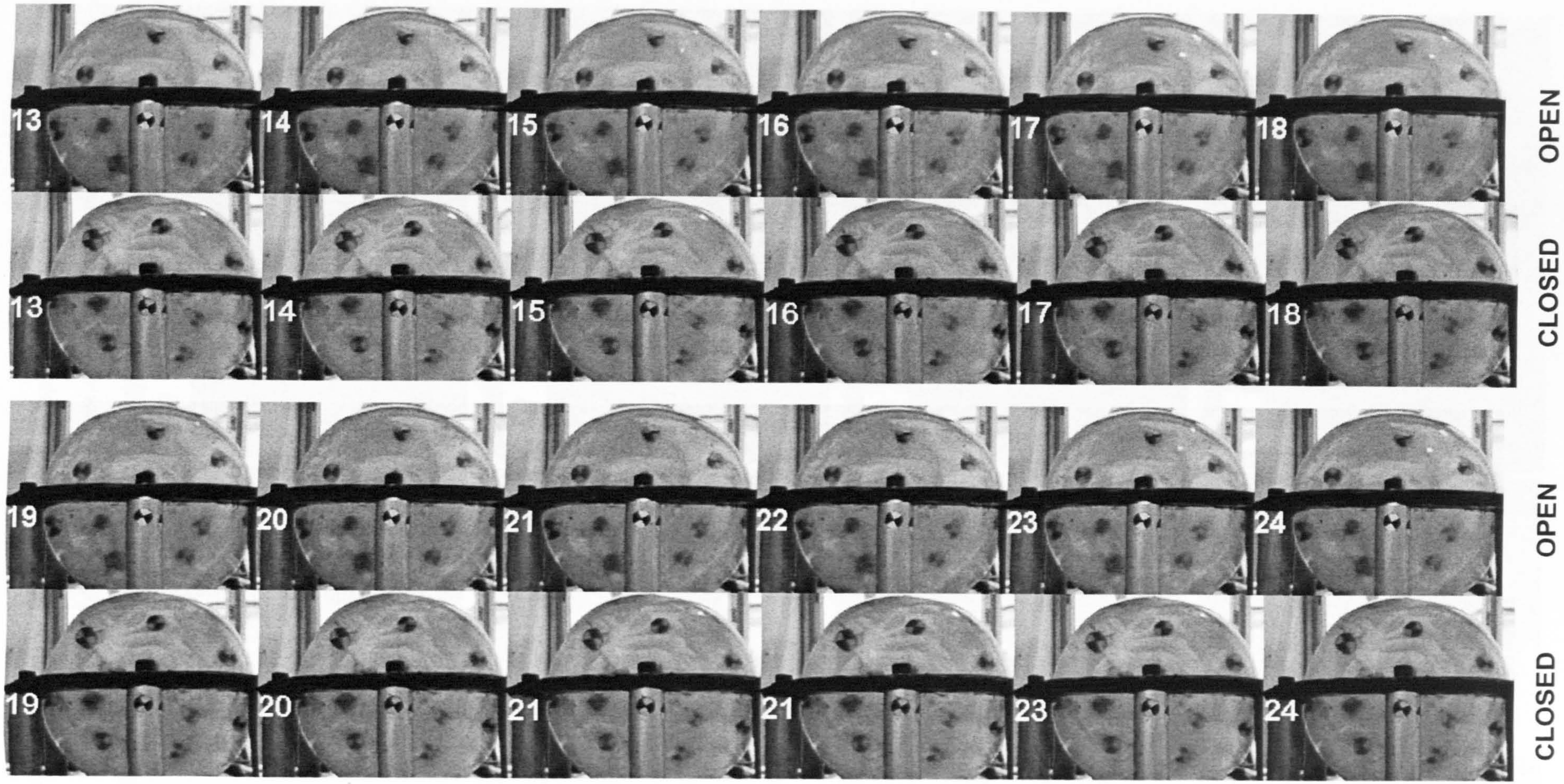

Figure 6.8. *Diagram of time sequence of experimental 150mm dome shaking. Each row: top-open, bottom-closedl. Each model was demonstrated by 24 pictures, approximately 2.5 shaking, lasts 1.60sec. The time step between each adjacent picture is 0.066sec.*

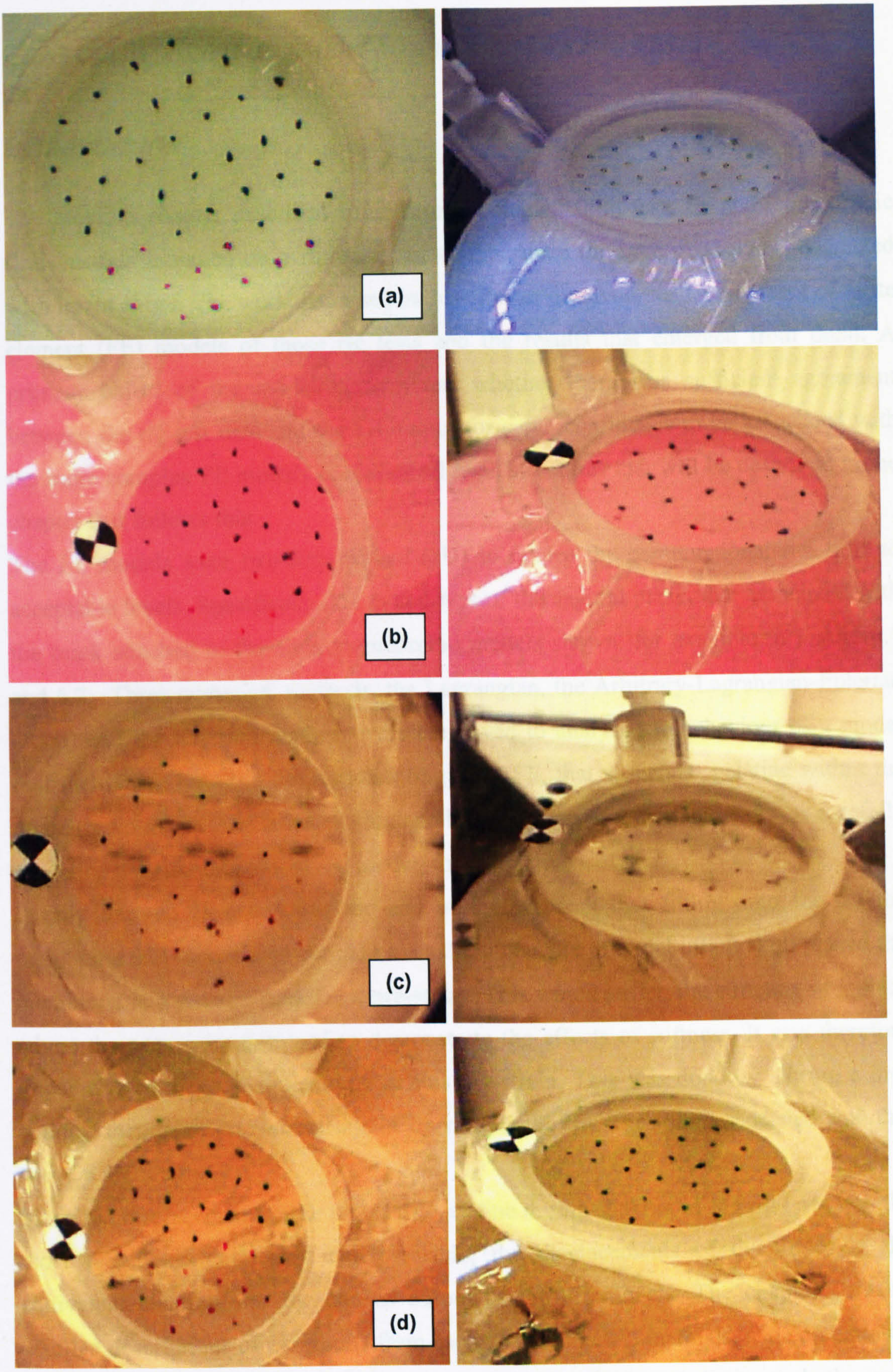

Figure 6.9. *The membrane from two webcam in top and angle view of (a) dome 100mm, water; (b) dome 150mm water; (c) dome 100mm gel; (d) dome 150mm gel.*

CHAPTER 7: *FINITE ELEMENT MODELS OF THE RIG TESTS*

INTRODUCTION

The previous chapter described some results obtained from tests on anthropomorphic skull models mounted on a rig designed to reproduce the type of shaking associated with infant abuse. The work discussed in this chapter involved the development of finite element (FE) models of those rig tests and the results that emerged from them. A primary object of the modelling was test whether there was sufficient agreement between the rig test data and the FE output for some confidence to be associated with the more complex FE models of biological head structures that will be described in the chapter that follows this.

The FE models were two-dimensional (2D) to reduce the computational run time to acceptable levels. Specifically, the model was of the sagittal plane, that associated with the mark attached to the anthropomeorphic models shown, for example in Figure 6.1 and 6.2. Three numerical methods, the Lagrangian, the Arbitrary-Lagrangian-Eulerian (ALE) and the Eulerian method, were employed to analyse the behaviour of a model that included a liquid, water, representing the CSF, that suspends gelatine within the dome (brain-skull). The soft spot (fontanelle) on the top of the infant head was carefully modelled with another closed top model, for comparison.

It only became clear towards the end of the research that fitting onto the rig the membrane that represented the skin over the fontanelle in a real infant skull placed the membrane in a state of significant pre-strain. This would stiffen the structure in a place where the tests were designed to demonstrate the effects of softness. It was therefore imperative to measure the amount of this pre-strain. This was done by slitting a pre-strained membrane and measuring the opening of the slit. The strain associated with this was the pre-strain.

Since the displacement of the top of the gelatine during shaking in the rig tests was the most reliable experimental data available, the displacements of the nodes at the equivalent position was the chosen output of the FE models. The chapter contains detailed descriptions of the results from each of the three FE methods, and comparisons between them and the data from the test rig. The conclusions point towards the most

effective way of creating a FE model of a real human infant skull, a study to be described in the chapter that follows this.

7.1. Finite Element Method Of The Rig Tests

The models of the rig head structures comprised two-dimensional slices in the sagittal plane and were constructed using ANSYS 8.0 (ANSYS Inc., Houston, PA) software. Two geometries were considered, one based on the "open top" model and consisted of a rigid dome, water, the gelatine mixture, and a latex membrane. The other was based on the "closed top" model and consisted of only a rigid dome, water, and the gelatine mixture (Figure 7.1). The tops of the gelatine in both geometries were modelled as flat surfaces to relate reasonably with physical reality and for ease of mesh generation. Inside both models, the water and gelatine were modelled by 1088 eight-noded linear brick elements. The rigid dome as well as the membrane in the "open top" case was modelled by using 63 four-noded shell elements.

Two geometric sizes were involved, with one using the 100mm diameter (1.5 month old infant) and another using the 150mm diameter (6 month old infant) for both open and closed models. The 150mm diameter 3D models are discussed in Appendix J.

Another 2D head model was also created for the Eulerian method whereby the void mesh was fixed during the simulation with only material advection inside (Figure 7.2). The geometry allowed a structural part for the skull, scalp and brain, and a fluid part for the CSF and void mesh. It consisted of 91 linear four-noded shell elements and 1652 linear eight-noded solid elements. A zoning study was undertaken to verify convergence.

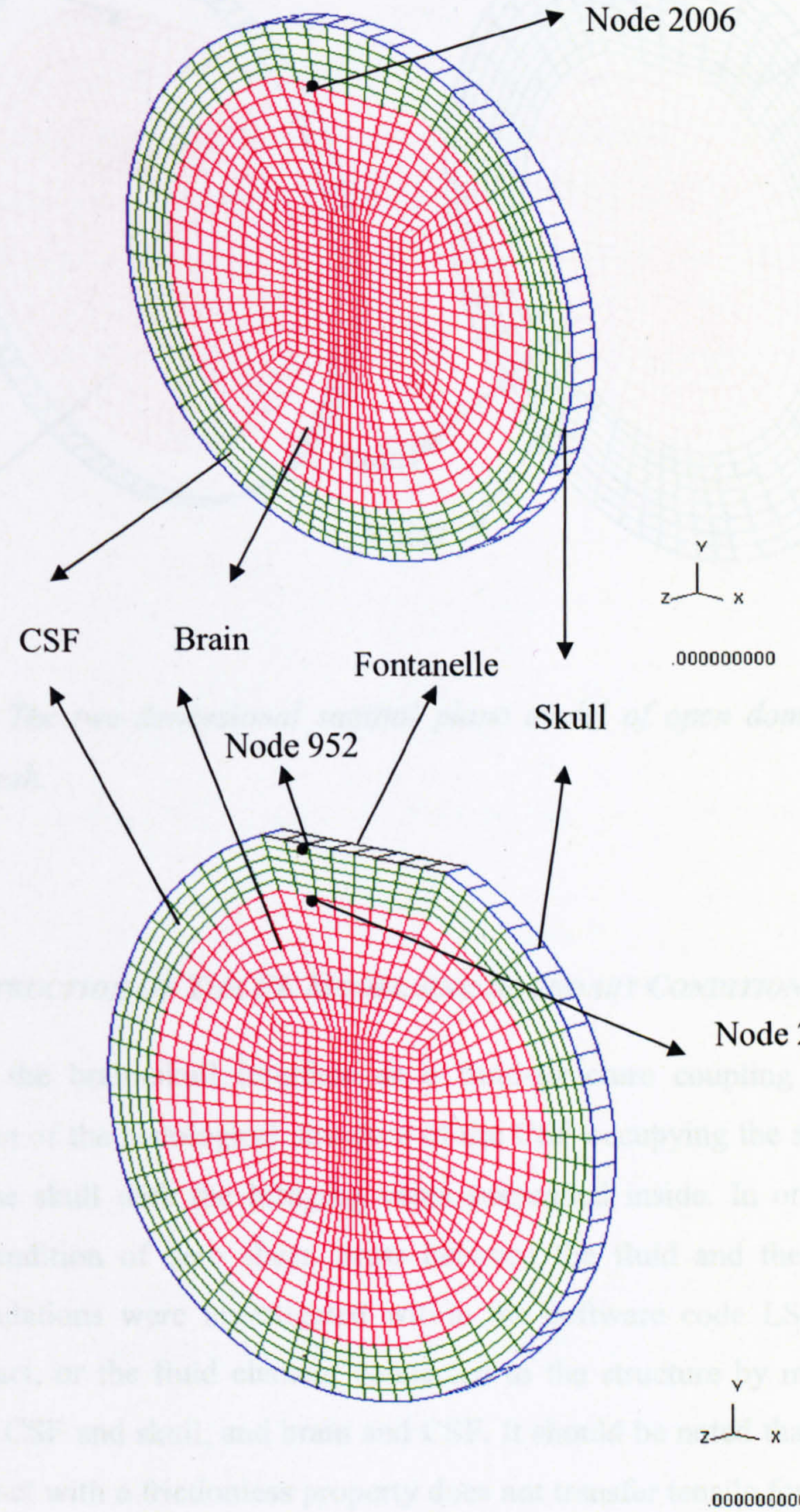

Figure 7.1. *The two-demonsional sagittal plane model of open and closed dome using Lagrangian and 1-point ALE method.*

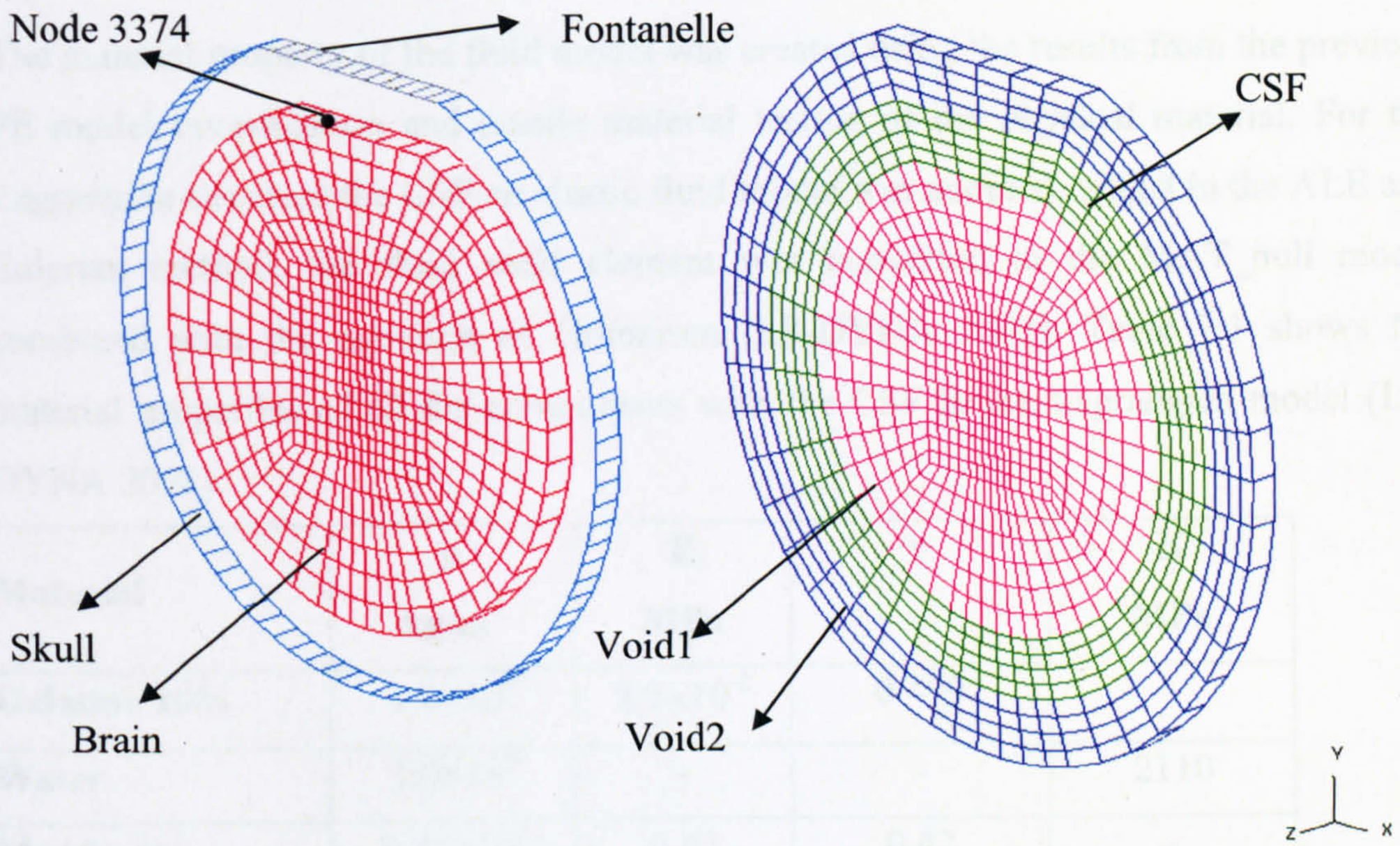

Figure 7.2. *The two-dimensional sagittal plane model of open dome using Eulerian fluid field mesh.*

7.1.1. Construction Of The FE Model And Boundary Conditions

Interpreting the brain-skull interface as a fluid-structure coupling is a mechanical simplification of the histological structure of the CSF occupying the space between the brain and the skull with the bridging veins suspended inside. In order to model the boundary condition of zero shear stress between the fluid and the solid structures, various simulations were investigated within the software code LS-DYNA, such as sliding contact, or the fluid element connected to the structure by merging the nodes between the CSF and skull, and brain and CSF. It should be noted that using surface to surface contact with a frictionless property does not transfer tensile forces in the normal direction and therefore it under-estimates the brain-skull coupling (Wittek and Omori 2003). It was not considered suitable for use in this instance. Therefore three approaches were used for the simulation, two of them, the Lagrangian method and the 1-point ALE method (Figure 7.1), work by rigidly attaching the fluid elements to the rigid dome and gelatine elements. The third method, allows fluid material flux transfer through the fitting mesh, and is modelling with a new mesh geometry (Figure 7.2).

7.1.2. THE MATERIAL CONSTITUTIVE MODEL

The material property of the fluid model was created using the results from the previous FE model investigation and tensile material testing of the physical material. For the Lagrangian structure the CSF an elastic fluid model was adopted, whilst in the ALE and Eulerian method, the fluid solid element was converted to the MAT_null model combined with the equation of Gruneisen (LS-DYNA 2003). Table 7.1 shows the material properties of all the components with the CSF in the Lagrangian model (LS-DYNA 2003).

Material	**ρ kg/m^3**	**E MPa**	**υ**	**K MPa**
Gelatine 10%	1.0×10^3	2.7×10^{-2}	0.499	-
Water	1.0×10^3	-	-	2110
Membrane	0.44×10^3	0.42	0.42	-
Dome	2.1×10^3	1300	0.22	-

E=Young's modulus (MPa); ρ=mass density (kg/m^3); υ=Poisson's ratio; K=bulk modulus (MPa);

Table 7.1. The material property of the head components.

$$p=\frac{\rho_0 C^2\mu\left[1+\left(1-\frac{\gamma_0}{2}\right)\mu-\frac{a}{2}\mu^2\right]}{\left[1-(S_1-1)\mu-S_2\frac{\mu^2}{\mu+1}-S_3\frac{\mu^3}{(\mu+1)^2}\right]}+(\gamma_0+a\mu)E \qquad (7.1)$$

where p is the pressure for compressed material, C is the intercept of the V_s-V_p curve; S_1, S_2, and S_3 are the coefficients of the slope of the V_s-V_p curve; γ_0 is the Gruneisen gamma; a is the first order volume correction to γ_0; and $\mu=\frac{\rho}{\rho_0}-1$.

7.1.3. PRE-STRAIN EFFECT AND ITS ANALYSIS

As already mentioned, the mounting of the membrane in the rig head model necessarily induces an unknown amount of pre-strain. Realistic finite element analysis of the rig

tests must, therefore, include its effect. This can only be done by first measuring its magnitude. The method was to release the strain by cutting, and to estimate the strain by the opening of the cut. Figure 7.3 illustrates the test to determine the pre-strain in the membrane. The membrane, which was normally stretched by the compression ring, was cut through the centre along a diameter, the resulting gap being 4mm wide at the centre. On removal of the ring, the membrane relaxed to a form with little or no gap along the cut.

These tests (Figure 7.3-7.4) showed that the membrane stretched on the rig model had a pre-strain of approximately 0.1, with an associated pre-stress of 0.042MPa (equation 7.2).

$$\sigma = E\varepsilon = 0.42 \times 0.1 = 0.042\,\text{MPa} \tag{7.2}$$

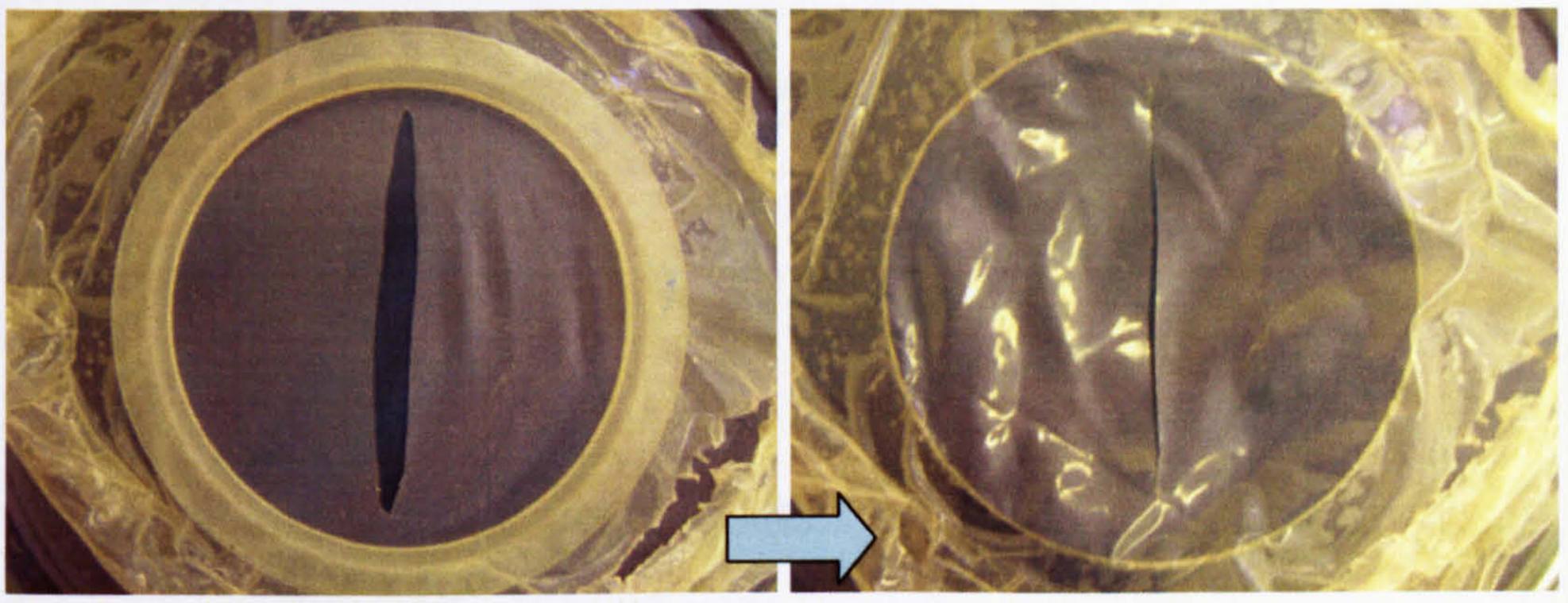

Figure 7.3. *Lab test of pre-stress effect, this effect disappears when the ring was removed.*

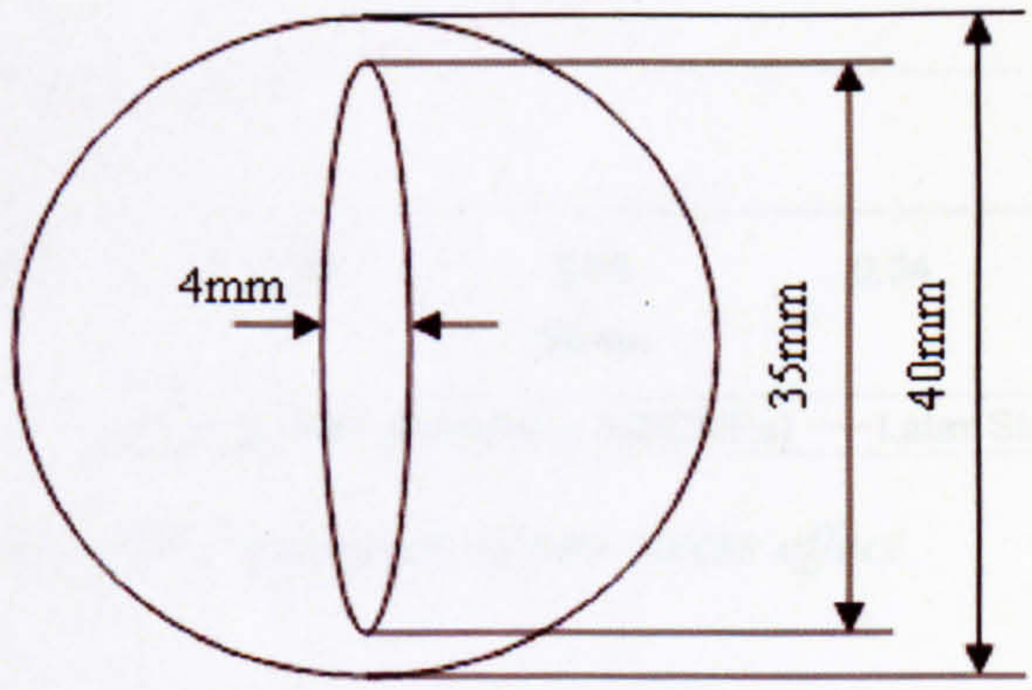

Figure 7.4. *The stretching was measured as equalling 0.1 strain.*

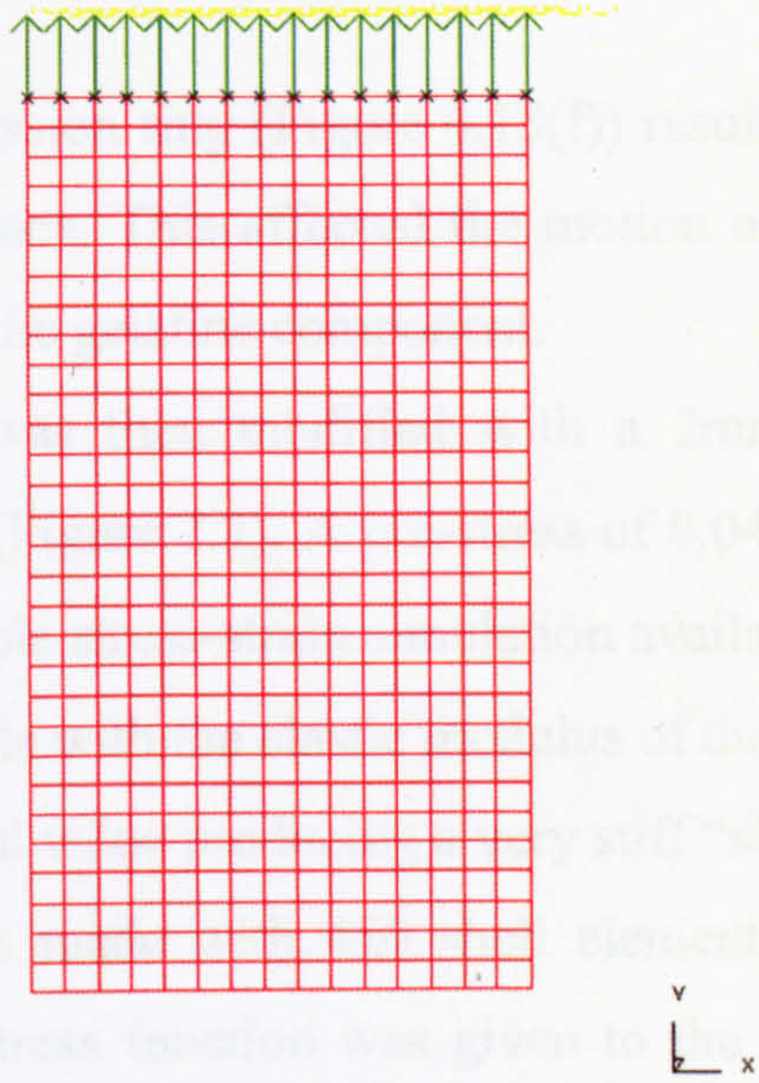

Figure 7.5. *The modelling of film sample under pre-stress tensile test.*

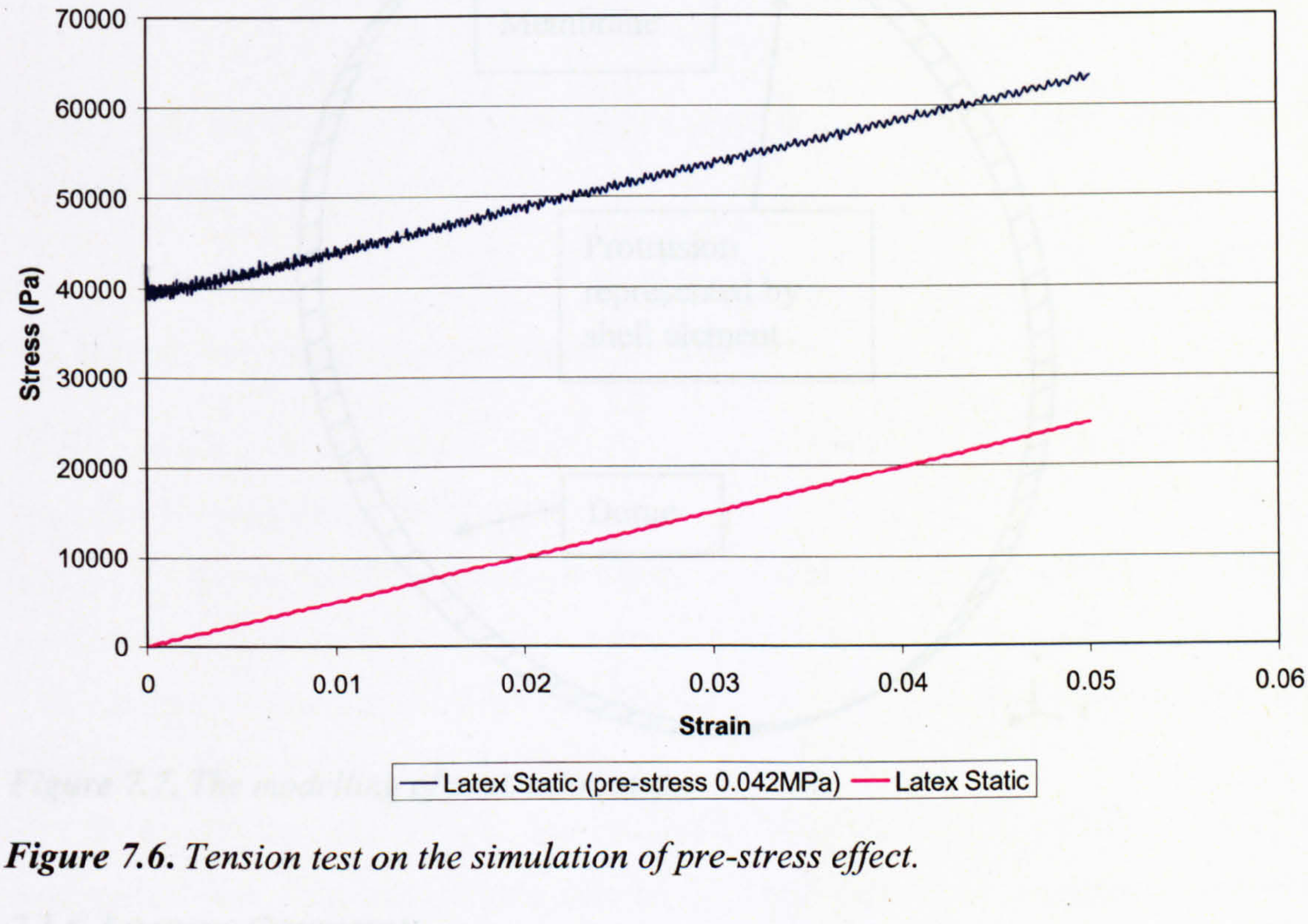

Figure 7.6. *Tension test on the simulation of pre-stress effect.*

Figure 7.5-7.6 shows the validation of the pre-stress effect on a simple tensile test to latex membrane through LS-DYNA.

7.1.4. PROTRUSION EFFECT ON THE COMPRESSION RING

The mounting of the compression ring (Figure 4.15(f)) resulted in part of the structure sticking out into the CSF space. This affected the motion of the CSF and necessarily reduced the displacement of the gelatine component.

The finite element model was then modified with a 2mm protrusion of the shell elements into the fluid field (Figure 7.7). A pre-stress of 0.042MPa was then applied to the membrane using the simple stress-strain simulation available in LS-DYNA. Finally, a comparison model was made with the elastic modulus of the membrane some 10 times greater than that of its original value producing a very stiff "skin" of modulus 4.2MPa.

A finite element model was made with 450 shell elements, and elastic modulus of 0.42MPa was applied. Pre-stress function was given to the model and the model was given tension with strain rate of 5Hz.

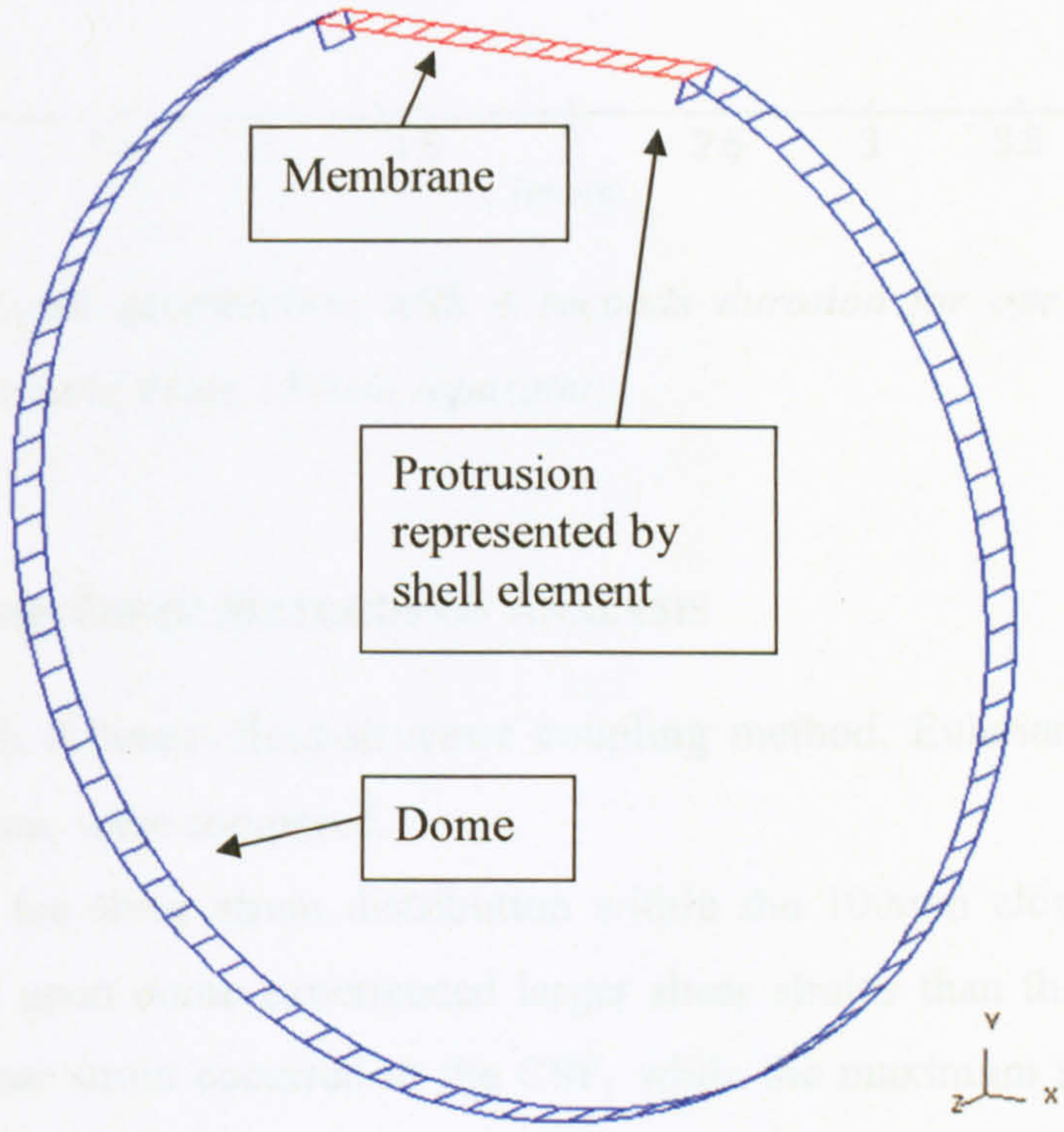

Figure 7.7. *The modelling of protrusion steps.*

7.1.5. LOADING CONDITION

The FE model was excited by the experimental rig output recorded on LVDT during the testing of the open and closed 100mm diameter domes. The displacement was always between -130mm and 100mm with the acceleration between -2g and 3g. The time history of the simulation was selected as a 4 second interval cropped from the middle of

the data, the 4 seconds being long enough to produce stable motion of the gelatine (Figure 7.8).

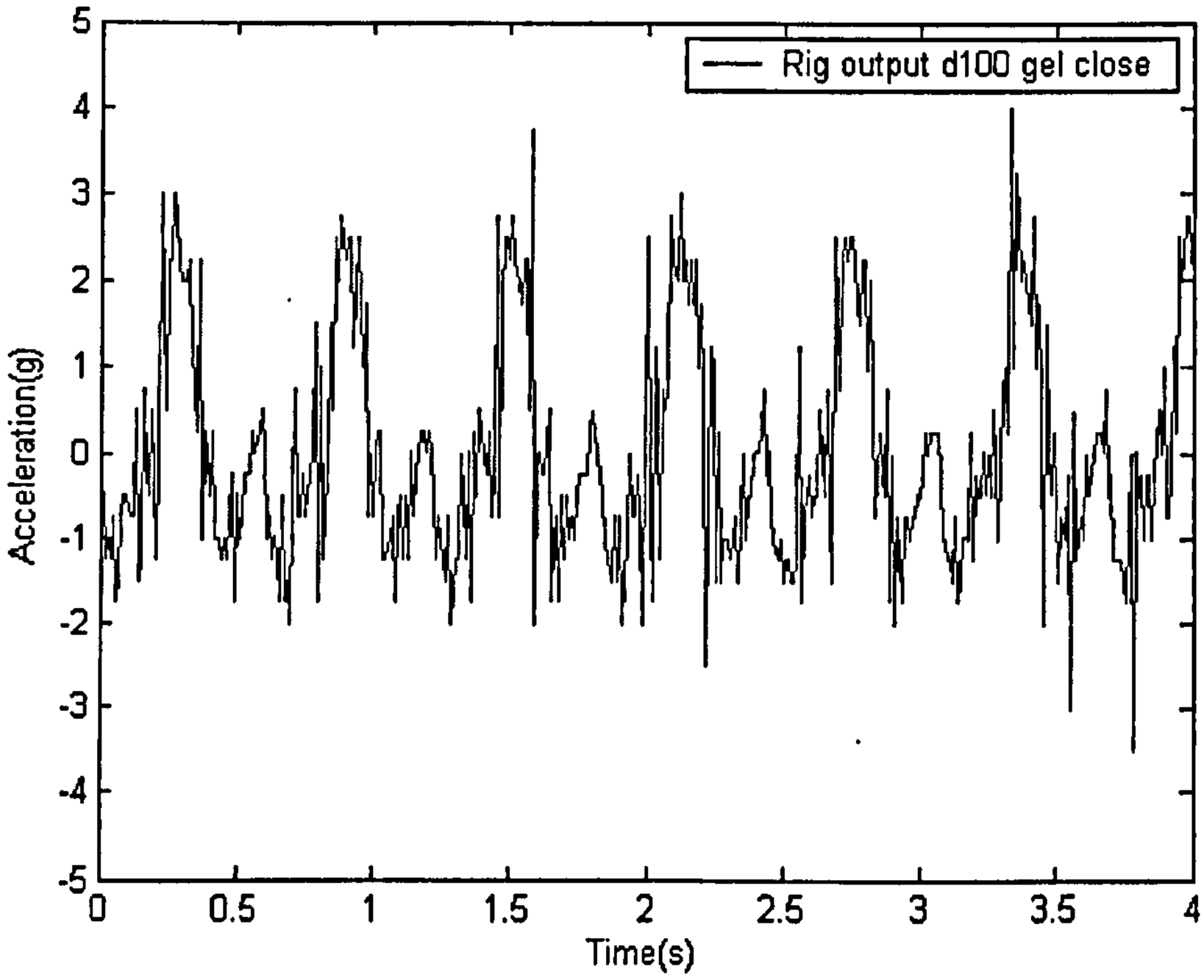

Figure 7.8. *The input acceleration with 4 seconds duration for open, closed dome 100mm, and open closed dome 150mm separately.*

7.2. RESULT OF THE THREE METHODS OF ANALYSIS

Three models with different fluid-structure coupling method, Eulerian (FSI), 1-point ALE and Lagrangian, were compared.

Figure 7.9 shows the shear strain distribution within the 100mm closed and 100mm open models. The open dome experienced larger shear strains than the closed model. The maximum shear strain occurred in the CSF, while the maximum shear stress was found to be on the top area of the gelatine.

For the Lagrangian model under 4 seconds shaking (Figure 7.8), node 2006 on top of the gelatine was selected and its horizontal (d_x) and vertical (d_y) displacements were sampled for both closed and open models. The maximum d_x for the 100mm open dome was 0.13mm. The maximum d_y for the 100mm open dome was 0.15mm and 0.09mm for the closed model. All in that, the displacement of the gelatine was bigger in the open dome than the closed dome.

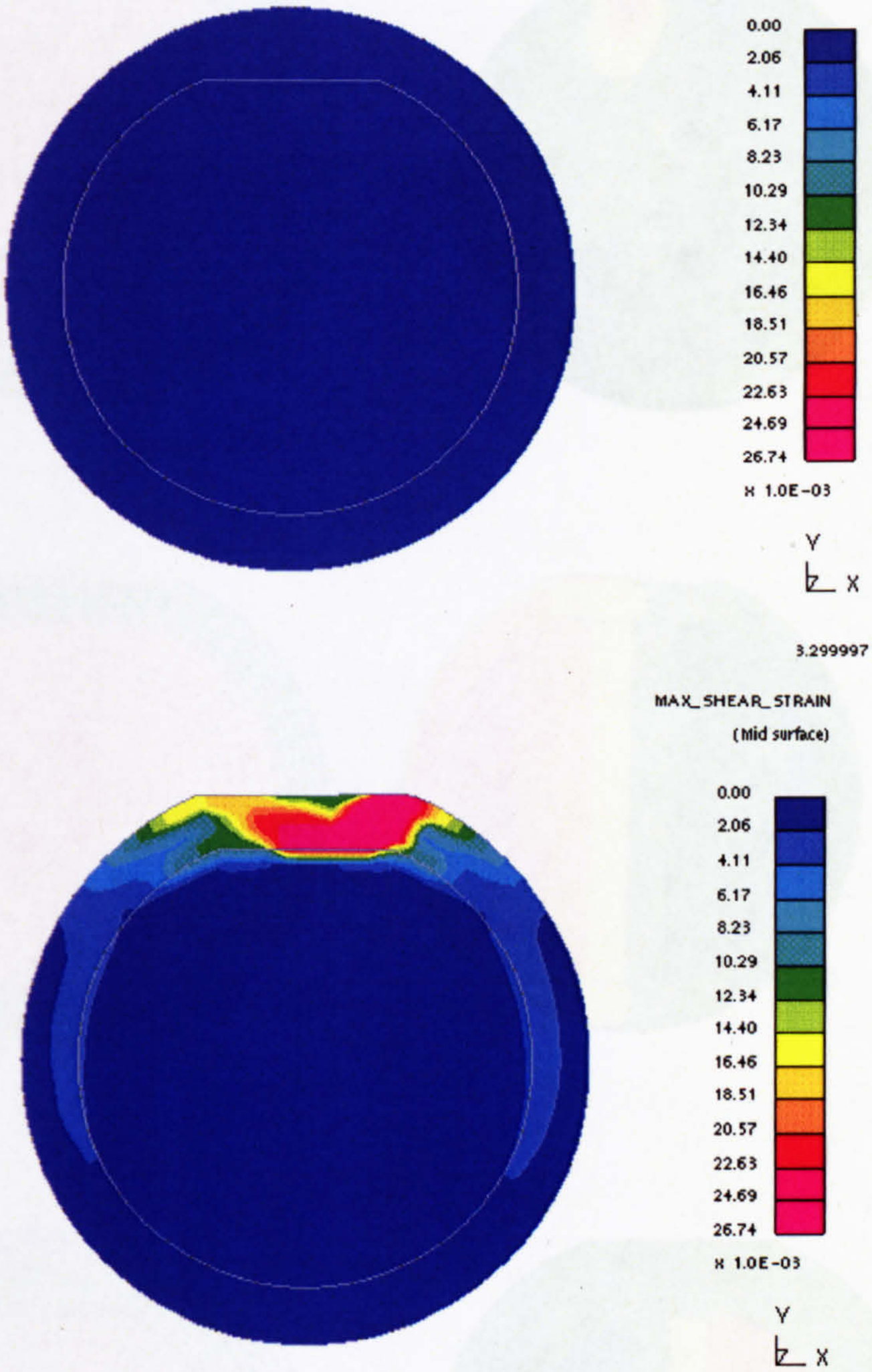

Figure 7.9. *Shear strain in the Lagrangian model of top: closed; and bottom: open dome.*

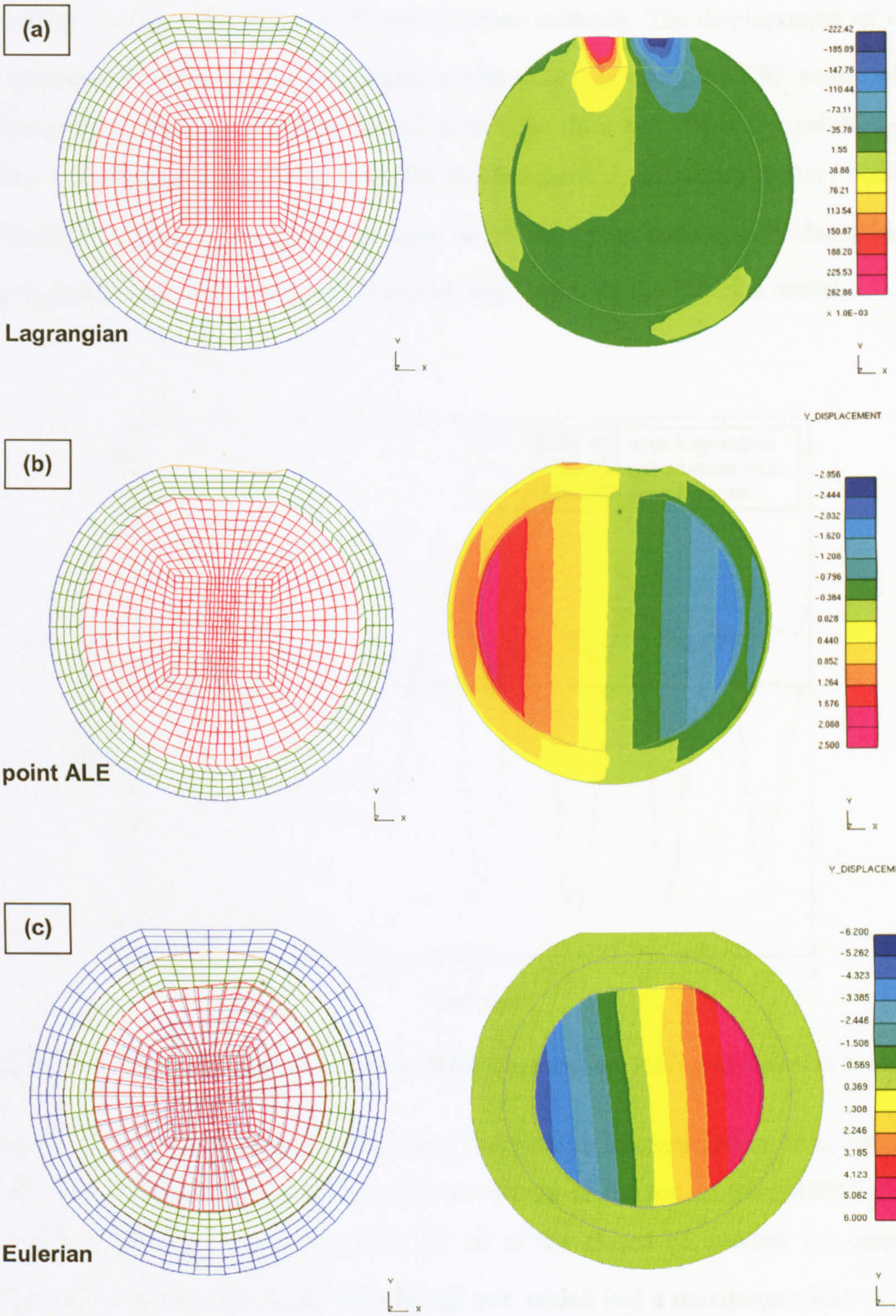

Figure 7.10. *The Vertical (d_y) motion of three methods: Lagrangian, ALE and Eulerian model.*

Figure 7.10 shows the displacements predicted by the FE models with the water modelling via the Lagrangian, ALE and Eulerian methods. The displacement of d_y of the gelatine is smaller in the Lagrangian model than it is using the CSF mesh, which indicates the influence of the deformed membrane does not affect the gelatine part. Figure 7.11 illustrates the variation of the displacement d_x between the three different methods in the model of the 100mm open dome. The magnitude d_x is 0.15mm for the Lagrangian model, 2mm for the ALE model, and 10mm for the Eulerian model.

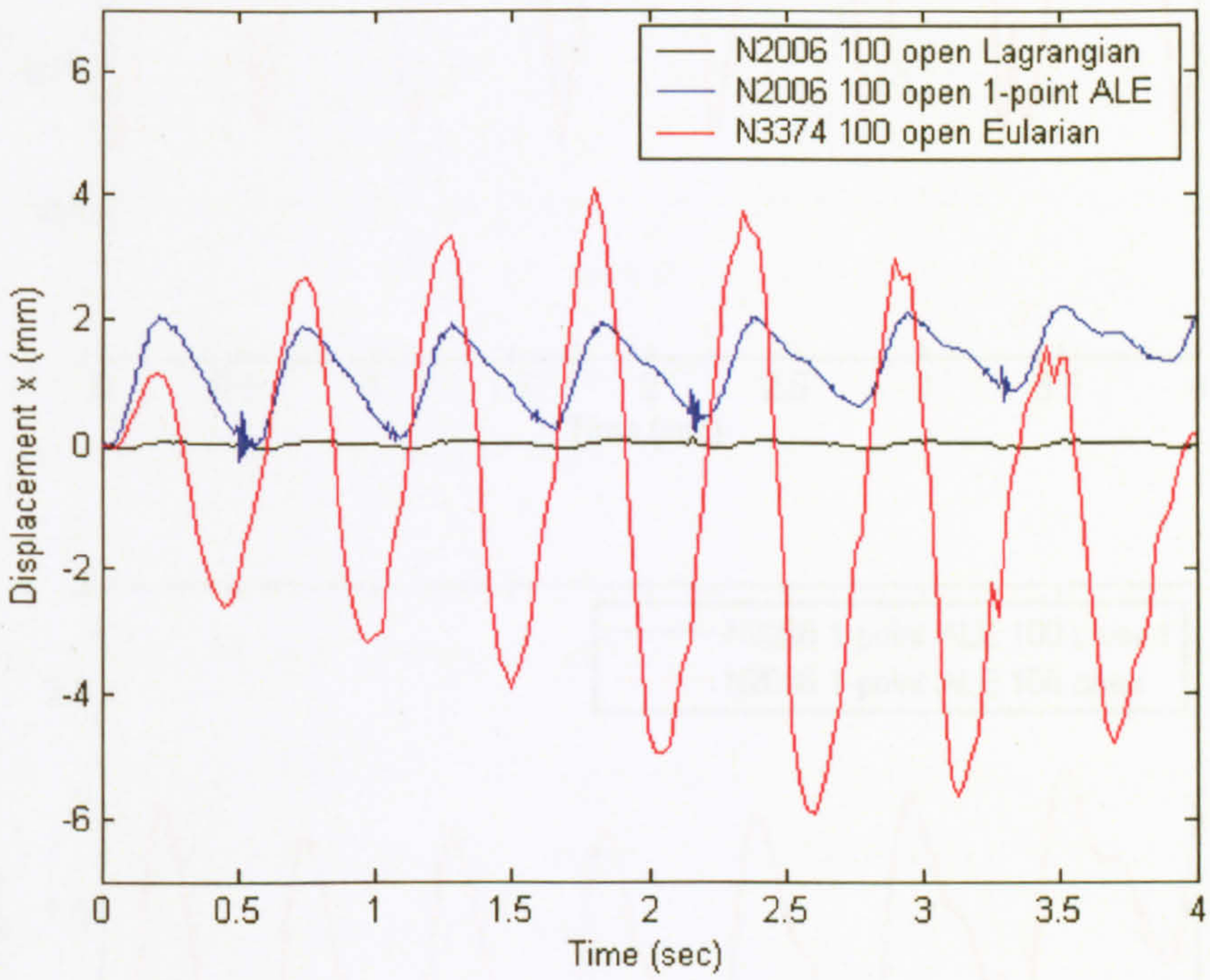

Figure 7.11. *The horizontal (dx) motion of the Lagrangian, ALE and Eulerian models.*

For both the ALE and Eulerian analyses, the gelatine motion inside both open and closed domes was again sampled by the movement of the top of the gelatine. Figure 7.12 shows that the d_x and d_y values for all of the closed FE models are generally significantly smaller than those from the rig test, which had a maximum value of 2mm for the horizontal displacement (§6.2, Figure6.3). The only comparable result was from the Eulerial model, where the value of d_x, whilst remaining small over most of the simulation, attained about 2mm after the full 4 seconds of the analysis. A bulging of the membrane is detectable in both the FE simulation and in the physical model (Figure 7.7,

Figure 6.9). It is obviously connected with the larger straining in this area in the open models compared with the closed one.

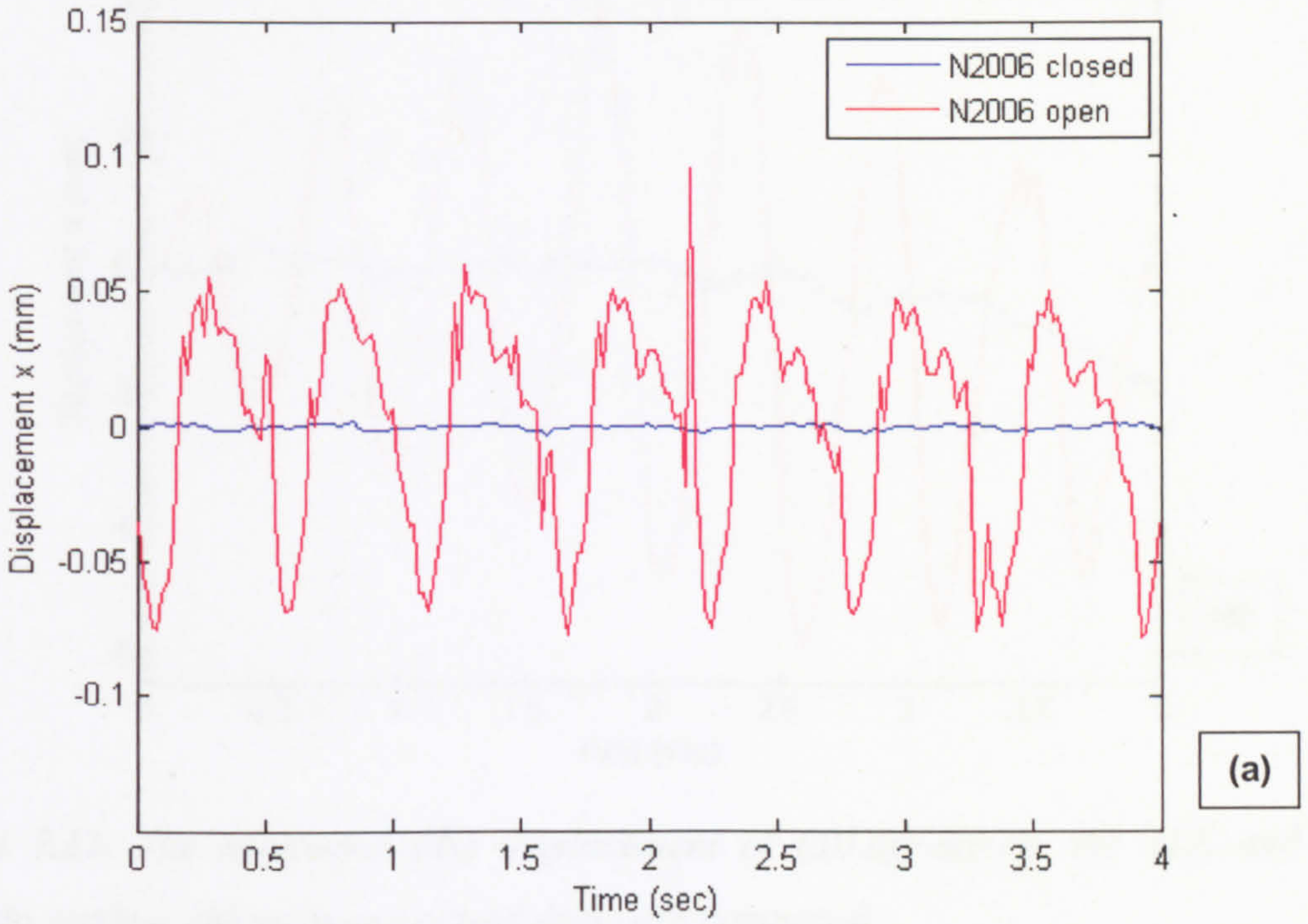

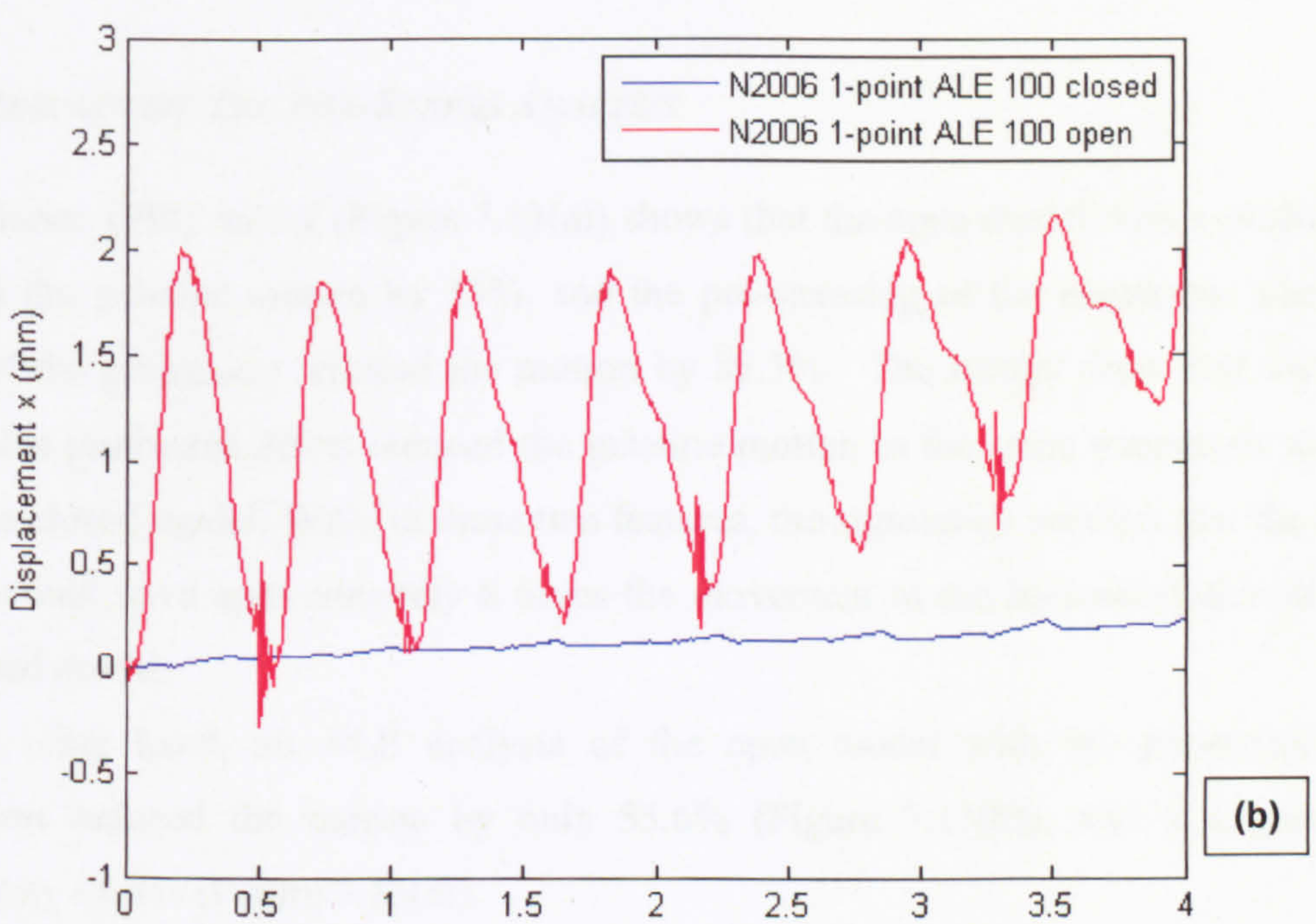

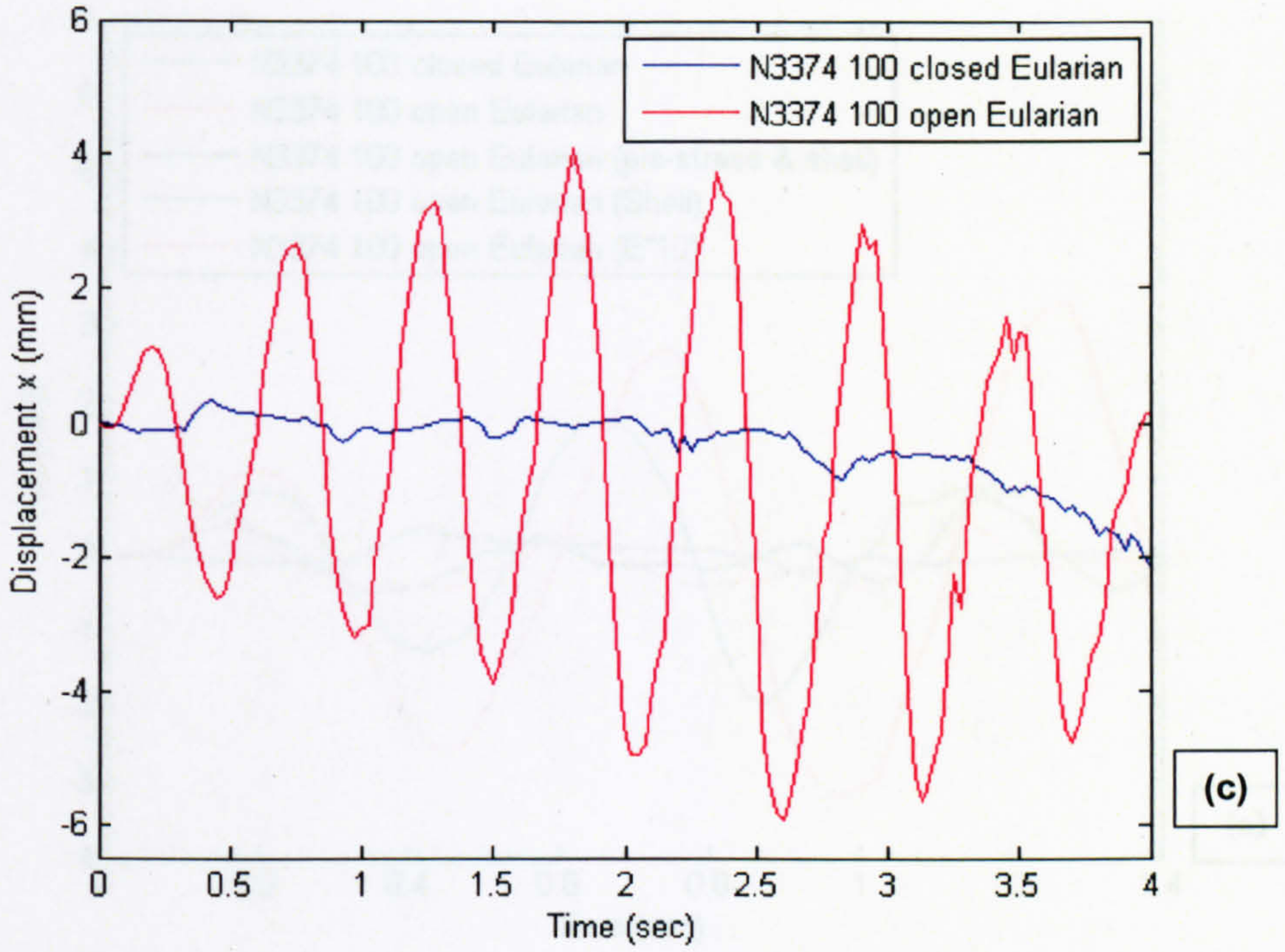

Figure 7.12. *The horizontal (dx) displacement of (a)Lagrangian, (b) ALE and (c) Eulerian method, the open and closed dome are compared.*

7.2.1. RESULTS OF THE PRE-STRESS ANALYSIS

The Eulerian (FSI) model (Figure 7.13(a)) shows that the open model with a protrusion reduced the gelatine motion by 33%, and the pre-stressing of the membrane plus the effect of the protrusion reduced the motion by 83.3%. The results show that the pre-stress plus protrusion effect reduced the gelatine motion to the same magnitude as that from the closed model. Without these two features, the simulation predicts that the open model would have approximately 6 times the movement in the horizontal direction of the closed model.

On the other hand, an ALE analysis of the open model with the pre-stress plus protrusion reduced the motion by only 55.6% (Figure 7.13(b)), and a Lagrangian analysis by 44.4% (Figure 7.13(c)).

Both the Eulerian (FSI) and ALE analyses predicted the gelatine motion to have a similar magnitude to that of the laboratory tests (Figure 6.3) but slightly smaller, while the Lagrangian analysis predicted only one tenth of the motion in the rig model.

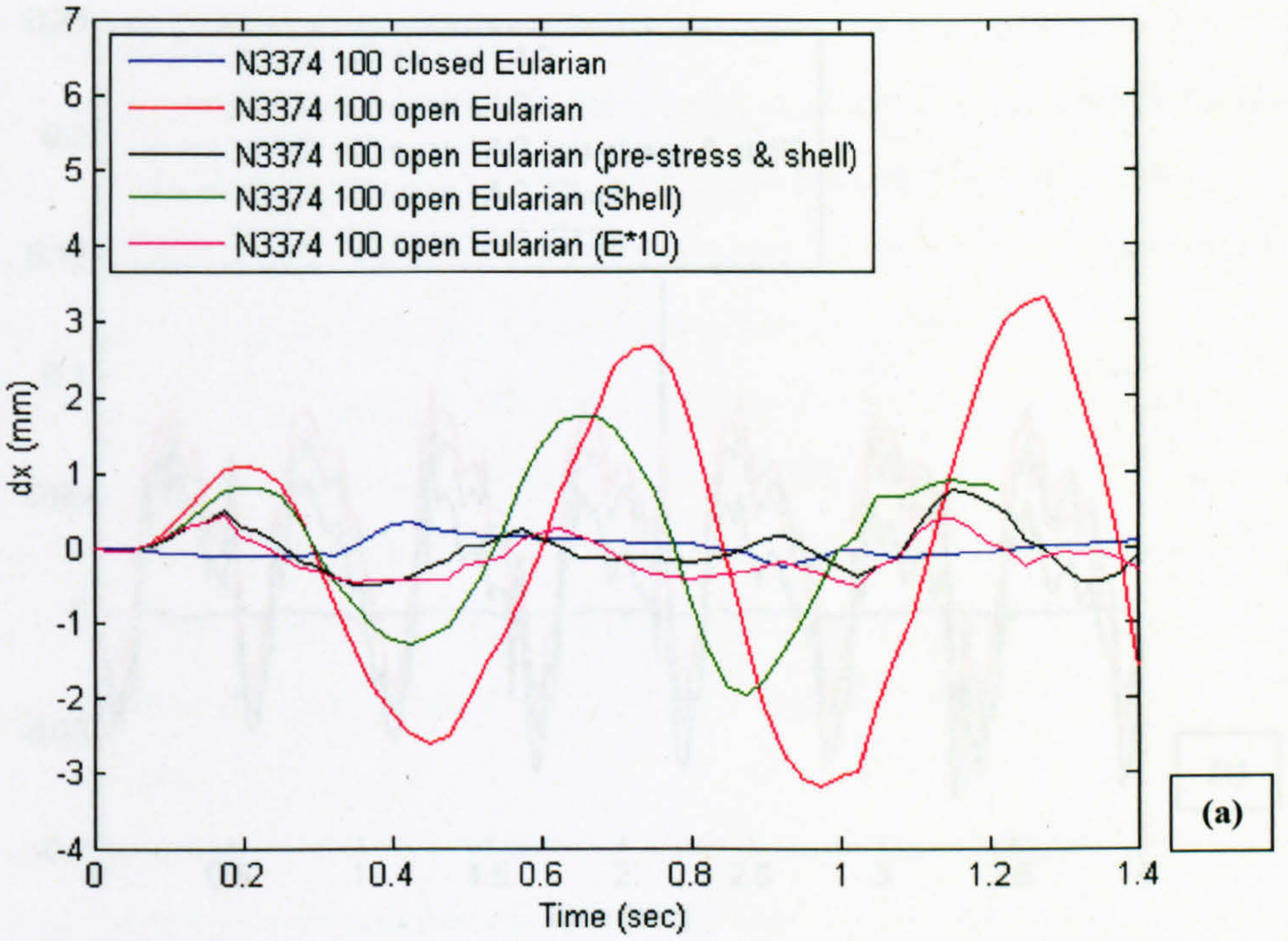
N3374 100 closed Eularian
N3374 100 open Eularian
N3374 100 open Eularian (pre-stress & shell)
N3374 100 open Eularian (Shell)
N3374 100 open Eularian (E*10)
dx (mm)
Time (sec)
(a)

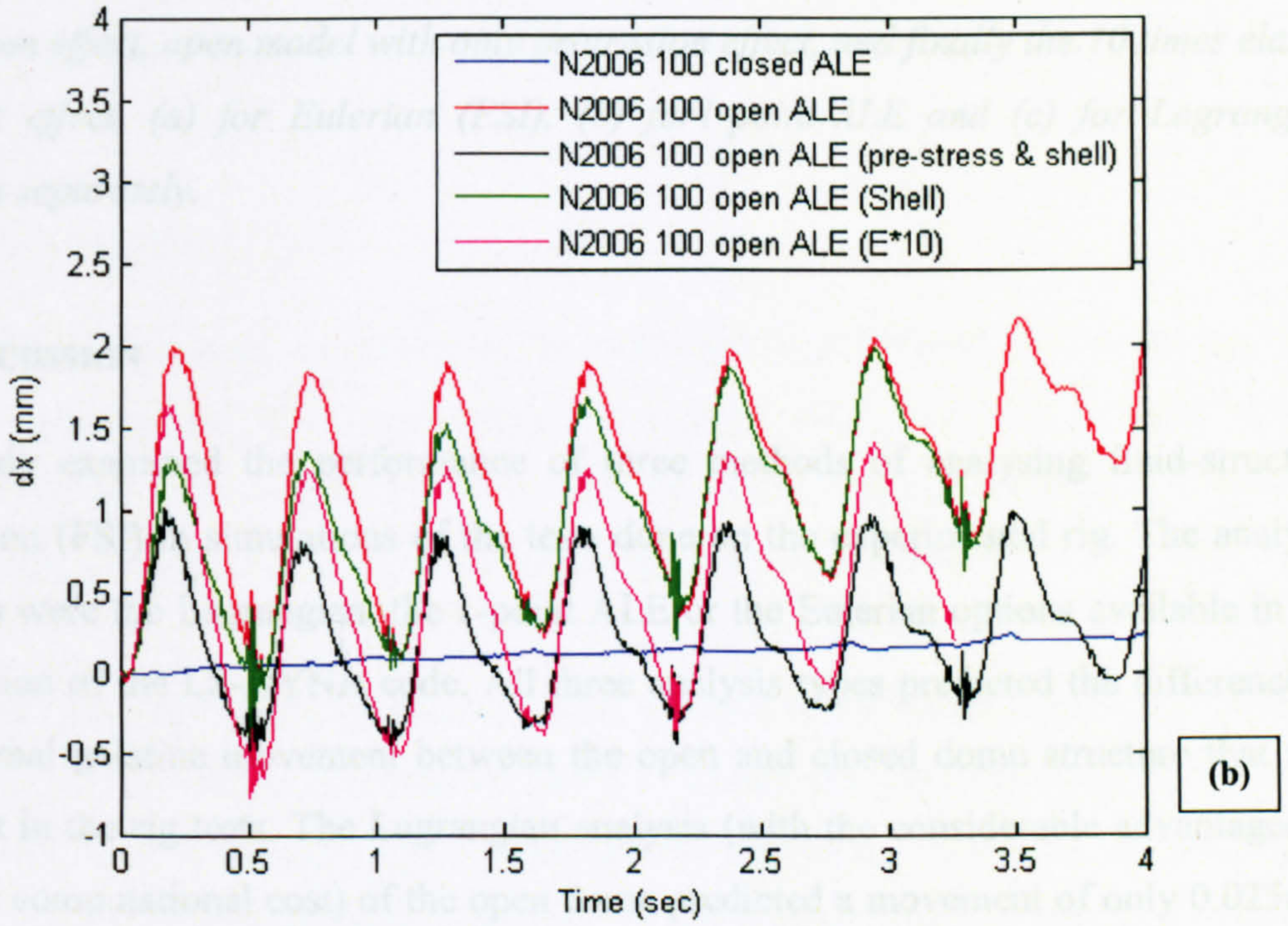
N2006 100 closed ALE
N2006 100 open ALE
N2006 100 open ALE (pre-stress & shell)
N2006 100 open ALE (Shell)
N2006 100 open ALE (E*10)
dx (mm)
Time (sec)
(b)

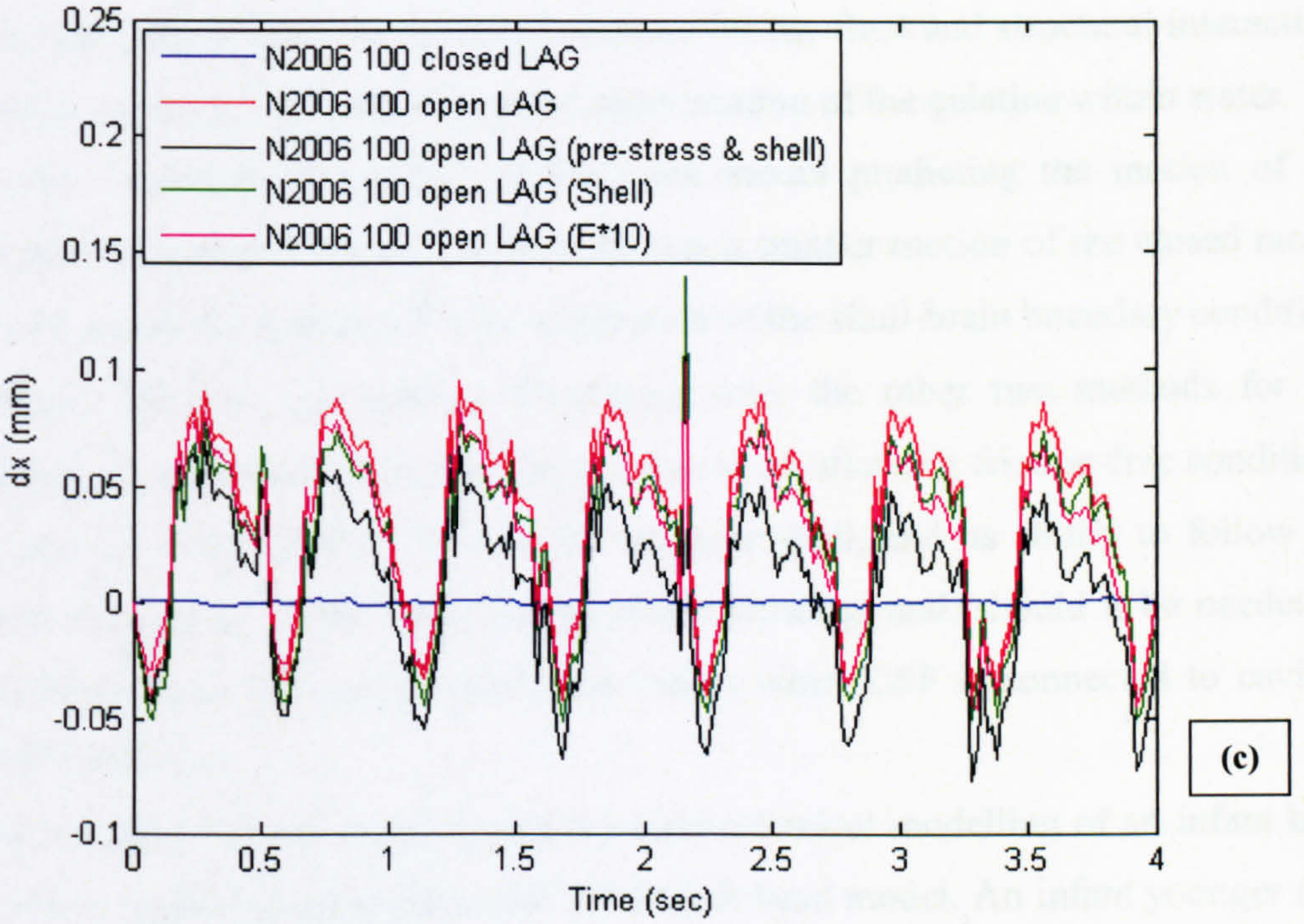

Figure 7.13. *Results for the closed model, open model, open with pre-stress plus protrusion effect, open model with only protrusion effect, and finally the 10 times elastic modulus effect, (a) for Eulerian (FSI), (b) for1-point-ALE and (c) for Lagrangian analyses separately.*

7.3. DISCUSSION

The study examined the performance of three methods of analysing fluid-structure interaction (FSI) in simulations of the tests done on the experimental rig. The analysis methods were the Lagrangian, the 1-point ALE or the Eulerian options available in the FSI section of the LS-DYNA code. All three analysis types predicted the difference in the internal gelatine movement between the open and closed dome structure that was apparent in the rig tests. The Lagrangian analysis (with the considerable advantages of smallest computational cost) of the open dome predicted a movement of only 0.025mm compared with the experimental result of about 2mm. On the other hand, the computationally expensive Eulerian analysis and its associated complicated mesh generation, showed a much larger movement of the gelatine inside the water with over 2.5 times that of the physical test.

All three analyses of the closed dome model predicted the movement of the gelatine to be much smaller than that in the experimental testing.

The reason for the behaviour of the Lagrangian and 1-point ALE analyses is likely to be due to the merging of node boundary conditions for the fluid and structural interaction. This tends to produce high restraint on the shear motion of the gelatine within water.

Despite the 1-point ALE analysis of the open model predicting the motion of the gelatine that is closest to the rig test data, its much smaller motion of the closed model damages its possible advantage for the simulation of the skull-brain boundary condition. The Eulerian method, has distinct advantages over the other two methods for the investigation of traumatic intracranial injury due to its allowing friction-free conditions on the interface between the CSF and the brain or skull, and its ability to follow the large fluid movement in the brain during severe shaking, and, should it be needed in future investigations, the complicated flow routes when CSF is connected to cavities inside the brain tissue.

The analyses suggest very strongly that the biomechanical modelling of an infant head should not be treated as a simple scaled MRI adult head model. An infant younger than six month, having an un-closed skull, is more vulnerable to the shaking baby syndrome than a model scaled down from an adult and having a closed skull.

7.4. CONCLUSIONS

During the FE element modelling of the experiments performed on the test rig, three methods of analysis, the Lagrangian, the 1-point ALE, and the Eulerian options available in LS-DYNA were used to model the fluid-structure interactions in the open and the closed dome structures. The following results were obtained.

(1) In the study of the movement of the gelatine brain model suspened in the CSF inside the dome, the original, simple, model analysed using all three options (Figure 7.1, Figure 7.2) all predicted the movement in the closed model to be much smaller than in the open one. In comparison, the two structures exhibited very similar amounts of movement in the rig tests.

(2) Recognition that the mounting of the membrane in the open dome structure necessarily strained it required that its value be measured and that its effect on the structural response be assessed through FE analysis. It is clear that the pre-strained membrane would produce a stiffer structural response than that without

any straining. In addition, the poor predictive performance of the simple models of (1) above precipitated a re-assessment of the test rig. It was then recognised that the mounting ring for the membrane protruded into the space of the CSF by a small amount that was, however, probably enough to affect the performance of the system. Again, the effect would stiffen the structure by the provision of a dam or step at the edge of the membrane that would restrict the flow of CSF across it. The effect could be investigated in FE models. FE analysis and its results (Figures 7.10, Figure 7.12) showed that the pre-strain on the membrane and the protrusion inside the fluid area in the dome very probably caused the open structure to behave too stiffly. This phenomenon was demonstrated by FE models using all three (Lagrangian, 1-point ALE and Eulerian) analysis options. All these analyses of the open structure showed some reduction in the motion of the gelatine, with the Eulerian analysis providing the best result, a reduction of the gelatine motion by 83%.

(3) The results summarised above indicate that the fluid-structure interaction in FE models of skulls with interacting brain, CSF and skull is more accurately and realistically assessed using an Eulerian analysis method than with the Lagrangian method that has been widely adopted in previous adult head simulations. Eulerian analysis should be encouraged for use in future studies of head injuy when fluid effects are significant, such as those in the Shaken Baby Syndrome.

(4) Despite these conclusions, there are currently real advantages associated with the use of the Lagrangian analysis method. They are due to the large amounts of time saved in a Lagrangian simulation compared with its Eulerian counterpart, an effect that is particularly important in performing complex three-dimensional analyses in an acceptable run-time. As a result, the Lagrangian analysis method was used for the paediatric reconstruction including both the geometry and the material properties in Chapter 8.

SUMMARY

This chapter described three methods of analysing fluid-structure interaction (FSI) in simulations of the tests done on the experimental rig. The analysis methods were the Lagrangian, the 1-point ALE or the Eulerian options available in the FSI section of the

LS-DYNA code. Each of the models was excited by an imposed motion derived from the LVDT output of the test rig with the displacement varying between -130mm and 100mm and the acceleration between -2g and 3g. An interval of 4 seconds of the time history was selected to ensure that the motion was suitably stable.

The magnitude of the simulated horizontal displacement of the gelatine was 0.15mm for Lagrangian, 2mm for ALE, and average 5mm (-6mm to 4mm) for Eulerian analyses of the open top model. On the other hand, all the three analyses of the closed model predicted displacements for the gelatine in the same direction smaller than 1mm.

Rig assembly of the membrane subjected it to pre-strain that could not be eliminated in the current study. Its magnitude was measured in a simple test, and its effect was incorporated into the FE models. A further stiffening effect was found to be due to the membrane mounting ring protruding into the space of the CSF and obstructed the CSF flow towards the membrane. After modifying the FE models to allow for both of these effects, the displacement in Lagrangian analysis reduced by 44%; in ALE analysis by 55.6%; and in Eulerian analysis by 83.3%. The Eulerian analysis with the pre-strain effect and in a model with a protruded mount reduced the predicted gelatine motion to a similar magnitude as that for the closed model (as was observed in the rig tests), while the other two analysis methods were not able to achieve this.

In conclusion, the Eulerian analysis method has significant advantages for the FSI modelling of brain-CSF-skull interactions than have more commonly used methods, e.g. the Lagrangian method.

The hypothesis that infants younger than six months and having an unclosed skull are more vulnerable under shaking than comparable infants with a closed skull is supported by the two-dimensional analyses reported in this chapter. Further three-dimensional work including paediatric geometric details to examine these effects is reported in the following chapter. As noted above, this used the Lagrangian analysis method to achieve acceptable computational times.

CHAPTER 8: *THE NUMERICAL MODELLING OF SHAKING MOTION*

INTRODUCTION

This chapter describes the use of the FE method to explore in detail the effects on the interior constituents of an infant's skull when it is shaken. Three geometric shapes of FE model were analysed, the shapes being spherical (as in the rig test model), an infant head derived from empirical data, and one derived from an MRI scan of the head of a nine month old infant (Owen 2002). Three-dimensional FE models were constructed for the simple shape and the MRI scan model. Also, two-dimensional FE models of each shape were constructed derived from a slice on the sagittal plane, and a further 2D FE model was made based on an empirical simplification of the MRI sagittal model. The modelling of the brain-skull boundary used the Lagrangian method with merging nodes between the fluid and the solid part of the head. The models were excited by a more complicated motion output from the physical tests described earlier in Chapter 3. The aim of the work was to test the hypothesis that the structure of the infant skull does indeed caused it to behave differently from that of an adult, and consequently that the interior deformation of an infant skull is qualitatively different from that of a scaled adult one due to the effects of the fontanelles and to the different shapes.

8.1. FINITE ELEMENT MODEL OF HUMAN HEAD

The finite element models of the infant head were developed using ANSYS 8.1 (ANSYS Inc., Houston, PA) and their motions and deformation during shaking by the LS-DYNA 970 (Livermore Software Technology Corporation, Livermore, CA, USA) explicit finite element code. The model geometry comes from three sources; that based on a simplified spherical geometry approximately the same volume as a real infant head, a new born infant head model based on empirical measurement, and an MRI head model based on magnetic resonance images from a scan of a particular infant. Analyses of the simplified and MRI geometry model include both the 2D sagittal plane model and 3D volume modelling. The new born infant geometry model was only assessed for its 2D sagittal plane.

Material	G_0 MPa	G_∞ MPa	ρ kg/m^3	β s^{-1}	E MPa	υ	K MPa
Brain	5.99×10^{-3}	2.32×10^{-3}	1.04×10^{3}	0.09248	-	0.499	2110
CSF	-	-	1.08×10^{3}	-	-	-	2110
Skull	-	-	2.1×10^{3}	-	1300	0.22	-
Dura	-	-	1.13×10^{3}	-	31.5	0.45	-
Scalp	-	-	1.0×10^{3}	-	0.42	0.42	-

E=Young's modulus (MPa); ρ=mass density (kg/m^3); υ=Poisson's ratio; K=bulk modulus (MPa); G_0=short term shear modulus (MPa); G_∞=long term shear modulus (MPa); β=decay factor (s^{-1})

Table 8.1. *Material properties of 1.5-month infant head applied in the FE model.*

The material properties used for each component are listed in Table 8.1. The brain tissue followed the linear viscoelastic model of Margulie (2000). The CSF was modelled by an elastic fluid as in those of the models of the rig test. The skull was taken to be effectively as a rigid body, and the model used the same properties as did McElhaney's (1970). The anterior fontanelle can be considered as a membrane consisting of the infant scalp and the tissue underneath. However, since the details of this and the material properties of the representative membrane are lacking in the literature, the present model used an elastic model with the properties of the latex membrane from Chapter 7.

8.1.1. 3D-SIMPLE SPHERE MODEL

3D simplified spherical models with corresponding geometry and intracranial components were constructed with the open (123mm diameter) and closed (144mm diameter) type being considered separately (Figure 8.1). Each model contained 695 four-noded shell elements and 10104 eight-noded solid elements, and represented a new born infant head size and a 6 month old infant head size.

8.1.2. 2D –SIMPLE SPHERE MODEL

A 2D simplified head model with sagittal slice shape was constructed and containing, for the open model, the brain, CSF, skull and scalp and the position of the anterior fontanelle. In contrast, a closed model was also constructed with the scalp and skull

fused together and the result given the properties of the skull (Figure 8.2). The diameters of the model included the size of the 123mm model of the 1.5 month old infant with a 40mm fontanelle width, and the size of the 144mm model of a 6 month old infant with the fontanelle width of 36mm. The width of the fontanelle in the 3D sliced model comes from the maximum measured length from the literature (Hall et al. 1995, Malas and Sulak 2000) and was kept the same for the other types of 3D sagittal sliced model. The thickness of the CSF was 5mm. The model consisted of 63 four-noded shell elements and 1088 eight-noded solid elements. The thickness of the model was 5mm.

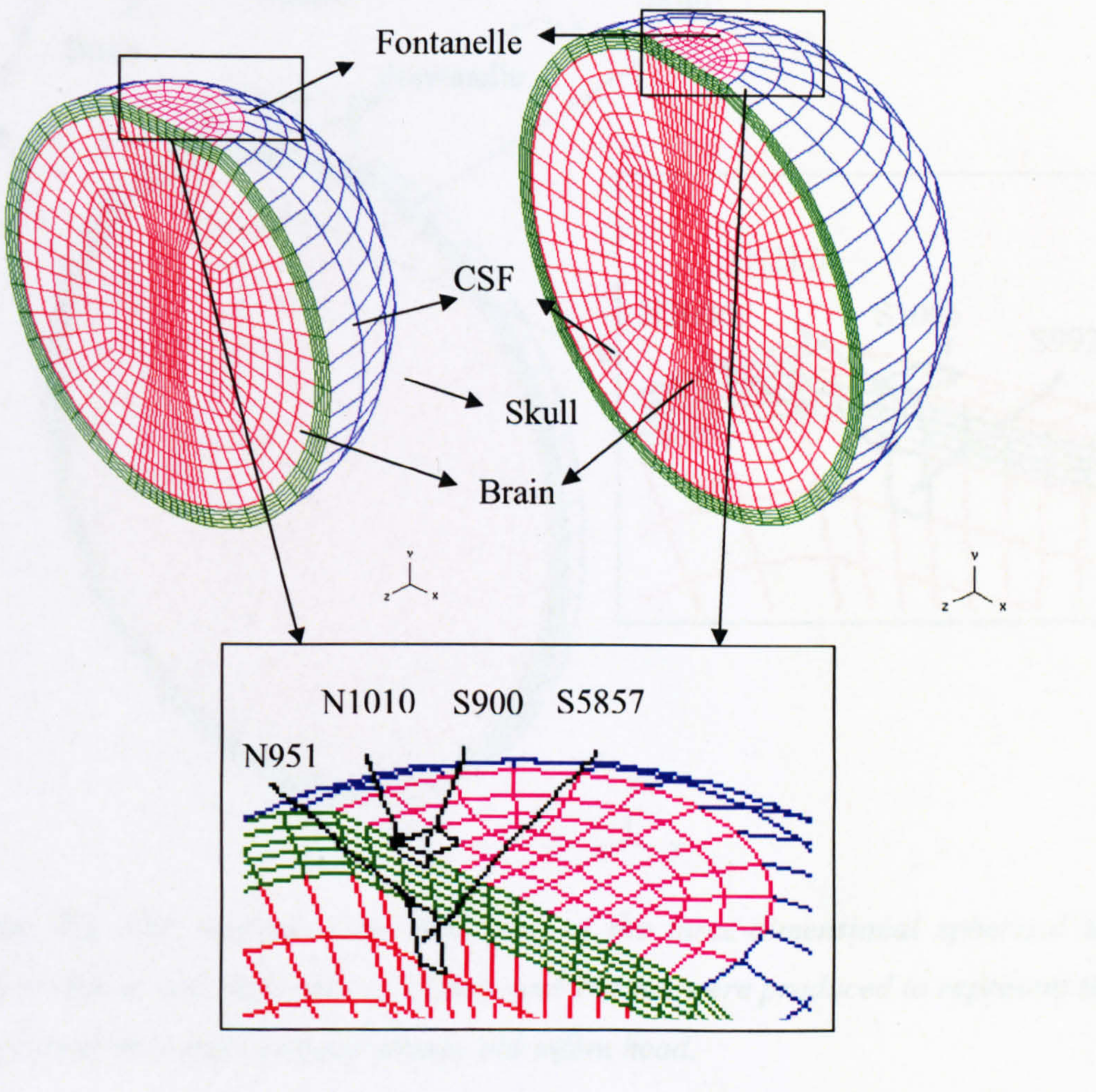

Figure 8.1. *The modelling of three-dimensional spherical simple models. Two diameters of 123mm and 144mm were produced to represent the 1.5 month newborn infant and a 6 months old infant head.*

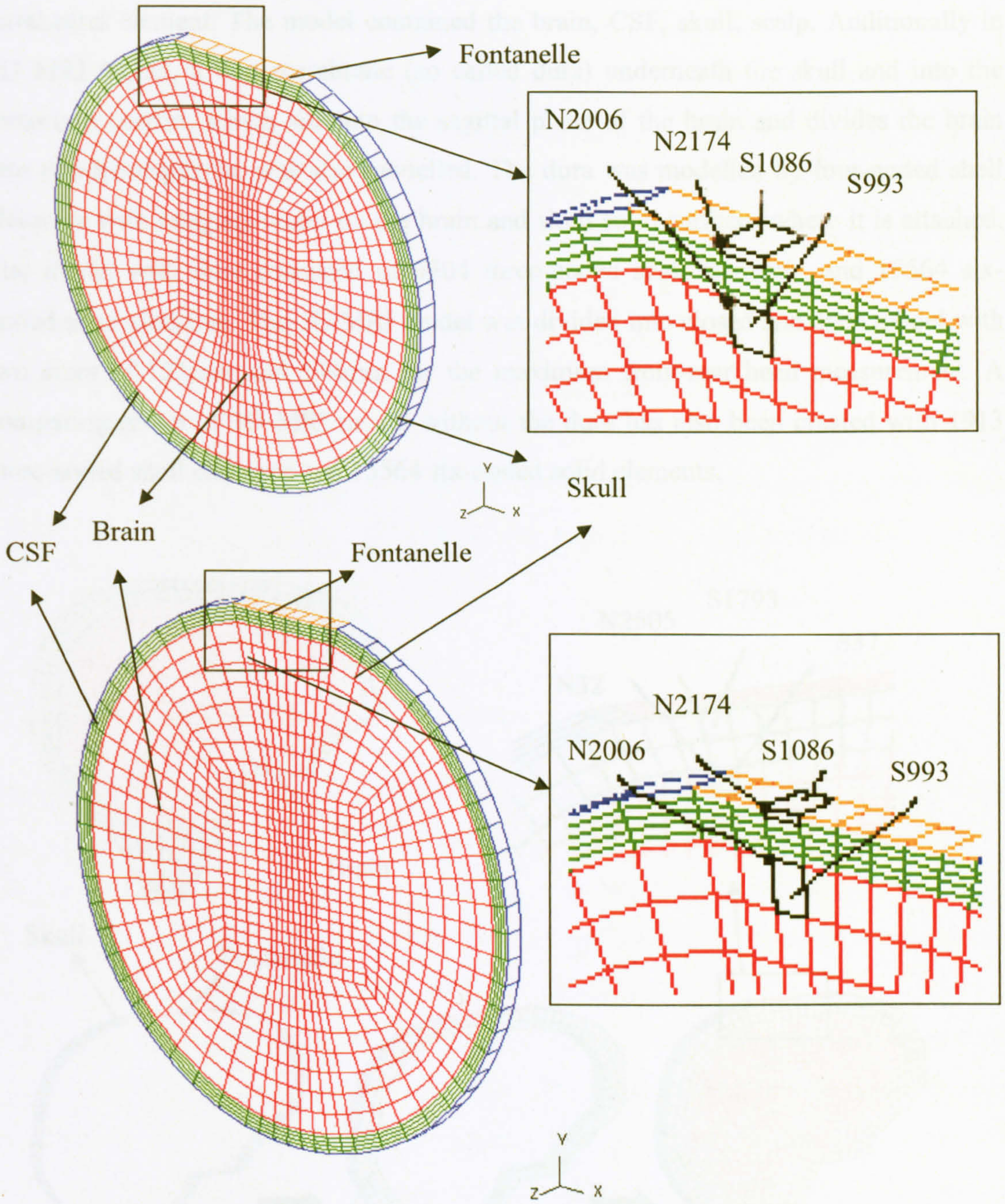

Figure 8.2. *The sagittal plane modelling of the three-dimensional spherical simple models. Again, two diameters of 123mm and 144mm were produced to represent the 1.5 month newborn infant and a 6 months old infant head.*

8.1.3. 3D- MRI Model

A 3D finite element model was reconstructed from the MRI imaging of nine month old infant patient (Owen 2000) (Figure 8.4). Unlike any of the 2D model that discussed in this chapter with hexahedron elements, the 3D MRI head geometry was meshed with

tetrahedral element. The model contained the brain, CSF, skull, scalp. Additionally in 3D MRI model, a thin membrane (so called dura) underneath the skull and into the tentorium cerebri, which sits into the sagittal plane of the brain and divides the brain into two hemispheres, was also modelled. The dura was modelled by four-noded shell elements with merging nodes on the brain and skull solid surfaces where it is attached. The model with dura consisted of 4204 three-noded shell elements, and 15564 six-noded solid elements. The 3D MRI model was divided into closed and open model with two sizes of 123mm and 144mm for the maximum front-rear head measurement. A comparing group of 3D MRI model without the dura has also been created with 1913 three-noded shell elements and 15564 six-noded solid elements.

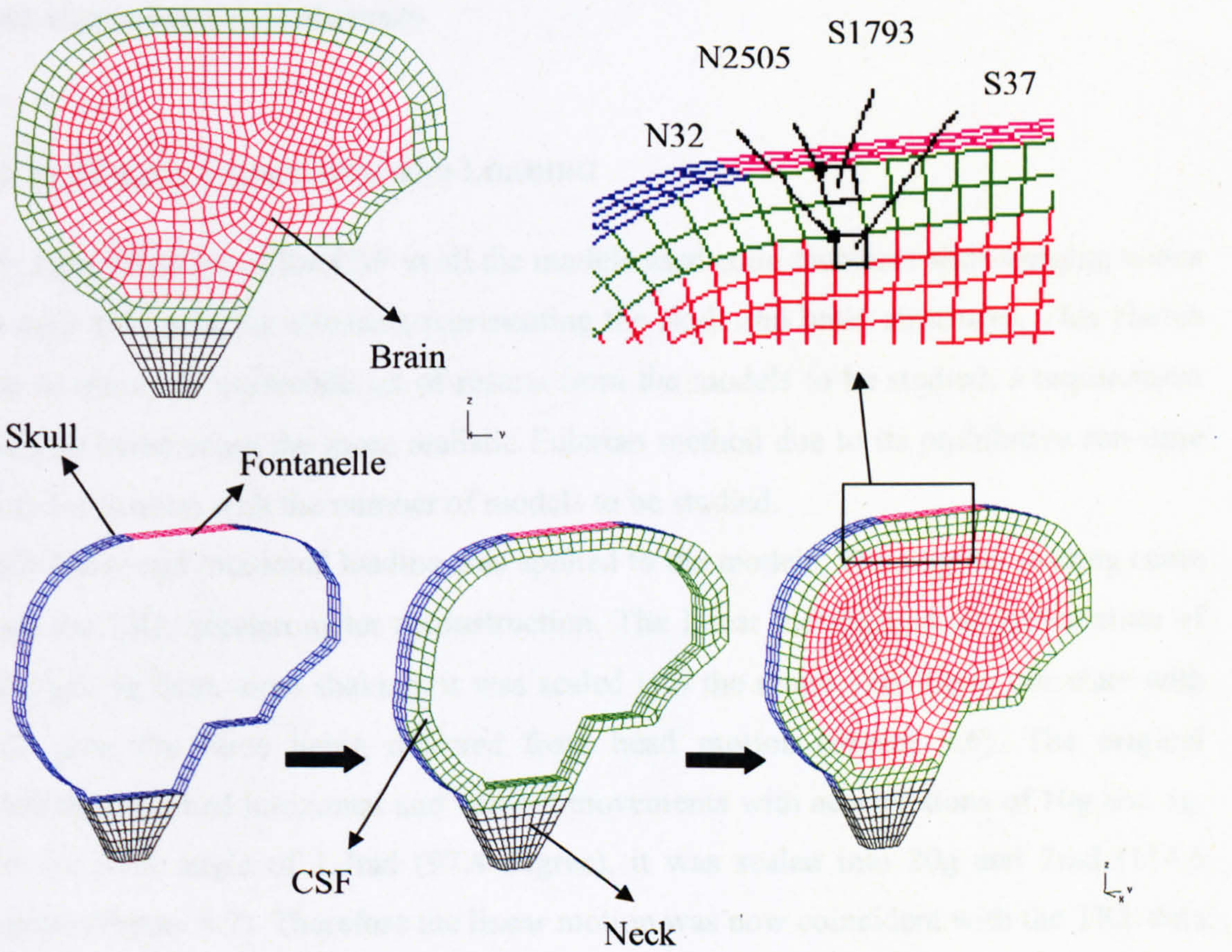

Figure 8.3. *Two-dimensional sagittal plane model of infant middle plane with brain, skull, CSF, dura, neck and fontanelle.*

8.1.4. 2D -INFANT AND MRI MODEL

The modelling of the 2D model with a new born infant shape (Figure 8.3) was done with the aid of empirical measurements of the infant head, and the modelling of the 2D MRI model with a specific natural shape was done with the aid of a 3D MRI geometry (Figure 8.5). They both consist of brain, CSF, skull and skin. The infant model has a CSF with the thickness of 6.6mm on the top area, and the MRI model has a CSF layer that is much thinner, that is, 1.8mm. The model was developed into two, one with the maximum front-rear distance of 123mm and the other of 144mm. For these, the fontanelle was 40mm and 36mm to represent a 1.5 month and a 6 month old infant respectively. The 2D infant model had 483 four-noded shell elements and 4287 eight-noded solid elements, and the 2D MRI model had 282 four-noded shell elements and 3865 eight-noded solid elements.

8.2. BOUNDARY CONDITIONS AND LOADING

The representation of the CSF in all the models used solid elements with merging nodes on each side with the elements representing the skull and brain structures. This choice was to ensure a reasonable set of results from the models to be studied, a requirement that precluded using the more realistic Eulerian method due to its prohibitive run-time costs for dealing with the number of models to be studied.

Both linear and rotational loading was applied to the models. The original loading came from the TRL accelerometer reconstruction. The linear motion had an acceleration of less than 5g from torso shaking, it was scaled into the range 15g-20g to correlate with TRL data the force being detected from head motion (Figure 8.6). The original rotational data had horizontal and vertical movements with accelerations of 10g and 5g, and the peak angle of 1.7rad (97.4 degree), it was scaled into 20g and 2rad (114.6 degree) (Figure 8.7). Therefore the linear motion was now coincident with the TRL data, and the rotational motion was coincident with the measurements of Prague et al. (2000).

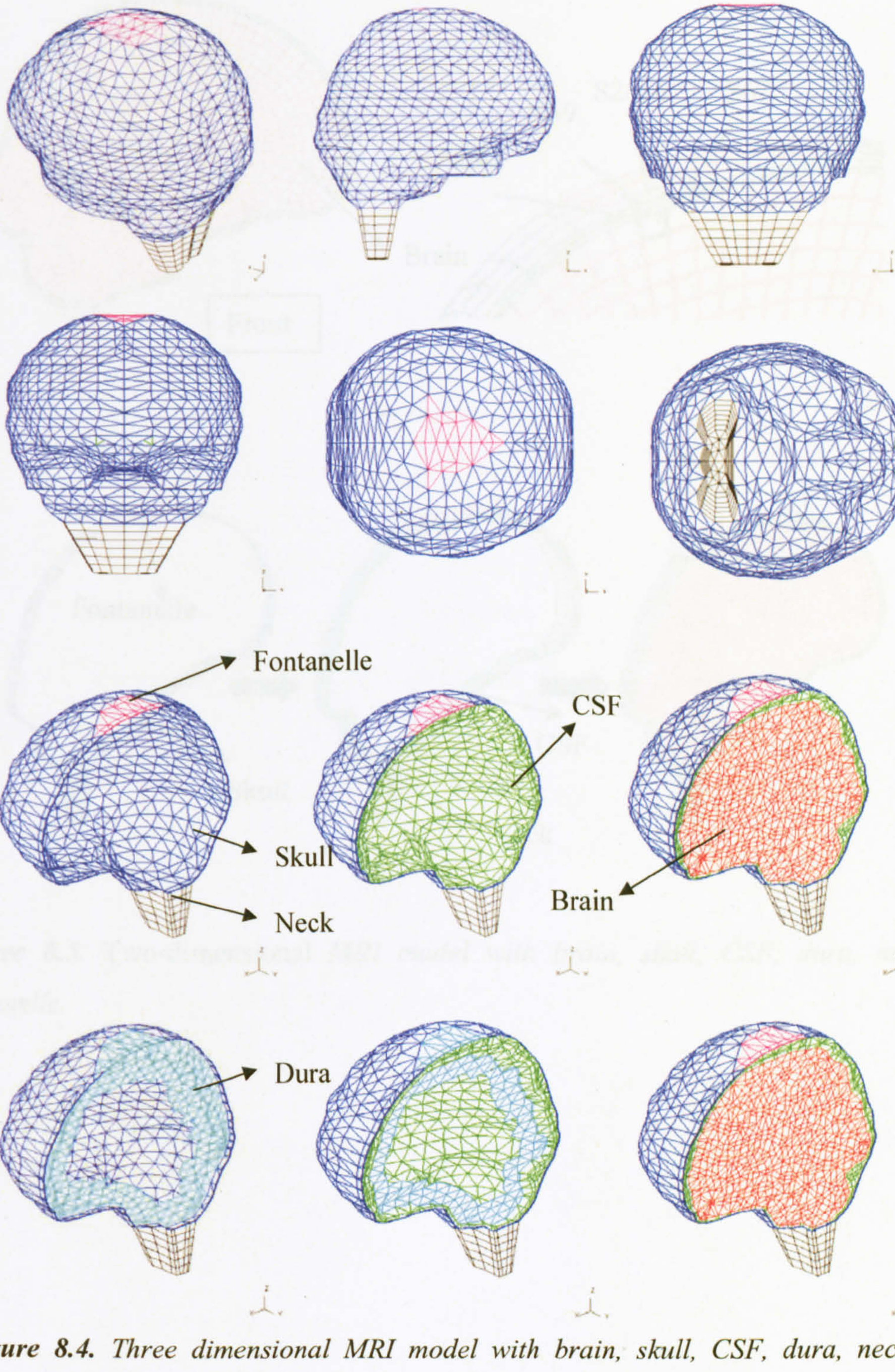

Figure 8.4. *Three dimensional MRI model with brain, skull, CSF, dura, neck and fontanelle.*

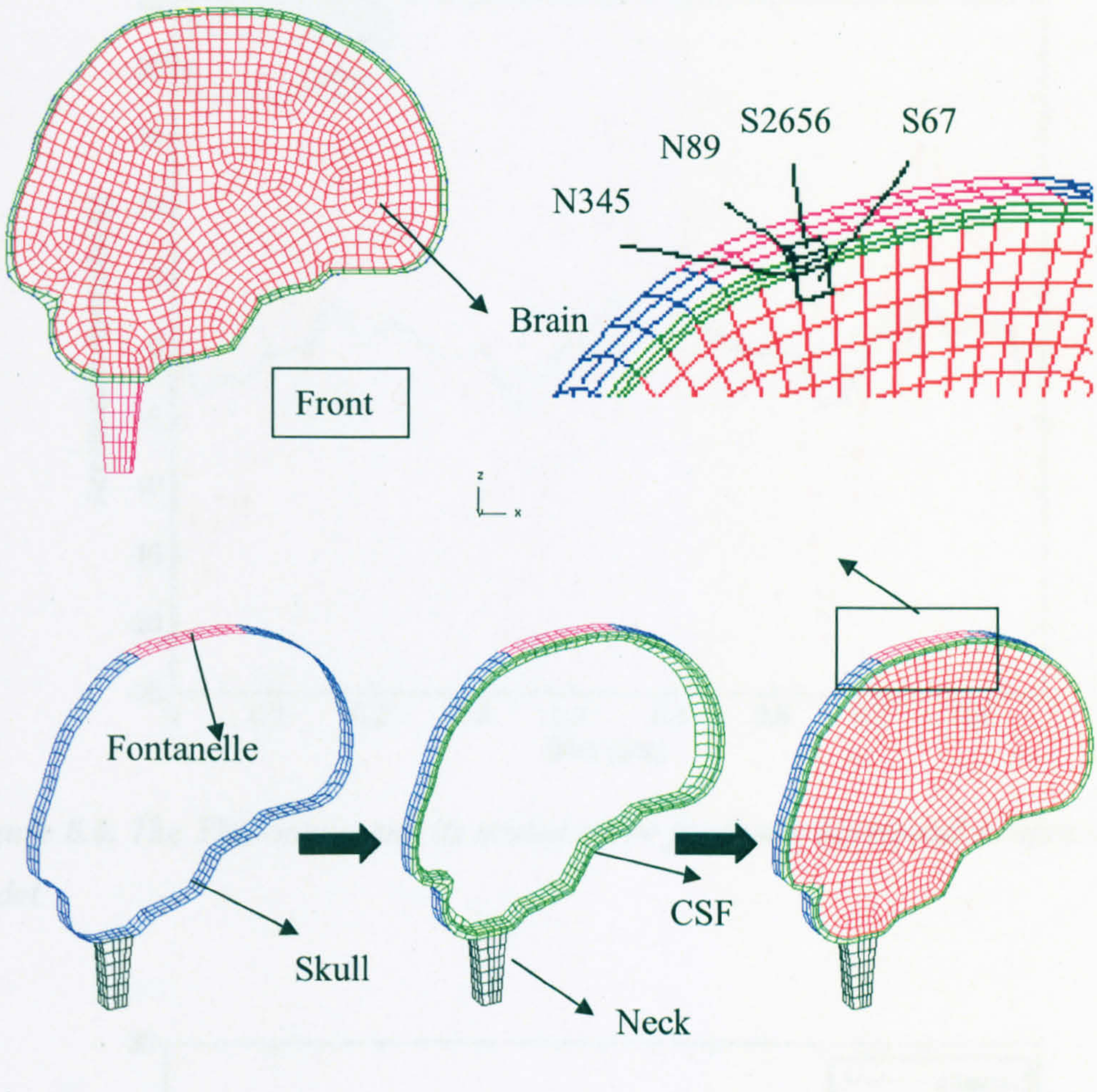

Figure 8.5. Two-dimensional *MRI model with brain, skull, CSF, dura, neck and fontanelle.*

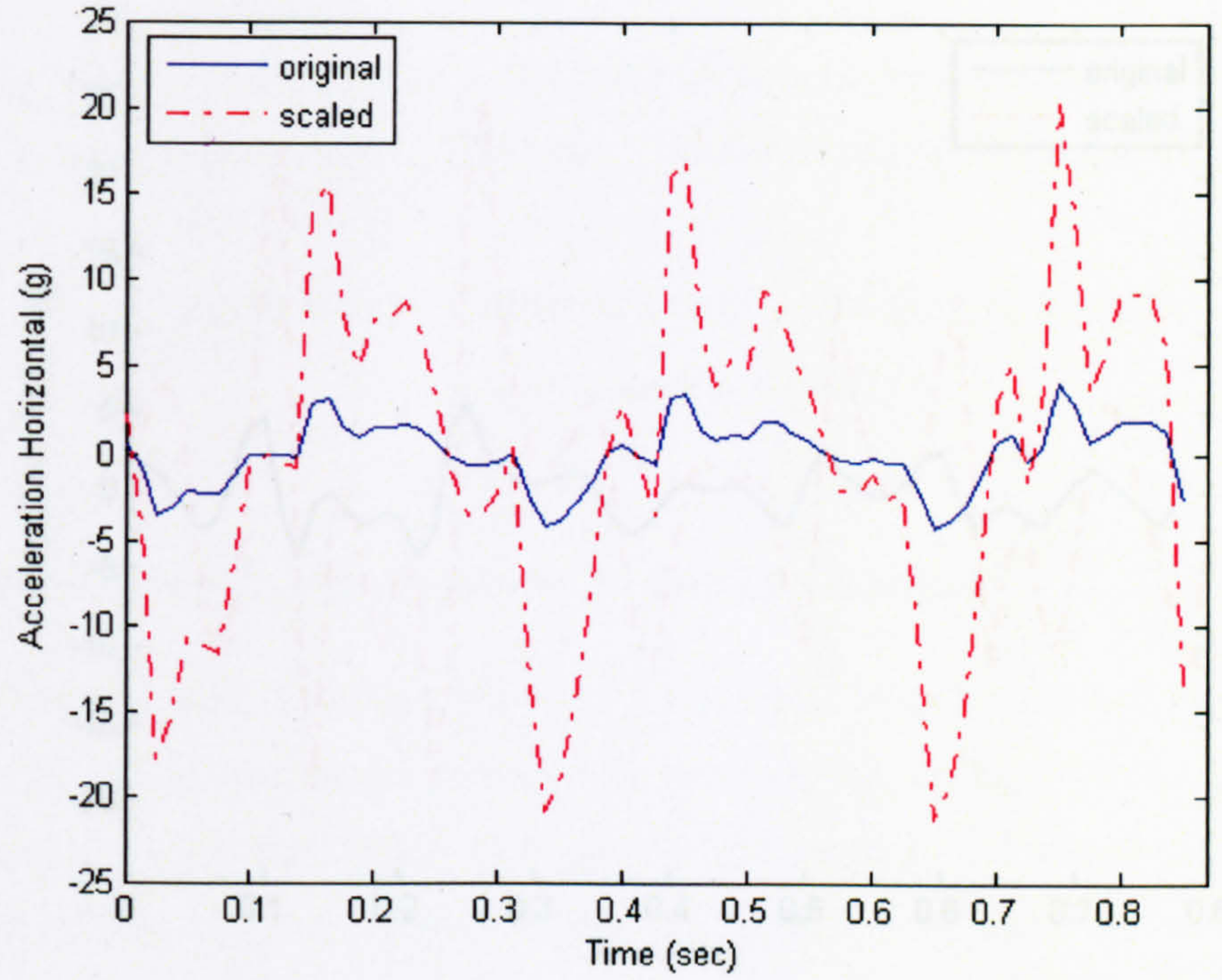

Figure 8.6. *The TRL output and its scaled curve for linear horizontal motion to the FE model.*

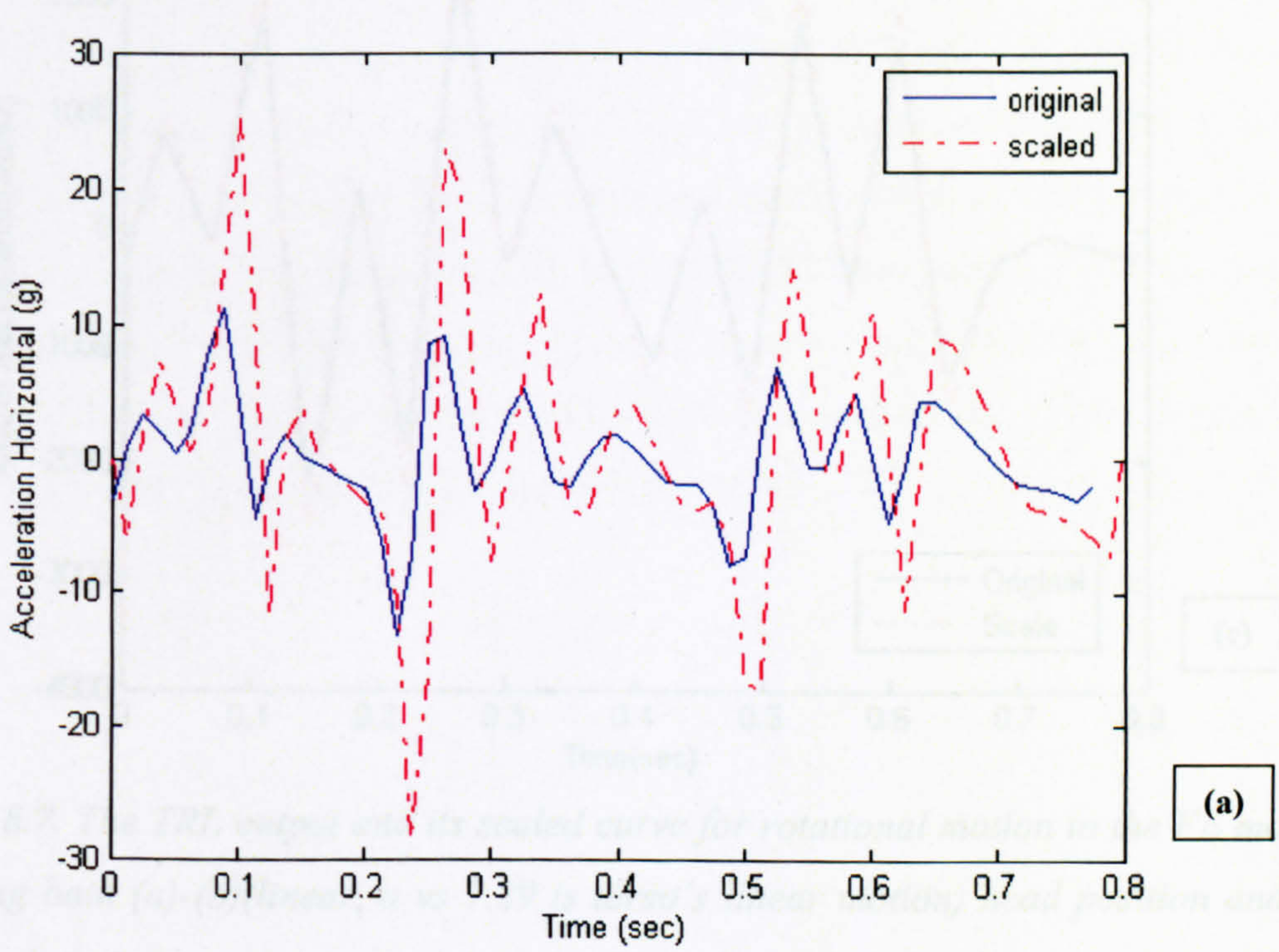

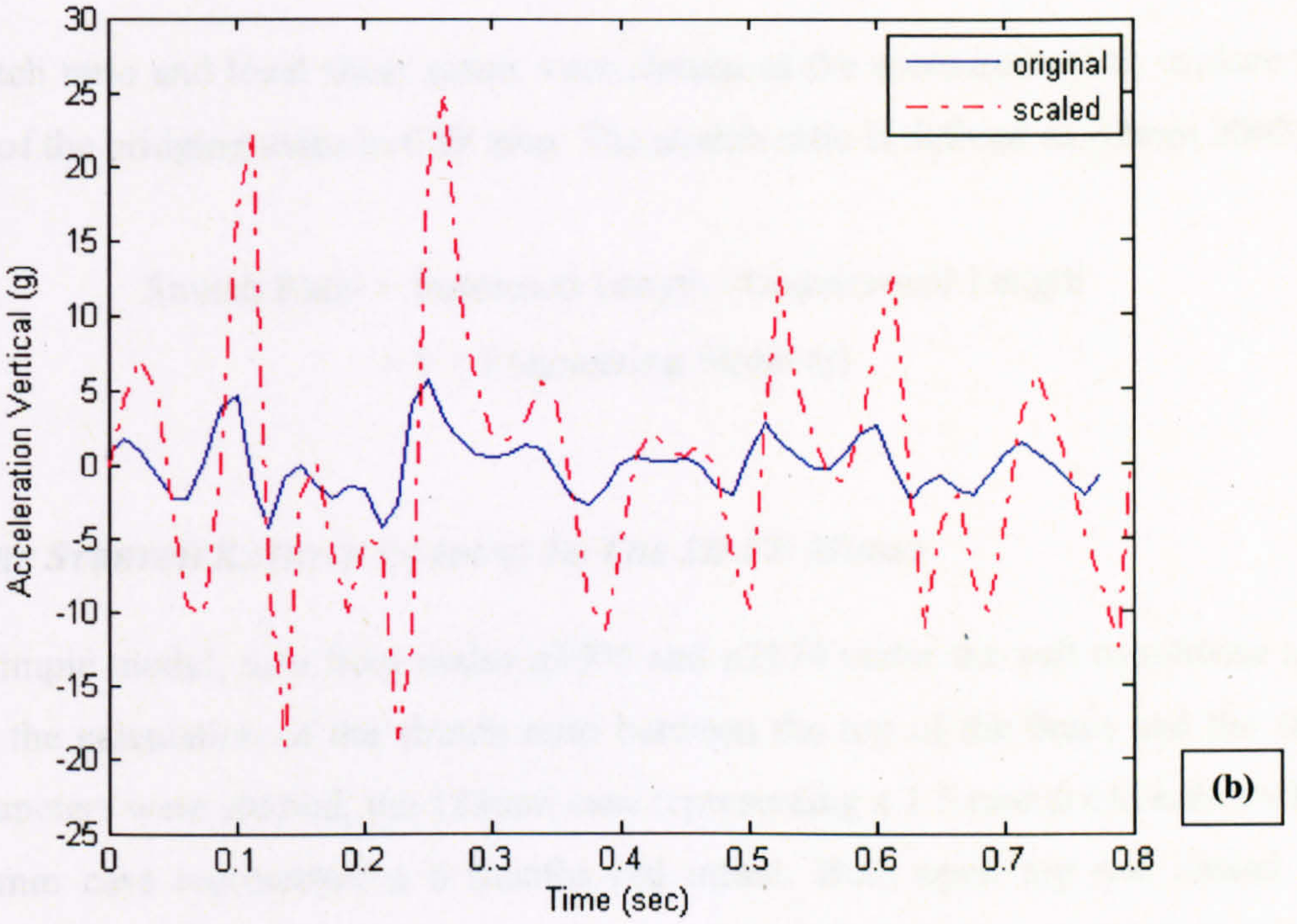

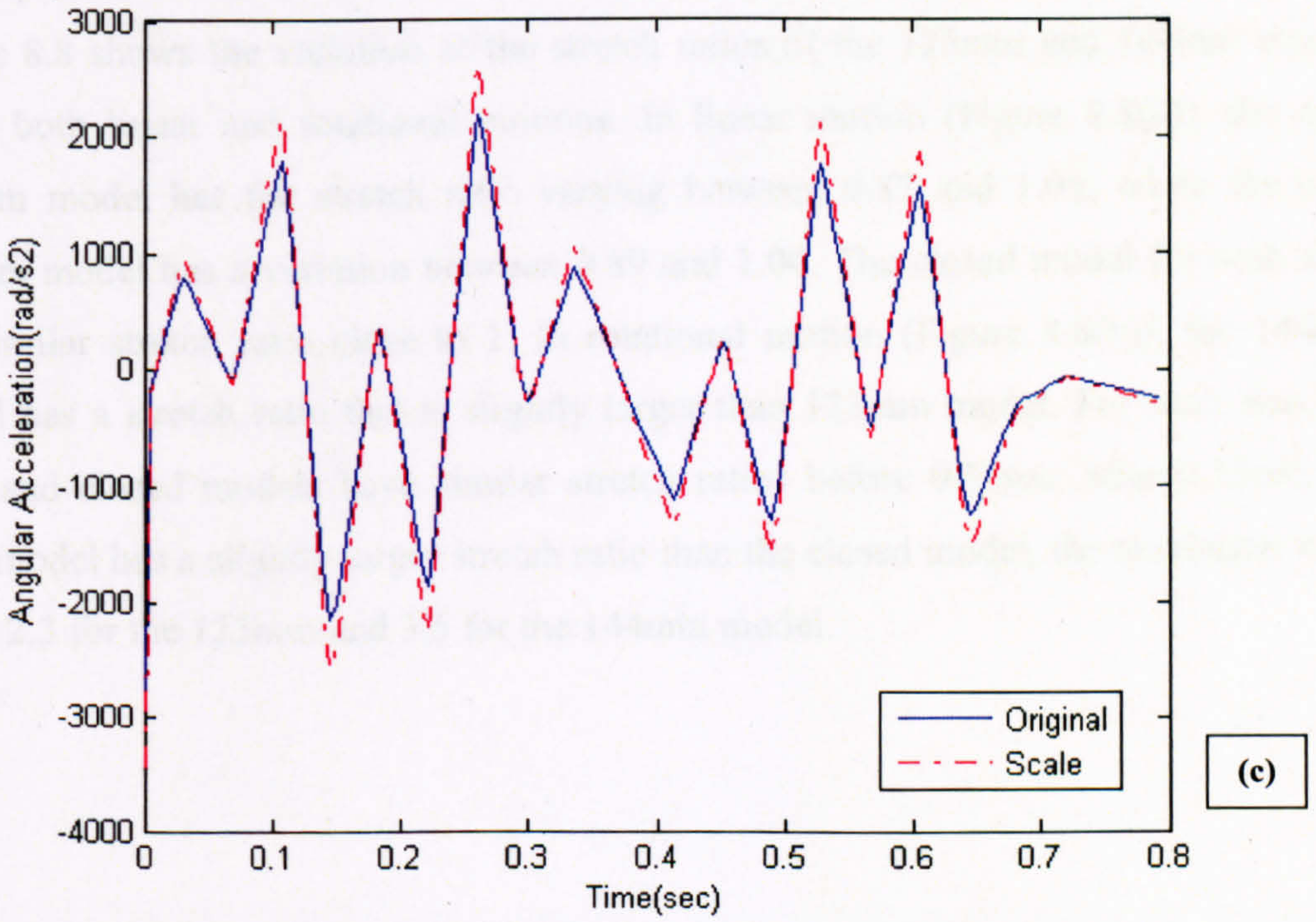

Figure 8.7. *The TRL output and its scaled curve for rotational motion to the FE model, including both (a)-(b)(linear, a vs 7.29 is torso's linear motion) head position and (c) head angle.*

8.3. RESULTS

The stretch ratio and local shear strain were chosen as the measurement to explore the damage of the bridging veins in CSF area. The stretch ratio is defined as (Owen 2002):

$$\text{Stretch Ratio} = \text{Deformed Length} / \text{Undeformed Length}$$
$$= 1 + \text{Engineering Strain } (\gamma)$$

8.3.1. THE STRETCH RATIO ACCORDING TO THE 2D FE MODEL

In this simple model, data from nodes n2006 and n2174 under the soft membrane area allowed the calculation of the stretch ratio between the top of the brain and the skin. Two diameters were studied; the 123mm case representing a 1.5 month old infant while the 144mm case represented a 6 months old infant. Both open top and closed top models were investigated for each size, the membrane in the open model being given the properties of skin while in the closed model it was given those of the skull.

Figure 8.8 shows the variation of the stretch ratios of the 123mm and 144mm models under both linear and rotational motions. In linear motion (Figure 8.8(a)), the open 123mm model has the stretch ratio varying between 0.87 and 1.06, while the open 144mm model has a variation between 0.89 and 1.04. The closed model for both sizes has similar stretch ratio close to 1. In rotational motion (Figure 8.8(b)), the 144mm model has a stretch ratio that is slightly larger than 123mm model. For each size, the open and closed models have similar stretch ratios before 0.35sec; after 0.35sec, the open model has a slightly larger stretch ratio than the closed model, the maximum value being 2.3 for the 123mm and 3.5 for the 144mm model.

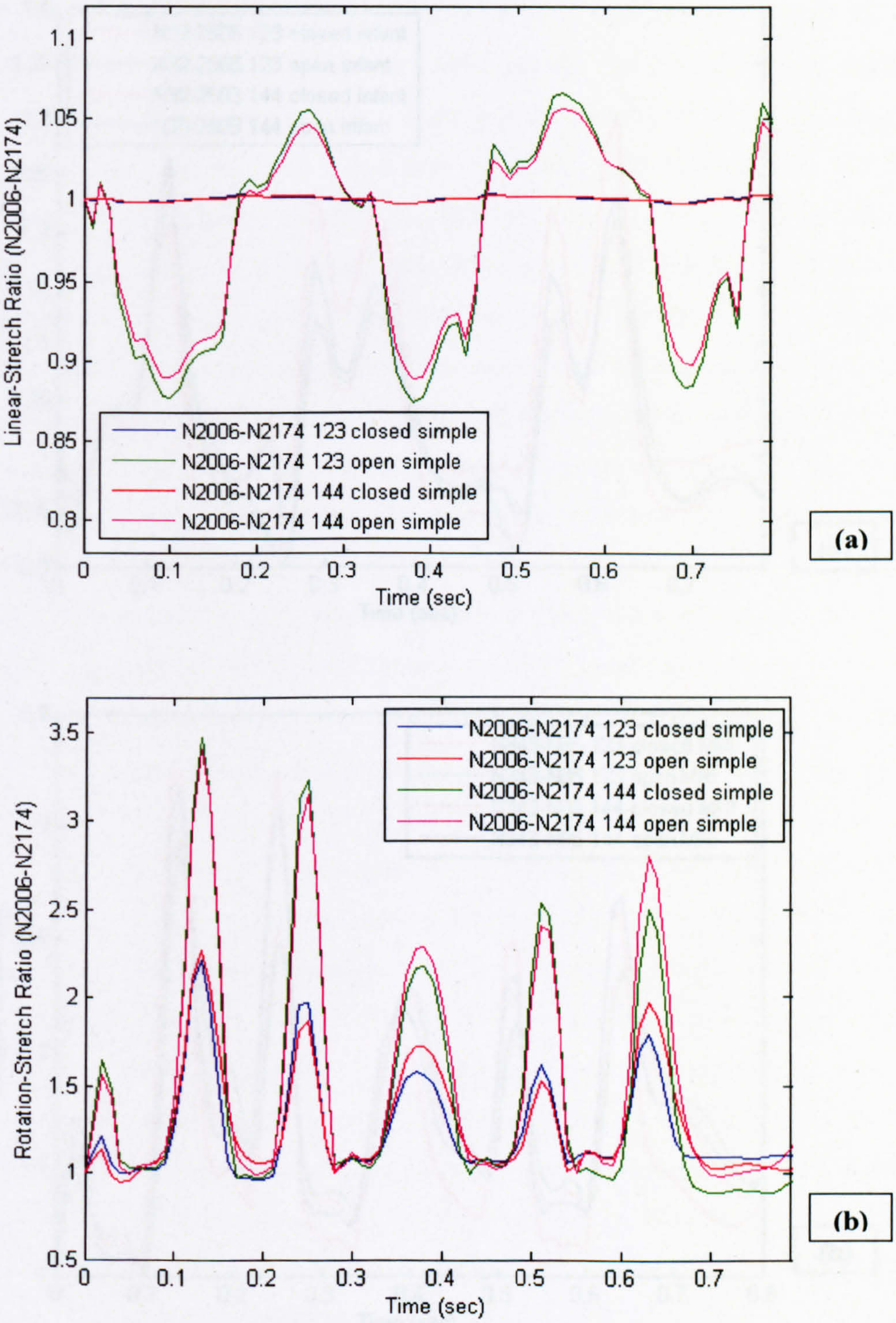

Figure 8.8. *The 2D simple model: data from node n2006 on the top of the brain and node n2174 underneath the membrane. The stretch ratio is compared between both open & closed models each type for 123mm and 144mm diameter skulls.*

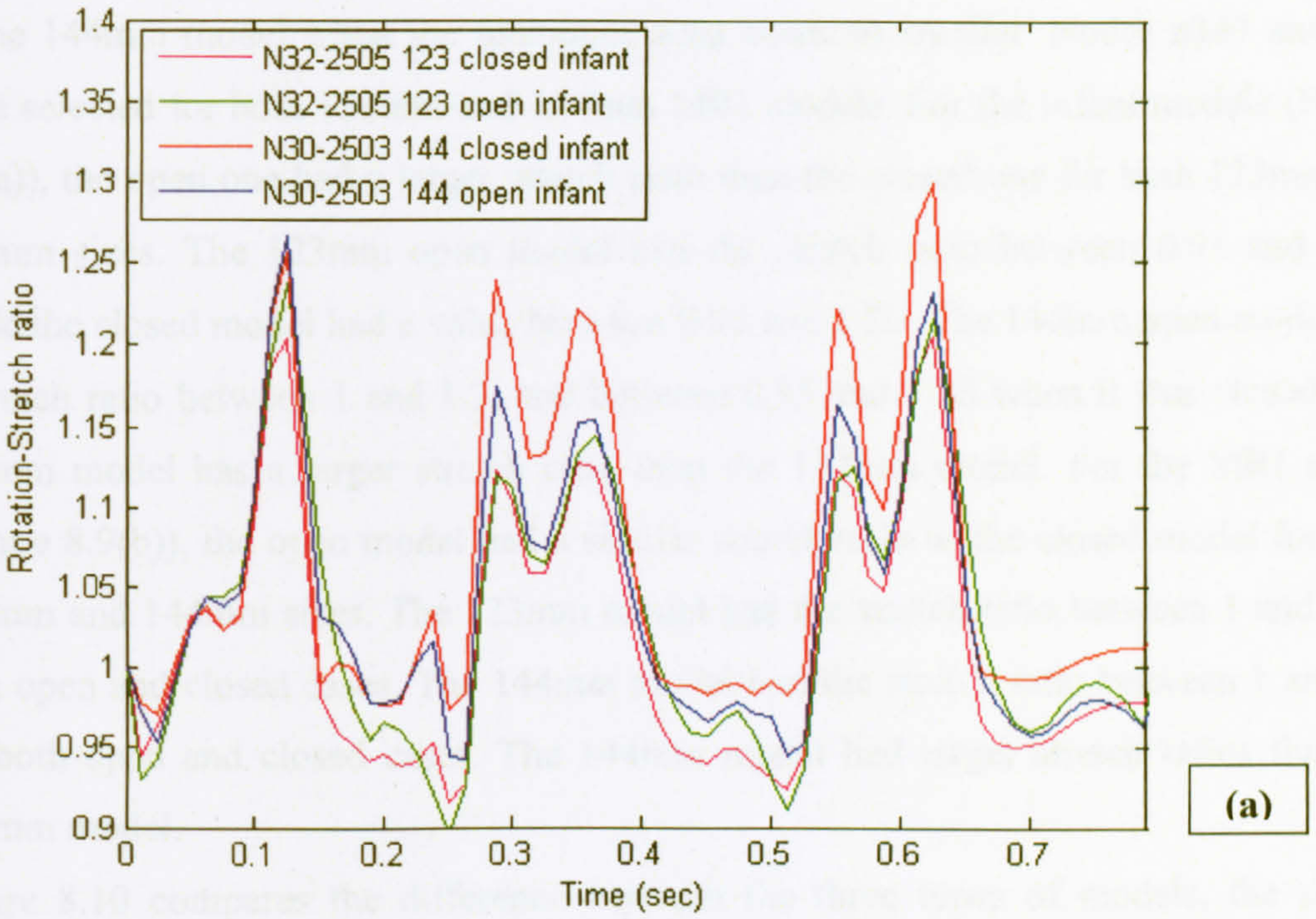

(a)

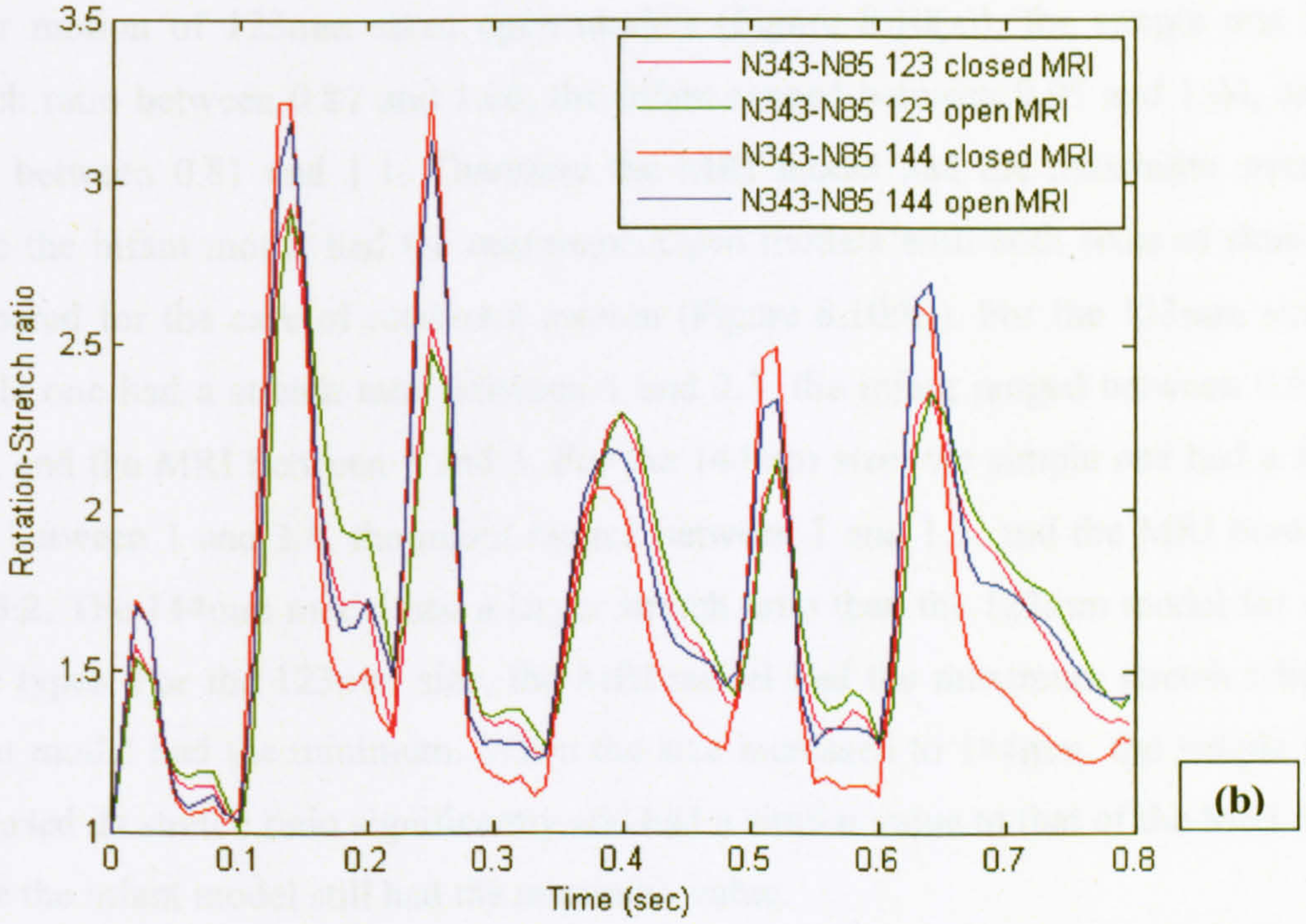

(b)

Figure 8.9. *The infant (123mm) and MRI (144mm) 2D model with its rotational stretch ratio at the same position is compared in open & closed models.*

Figure 8.9 shows data from the infant and the MRI model in rotational motion. Nodes n32 and n2505 were selected for the 123mm infant model, and nodes 30 and n2503

were selected for the 144mm infant model, because n32 and n2505 were under the skull in the 144mm model when the fontanelle area becomes smaller. Nodes n343 and n85 were selected for both 123mm and 144mm MRI models. For the infant models (Figure 8.9(a)), the open one had a larger stretch ratio than the closed one for both 123mm and 144mm sizes. The 123mm open model had the stretch ratio between 0.95 and 1.25, while the closed model had a value between 0.92 and 1.20. The 144mm open model had a stretch ratio between 1 and 1.3, and between 0.95 and 1.25 when it was closed. The 144mm model has a larger stretch ratio than the 123mm model. For the MRI model (Figure 8.9(b)), the open model had a similar stretch ratio to the closed model for both 123mm and 144mm sizes. The 123mm model had the stretch ratio between 1 and 3 for both open and closed cases. The 144mm model had the stretch ratio between 1 and 3.3 for both open and closed cases. The 144mm model had larger stretch ratios than the 123mm model.

Figure 8.10 compares the difference between the three types of models, the simple model, the infant model and the MRI model, in both linear and rotational motion. In linear motion of 123mm sized open models (Figure 8.10(a)), the simple one had a stretch ratio between 0.87 and 1.06, the infant ranged between 0.95 and 1.04, and the MRI between 0.81 and 1.1. Therefore the MRI model had the maximum stretching while the infant model had the minimum. Open models with both sizes of skull were compared for the case of rotational motion (Figure 8.10(b)). For the 123mm size, the simple one had a stretch ratio between 1 and 2.3, the infant ranged between 0.95 and 1.25, and the MRI between 1 and 3. For the 144mm size, the simple one had a stretch ratio between 1 and 3.4, the infant ranged between 1 and 1.3, and the MRI between 1 and 3.2. The 144mm model had a larger stretch ratio than the 123mm model for all the three types. For the 123mm size, the MRI model had the maximum stretch while the infant model had the minimum. When the size increased to 144mm, the simple model increased its stretch ratio significantly and had a similar value to that of the MRI model, while the infant model still had the minimum value.

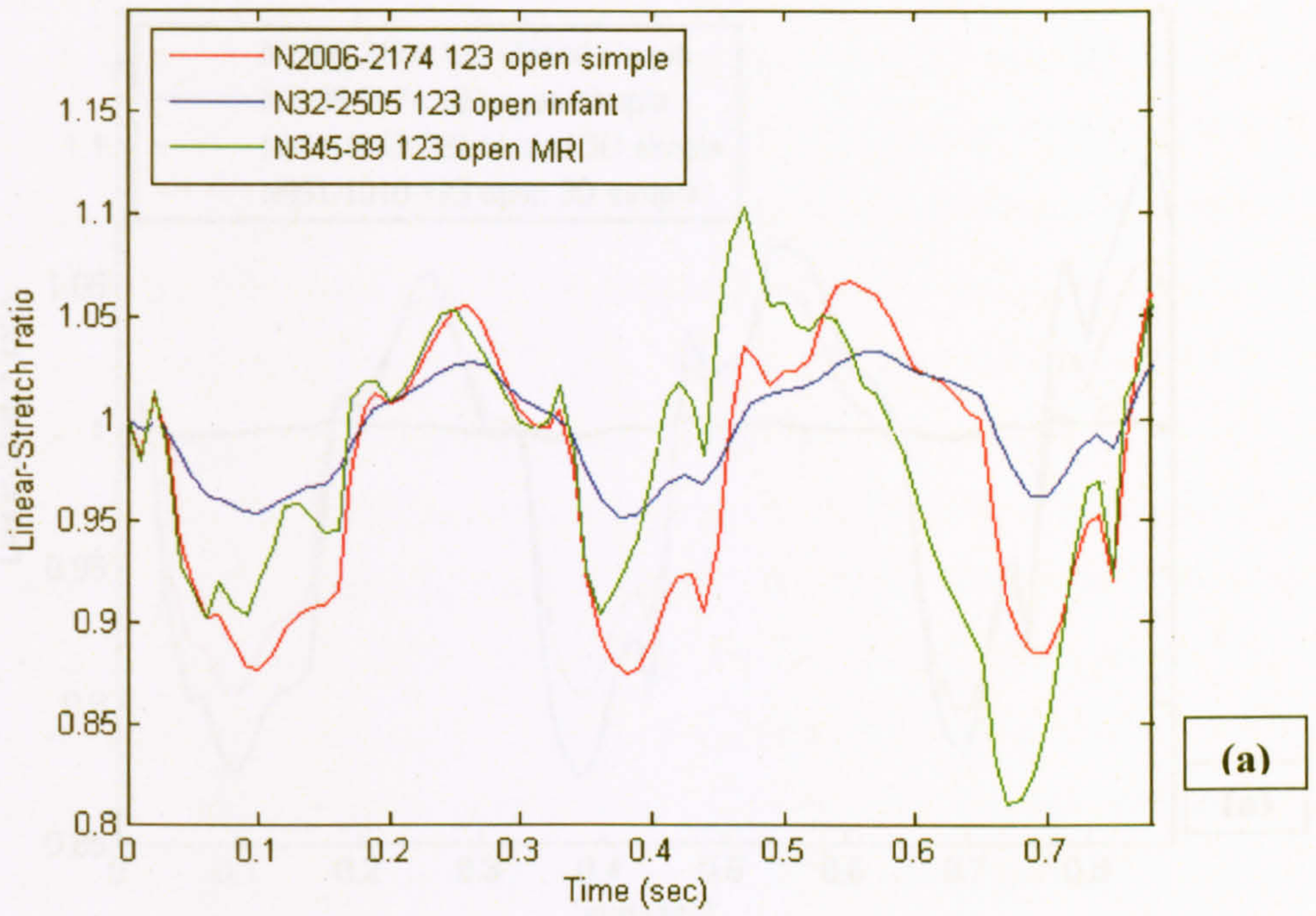

Figure 8.10. *Stretch ratios for 123mm and 144mm sizes of simple, infant and 2D MRI open models. (a)-linear excitation of the model and (b)-rotational excitation.*

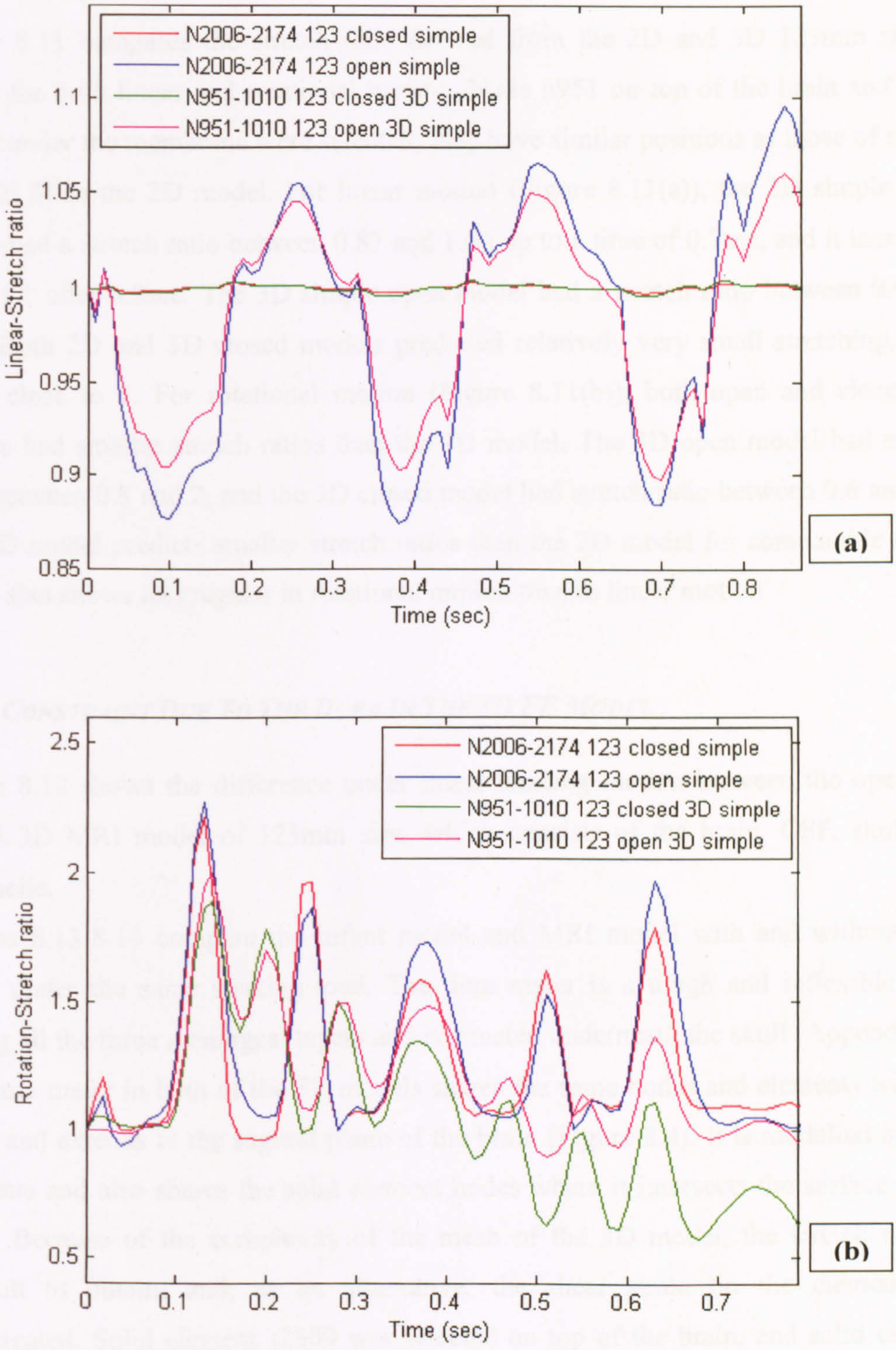

Figure 8.11. *Stretch ratio in linear and rotational motion in 2D simple sagittal plane model and 3D spherical simple model with dimension of 123mm.*

8.3.2. THE STRETCH RATIO IN THE 3D FE MODEL

Figure 8.11 compares the stretch ratio derived from the 2D and 3D 123mm simple model for both linear and rotational motion. Node n951 on top of the brain and node n1010 under the membrane were selected; they have similar positions as those of n2006 and n2174 in the 2D model. For linear motion (Figure 8.11(a)), the 2D simple open model had a stretch ratio between 0.87 and 1.06 up to a time of 0.7sec, and it increased up to 1.1 after 0.8sec. The 3D simple open model had a stretch ratio between 0.9 and 1.05. Both 2D and 3D closed models predicted relatively very small stretching, with ratios close to 1. For rotational motion (Figure 8.11(b)), both open and closed 3D models had smaller stretch ratios than the 2D model. The 3D open model had stretch ratio between 0.8 and 2, and the 3D closed model had stretch ratio between 0.6 and 1.8. The 3D model predicts smaller stretch ratios than the 2D model for comparable cases, and is also shows less regular in rotational motion than in linear motion.

8.3.3. CONSTRAINT DUE TO THE DURA IN THE 3D FE MODEL

Figure 8.12 shows the difference under linear shaking motion between the open and closed 3D MRI model of 123mm size, which consists of the brain, CSF, skull and fontanelle.

Figures 8.13-8.14 compare the infant model and MRI model with and without dura mater under the same shaking load. The dura mater is a tough and inflexible layer among all the three meningeal layers and is situated underneath the skull (Appendix D). The dura mater in both of the FE models shares the same nodes and elements with the skull, and extends to the sagittal plane of the brain (Figure 8.4). It is modelled in shell elements and also shares the solid element nodes where it intersects the surface of the brain. Because of the complexity of the mesh of the 3D model, the stretch ratio is difficult to obtain, and, as an alternative, the shear strain on the element was investigated. Solid element s2309 was selected on top of the brain, and solid element s9715 was selected under the membrane.

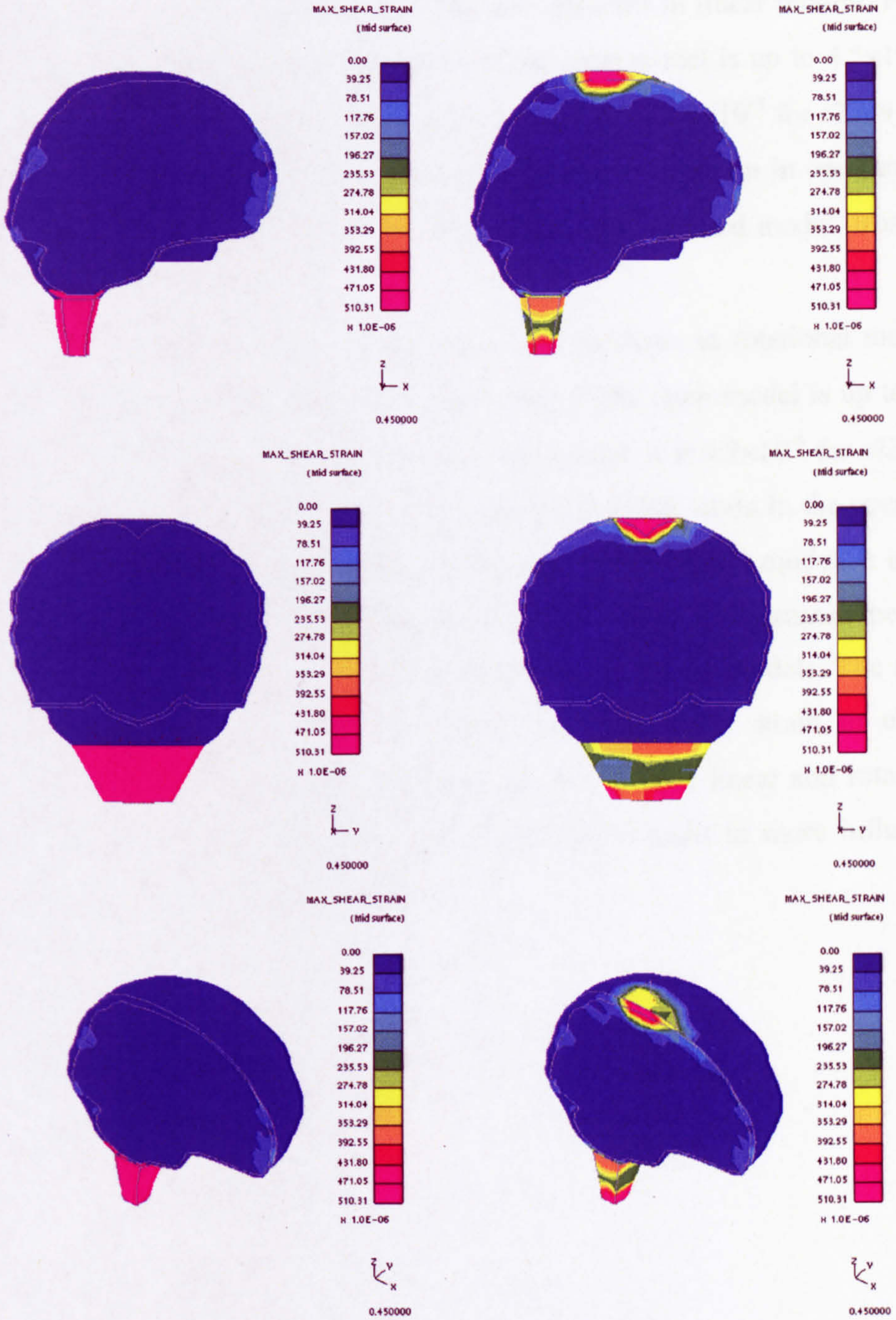

Figure 8.12. *Shear strain distribution in 3D MRI model with dimension of 123mm in linear motion. Left column: closed model; right column: open model.*

Figure 8.13 shows the shear strain of the two elements in linear motion. For the model without dura, the maximum shear strain in the open model is up to 4.5×10^{-5} for s2309 and 1.45×10^{-4} for s9715, and, in the closed model, it is 1.2×10^{-5} for s2309 and 1.5×10^{-5} for s9715. For the model with dura, the maximum shear strain in open model is up to 3.4×10^{-5} for s2309 and 5.5×10^{-5} for s9715, and, in the closed model, it is 1.3×10^{-5} for s2309 and 1.0×10^{-5} for s9715.

Figure 8.14 shows the shear strain of the two elements in rotational motion. For the model without dura, the maximum shear strain in the open model is up to 7.2×10^{-3} for s2309 and 0.047 for s9715, and, in the closed model, it is 4.3×10^{-3} for s2309 and 0.037 for s9715. For the model with dura, the maximum shear strain in the open model is up to 4.9×10^{-3} for s2309 and 0.045 for s9715, and in the closed model, it is 4.0×10^{-3} for s2309 and 0.036 for s9715. So, involving of the dura mater increases the constraint on the structure and thereby reduces the shear strain in all the models. The shear strain in element s2309 (on top brain) is smaller than the shear strain in element s9715 (underneath the membrane) for the open model, in both linear and rotational motion, therefore during the shaking the soft membrane brought in more influence near the membrane than near the brain surface.

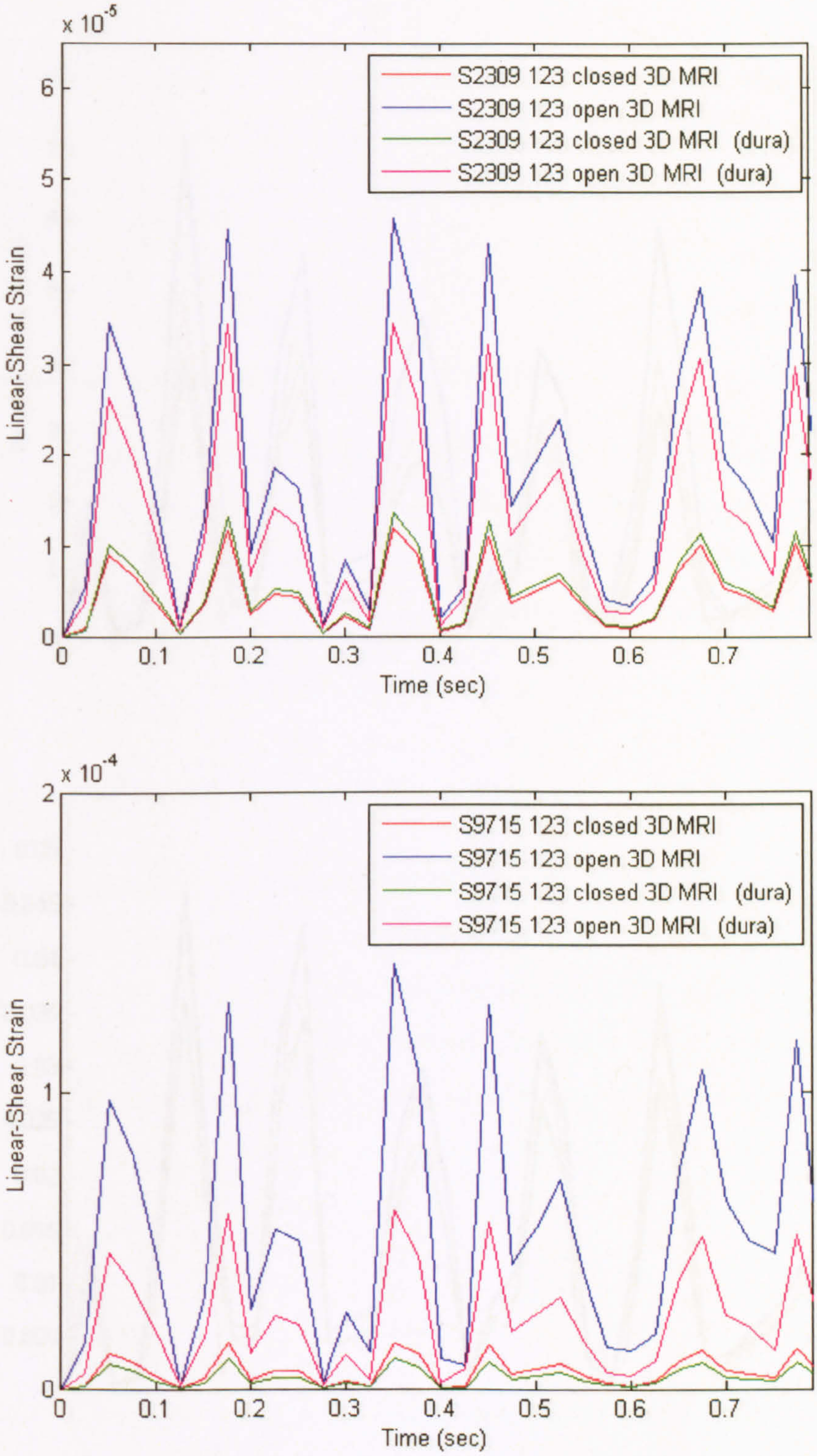

Figure 8.13. *Shear strain in linear motion in 3D 123mm MRI model with and without dura. Top: solid s2309 from the top of the brain; bottom: solid S9715 from underneath the membrane.*

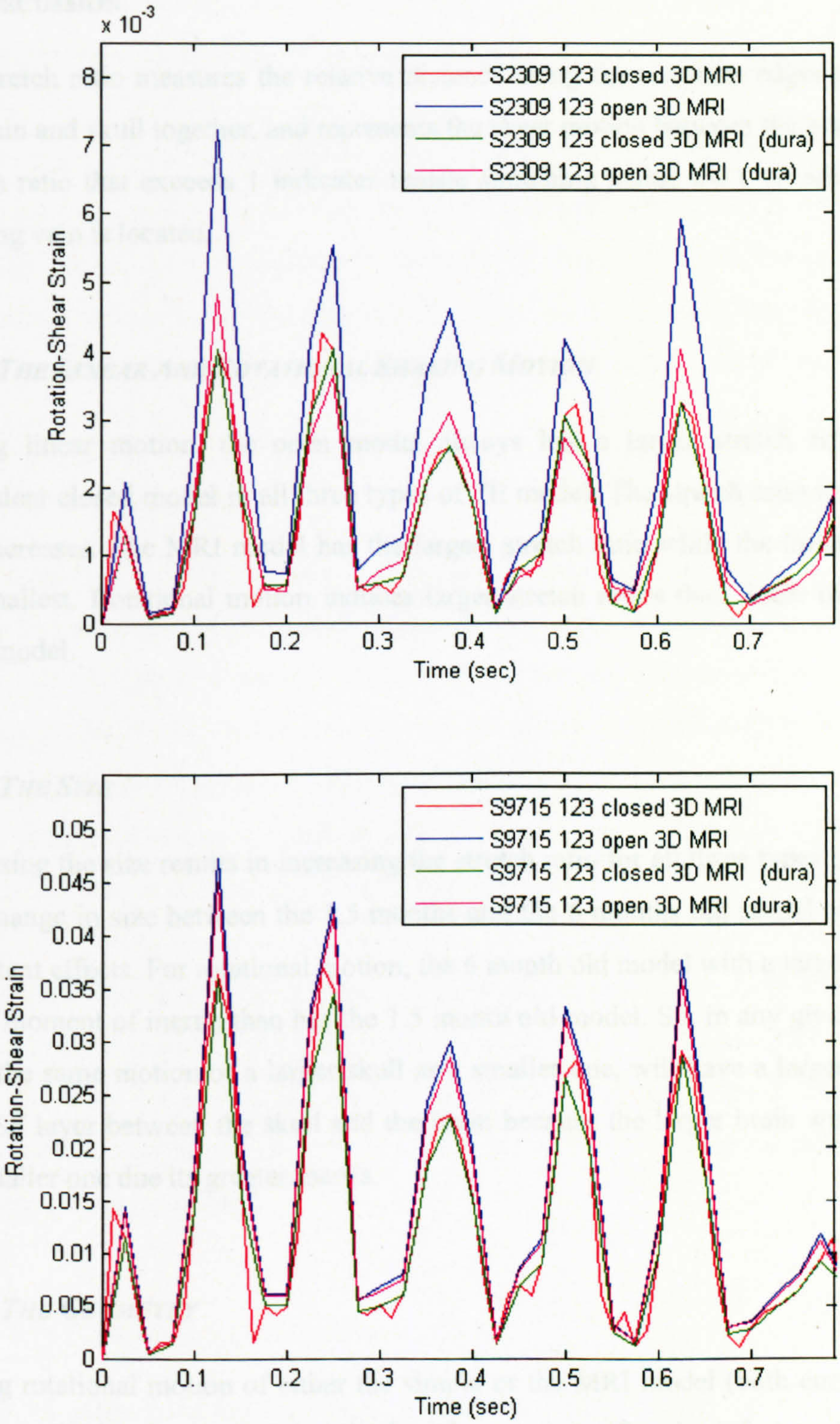

Figure 8.14. *Shear strain in rotational motion in 3D 123mm MRI model with and without Dura. Top: solid s2309 from the top of the brain; bottom: solid S9715 from underneath the membrane.*

8.4. DISCUSSION

The stretch ratio measures the relative distance along the elements edges that connect the brain and skull together, and represents the shear motion between the brain and skull. Stretch ratio that exceeds 1 indicates tensile stretching inside the CSF area where the bridging vein is located.

8.4.1. THE LINEAR AND ROTATIONAL SHAKING MOTION

During linear motion, the open model always has a larger stretch ratio than the equivalent closed model in all three types of FE model. The stretch ratio reduces as the size increases. The MRI model has the largest stretch ratio while the infant model has the smallest. Rotational motion induces larger stretch ratios than linear motion of the same model.

8.4.2. THE SIZE

Increasing the size results in increasing the stretch ratio for all three types of FE model. The change in size between the 1.5 months and the 6 months old model also produces important effects. For rotational motion, the 6 month old model with a larger brain has a larger moment of inertia than has the 1.5 month old model. So, in any given interval of time, the same motion of a larger skull as a smaller one, will have a larger shearing in the CSF layer between the skull and the brain because the larger brain will lag behind the smaller one due its greater inertia.

8.4.3. THE GEOMETRY

During rotational motion of either the simple or the MRI model (both curved top), the closed model has larger stretch ratio than the open one. For the infant model (flat top), the stretch ratio of the open model is larger than that of the closed model.

The infant model, which has a relatively flat top to the skull, is close in shape to a real infant head. On the other hand, the 2D simple and 2D MRI model have a curved shape at the top of the skull, a feature that is typically adult.

During rotational motion, a deformed membrane with a flat characteristic will tend to apply more shearing to the CSF between the brain and the skull than one with a curve profile.

A head model with a curved profile has more space between the brain and the skull than one with a flat top. Since thinner spaces for the CSF induce shearing rather than normal straining, we expect that flat models will exhibit larger shearing strains than curved ones, which will tend to produce larger amounts of normal strain. Therefore the shape of the FE modelling should not be ignored during the study of infant head injury.

8.4.4. THE 3D HEAD MODEL

In linear motion, the 2D and 3D simple models have very similar profiles for the stretch ratio with that from the 2D model being slightly larger (Figure 8.11(a)). In rotational motion, the situation is more complex. The more realistic 3D model has a more complex profile for the stretch ratio than the 2D representation, and drifts away from the comparatively simple pattern suggested by the 2D model. This is almost certainly due to induce motions in the out-of-plane direction in the 3D model (Figure 8.11(b)).

The stretch ratio is difficult to extract from the complexity of the mesh of the 3D MRI model, and so the shear strain was chosen as the best equivalent measure of local deformation. The shear strains under the fontanelle area in linear motion were larger in the open model than in the closed one. The shear strain both open and closed models was reduced by the presence of the dura mater compared with when it was absent. The difference in shear strain between open and closed models is larger near the membrane than near the brain surface.

8.4.5. THE FE MODEL AND MEDICAL EVIDENCE

Compared to the shear strain in the CSF area, the shear strain on top of the brain is very small.

The medical literature (Geddes, Hackshaw et al. 2001, Shannon and Becker 2001) reports that most of the severe injury in the shaken baby syndrome occurs in the subdural area. Standard anatomy texts (Moore 1999 for example) illustrate this has being much closer to the skull and fontanelle skin than to the brain. Also, the evidence

suggests that little damage to the brain surface occurs during shaking because it is not violent enough to provide the local accelerations typical experienced in traffic accidents or similar impacts. The limited medical evidence therefore suggests that parameters like the stretch ratio in the CSF or the local shear strain are useful candidates for measuring damage to the bridging vein underneath the top of the skull or under the fontanelle.

The work clearly shows the local geometry of the top of the skull has a significant effect on the pattern of stretch ratio and shear strain during shaking. Since the shape of the skull of infants changes as the age, local geometry is therefore an important influence on the susceptibility to injury during shaking.

The research shows that there is an influence of the fontanelle on the concentration of potential damage in the region of the bridging veins. However, the effect was not clear cut according to the comparatively unsophisticated models that formed the basis of this research. As we have already noted, these models were chosen only because the more accurate Eulerian FSI analyses techniques produced run times that would have been far too long to complete a realistic research programme.

Despite this, there is clearly much to be gained by using more realistic and accurate models to investigate the influence of the fontanelle. The work reported here strongly suggests that this should be done using Eulerian FSI analyses for the CSF in models with reasonably accurate skull and brain shapes. This is a basis for future work which will be introduced in Chapter10.

SUMMARY

Following on from Chapter 7, which discusses the validation of FE modelling by comparison with data from the experimental rig tests, this chapter describes the FE analysis of various infant head models during shaking. Three geometries of FE model were constructed, one with a simple spherical shape, one with an empirical infant head shape, and one derived from a MRI scan of a child head. The brain-skull connection was constructed using the Lagrangian method. The simple and MRI models had both 2D and 3D geometries, while the infant model had only 2D geometry. Linear and rotational motions reconstructed from data discussed in Chapter 3 were selected to excite the models. The relative movement between the brain and skull was investigated using the stretch ratio in the 2D models and the shear strain in the 3D MRI model. Two

sizes of skull were considered, one 123mm diameter to represent a 1 month old infant, and the other of 144mm diameter to represent a 6 month old infant head.

The results demonstrated that the deformation of the material between the brain and the skull depends on the motion, the size and the geometry of the model and the FE modelling of the structure.

For linear motion, the open model has a larger stretch ratio than the closed model in all three types of FE model. In rotational motion, the models have larger stretch ratios than in linear motion, but only the infant open model has a larger stretch ratio than the closed case, whilst the closed model has a larger value than the open case for the simple and MRI models. Increasing the size results in increasing stretch ratio for all three types of FE model, and this can be explained by effects of a larger mass of brain during angular acceleration.

Linear and rotational motions were also applied to 3D simple and MRI models. For the open model in linear motion, the 3D simple model predicts a smaller stretch ratio than the 2D simple model. In rotational motion, the stretch ratio from the 3D simple model is less regular then the 2D cases and tends to fall below 1 after 0.35sec.

For the 3D MRI model, a comparison was made between the model with and without the dura mater. Elements on top of the brain and under the membrane were selected and the shear strain was compared. The shear strain of both open and closed geometries is reduced by the presence of the dura mater. The shear strain in both linear and rotational motion has a larger value in the open model than in the closed model under the fontanelle area, and the difference in shear strain between open and closed model is larger near the membrane than near the brain surface. This is consistent with the medical evidence that the subdural haemorrhaging has been discovered underneath the skull where the bridging veins were ruptured during incidents of the shaken baby syndrome. There is very little, if no, evidence that the brain surface can be injured when the shaking accelerations are significantly smaller than those induced by impact.

In conclusion, for 2D modelling, the infant model is a better representation than the simple and MRI models. For 3D modelling, the introduction of structures that change the brain-skull connection conditions will produce different results from the those of the model with a simple skull-CSF-brain connection. This study, although provisional and preliminary, suggests that future numerical study of the shaken baby syndrome requires accurate representation of the infant head using paediatric geometry and structure and material properties. Also, the discussion of fluid-structure interaction in chapter 7

suggests that different results may emerge when the more realistic Eulerian method is introduced. Practical computational run times for such 3D Eulerian FSI models will require substantially faster computer power than that available during the research reported here.

CHAPTER 9: *CONCLUSIONS*

INTRODUCTION

This chapter summarises the procedure, achievements, and important findings obtained in each of the previous chapters. Investigating the mechanism of head injury through experimental and computational method in the contribution to the pathological understanding of shaken baby syndrome is described in the initially (Chapters 1- 2). The experimental study (Chapter 3) includes the shaking of an anthropomorphic dummy, and the reconstruction via kinematic equations and imaging analysis to trace the position of the head. A custom designed test rig (Chapter 4-6) was constructed to enable a shaking test on a simplified head model with the fundamental paediatric structures, to be assessed under shaken baby conditions. The development of the finite element (FE) model of those rig tests was discussed, while three numerical algorithms was chosen to represent the skull-brain boundary condition (Chapter 7). The agreement of the results that emerged from rig tests and FE models were discussed. With the sufficient consistence, the more complex FE models of biological head structures were described in the chapter 8, and the results demonstrated the influence to a certain degree from the fontanelle and uncompleted skull in the early age of infancy for studying the shaken baby syndrome. Further development of the research will be presented in Chapter 10 with a prediction of the research direction.

9.1. RECONSTRUCTION OF THE TRL DUMMY SHAKING

A shaking test on an anthropomorphic dummy was performed by volunteers in the Transportation Research laboratory (TRL) in 2000 (Brudenell 2000). The information was collected by the author and the kinematic movement was analysed using both the kinematic equation and image analysing methods. It was found that the maximum linear acceleration the dummy head obtained was 20g (196.2mm/s^2) no matter how violent the shakes were, whilst the maximum linear acceleration value for the torso was found to be around 7g-8g (68.7 mm/s^2-78.5mm/s^2). The angular velocity of the head was -60rad/s to 60rad/s with angular acceleration of -2000rad/s^2 to 2000rad/s^2. Although the kinematic equation method with the accelerometer was considered to be cost effective and time saving, the limitation of the sensing equipment on the dummy prevented the

reconstruction and understanding the dummy motion via the analytical equaitons. Meanwhile, the analysing the stills in the video output enable to reconstruct the head rotational motion across a 2D plane. The limitation of this method was that it was unable to capture the frequency of the movement higher than 30Hz, which is the capture rate of the normal video camera used in tests. However, this is not a great problem in practice, as it is the load but not displacement to define the shaking injury. The results were found to be consistent with published literature (Duhaime et al. 1987, Wolfson et al. 2004, Chapter 2 Figure 2.24) and were taken to be sufficient for the motion input source into the computational model.

9.2. Test Rig Construction

An experimental investigation of shaking head injury was performed by constructing an adjustable pneumatic test rig that mimics the human limb motion to produce repetitive shaking on a custom designed head model. The current rig enables accelerations of 2g-3g (19.6 mm/s^2-29.4mm/s^2). The shaking power can be improved in further work by reducing the distance of the micro-switches and increasing the airflow inside the circuit. The simulation of the rig maintains steady and repeatable with the peak acceleration from -2g to 2.5g (-19.6 mm/s^2 to 64.5mm/s^2), peak velocity from -1200mm/s to 1500mm/s and displacement magnitude from -140mm to 125mm. It was found that the use of pneumatic technology is a major advantage for the simulation of biological joint movement.

9.3. Phiysical Head Model Construction

A custom designed model was used to study the infant head intracranial behaviour under whiplash movement. The anatomical detail of the model was ignored and skull, brain, CSF, and anterior fontanelle (a paediatric suture during the first few months after born), were retained. Gelatine mixtures with 10% by mass content and latex were carefully selected to construct the brain and fontanelle components. The material properties were obtained by a series of dynamic tests using VISCOANALYZER 2000. The skull was made of two hemispherical domes with flanges mounting together.

Some of the models were run with an open part at the top to represent the effect of the fontanelles, while some other were run with only closed dome. The deformation and relative motion of the membrane as well as the gelatine suspended into the water inside the dome were recorded by two web cameras from different angles. The motion of the gel inside the dome gave a similar impulse response history between the open and closed models.

It became clear later that two major factors stiffen the open structure in place where it was designed to demonstrate the softness, which are the significant pre-strain applied on the membrane during the assembling and the protrusion structure inside the CSF space. Therefore the pre-strain was measured and calculated, and later was considered into the finite element modelling associated with the protrusion effect.

9.4. Finite Element Models Of The Rig Tests

Two-dimensional finite element (FE) models were constructed to simulate the rig tests. Three fluid structure interaction (FSI) methods of Lagrangian, 1-point ALE and Eulerian formulations separately were employed to represent the skull-brain boundary. The models were excited using the rig output with the soft spot (fontanelle) modelled carefully on the top. In contrast, another group of closed top models were also produced and simulated for comparison.

The horizontal displacement on top of the gelatine was traced, with 0.15mm for Lagrangian, 2mm for ALE, and 5mm for Eulerian analyses of the open top model. Meanwhile all the closed models displayed the magnitude that is smaller than 1mm. The FE models were then modified with the stiffening effect, which are the pre-strain on the membrane and the protrusion structure inside the fluid. The reduction of the displacement in Lagrangian analysis is 44%; in ALE analysis is 55.6%; and in Eulerian analysis is 83.3%. The Eulerian analysis with reduced the predicted motion for the open model to a similar magnitude as that for the closed model, which is consistent with the experimental test. The Eulerian method shows the significant advantages than the other two methods that are not able to achieve this. Therefore the Eulerian analysis should be encouraged in future simulation of FE head model when CSF circulation and a reservoir system for instance the cranial cavity are involved during the study of shaken baby syndrome. The larger magnitude of the gelatine movement in open model than that in

closed model, shown in the FE models during the removing of the stiffening effect, indicated the different dynamic mechanism by the fontanelle on the skull structure. The further biomechanical study with SBS expects an infant head model with a compliant, separate cranial bones and sutures that is different from the adult one.

9.5. Finite Element Models Of The Human Infant Head

Three FE models of infant head were constructed, which consisted of the brain, skull, CSF, fontanelle, and the dura mater. The geometry came from a simple spherical shape, an empirical infant head shape, and a MRI scan of a nine month old infant respectively. Lagrangian analysis was used as the FSI method for simulating the CSF to reduce the run time. Both 2D and 3D geometries were produced in the simple and the MRI models, while only 2D geometry was involved in the infant model. All the models were divided into two diameters group, which is 123mm for 1.5 month old, and 144mm for 6 month old infant. They were excited using both linear and rotational motions that came from the TRL tests.

The stretch ratio in the CSF area and local shear strain were selected as the parameters to measure the damage of the bridging vein during shaking motion. It was found out that they were affected by several crucial factors in the FE modelling including the input motion, the size, and the geometry of the model.

(1) Input motion

The stretch ratio is always larger in rotational motion than it is in linear motion. During the linear motion, all the models predicted a larger stretch ratio in the open model (with fontanelle) than the one in the closed model; and for rotational motion only the infant model predicted a larger stretch ratio in the open model than the one in the closed model, while the simple and the MRI models experienced larger stretch ratio in the closed model than the open model.

(2) Size

The 123mm model demonstrated larger stretch ratio in linear motion, while gave smaller stretch ratio in rotational motion than the 144mm model. This can be explained by the effects of larger mass of the brain. When the larger brain lag behind the smaller one by given the same time interval and the input motion, it reduced the stretch ratio in linear motion while increased the stretch ratio in rotational motion due its greater inertia.

(3) Geometry

During the rotational motion, the 2D infant model with the flat top of the skull predicted larger stretch ratio in the open model than the one in the closed model. By contrast, the 2D simple and MRI models with the curved top of the skull predicted smaller stretch ratio in the open model than the one in the closed model. During the shaking of the head model, the larger space in the CSF area in the curved top will tend to exhibit more normal strain than the shear strain, therefore reduced the shearing effect. The accurate modelling of the infant head with a relatively flat top to the skull should not be ignored during the study of infant head injury.

When comparing the 3D MRI model with the 2D MRI model, the stretch ratio in the 3D MRI model demonstrated more reduction and complexity than the one in the 2D MRI model. One of the reasonable explanation is the induction of the motion in out-of-plane direction in the 3D model. Further more, the influence of the extra involvement of the dura mater in the 3D MRI model predicted the smaller shear strain than when it was absent from the same model. This is certainly due to the restraint to the FE mesh when the dura mater, which has larger elastic modulus than the brain tissue, was modelled on the surface of the brain.

Associated with the limited medical report, the work contributes to our hypothesis, by setting up the link between the fontanelle, the geometry of the skull and the potential damage of the bridging veins, without showing the clear cut due to the relatively unsophisticated models used during the research.

It is strongly suggested that the Eulerian FSI analysis for the CSF with reasonably accurate skull and brain shapes is expected during the further FE study of the shaken baby syndrome.

SUMMARY

This chapter summarized the PhD work as well as the achievements from chapter 3 to chapter 8. Chapter 3 described the shaking motion reconstruction from the anthropomorphic dummy test conducted by the shaken baby research group in 2000

(Brudenell 2000). The results predicted a good correlation within the scale of the other engineering tests in literature (Prange et al. 2003, Wolfson et al. 2005). Chapter 4 described the design and the construction of the experimental test rig that is used to provide the stable human shaking to an custom designed anthropomorphic infant head model. Chapter 5 and Chapter 6 discussed the record and the analysis of the experimental tests obtained from the test rig. Chapter 7 investigated the development of the finite element (FE) models for the experimental rig tests and the result emerged from them. Chapter 8 continues the using of the FE method to explore the interior constituents of an infant skull by shaking.

The next chapter (Chapter 10) will provide the details of the further development of this work.

CHAPTER 10: *FUTURE WORK*

SUMMARY

In this research work, an experimental study was designed and performed in conjunction with some corresponding mathematical modelling in order to testify the hypothesis that the paediatric structure of new born infant head produces internal movement of the intracranial tissue that is different from the adult head under similar shaking conditions. Hence this can explain the vulnerability of the infantile group exposed to the severe shaking forces even though these forces are much lower than impact forces. The limitations in the current work are restricted to the rotational head reconstruction of the laboratory dummy test, notably in the shaking pattern and power of the pneumatic rig. Limitations in the mathematical model were associated with insufficient geometric detail, material accuracy and simplified skull-brain boundary conditions. The research, although provisional and preliminary, should be extended into several new directions outlined in the following sections.

10.1. THE SHAKING TEST USING ANTHROPOMORPHIC DUMMY

The kinematic reconstruction of shaking baby motion from an anthropometric dummy test is limited the linear motion of the torso and the rotational motion of the head into one plane. This limitation was due to the insufficient kinematic transducer and low catching frame rate of video camera, which restraints the application of the kinematic equation method and the imaging analysis method.

The kinematic equation method could be improved by adding an additional accelerometer on the top or bottom of the head with the local x (gaze) direction (Figure 3.1, page 80). The 3D head motion with 3 linear and 3 rotational directions could then be deduced combining all six independent equations. Without the previous assumption (moving dynamic information from torso on the neck), the equation groups could be effectively optimized and the error generated by the discrepancy of the assumed result and real result could be eliminated. Therefore $a_{DL} = \left[a_{D\xi}, a_{D\mu}, a_{D\varsigma}\right]$ is not identical to $a_{TG} = \left[a_{TX}, a_{TY}, a_{TZ}\right]$ (Chapter 3 Figure 3.1, page 80) and is more reliable.

Moreover, the imaging analysing method could be improved by using two synchronized high speed cameras to capture the shaking progress of dummy's motion from two different views. The high speed camera could avoid the blurred images produced by the normal video camera and was not able to capture the high frequency whiplash higher than 30 frame/second (Chapter 3, Figure 3.13-3.14). Synchronization of the two fields of view enables the full reconstruction of the 3D motion via image reconstruction methods (Bouguet, 2007).

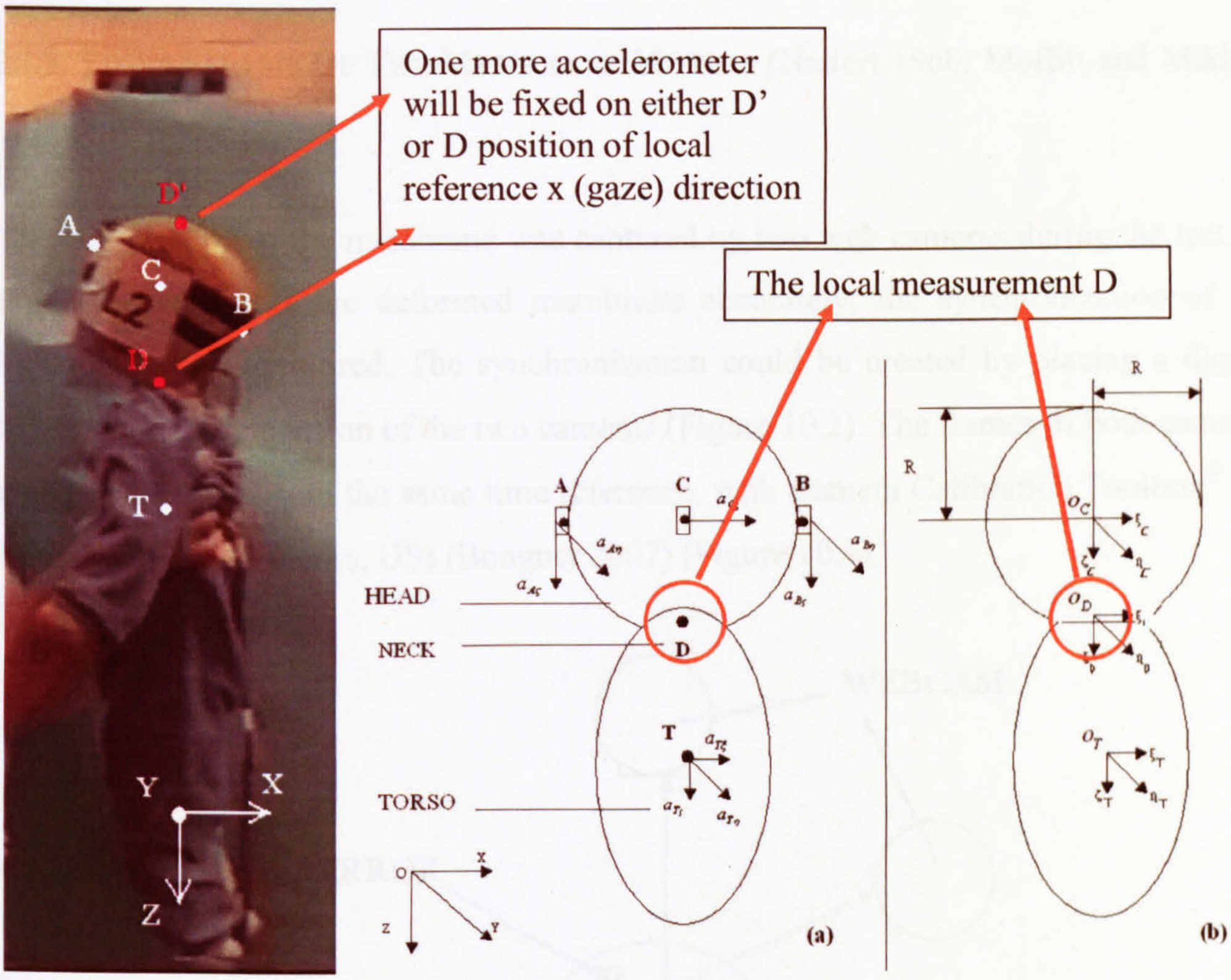

Figure 10.1. *Diagram of position of accelerometer.*

10.2. The Shaking Test Using Pneumatics Rig

During the current tests result in the pneumatic rig, the average peak acceleration produced was 2g-3g. Although this acceleration is within the same magnitude as the human shaking, the force generated was still smaller than average measured result of 7g-8g. Since the theoretical calculation of 11g was expected, further improvement should be focused on increase the power of the stroke inside the pneumatic circuit.

Furthermore, the platform driven by pneumatic cylinder produces only linear movements. According to the laboratory dummy test and computational simulations, the

whiplash of a rotating head was considered to be responsible for bridging veins damage and possibly neck fracture. Hence the rotational study of the head model should be reconstructed on the rig with further improvements to the mounting system between the platform and the model. This could be made more realistic by designing a hinge mechanism between the platform and the model. The spring or damping of the joint could then be adjusted to mimic the resistance of a proper neck.

10.3. THE ANALYSIS OF THE MEMBRANE MOTION (Hallert 1960, Moffitt and Mikhail 1980)

The deformation of the membrane was captured by two web cameras during the test. In order to reconstruct the deformed membrane accurately, the synchronization of the video cameras is required. The synchronization could be created by placing a digital LED counter in the vision of the two cameras (Figure 10.2). The frames of both cameras could be recorded with the same time reference, with Camera Calibration Toolbox® for Matlab (The MathWorks, US) (Bouguet 2007) (Figure 10.3).

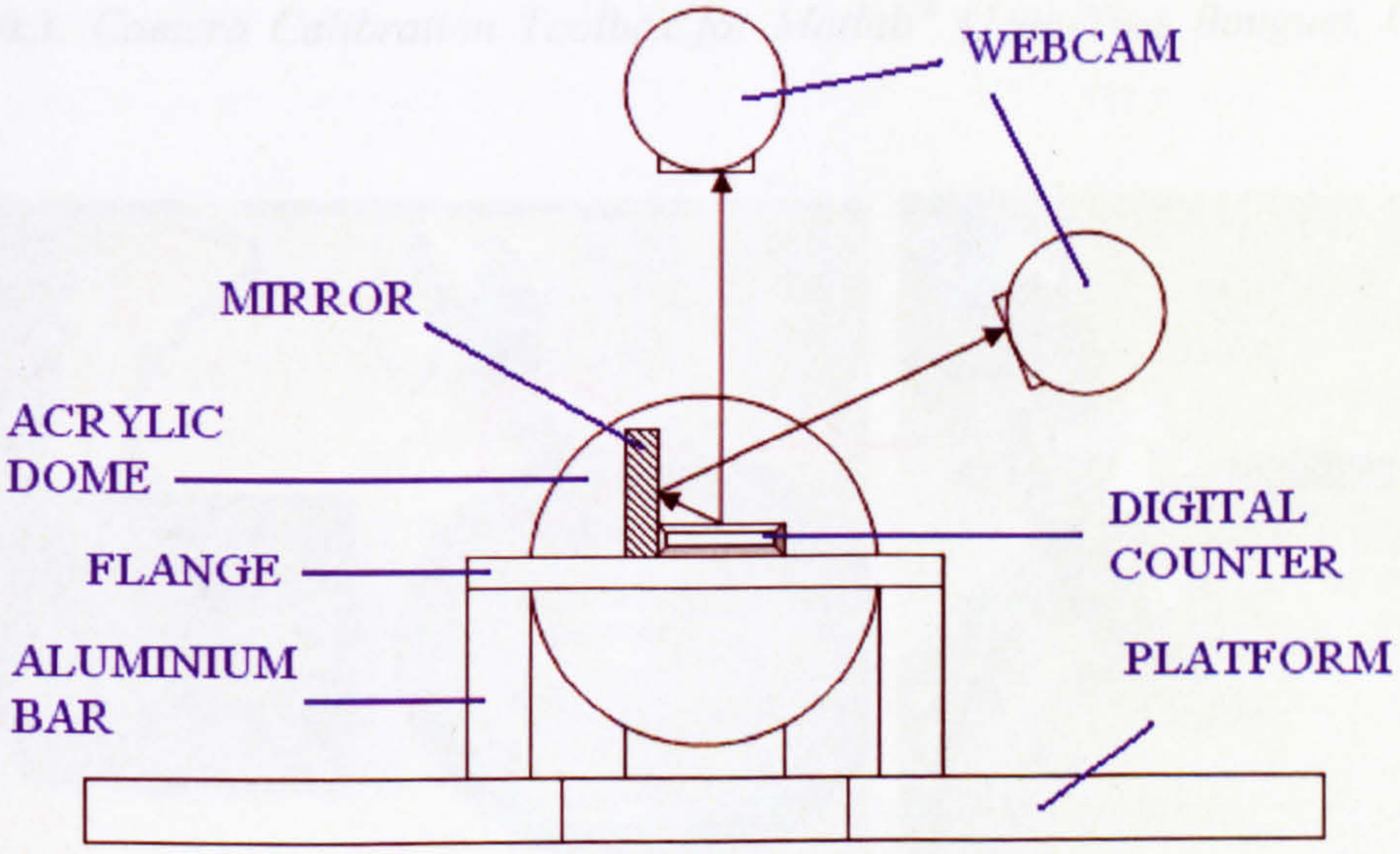

Figure 10.2. *Synchronization via digital counter.*

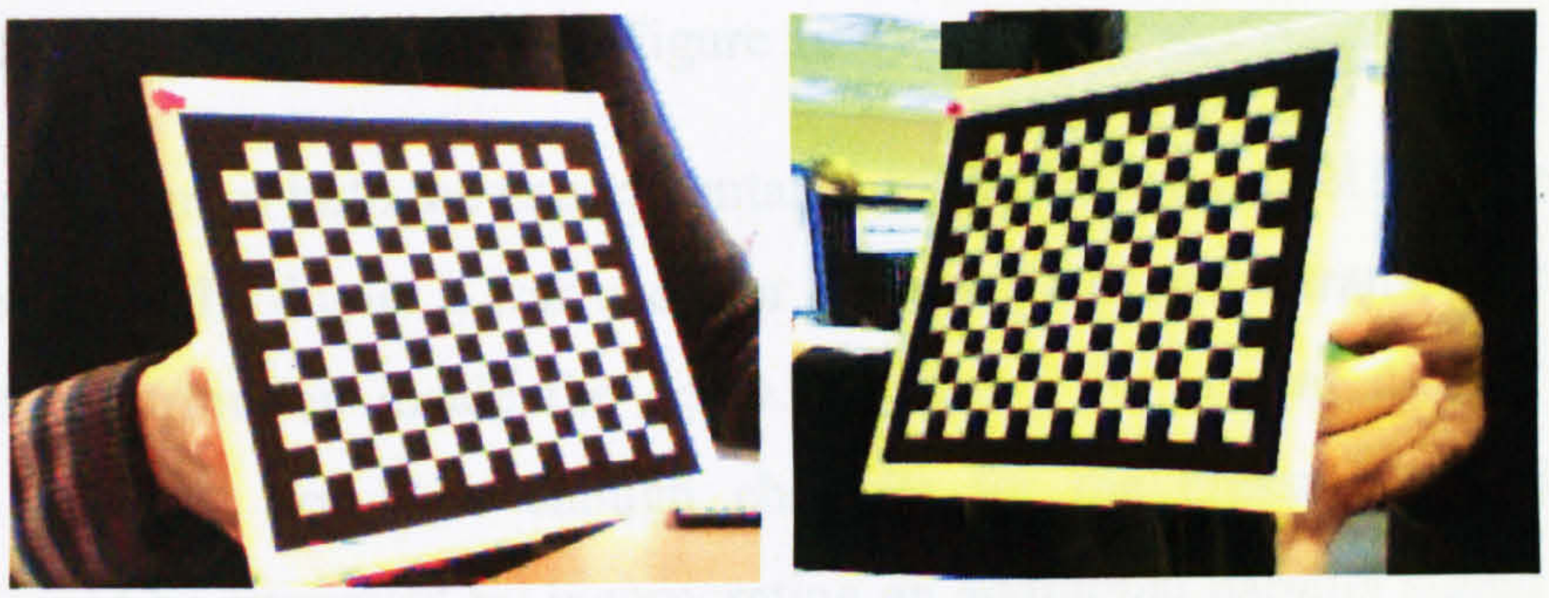

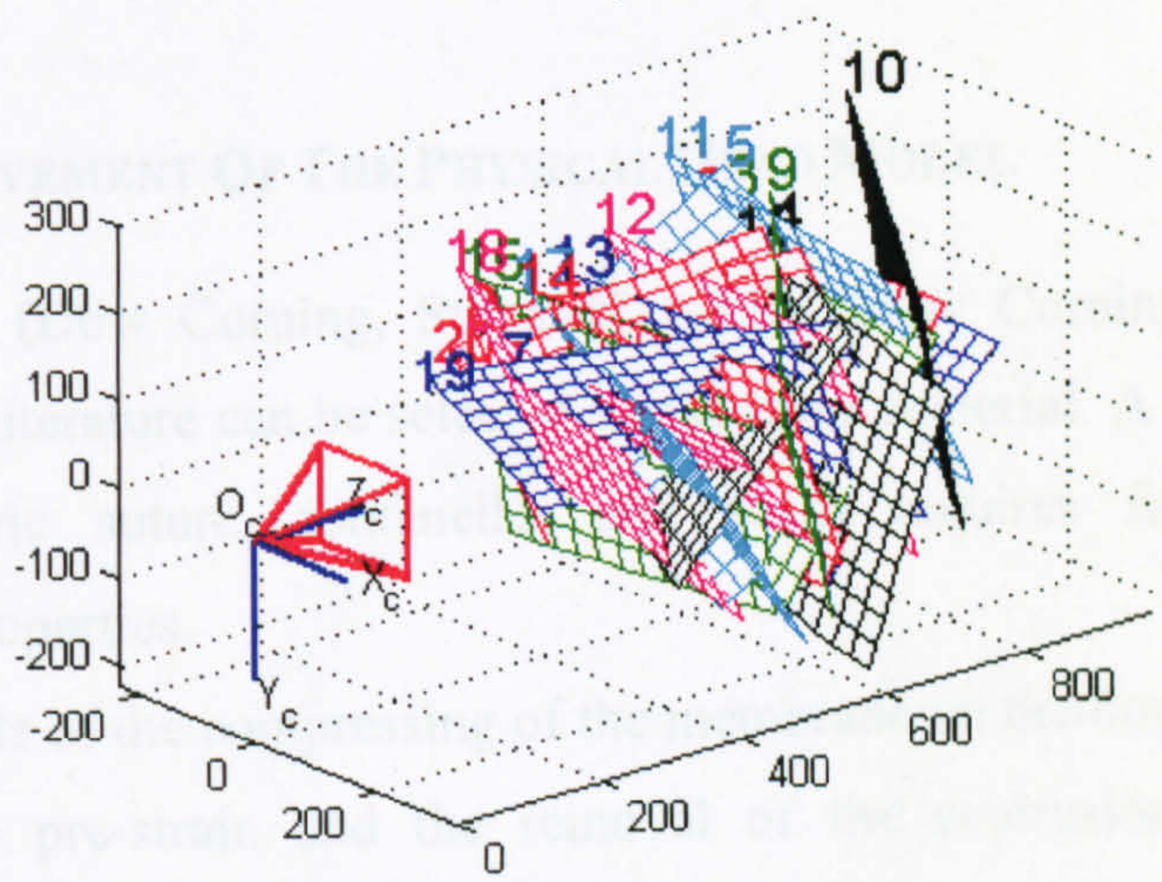

Figure 10.3. *Camera Calibration Toolbox for Matlab® (Jean-Yves Bouguet, Caltech, 2007).*

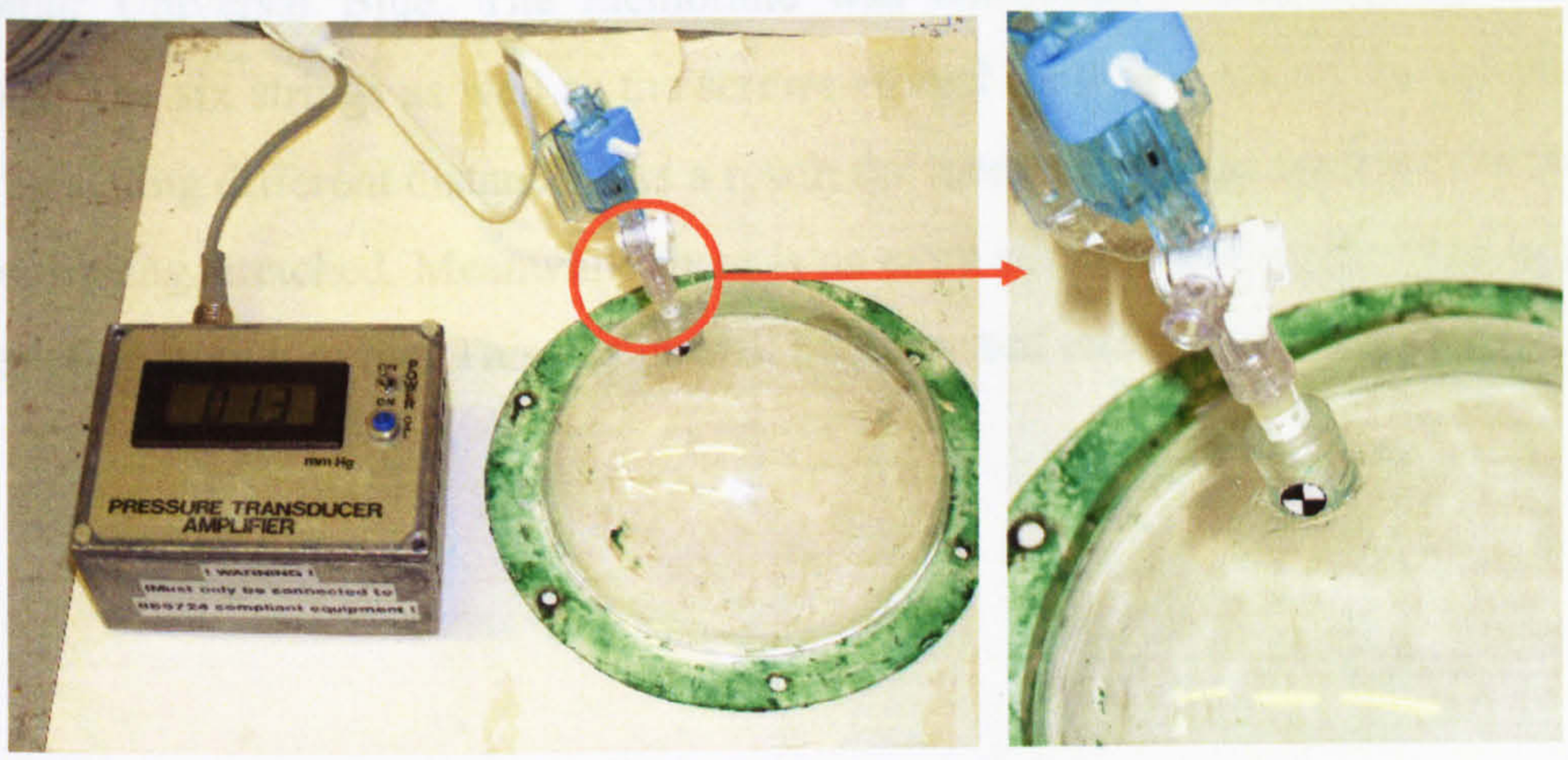

Figure 10.4. *Pressure sensor and its connection on the dome.*

10.4. THE PRESSURE TRANSDUCER (Figure 10.4)

The original design of both the experimental open and closed model involved a medical luer on the top of the dome. It was used for mounting a pressure transducer to caputure the pressure distribution inside the dome. However, the current design of the data requisition cell did not have enough channels for the pressure transducers. This limitation could be improved by incorporating an additional parallel signal channel for the pressure transducer into the system.

10.5. THE IMPROVEMENT OF THE PHYSICAL HEAD MODEL

The silicone gel (Dow Corning, Sylgard® A&B) (Dow Corning Corporation 2008) according to the literature can be selected as the brain material. A replacement matieral for the paediatric suture, fontanelle, and scalp requires further study of the biomechanical properties.

The improvements of the compressing of the membrane on the dome should include the reduction of the pre-strain and the removal of the protrusions, while enable the assembly and the sealing efficiently in the new design. Figure 10.5 demonstrated the concept design of the new compression ring. It consists of one aluminium compression ring with six holes on the edge, six screws, six strings and the waterproof filling such as Hylomar Universal Blue. The membrane was compressed exteriorly on the dome surface. The six strings as well as the screws around the dome adjust the tension of the ring by setting different distances. As a result the membrane is compressed on the dome without being stretched. Meanwhile there is no extra structure inside the fluid to prevent the gelatine from moving. This design will be discussed and tested in future work.

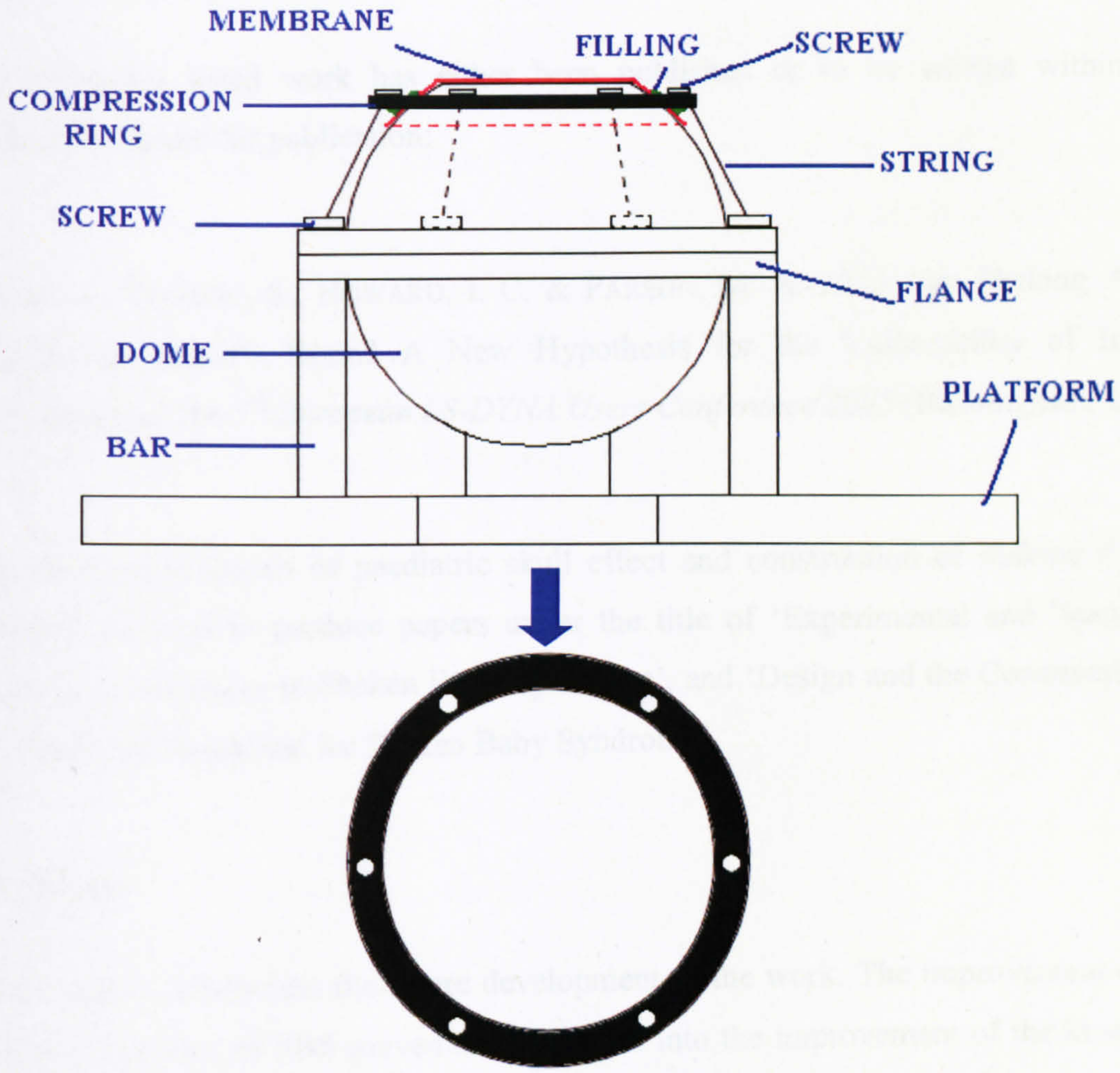

Figure 10.5. *The design of the new compression ring and the fixing of the membrane.*

10.6. The Analysis Of The Finite Element Model

The FE models of various infant heads revealed that the geometry, the material properties and the brain-skull boundary conditions are several crucial factors that affect the results. The FE model should be developed by using more accurate infant head data obtained from the MRI data, and by updating the material properties from the literature. The Eulerian method for the FSI representation of the brain-CSF-skull is encouraged.

the pre-strain on the membrane and the protrusion inside the fluid should be removed during the assembly of the membrane by the compression ring to improve the motion of the gelatine.

The future numerical model should have improved geometric details, the correct material properties and improved brain-skull boundary conditions. The Eulerian method, which was used for brain-CSF-skull boundary representation, is an advanced method to simulate the fluid structure interaction (FSI) better than the current Lagrangian or 1-point ALE analyses. Finally the previous and the future publications of the author were listed by the end of this chapter.

REFERENCES

AGAMANOLIS, D. P. 2006 Chapter 4 Traumatic Brain Injury and Increased Intracranial Pressure.*http://www.neuropathologyweb.org/chapter4/chapter4bContusions_dai_sbs.html.*

ADEYEMO, A. A. AND OMOTADE, O. O. 1999 Variation in fontanelle size with gestational age. *Early Human Development* **54**: 207-214.

ALEXANDER, R., SATO, Y. ET AL. 1990 Incidence of impact trauma with cranial injuries ascribed to shaking. *American Journal of Diseases of Children* **144**: 724–726.

ALLARD, P., STOKES, I. A. F. ET AL. 1995 Three dimensional analysis of human movement. Leeds, Champaign: *Human Kinetics*.

AOKI, N. AND MASUZAWA, H. 1984 Infantile Acute Subdural Hematoma-Clinical analysis of 26 Cases. *Journal of Neurosurgery* **61**: 273-280.

AOMURA, S., FUJIWARA, S. ET AL. 2003 Study on the influence of different interface conditions on the response of finite element human head models under occipital impact loading. *JSME international Journal Series C - Mechanical Systems, Machine Elements and Manufacturing* **46**(2): 583-593.

ARBOGAST, K. B., THIBAULT, K. L. ET AL. 1997 A High-Frequency Shear Device for Testing soft Biological Tissues. *Journal of Biomechanics* **30**(7): 757-759.

BBC 1997-2005 Shaken Baby Syndrome. *http://search.bbc.co.uk/cgi-bin/search/results.pl?scope=all&edition=d&q=Shaken+Baby+Syndrome.*

BBC 1998 UK Shaken Baby Syndrome. from http*://news.bbc.co.uk/1/hi/uk/136249.stm.*

BERKOVITZ, B. K. B. AND MOXHAM, B. J. 1998 *A Text book of head and neck anatomy.* London, England, Wolfe Medical Publications Ltd.

BERTOCCI, G. E., PIERCE, M. C. ET AL. 2003 Using Test Dummy Experiments to Investigate Pediatric Injury Risk in Simulated Short-Distance Falls. *Archives of Pediatrics & Adolescent Medicine* **157**: 480-486.

BOITO, S. M. E., LAUDY, J. A. M. ET AL. 2002 Three-Dimensional US Assessment of Hepatic Volume, Head Circumference, and Abdominal Circumference in Healthy and Growth-Restricted Fetuses. *Radiology* **223**(3): 661-665.

BOSCH REXROTH AG 2005 Basic Mechanic Element (MEG 9.0), *Bosch Rexroth AG Linear Motion and Assembly Technologies.*

BOUGUET, J. Y. 2007 Camera Calibration Toolbox for Matlab. *http://www.vision.caltech.edu/bouguetj/calib_doc/.*

BRADSHAW, D. R. S., IVARSSON, J. ET AL. 2001 Simulation of acute subdural hematoma and diffuse axonal injury in coronal head impact. *Journal of Biomechanics* **34**: 85-94.

BRANDS, D. W. A. 2002 Predicting brain mechanics during closed head impact: numerical and constitutive aspects. *PhD thesis. Department of Mechanical Engineering. Eindhoven, The Netherlands, Eindhoven University of Technology.*

BRANDS, D. W. A., PETERS, G. W. M. ET AL. 2004 Design and numerical implementation of a 3-D non-linear viscoelastic constitutive model for brain tissue during impact. *Journal of Biomechanics* **37**: 127-134.

BRANDT, I., HODES, D. T. ET AL. 1986 Anterior fontanelle as a window to the brain-normal values and timing of closure. *Klinische Padiatrie* **198**(4): 330-6.

BROUSSEAU, T. J., KISSOON, N. ET AL. 2005 Vitamin K Definciency Mimicking Child Abuse. *The Journal of Emergency Medicine* **29**(3): 283-288.

BRUDENELL, E. 2000 Finite Element Modelling of the Eye Relating to Non-Accidental Injury to Children. *MSc thesis. Department of Mechanical Engineering. Sheffield, UK, University of Sheffield.*

BUBCHENCO, L. O. AND HANSMAN C. 1966 Intrauterine growth in length and head circumference as estimated form live births at gestational ages from 26 to 42 weeks. *Pediatrics* **37**(3): 403-408.

BYLSKI, D. I., KRIEWALL, T. J. et al. 1986 Mechanical behaviour of fetal dura mater under large deformation biaxial tension. *Journal of Biomechanics* **19**(1): 19-26.

CAFFEY, J. 1972 On the Theory and Practice of Shaking Infants. Its Potential Residual Effects of Permanent Brain Damage and Mental Retardation. *American Journal of Diseases of Children* **124**: 161-169.

CANAPLE, B., RUNGEN, G. ET AL. 2003 Towards a finite element head model used as a head injury predictive tool. *International Journal of Crashworthiness* **8**: 41-52.

CHADWICK, D. L., CHIN, S. ET AL. 1991 Deaths from Falls in Children: How Far is Fatal? *The Journal of Trauma* **31**(10): 1353-1355.

CHALLIS, J. H. 1994 A procedure for determining rigid body transformation parameters. *Journal of Biomechanics* **28**(6): 733-737.

CHENG, J., CIROVIC, S. ET AL.2005 Can Shaking Alone Damage an Infant's Brain? A New Hypothesis for the Vulnerability of Infant. *The 5th European LS-DYNA Users Conference* 2005 Birmingham, UK.

CHU, C. S., LIN, M. S. ET AL. 1994 Finite Element Analysis of Cerebral Contusion. *Journal of Biomechanics* **27**(2): 187-194.

COATS, B. AND MARGULIES, S. S. 2006 Material Properties of Porcine Parietal Cortex. *Journal of Biomechanical Engineering* **39**(13): 2521-2525.

COOK, R. D., MALKUS, D. S. ET AL. 2002 *Concepts and applications of finite element analysis*. New York, John Wiley & Sons. Inc.

CORY, C. Z. AND JONES M. D. 2003 Can shaking alone cause fatal brain injury?-A biomechanical assessment of the Duhaime shaken baby syndrome model. *Medicine, Science and the Law* **43**(4): 317-333.

COTE, C. J., TODRES, I. D. ET AL. 2001 A Practice of Anesthesia for Infants and Children. Philadelphia, W.B. Saunders Company.

DALLY, J. W. AND RILEY, W. F. 1991 Experimental Stress Analysis. Singapore, McGraw-Hill International Editions.

DARVISH, K. K. AND CRANDALL, J. R. 2001 Nonlinear Viscoelastic Effects in Oscillatory Shear Deformation of Brain Tissue. *Medical Engineering & Physics* **23**: 633-645.

DONOHOE, M. 2003 Evidence-Based Medicine and Shaken Baby syndrome Part I: Literature Review, 1966-1998. *American Journal of Forensic Medicine and Pathology* **24**(239-242).

DOW CORNING CORPORATION 2008 Electronics Gels *http://www.dowcorning.com/content/etronics/etronicsgels/etronics_gels_stdov.asp*

DUHAIME, A. C., GENNARELLI, T. A. ET AL. 1987 The shaken baby syndrome-A clinical, pathological, and biomechanical study. *Journal of Neurosurgery* **66**: 409-415.

ESPOSITO, A. 1980 *Fluid Power with Applications*. Englewood Cliffs, N.J., Prentice-Hall, Inc.

ESTES, M. S. AND MEELHANEY, J. H. 1970 Response of Brain Tissue of Compressive Loading. *Journal of Biomechanical Engineering* **70**: 1-4.

FALLENSTEIN, G. T. AND HULCE, V. D. 1969 Dynamic Mechanical Properties of Human Brain Tissue. *Journal of Biomechanics* **2**: 217-226.

FUNG, Y. C. 1993 Biomechanics-Mechanical Properties of Living Tissues. New York, Springer-Verlag.

GEDDES, J. F., HACKSHAW, A. K. ET AL. 2001 Neuropathology of inflicted head injury in children-I. Patterns of brain damage. *Brain* **124**(2001): 1290-1298.

GEDDES, J. F. AND PLUNKETT J. 2004 The evidence base for shaken baby syndrome-We need to question the diagnostic criteria. *British Medical Journal* **328**: 719-720.

GEDDES, J. F., TASKER, R. C. ET AL. 2003 Dural haemorrhage in non-traumatic infant deaths: does it explain the bleeding in 'shaken baby syndrome'? *Neuropathology and Applied Neurobiology* **29**: 14-22.

GEDDES, J. F., VOWLES, G. H. ET AL. 2001 Neuropathology of inflicted head injury in children-II. Microscopic brain injury in infants. *Brain* **124**(2001): 1299-1306.

GEDDES, J. F. AND WHITWELL, H. L. 2004 Inflicted head injury in infants. *Forensic Science International* **146**(2004): 83-88.

GEFEN, A. AND MARGULIES, S. S. 2004 Are in vivo and in situ brain tissues mechanically similar? *Journal of Biomechanics* **37**: 1339-1352.

GENNARELLI, T. A. AND THIBAULT, L. E. 1982 Biomechanics of Acute Subdural Hematoma. *Journal of Trauma* **22**: 680-686.

GERE, J. M. AND TIMOSHENKO, S. P. 1997 Mechanics of materials. Boston, PWS publishing company.

GILCHRIST, M. D. 2003 Modelling and Accident Reconstruction of Head Impact Injuries. *Key Engineering Materials* **245-246**: 417-430.

GILLILAND, M. AND FOLBERG, R. 1996 Shaken babies—Some have no impact injuries. *Journal of Forensic Sciences* **41**: 114-116.

GOLDSMITH, W. 2001 The State of Head Injury Biomechanics: Past, Present, and Future: Part 1. *Critical Reviews in Biomedical Engineering* **29**(5&6): 441-600.

GOLDSMITH, W. AND MONSON, K. L. 2005 The State of Head Injury Biomechanics: Past, Present, and Future Part 2: Physical Experimentation. *Critical Reviews in Biomedical Engineering* **33**(2): 105-207.

GOLDSMITH, W. AND PLUNKETT, J. 2004 A Biomechanical Analysis of the Causes of Traumatic Brain Injury in Infants and Children. *The American Journal of Forensic Medicine and Pathology* **25**(2): 89-100.

GUTHKELCH, A. N. 1971 Infantile Subdural Hematoma and Its Relationship to Whiplash Injuries. *British Medical Journal* **2**: 430-431.

HALL, J. G., Froster-iskenius, U. G. et al. 1995 Handbook of normal physical measurements. Oxford, Oxford Medical Publications.

HALLERT, B. 1960 Photogrammetry-Basic principles and general survey. New York, McGraw-Hill Book Company.

HALLQUIST, J. O. 1998 LS-DYNA Theoretical Manual. Livermore, CA, USA, Livermore Software Technology Corporation.

HALLQUIST, J. O. 2003 LS-DYNA Keyword User's Manual. Livermore, CA, USA, Livermore Software Technology Corporation.

HAMILTON, W. R. 1853 "Lectures on Quaternions". *Royal Irish Academy.*

HARDING, B., RISDON, R. A. et al. 2004 Shaken baby syndrome-Pathological diagnosis rests on the combined triad, not on individual injuries. *British Medical Journal* **328**: 720-721.

HAYAKAWA, K., KONISHI, Y. ET AL. 1993 Cerebrospinal fluid flow void in children. *Neuroradiology* **35**(443-446).

HEPCOMOTION 2004 HepcoMotion e-catalog & 3D CAD, Hepco Slide Systems Limited.

HILDEBOLT, C. F., VANNIER, M. W. ET AL. 1990 Validation study of skull three-dimensional computerized tomography measurements. *American Journal of Physics Anthropology* **82**(3): 283-294.

HOFFMAN, J. M. 2005 A Case of Shaken Baby Syndrome After Discharge From the Newborn Intensive Care Unit." *Advances in Neonatal Care* **5**(3): 135-146.

HORGAN, T. J. AND GILCHRIST, M. D. 2003 The creation of three-dimensional finite element models for simulating head impact biomechanics. *International Journal of Crashworthiness, 8(4): 353-366.*

HOSE, D. R., HOWARD, I. C. ET AL. 2003 Modelling of Non-Accidental Injury in Infants: The Significance of Intra-Ocular Damage in the Shaken Baby Syndrome. *Research Proposal. Sheffield, UK, University of Sheffield.*

ILLINGWORTH, R. S. 1987 The development of the infant and young child normal and abnormal. New York, Chruchill Livingstone.

IVARSSON, J., VIANO, D. C. ET AL. 2000 Strain relief from the cerebral ventricles during head impact: experimental studies on natural protection of the brain. *Journal of Biomechanics* **33**: 181-189.

JOHNSON, E. A. C. AND YOUNG, P. G. 2005 On the Use of a Patient-specific Rapid-Prototyped Model to Simulate the Response of the Human Head to Impact and Comparison with Analytical and Finite Element Models. *Journal of Biomechanics* **38**: 39-45.

KLEIVEN, S. AND HOLST, H. V. 2002 Consequences of head size following trauma to the human head. *Journal of Biomechanics* **35**: 153-160.

KLINICH, K. D. 2002 Estimating Infant Injury Criteria and Impact Response Using Crash Reconstruction and Finite Element Modelling. *41th Stapp Car Crash Conference.*

KRIEWALL, T. K. 1981 Bending Properties and Ash Content of Fetal Cranial Bone. *Journal of Biomechanics* **14**: 73-79.

KRIEWALL, T. K. 1982 Structural, Mechanical, and Material Properties of Fetal Cranial Bone. *American Journal of Obstetrics and Gynecology* **143**: 707-714.

LANGLEY, J. 2000 Development of a 3D Finite Element Model of the Human Head to Simulate Shaken Baby Syndrome. *MSc thesis. Department of Mechanical Engineering. Sheffield, UK, University of Sheffield.*

LANIR, Y. 1994 Plausibility of Structural constitutive Equations for Isotropic Soft Tissues in Finite Static Deformations. *Journal of Applied Mechanics* **61**: 695-702.

LAPEER, L. J. AND PRAGER, R. W. 2001 Fetal head moulding: finite element analysis of a fetal skull subjected to uterine pressures during the first stage of labour. *Journal of Biomechanics* **34**(2001): 1125-1133.

LEE, M. C., MELVIN, J. W. ET AL. 1989 Finite Element Analysis of Traumatic Subdural Hematoma. *31th Stapp Crash Car Conference*, USA.

LEFANU, J. AND EDWARDS-BROWN, R. 2004 Letters-Patterns of presentation of the shaken baby syndrome. *British Medical Journal* **328**: 766-767.

LEHMAN, D. AND SCHONFELD, N. 1993 Falls from Heights: A Problem Not Just in the Northeast. *Pediatrics* **92**(1): 121-127.

LEVIHN, W. C. 1967 A cephalometric roentgenographic cross-sectional study of the craniofacial complex in fetuses from 12 weeks to birth. *American Journal of Orthodontics* **53**(11): 822-848.

LEWIS, F. L. AND STEVENS, B. L. 2003 Aircraft Control and Simulation, Wiley-IEEE.

LÖWENHIELM, P. 1974 Dynamic Properties of Parasagittal Bridging Veins. *Z Rechtsmed* **74**: 55-62.

LSTC 2005 LS-DYNA Advanced Course in ALE and Fluid/Structure Coupling. Livermore, CA, USA, Livermore Software Technology Corporation.

LUBCHENCO, L. O. AND HANSMAN, C. 1966 Intrauterine growth in length and head circumference as estimated form live births at gestational ages from 26 to 42 weeks. *Pediatrics* **37**(3): 403-408.

MALAS, M. A. AND SULAK, O. 2000 Measurements of Anterior Fontanelle during the Fetal Period" *Journal of Obstetrics and Gynaecology* **20**(6): 601-605.

MARGULIES, S. S. 1992 A Proposed Tolerance Criterion for Diffuse Axonal Injury in Man. *Journal of Biomechanics* **25**(8): 917-923.

MARGULIES, S. S. AND THIBAULT, K. L. 2000 Infant skull and suture properties: measurements and implications for mechanisms of paediatric brain injury. *Journal of Biomechanical Engineering* **122**: 364-371.

MARGULIES, S. S., THIBAULT, L. E. ET AL. 1990 Physical Model Simulations of Brain Injury in the Primate. *Journal of Biomechanics* **23**(8): 823-836.

MARTIN, G. H. 1969 Kinematics and dynamics of machines. New York, McGraw-Hill book company.

MCMINN, R. 1994 Colour atlas of head and neck anatomy. London, England, Times Mirror International Publishers Limited.

MCPHERSON, G., K. 1980 The elastic modulus of fetal cranial bone: a first step towards an understanding of the biomechanics of fetal head moulding. *Journal of Biomechanics* **13**: 9-16.

MCPHERSON, G. K. 1980 Fetal Head moulding: An investigation utilizing a finite element model of the fetal parietal bone." *Journal of Biomechanics* **13**: 17-26.

MEDELE, R. J., STUMMER, W. ET AL. 1998 Terson's Syndrome in Subarachnoid Henorrhage and Severe Brain Injury Accompanied by Acutely Raised Intracranial Pressure. *Journal of Neurosurgery* **88**: 851-854.

MENDIS, K. K., STALNAKER, R. L. ET AL. 1995 A Constitutive Relationship for Large Deformation Finite Element Modeling of Brain Tissue. *Journal of Biomechanical Engineering* **117**: 279-285.

MENKE, J., A., MILES, R. ET AL. 1982 The fontanelle tonometer: A noninvasive method for measurement of intracranial pressure. *The Journal of Pediatrics* **100**(6): 960-963.

MERIAM, J. L. AND KRAIGE, L. G. 1998 Engineering mechanics - Vol.2 : Dynamics. New York, Chichester : Wiley.

METZ, H., MEELHANEY, J. H. ET AL. 1970 A Comparison of the Elasticity of Live, Dead, and Fixed Brain Tissue. *Journal of Biomechanics* **3**: 453-458.

MILLER, K. 1999 Constitutive model of brain tissue suitable for finite element analysis of surgical procedures. *Journal of Biomechanics* **32**: 531-537.

MILLER, K. 2005 Method of Testing Very Soft Biological Tissues in Compression. *Journal of Biomechanics* **38**: 153-158.

MILLER, K. AND CHINZEI, K. 1997 Constitutive modelling of brain tissue: experiment and theory. *Journal of Biomechanics* **30**: 1115-1121.

MILLER, K., CHINZEI, K. ET AL. 2000 Mechanical properties of brain tissue in-vivo: experiment and computer simulation. *Journal of Biomechanics* **33**: 1369-1376.

MINNS, R. A. AND BUSUTTIL, A. 2004 Patterns of Presentation of the Shaken Baby Syndrome. *British Medical Journal* **328**: 766-767.

MOAVENI, S. 2003 Finite element analysis: theory and application with ANSYS - Theory and application with ANSYS. New Jersey, Pearson Education.

MOFFITT, F. H. AND MIKHAIL, E. M. 1980 Photogrammetry. New York, Harper & Row, Inc.

MONSON, K. L. AND GOLDSMITH, W. 2003 Axial mechanical properties of fresh human cerebral blood vessels. *Journal of Biomechanical Engineering* **125**: 288-294.

MOONEY, M. 1940 A Theory of Large Elastic Deformation. *Journal of Applied Mechanics*: 582-592.

MOORE, K. L. 1999 Clinically oriented anatomy, Lippincott Williams & Wilkins.

MORAD, Y., AVNI, I. ET AL. 2004 Shaken baby syndrome without intracranial hemorrhage on initial computed tomography. *Journal of AAPOS (American Association for Pediatric Ophthalmology and Strabismus)* **8**: 521-527.

NAHUM, A. M. 1977 Intracranial Pressure Dynamics During Head Impact. *21th Stapp Car Crash Conference*, Warrandale.

NICOLLE, S., LOUNIS, M. ET AL. 2005 Shear Linear Behavior of Brain Tissue over a Large Frequency Range. *Biorheology* **42**: 209-223.

NORGREN 1998 Pneumatics'98, Norgren Technical.

O'RIORDAIN, K., THOMAS, P. M. ET AL. 2003 Reconstruction of real world head injury accidents resulting from falls using multibody dynamics. *Clinical Biomechanics* **18**: 590-600.

OKA, K., RHOTON, A. L. ET AL. 1985 Microsurgical Anatomy of the Superficial Veins of the Cerebrum. *Neurosurgery* **17**(5): 711-748.

OLOVSSON, L., SOULI, M. ET AL. 2003 LS-DYNA – ALE Capabilities (Arbitrary-Lagrangian-Eulerian) Fluid-Structure Interaction Modeling. Livermore, CA, USA, Livermore Software Technology Corporation.

OMMAYA, A. K. 1968 The Mechanical Properties of Tissues of The Nervous System *Journal of Biomechanics* **July 1**(2): 127-138.

OMMAYA, A. K. 1968 Whiplash Injury and Brain Damage. *The Journal of the American Medical Association* **204**(4): 75-79.

OMMAYA, A. K. 1971 Tolerances for Cerebral Concussion from Head Impact and Whiplash in Primates. *Journal of Biomechanics* **4**: 13-21.

OMMAYA, A. K., GOLDSMITH, W. ET AL. 2002 Biomechanics and neuropathology of adult and paediatric head injury. *British Journal of Neurosurgery* **16**(3): 220-242.

OPPENHEIM, A. V. 1975 Digital signal processing, Englewood Cliffs, N.J.; London: Prentice-Hall, 1975.

OWEN, S. 2002 Simulation of Brain/Skull Interaction During Traumatic Events. *MSc thesis. Department of Mechanical Engineering. Sheffield, UK, University of Sheffield.*

PAMIDI, M. R. AND ADVANI, S. H. 1978 Nonlinear Constitutive Relations for Human Brain Tissue. *Journal of Biomechanical Engineering* **100**: 44-48.

PARR, A. 1998 Hydraulics and Pneumatics-A technician's and engineer's guide. Oxford, Butterworth-Heinemann.

PLUNKETT, J. 2001 Fatal Pediatric Head Injuries Caused by Short-Distance Fall. *The American Journal of Forensic Medicine and Pathology* **22**(1): 1-12.

PRANGE, M. T., COATS, B. ET AL. 2003 Anthropomorphic Simulations of Falls, Shakens, and Inflicted Impacts in Infants. *Journal of Neurosurgery* **99**: 143-150.

REMONTET, L., MAMELLE, N. ET AL. 1999 Growth Charts from Birth to 6 Years: Weight, Height and Cranial Circumference Growth According to Sex. *Archives des Pediatrie* **6**: 520-529.

RICHARDS, P. G., BERTOCCI, G. E. ET AL. 2006 Shaken Baby Syndrome. *Arch Dis Child* **911**(205-206).

RUAN, J. S., KHALIL, T. ET AL. 1991 Human Head Dynamic Response to Side Impact by Finite Element Modelling. *Journal of Biomechanical Engineering* **113**(276-283).

RUAN, J. S., KHALIL, T. ET AL. 1994 Dynamic Response of The Human Head to Impact by Three-Dimensional Finite Element Analysis. *Journal of Biomechanical Engineering* **116**: 44-50.

SANDERS, M. J. AND MCKENNA, K. 2001 Chapter 22, Head and Facial Trauma. *Mosby's Paramedic Textbook, 2nd revised Ed.*, Mosby.

SCHUNCK, S. 2007 Shaken Baby Syndrome-Increasing of Accuracy for The Movement Measurements of The Jelly Model. *Erasmus Project. Department of Mechanical Engineering. Sheffield, UK, University of Sheffield.*

SCHWARTZ, J., H. 1995 Skeleton keys-An introduction to human skeletal morphology development and analysis. New York, Oxford University Press.

SHANNON, P. AND BECKER, L. 2001 Mechanisms of brain injury in infantile child abuse. *The Lancet* **358**: 686-687.

SHEPARD, S. 2004 Head Trauma. from http://www.emedicine.com/med/topic2820.htm.

SHIGLEY, J. E. AND MISCHKE, C. 2001 Mechanical engineering design, Boston: McGraw Hill.

SINCLAIR, D. 1998 Human growth after birth. Oxford, Oxford University Press.

SOBOLESKI, D., MCCLOSKEY, D. ET AL. 1997 Sonography of normal cranial sutures. *American Journal of Roentgenology* **168**: 819-821.

SPOOR, F., JEFFERY, N. ET AL. Imaging Skeletal growth and evolution. Development, Growth and Evolution: implications for the study of the hominid skeleton. P. O'Higgins and M. Cohn. London, Academic Press.

STEDMAN'S 2006, Stedman's Medical Dictionary 28th Edition Illustrated in Colour. Baltimore, Lippincott Williams & Wilkins, A wolters Kluwer Company

STEIN, K. M., RUF, K. ET AL. 2005 Representation of Cerebral Bridging Veins in Infants by Postmortem Computed Tomography. *Forensic Science International.* **163**(1-2): 93-101

TAYLOR, Z. AND MILLER, K. 2004 Reassessment of brain elasticity for analysis of biomechanisms of hydrocephalus. *Journal of Biomechanics* **37**(8): 1263-1269.

THIBAULT, K. L. AND MARGULIES, S. S. 1998 Age-dependent material properties of the porcine cerebrum: effect on pediatric inertial head injury criteria. *Journal of Biomechanics* **31**(1998): 1119-1126.

TROSSEILLIE, X., TARRIERE, C. et al. 1992 Development of a F.E.M. of the Human Head According to a Specific Test Protocol. *Proceedings of the 36th Stapp Car Crash Conference*, SAE Paper No. 922527, Society of Automotive Engineers, 235–253.

TURQUIER, F. 1996 Validation Study of a 3D Finite Element Head Model Against Experimental Data. *Proceedings of the 40th Stapp Car Crash Conference,* SAE Paper No. 962431, Society of Automotive Engineers, 283-294.

UENO, K., MELVIN, J. W. ET AL. 1995 Development of Tissue Level Brain Injury Criteria by Finite Element Analysis. *Journal of Neurotrauma* **12**(4): 695-706.

USCINSKI, R. H. 2006 Shaken Baby Syndrome: An Odyssey. *Neurol Med Chir (Tokyo)* **46**: 57-61.

VAN DEN BOGERT, A. J., READ, L. ET AL. 1996 A method for inverse dynamic analysis using accelerometry. *Journal of Biomechanics* **27**(7): 949-954.

VAN LIERDE, DEPREITERE, C., B. ET AL. 2005 Cerebral bridging vein rupture in humans: an experimental evaluation. *Proceedings of the IUTAM Symposium on Impact Biomechanics: From Fundamental Insights to Applications* **124**:305-312

VANNIER, M. W., CONROY, G. C. ET AL. 1985 Three-dimensional cranial surface reconstructions using high-resolution computed tomography. *American Journal of Physics Anthropology* **67**: 299-311.

VERSACE, J. 1971 A review of the Severity Index. *15th Stapp Car Crash Conference.*

WALSH, E. K. AND SCHETTINI 1984 Calculation of Brain Elastic Parameters in Vivo. *American Journal of Physiology* **247(4 Pt 2)**:R693-700

WASSERMAN, J. R. 2007 Diffuse Axonal Injury. from http://www.emedicine.com/radio/topic216.htm.

WEISSTEIN, E. W. 2004 Quaternion. from http://mathworld.wolfram.com/Quaternion.html.

WHITE, F. M. 2003 Fluid Mechanics 5th [International]ed. New York, London, MeGraw-Hill.

WHITING, W. C. 1998 Biomechanics of musculoskeletal injury. Leeds, Champaign, Ill. ; Leeds : Human Kinetics.

WILLIAMS, R. A. 1991 Injuries in Infants and Small Children Resulting from Witnessed and Corroborated Free Falls. *The Journal of Trauma* **31**(10): 1350-1351.

WILLINGER, R., TALEB, L. ET AL. 1995 Head Biomechanics: From The Finite Element Model to The Physical Model. *International Conference on the Biomechanics of Impacts (IRCOBI), September 13–15, 1995, Brünnen (CH)* (1995), pp. 245–259.

WITTEK, A. AND OMORI, K. 2003 Parametric study of effects of brain-skull boundary conditions and brain material properties on responses of simplified finite element brain model under angular acceleration impulse in sagittal plane. *JSME international Journal Series C - Mechanical Systems, Machine Elements and Manufacturing* **46**(4): 1388-1399.

WOLFSON, D. R., MCNALLY, D. S. ET AL. 2005 Rigid-body modelling of shaken baby syndrome. *Proceedings of the Institution of Mechanical Engineers. Part H. Journal of engineering in medicine* **219**: 63-70.

WOLTRING, H. J., LONG, K. ET AL. 1994 Instantaneous helical axis estimation from 3-D video data in neck kinematics for whiplash diagnostics. *Journal of Biomechanics* 27(12): 1415-1432.

WORDEN, K. 1990 Data processing and experiment design for the restoring force surface method, part I: Integration and differentiation of measured time data. *Mechanical system and signal processing* 4(4): 259-319.

ZATSIORSKY, V. M. 2002 Kinematics of human motion. III: Human Kinetics. Leeds, Champaign.